Proceedings of the 5th International
Digital Human Modeling Symposium

baua: Report

Proceedings of the 5th International Digital Human Modeling Symposium

This publication are the conference proceedings of the "5th International Digital Human Modeling Symposium". The symposium was held from June 26-28, 2017 at the Fraunhofer-Institute for Communication, Information Processing and Ergonomics (FKIE), in cooperation with the Federal Institute for Occupational Safety and Health (BAuA).
The responsibility for the contents of this publication lies with the authors.

Table of Contents

Abstract

The proceedings present the the peer-reviewed articles of the 5th International Digital Human Modeling Symposium. The symposium was held from June 26-28, 2017 at the Fraunhofer-Institute for Communication, Information Processing and Ergonomics (FKIE), in cooperation with the unit "human factors and ergonomics" of the Federal Institute for Occupational Safety and Health (BAuA).

Key words:

Digital Human Modeling, Digital Human Simulation

Kurzreferat

Der Tagungsband beinhaltet die Artikel (peer-reviewed) des „5th International Digital Human Modeling Symposium". Das Symposium wurde vom 26. bis 28. Juni 2017 am Fraunhofer-Institut für Kommunikation, Informationsverarbeitung und Ergonomie (FKIE) in Bonn Bad Godesberg, in Kooperation mit der Fachgruppe „Human Factors, Ergonomie" der Bundesanstalt für Arbeitsschutz und Arbeitsmedizin (BAuA) durchgeführt.

Schlagwörter:

Digitale Menschmodelle, Humansimulation

Introduction

Digital Human Models (DHM) have matured from simple drawing templates and topics of abstract research to complex and integrated design and analy-sis tools for multiple industrial applications. They are frequently used by engineers, designers and others to allow an early consideration and inclusion of characteristic human factors in the design of new products, processes and systems. DHMs support the ergonomic evaluation of new product designs during early design stages by modeling anthropometry, posture, motion or predicted discomfort. It is also an effective and efficient way to accelerate the total design process.

Today, most DHMs model human anthropometry and biomechanics to facilitate, e.g., sight, reach, and comfort analyses. Others model human simulate performance and allow planning and optimization of workplaces and production processes. By integrating different types of DHM systems in a holistic approach, more comprehensive simulations and analyses during early design phases will become possible. Such a holistic approach will increase speed of design for innovative products and production systems significantly.

The Digital Human Modeling Symposium is an international forum for re-searchers to report their latest innovations, summarize state-of-the-art as well as exchange ideas, results, and visions in all fields of digital human modeling research. Topics of interest include, but are not limited to:

- DHM validation methods
- Anthropometry & Biomechanics
- Elderly, disabled and other special populations
- Human body segments and joints modeling
- Industrial applications of DHM
- Impact and deformation analysis
- Manikin models standardization
- Mental/cognitive models and integrated models
- Mesh and skinning modeling
- Modeling of subjective responses
- Motion Capture reconstruction
- Musculoskeletal human models
- Posture and motion simulation
- Virtual reality

In 2017, the symposium was held at the Fraunhofer-Institute for Communication, Information Processing and Ergonomics (FKIE) in cooperation with the Federal Institute for Occupational Safety and Health (BAuA) in association with the International Ergonomics Association Technical Committee on Human Simulation and Virtual Environments.

Technical Session 1 – Mesh and skinning modeling

Scataglini et al.:
Smart Clothing for Human Performance Evaluation: Biomechanics and Design Concepts Evolution

Scataglini, S. [1,2], Truyen, E. [1], Perego, P. [2], Gallant, J. [1], Van Tiggelen, D. [3], Andreoni, G. [2]

[1] Royal Military Academy, Brussels, Belgium
[2] Politecnico di Milano, Design Dept., Milan, Italy
[3] Military Hospital Queen Astrid, Belgium

Abstract

Evaluating human performance and identifying critical constraints in the human-machine-environment system is a challenge: the high number of variables and their mutual relationships and influence on the multiple degrees of freedom make it a complex task.

Despite this complexity an ecologic approach is needed to analyse the system in its natural functioning. Smart clothing provides a solution to monitor in real time mechanical, environmental, and physiological parameters in this ecological and non-intrusive approach. These parameters can be used to detect gesture or specific patterns in movements, to design more efficient specific training programs for performance optimization, and screen for a potential cause of injury.

Designing a fitting and comfortable sensing garment should consider at the beginning the analysis of human dimensions and requested actions to be carried out. Starting from an anthropometric approach collected on 1615 Belgian soldiers, the paper presents all the steps involved in designing our functional smart clothing for human performance evaluation, taking in consideration the biomechanical evaluation of user gestures such as fitness, shooting, climbing, cycling, etc.

Physiological and biomechanical acquisitions of the soldier's performances, wearing the smart clothing, were monitored and quantified permitting the redesign and the technological refinement of the garment.

Key words:

Smart Clothing, Human Factor, Performance, Monitoring

1   Introduction

Stress, training, fatigue, and environmental conditions have a great influence on human-machine-environmental system performance (SCATAGLINI et al., 2016). Combining data from the different components of the system is mandatory. Smart clothing technology together with environmental and performance data, provides a detailed live feedback from the wearers, monitoring their physical function and recording change in ability over time.

The design of a smart cloth is crucial to obtain the best results. Identifing all the steps involved in the functional design clothing workflow can prevent a decrease in wearer's performance, ensuring a more successful design.

The smart cloth represents a "second skin" that has a close, "intimate" relation with the human body. The relation is physiological, psycological, biomechanical and ergonomical.
Effectiveness of functional wear is based on the integration of all these considerations into the design of a smart clothing system (GUPTA, 2011). The design process begins through the analysis of the anticipated user and the identification of the end-user's needs. Design and technological issues are the two main macro areas involved in the process together with the esthetical one (ANDREONI, 2015). Once these criteria have been established, the initial esthetic design is created within the framework of the user's needs. Design decisions are evaluated and re-evaluated based on physiological, ergonomical and biomechanical monitoring of the wearer's performance. As a consequence, alternative solutions are generated for each decision. Alternatives are then evaluated on a weighted scale, to arrive at the best solution or combination of solutions for each decision.
Iterative co-design steps are used to influence the modifications made in the next prototype, and the design process begins again. This ensures that corrections have been made before the design is finalized. When resources permit, multiple designs will be compared to each other, in order to examine the strengths and weaknesses of each.

This paper presents all the steps involved in the workflow for the design of our smart t-shirt for monitoring a soldier's performance. The smart t-shirt is capable of monitoring the heart rate (ECG) and the 3D body accelerations of the trunk in real time. Bluetooth communication allows the real-time communication with a custom-made APP suited for the purpose. The information can be either stored or immediately transferred to a nearby computer for the successive analysis. Smart t-shirt capabilities can potentially monitor the soldier's performance in terms of training, injuries, and psychological status monitoring. Physiological, ergonomical and biomechanical evaluation of soldier's performance were considered for the functional need of the end-user.

2   Garment co-design workflow
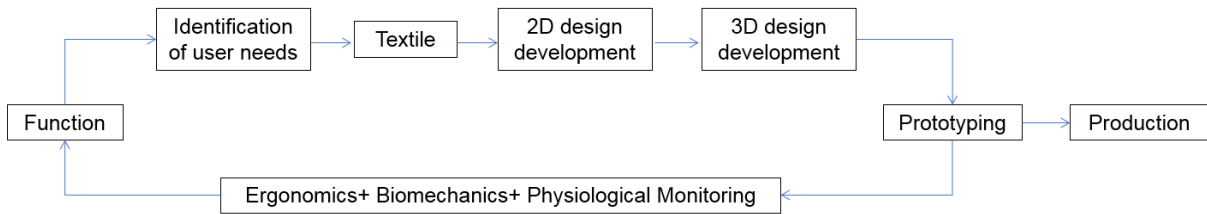
Fig. 2.1   Co-design workflow

At the beginning of the workflow (see Figure 2.1), we identified the user's need through a questionnaire collected on a population. The needs and the wishes were transformed in product requirements. After that, the product requirements were translated in design requirements for the functional design cloth.

Starting from an anthropometrical data retrieval on 1615 soldier database called "Total Health" we defined the "average anthropometrical soldier measure" (SCATAGLINI et al. 2016). To obtain the single segment length we used Drillis and Contini tables (DRILLIS et al.1966) that expresses the segment length as a function of the body height. Thanks to this calculation we were able to define the horizontal (width at chest, waist) and vertical measurement (sleeve length, total length) of the smart cloth t-shirt.

2.1   Fabric selection and traditional pattern for physical demands

Flattened pattern cutting begins with the drafting of the standard blocks that represents the silhouette of the smart garment. A first draft was designed taking in consideration the body mapping of sweating in male athletics (SMITH et al., 2011) in Figure 2.2.
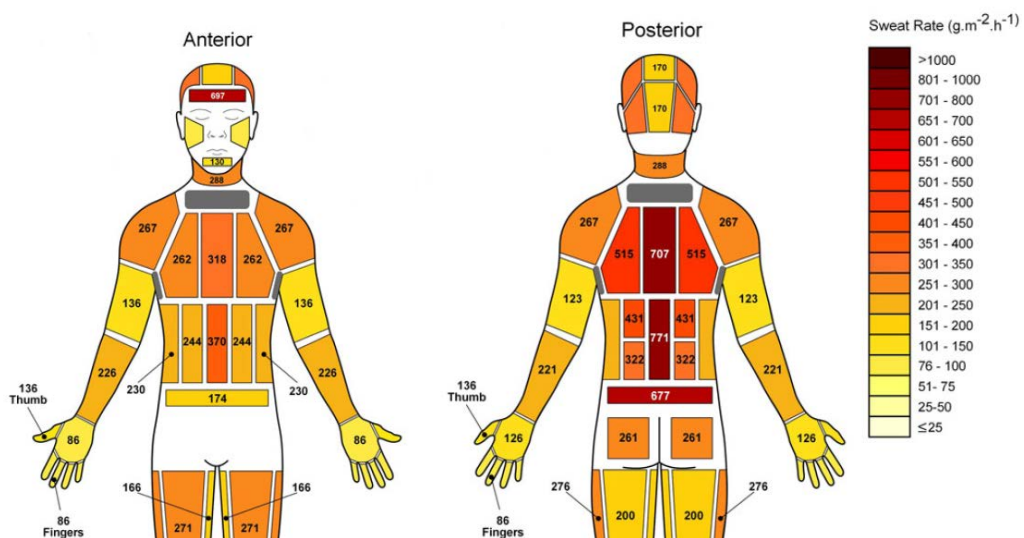
Fig. 2.2   Body mapping of sweating in male athletics (SMITH et al., 2011).

Two different textiles were combined, trying to respect the sweat rate of the subject. The first (80% Microfibre PA/20%EA (LYCRA®), weight 230 g/m^2) was used as a principle structure because of the reduced elongation and sweating rate. Despite the high number of grams per meter it is 50% tinner than any other LYCRA® of similar weight. This make it also breathable but less than the other. In fact, the second textile (72% Microfibre PA/28%EA (LYCRA®), weight 164 g/m^2) was used in higher sweating rate areas and where more freedom and elongation was necessary. Regarding the performance both materials have honeycomb construction allowing air circulating between the fibers. A bonding technique with adhesive tape was used to join the fabrics together creating the 3D shell.

A Digital Human Modelling (DHM) of our soldier wearing the smart garment was created through the use of an open source programme (Blender). The armature or skeleton was scaled with the average anthropometric soldier measurements (SCATAGLINI et al., 2016) using an inertial system programme (Mocap Studio, YEI Technology ®).

Through Adobe ® Mixamo ® we created the avatar mesh that was imported as a collada file in Blender. Next, every single 2D pattern was transformed through Adobe ® Photoshop ® in a texture, able to create the smart t-shirt in Blender (see Figure 2.3 and Figure 2.4).

Fig. 2.3   DHM and flattening of 3D patterns (front)

Fig. 2.4   Design of 3D patterns (back)

The second draft involves another concept were the smart garment is composed of a single textile (72% Microfibre PA/28%EA (LYCRA®), weight 164 g/m^2). This concept

aim at reducing the number of patterns and consequently the number of seams of the fabrics permitting more comfort and flexibility (see Figure 2.5).

Fig. 2.5   DHM (second draft) and flattening of 3D patterns (front)

3   Functional Evaluation

The evaluation of functioning in the two prototypes started with biomechanical, ergonomical and physiological requirements of the end-user during different tasks. The physiological evaluation was specifically related to the position of the garment and the adherence ('fit') of the textile to the body, while the biomechanics and ergonomics dealt with the thermal discomfort and agility.

3.1   Physiological Evaluation

Once the technical and esthetical details of the cut and the proportion of the initial garment prototypes have been fitted, the next step was the introduction of smart technology into the garment. Normally, at that phase technical and clothing experts meet for evaluating the functional design process that integrates embedded sensors into the cloth. In order to have a qualitative and numerical evaluation our team decided to choose different types of fabrics in which to introduce the electrodes area.

Three different textiles have been chosen for these experiments: a first textile (72% Microfibre PA/28%EA (LYCRA®), weight 164 g/m^2), a second bonded textile (72% Microfibre PA/28%EA (LYCRA®), weight 328 g/m^2) and finally a third bonded textile (72% Microfibre PA/28%EA (LYCRA®),weight 370 g/m^2). For every textile a belt of 8 cm width was created that was introduced at chest level for the electrodes placement. Due to the body positioning decision, the textile needed to be fix adherent and at the same time needed to be elastic and rigid combined. At the middle of each belt two snap buttons were created in order to attach the sensing device technology.

Three different belts were tested, joined with adhesive technique at the middle of the first prototype. All data processing was performed off-line using MATLAB R2016b, (The MathWorks Inc., Natick, MA, 2016). Three different monitorings of the subjects in standing demonstrate the wearability and the reliability of the garment. The belt

with less weight was rejected due to the stretch and flexibility that provoke an instability of the sensing device to the chest causing an artifact in the signal movement.

The second bonded textile solved this problem, eliminating the artifact of movement due to the adherence to the chest and the vertical stiffness of the fiber (Figure 3.1).
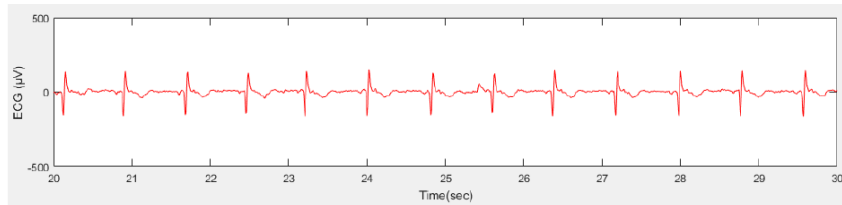
Fig. 3.1 ECG signal from the second textiles ((72% Microfibre PA/28%EA LYCRA®), weight 328g/m^2))

The difference between the second and the third fabric was only the weight. Therefore the second was chosen because it enables more breathability on the chest. For the second prototype the third bonded fabric with more g/m^2 was chosen.

This shirt has already a breathable fabric (72% Microfibre PA/28% EA (LYCRA®), weight 164 g/m2) lighter than the other requires a rigid structure on the chest to block the elasticity of the fiber in order maintain the electrodes adherence to the skin as whell as the sensing technology stable to the chest.

3.2   Ergonomical and Biomechanical Evaluation

Comfort includes the physiological and psychological aspects on one hand, and the biomechanical and ergonomical aspects on the other.

More attention should to be paid to understanding ergonomic issues, heat stress implications and the relationship between the task and the clothing. The degree of thermophysiological comfort, is defined by the thermophysiological characteristics of the textile as well the range of motion while performing a task.

Starting from this assumption we evaluated the thermophysiological comfort of the two prototype smart shirts using a thermal image from a FLIR camera, (FLIR ®, Wilsonville, OR, USA with an infrared resolution of 4,800 pixels, MSX resolution 320x240, thermal sensitivity below 0.15 °C, and accuracy of ±2 °C) applied on the digital human model (DHM), (Figure 3.2 and Figure 3.3).

Fig. 3.2   Thermophisyological evaluation in DHM on the first prototype after 30 minutes of exposure

Fig. 3.3   Thermophisyological evaluation in DHM on the second prototype after 30 minutes of exposure

Comparing the first prototype with the second one,we saw a strong difference in temperature between the first and the second prototype. The second prototype revealed to be more thermophysiologically comfortable than the first.

The second evaluation wants to compare the two shirts in terms of limit of range of motion while we are performing a task.

We start with the first prototype at the shooting range to verify a limit in flexion-extension during the aiming. Comfort questionnaires of ten volunteer subjects after the shooting give the same results revealing that the first t-shirt is unconfortable at the armpits. This limits the range of motion on the shoulder during a simple gesture as a flex-extension.

The second t-shirt solved that limit due the use of stretch fabric at the armpits. That feature allows us to extend the use of the smart t-shirt in sports where a high range of motion at the armpit is requested such as climbing, shooting, rowing, archery, basket ball, volley ball and especially military training (Figure 3.4). A three-dimensional (3D) accelerometer on the trunk can quantify and evaluate the symmetry and the intensity of a motory task giving a complete evaluation of the performance (Figure 3.5).

Fig. 3.4   Use of the smart t-shirt during sport activity
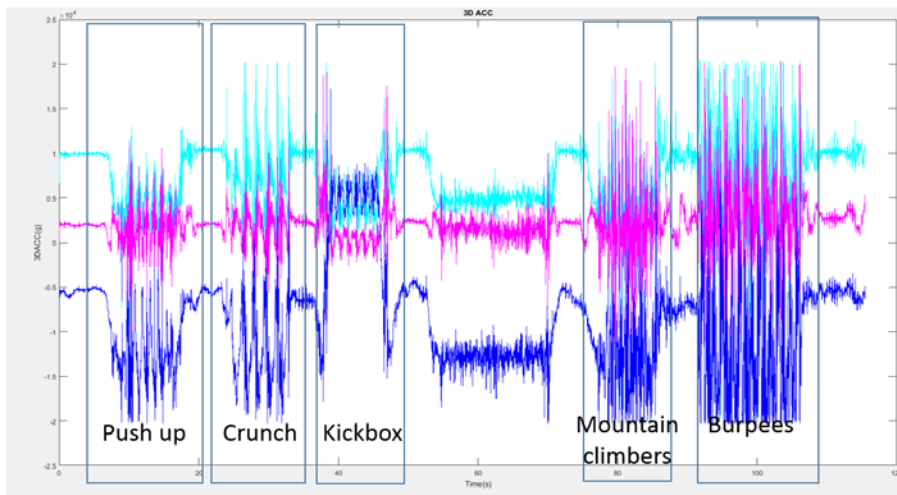
Fig. 3.5   3D accelerations during sport training wearing the smart t-shirt

4   Conclusion

Iterative studies on the co-design workflow permitted us to define the final functional cloth that will be used for monitoring soldier's performance in terms of training, injuries, and psychological status monitoring. This technology can provide essential data, enabling the development of strategies to increase resilience and prevent unacceptable impairment of performance. Smart t-shirt monitoring capabilities can be extended from the lab to the field permitting a continuous monitoring of the wearer's performance.

We acknowledge Alain Vanhove of the Royal Military Academy for his contribution in the 3D modeling. We would also like to thank all the participants in this study.

List of references

Andreoni, G.; Standoli, C. E.; Perego, P.: Defining Requirements and Related Methods for Designing Sensorized Garments, Sensors 2016,16*(6), pp. 769.*

Andreoni, G.; Sistemi di sensori indossabili per il monitoraggio : dalla Ricerca al Mercato, in in Bonfiglio, A.; Cerutti, S.; De Rossi, D.; Magenes, G. (eds): Sistemi indossabili intelligenti per la Salute e la Protezione dell'Uomo, ed. Patron, 2008, pp. 357-384. – Andreoni, G.; Il fattore Uomo nel Design Aracne Editrice, 2012.

https://www.blender.org/

Drillis, R.; Contini R.: Body segment parameters. DHEW 1166-03. New York University, School of Engineering and Science, 1966.

Gupta, D.: Design and engineering of functional clothing, Indian Journal of Fibre & Textile Research*, Vol.36,* December 2011, pp. 327-335.

https://it.mathworks.com/

https://www.mixamo.com

Scataglini, S.; Andreoni, G.; Truyen, E.; Warnimont, L.; Gallant, J.; Van Tiggelen, D.: Design of smart clothing for Belgian soldiers through a preliminary anthropometric approach", Paper, Proceedings 4th DHM Digital Human Modeling, Montréal, Québec, Canada, 2015.

Smith, C. J.; Havenith, G.: Body mapping of sweating patterns in male athletes in mild exercise-induced hyperthermia. Eur J Appl Physiol. 2011 Jul;111(7):1391-404.

Wakaiki et al.:
Individualization of Musculoskeletal Model to Analyze Pelvic Floor Muscles Activity

Wakaiki, T.[1], Tanaka, T.[1], Shimatani, K.[2], Iida, T.[2], Tsuchiya, Y.[1], Sugihara, K.[3], Sugiyama, Y.[4]

[1] Hokkaido University, Japan
[2] Prefectural University of Hiroshima, Japan
[3] Kisaka Hospital, Japan
[4] Kanmon Medical Center, Japan

Abstract

Strengthening the Pelvic Floor Muscles is an effective means for preventing Stress Urinary Incontinence. Although it can be strengthened by training, there are individual differences in effect and it is need to develop training considering them. The cause of individual differences must be identified to develop the method. Since we could confirm that the individual differences in pelvic shape and posture from x-ray images, we hypothesized that such individual differences arise from shape and posture of the pelvis and proved this hypothesis. However, it is difficult to directly measure pelvic floor muscle activity. Therefore, we individualized a musculoskeletal model and analyzed pelvic floor muscles activity with Opensim and proved the hypothesis by comparing the result of the standard model and the individualized model.

Key words:

Pelvic Floor Muscles, Individualization, Musculoskeletal Model

1 Introduction

Stress Urinary Incontinence (SUI) is a disease that frequently reduces quality of life in women. The prevalence of urinary incontinence in Japanese women is about 30%, about 80% of which have symptoms of SUI(MIKAKO,OKAMOTO et al., 2012). As a characteristic symptom, incontinence occurs without the desire to urinate when coughing, sneezing or holding heavy things. The cause is the relaxation of the Pelvic Floor Muscle due to obesity and aging and its damage due to childbirth. Thus, strengthening the Pelvic Floor Muscles is an effective means for preventing SUI. Currently, it can be strengthened by training or wearing a support underwear. However, there are individual differences in effect with these methods. Consequently, it is necessary to develop the training program or support underwear considering individual difference.

Therefore, we hypothesized that such individual differences arise from shape and posture of the pelvis and proved this hypothesis. However, we performed a simulation using a Musculoskeletal Model reflecting individual difference since it is difficult to direct measure Pelvic Floor Muscles activity. Accordingly, we performed individualization of Musculoskeletal Model from the X-ray images and analyze Pelvic Floor Muscles activity in this study.

2 Pelvis Individualization

In this study, we individualize pelvis form and posture of musculoskeletal model. Figure 2.1 shows the process of individualizing standard pelvis model. Firstly, we obtain feature points and feature angles in individual pelvis with the 2 X-ray images, sagittal and coronal, and Motion capture data measured at same time. Secondly, the form of standard pelvis model is deformed with GFFD(Generalized Free-Form Deformation) processing (KITAJIMA KATSUHIRO et al., 2008) using the obtained feature points and feature points of standard model. Finaly, the deformed model is fitted to individual pelvis posture with feature angles obtained from X-ray images and from deformed model. The detail is described below.
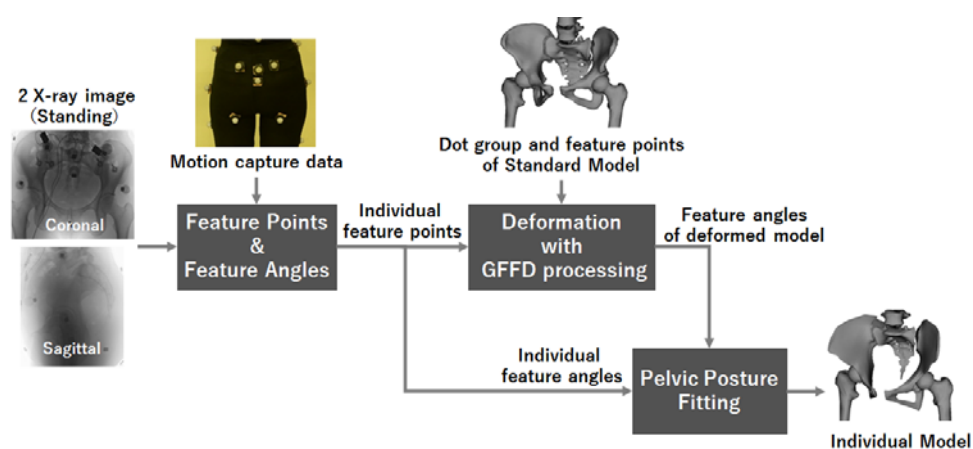
Fig. 2.1 Process of pelvis individualization

2.1 Individualization of pelvis form

Magnification factor at earch feature point

The feature points is plotted on pelvis, 31 points on sacrum, 36 points on hip bone (Figure 2.2). It is necessary to obtain the three-dimensional coordinates of the feature points for deforming the pelvis. However, it is not possible to obtain accurate three-dimensional coordinates with simple projection because of the magnification factor included in the X-ray image. Accordingly, the magnification factor at feature points are calculated by solving below simultaneous equations with the magnification factor at the motion capture marker in the X-ray image. ($^{S}m_i$: magnification factor at feature points on sagittal image, $^{C}m_i$: magnification factor at feature points on coronal image, $^{S}m_B$: magnification factor at marker on sagittal image, $^{C}m_B$: magnification factor at marker on coronal image, $^{S}D_i$: distance between feature points and marker on sagittal (mm), $^{C}D_i$: distance between feature points and marker on coronal (mm), $^{S}\mu$: distance per 1 pixel on sagittal image (mm/px) , $^{C}\mu$: distance per 1 pixel on coronal image image (mm/px), $^{S}u_i$: pixel at feature points on sagittal image (px), $^{C}u_i$: pixel at feature points on coronal image image (px), $^{S}u_B$: pixel at marker on coronal image image (px), $^{C}u_B$: pixel at marker on coronal image image (px))

$$^{S}D_i = {}^{S}\mu({}^{S}m_i{}^{S}u_i - {}^{S}m_B{}^{S}u_B)$$
$$^{C}D_i = {}^{C}\mu({}^{C}m_i{}^{C}u_i - {}^{C}m_B{}^{C}u_B)$$

(2.1)

$$^{S}m_i = {}^{S}m_B - \frac{^{S}D_i}{^{S}d_f}, \quad ^{C}m_i = {}^{C}m_B - \frac{^{C}D_i}{^{C}d_f}$$

(2.2)

We got three-dimensional coordinate of each feature point with obtained magnification factor, and deformed pelvis with GFFD processing (KITAJIMA KATSUHIRO et al., 2008).
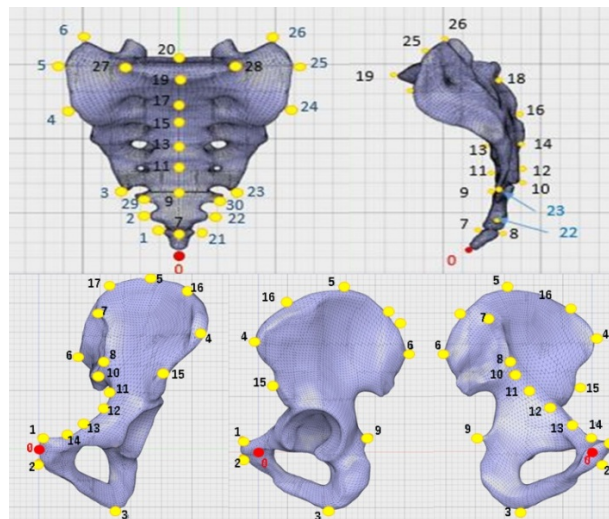
Fig. 2.2 Feature points

Result of deformation

Individual model, standard model and X-ray image are projected from front and side for visual evaluating(Figure 2.3). it is showed that Individual model is deformed from standard model in Figure 2.3. The hip bone width of individual model is nearer to one of the X-ray image than standard model. The position of ASIS, PSIS, acetabulum and pubic bone are nearer than standard model. Furthermore, sacrum size of individual model is also near to one of the X-ray image. As this results, it is suggested that we can individualize the pelvis form with this method. However, the position of ischial spine of individual model leaves more from one of the X-ray image. In this study, the feature points are plotted on X-ray image manually. It is thought that the position is not fitted since it is difficult to confirm the position of that in the coronal X-ray image.
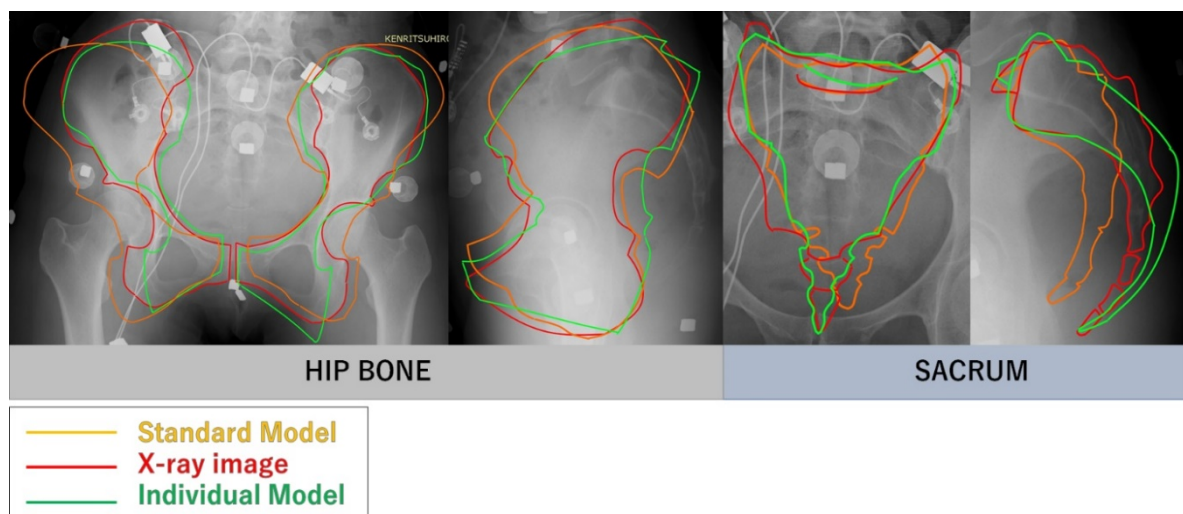
Fig. 2.3   Projection of result

2.2   Individualization of pelvis posture

Feature angles

We defined 8 Pelvic Posture Angles as shown in Figure 2.4 to quantitatively evaluate the pelvic posture. Front sacrum (FS) is the angle between horizon and wing of sacrum. Center Edge (RCE and LCE) is the angle between perpendicular and the line connecting the center of the femoral head and the upper edge of the acetabulum(MINETA 2016). ASIS-PSIS (RAP and LAP) is the angle between horizon and the line connecting the ASIS and PSIS(HARUAKI KOGA et al., 2014). Sacrum Slope (SS) is the angle between horizon and base of sacrum(LE HUEC et al., 2011). Pelvic tilt (RPT and LPT) is the angle between perpendicular and the line connecting the center of the femoral head and the center of base of sacrum(LE HUEC et al., 2011).

The difference between the feature angles on the X-ray image (φ) and on standard model (θ) is defined as pelvic distortion degree (ε) and used as index for evaluating pelvic distortion. By adding these pelvic distortion degrees to the corresponding joint angle of the musculoskeltal model, it refelects the individual pelvis posture.

$$\theta = [\theta_{LCE} \quad \theta_{RCE} \quad \theta_{LAP} \quad \theta_{RAP} \quad \theta_{SS} \quad \theta_{FS} \quad \theta_{LPT} \quad \theta_{RPT}]^T$$

$$\varphi = [\varphi_{LCE} \quad \varphi_{RCE} \quad \varphi_{LAP} \quad \varphi_{RAP} \quad \varphi_{SS} \quad \varphi_{FS} \quad \varphi_{LPT} \quad \varphi_{RPT}]^T$$

$$\varepsilon = \varphi - \theta = [\varepsilon_{LCE} \quad \varepsilon_{RCE} \quad \varepsilon_{LAP} \quad \varepsilon_{RAP} \quad \varepsilon_{SS} \quad \varepsilon_{FS} \quad \varepsilon_{LPT} \quad \varepsilon_{RPT}]^T$$

(2.3)
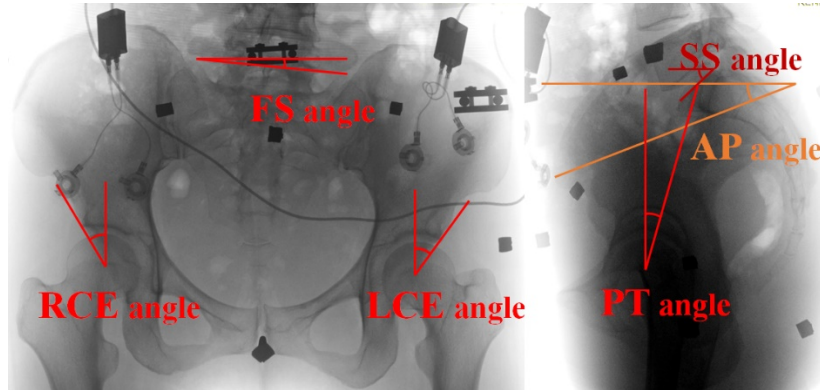
Fig. 2.4   Feature angles

2.2.1 Result of pelvis posture fitting

As the result, the pelvic distortion was expressed as shown in the Figure 2.6. Thus, it was suggested the it could be individualized with this method. However, it became an over expression in individual model. Therefore, we evaluate quantitatively by difference of feature angles from X-ray image (Figure 2.5). It shown that RCE and LPT angle in individual model are larger than in standard model in Figure 2.6. However, others are about 10 degrees less than in standard model. Both of RCE and LPT angle depend on the position of the center of femoral head and the shape of the acetabulum. Hence, this over expression is considered to be caused by deformation of the acetabulum shape. In the future, it seems to be need countermeasure such as establishing feature points at the acetabulum.

Fig. 2.5   Difference of feature angle from the X-ray (absolute value)
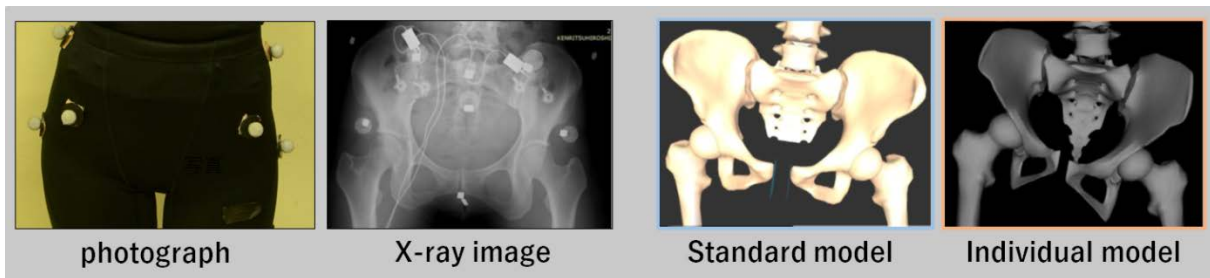
Fig. 2.6 Result of posture fitting

3 Analization of pelvic floor muscles activity

3.1 Pelvic floor muscles

In this study, we analyze of muscle activity with musculoskeletal model in Opensim3.3. This model dose not have pelvic floor muscles. Thus we added them, coccygeus muscle, iliococcygeus muscle and pubococcygeus muscle, as Figure 3.1. In this study, the tendon slack length was definded as a half of the distance between the muscle attachment positions because the true value of tendon slack length is unkown.
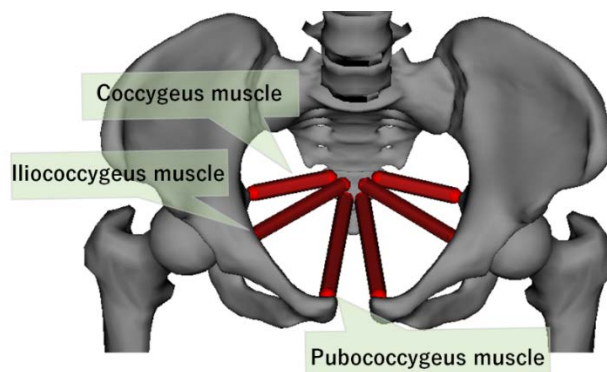
Fig. 3.1 Pelvic floor muscle

3.2 Analization with each model

We analyzed pelvic floor muscle activity during the hung out a laundly motion such as Figure 3.2 with standard model and individual model and compared the result. The laundly hanging task is a kind of general daily activity in Japan and this is not sexist choice.
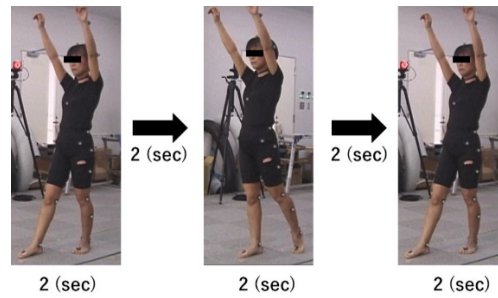
Fig. 3.2 Hung out a laundly motion

In Figure 3.3, it is shown that iliococcygues muscle activity analyzed with standard model and individual model. The blue one is right iliococcygues muscle, the light blue one is left one with standard model. The orange one is right iliococcygues muscle and the yellow one is left one with individual model. In individual model, the variation of the muscle activity during the motion is no large. On the other hand, in standard model, the muscle activity changes greatly. It shows that the pelvis form and posture can influence the pelvic floor muscles activity from this result. In the future, it is necessary that the pelvic floor muscle activity is measured directly for a larger group of subjects.
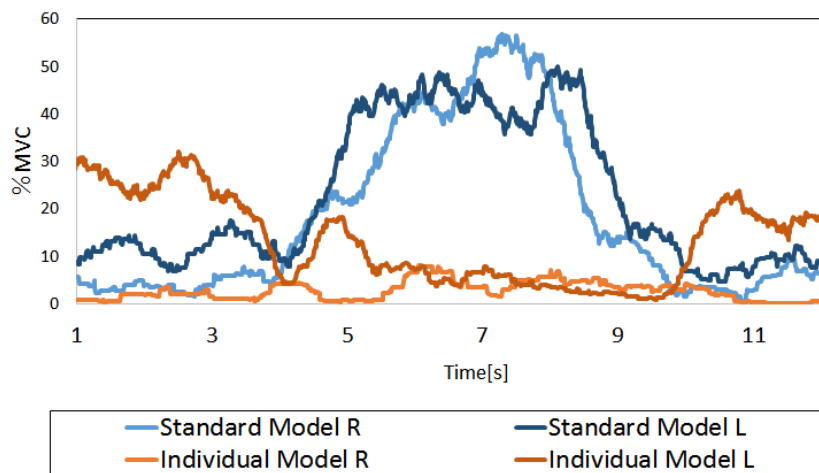
Fig. 3.3 Iliococcygues muscle activity analyzed with Standard and Individual Model

4 Conclusions

The musculoskeletal model is individualized with 2 X-ray images, coronal and sagittal. We suggested the method to deform pelvis form and fit its posture from the standard model. The result of analization with Opensim3.3 had difference between each model. Hence, it was suggested that the pelvis form and posture can influence the pelvic floor muscles activity.

List of references

Mikako, O.; Ryoko, M.; Yoshihide, H.: Development and evaluation of pelvic floor muscle exercise program for preventing stress urinary incontinence in postpartum women, Research-Aid Report 2012, Vol.27, pp.23-33

Kitajima, K.; Akagi, Y.; Yamauchi, A.; Okazawa, N.; Higuchi, Y.: A Study on Facial Modeling Based on the GFFD Method, The Japan Society Percision Engineering 2008,Vol.74, No.8, pp.883-890

Le Huec, J. C.; Aunoble, S.; Philippe, L.; Nicolas, P: Pelvic parameters: origin and significance. European Spine Journal 2011, 20(5), 564

Kogo, H.; Murata, J.: Effects of the Dominant Leg and Leg-crossing Preference on Pelvic Anteversion Angle, Rigakuryoho Kagaku 2014, 29(1), pp.39-43

Mineta, K.: CT-based morphological assessment of the hip joint in Japanese patients, The bone & joint journal 2016, VOL.98-B,No.9

Mucher & Bradtmiller:
Use of Landmarks in 3D Head and Face Models

Mucher, M. C., Bradtmiller, B.

Anthrotech, Yellow Springs OH, USA

Abstract

Landmarks are often used in the creation of models from 3-D scan data. However, there is little consensus on which, or how many, landmarks should be used. In this paper, we present the results of a series of experiments to identify whether or not there are critical landmarks. We used two complementary analytic tools to judge the effects of using different sets of landmarks. First, we conducted a Principal Component Analysis of the mesh vertices, using the total amount of explained variance as the comparison criterion. Second, we used a deviation analysis comparing the average PCA model of each test with the average model using all landmarks. Using head and face landmarks, the PCA analysis showed that there is little difference between models created using a full set of landmarks, and those created using fewer – or no – landmarks. The deviation analysis showed, however, that for individual areas of the face, landmarks were helpful in maximizing convergence.

Key words:

Principal component analysis, landmark, 3-D scan, model

1 Introduction

There are a number of ways to make use of 3D scan data. Many of these methods involve the creation of models representing the scanned images, and subsequent statistical analysis on the models rather than the scans. Further, models allow a user to place a digital human in novel poses or postures, distinct from the original posture of the human being scanned. There are a number of ways to create models from scans and some of these involve the use of landmarks (RAMAKRISHNA et al., 2012; YU et al, 2012). Because landmarks are also used in traditional anthropometry, there is an appeal to the use of landmarks, as this allows correspondence between 3D data analysis and the analysis of traditional tape and caliper measurements (BEN AZOUZ et al., 2006; KOUCHI and MOCHIMARU, 2011; KOUCHI et al., 2012; TOMA et al., 2008). Beyond the general appeal of using landmarks, however, there is no consensus on which, or how many, landmarks to use in any given analysis. In this paper, we present the results of a series of experiments to identify whether or not there are critical landmarks. We used two complementary analytic tools to judge the effects of using different sets of landmarks. First, we conducted a Principal Component Analysis of the mesh vertices, using the total amount of explained variance as the comparison criterion. Second, we used a deviation analysis comparing the average PCA model of each test with the average model using all landmarks. Our analysis is restricted to the head and face; whole body results may differ.

2   Methods

Some 120 male and female head scans were captured using a Cyberware 3-D digitizer with motion platform. We developed a list of 35 head and face landmarks, based on our experience with customer requests. These represent most of the landmarks from classic anthropometry and anatomy, as well as those useful for the development of goggles, eyewear, hearing protection and respiratory protection. The full landmark list is seen in Table 2.1. To examine that possibility that smaller sets of landmarks might produce adequate results, we created two subsets of the full list. The first is a subset that represents the edges of various facial features (Otobasion Superior and Inferior, for example), and the second subset included just the right side and midline landmarks. These lists are seen in Tables 2.2 and 2.3.

Table 2.1 Full Landmark List

Otobasion Inferior Right	Right Zygofrontale
Rhinion	Right Ectocanthus
Chelion Right	Right Endocanthus
Gnathion	Left Endocanthus
Infraorbitale Right	Left Ectocanthus
Tragion Left	Left Zygofrontale
Chelion Left	Left Frontotemporale
Otobasion Superior Left	Glabella
Sellion	Back of Head
Infraorbitale Left	Right Midpupil
Otobasion Superior Right	Left Midpupil
Subnasale	Left Alare
Right Alare	Menton
Pronasale	Vertex
Otobasion Inferior Left	Crown
Tragion Right	Right Zygion
Stomion	Left Zygion
Right Frontotemporale	

Table 2.2 Edge Landmark List

Otobasion Inferior Right	Right Alare
Chelion Right	Otobasion Inferior Left
Chelion Left	Right Ectocanthus
Otobasion Superior Left	Left Ectocanthus
Sellion	Left Alare
Otobasion Superior Right	

Table 2.3 Right Side and Midline Landmark List

Otobasion Inferior Right	Right Frontotemporale
Rhinion	Right Zygofrontale
Chelion Right	Right Ectocanthus
Gnathion	Right Endocanthus
Infraorbitale Right	Glabella
Sellion	Back of Head
Otobasion Superior Right	Right Midpupil
Subnasale	Menton
Right Alare	Vertex
Pronasale	Crown
Tragion Right	Right Zygion
Stomion	

The landmarks were previously placed, by trained investigators, on each of the scan images. We created models using mHBM (Medic Engineering Corporation, Kyoto, Japan) obtained through AIST. mBHM uses non-rigid mesh deformation to create a model by registering a generic template mesh with target scan data. We used this tool to create models with no landmarks, with all the landmarks and with the two landmark subsets. In a second set of experiments to identify significant effects of individual landmarks, we removed each of the landmarks from the analysis in sequence, leaving the remaining landmarks in place.

The homologous models have 4759 vertices, each with x, y and z coordinates. Those coordinate values were used in the Principal Component Analysis (PCA). The analysis was stopped when the contribution of the next component was less than 1% of the total variance.

We then use a deviation analysis (Geomagic, 3D Systems, North Carolina, USA) to compare the resulting model with the average PCA model.

3 Results - PCA

The PCA with all landmarks included explained 86.7% of the variance in the first 14 PCs. Recall that the analysis stopped when the next PC contributed less than 1% of additional variance. We treated this PCA with all the landmarks as the benchmark against which the smaller landmark sets would be compared. The results were not unexpected, since the number of landmarks was very small compared to the number of vertices in the PCA. In the case of the right side and midline landmarks only, 86.9% of the variance was explained (again, with 14 PCs), a slightly greater proportion than our benchmark. Similarly, the landmark subset with only feature edge landmarks explained 87.6% of the variation (14 PCs). Conducting the analysis with each landmark removed in turn, produced roughly similar results. The most important landmark of the set, by this criterion, was Otobasion Superior (Right), because without that landmark, the variance explained dropped to 85.6%, but clearly that is not a significant change. Removing all the landmarks also explained 87.6% of the variation, again, in 14 PCs.

4   Results – Deviation Analysis

Using Geomagic we compared the resulting models created with missing landmarks with the model created from all the landmarks. The deviation analysis shows, by color, where the two models are similar and where they are different. Green indicates complete concurrence. For example, Figure 5.1 shows the baseline model on the left, and the model created with a missing right frontotemporale landmark on the right. Figure 5.2 shows the models created without the right infraorbitale, and menton, respectively. The results for the rest of the landmarks are similar.

5   Discussion & Conclusion

These results suggest that, in general, landmarks on the head and face are not needed in the creation of a generic head model with mHBM. Indeed the model created without any landmarks explained more of the variation than the model created with all the landmarks. This suggests that the model creation process in mHBM is quite robust. It is also reflective of the vast number of vertices used in the PCA, relative to the small number of landmarks in question. Naturally, these results cannot necessarily be extended to other software applications, but similar results would be expected if models were created using a large number of scan vertices.

The deviation analysis, however, showed that landmarks are useful in controlling the model creation in specific areas of the head and face. There was a consistent pattern in which a missing landmark resulted in areas of mis-registration near the landmark. As a practical matter, individual landmarks appear to have particular utility when a model is intended for a specific purpose, such as the design of eyewear. For more generic use, or statistical analysis of the head as a whole, the landmarks seem to be less important.

Although the landmarks may have limited utility in the creation of head and face models, we have not tested their utility for models of other body parts or of the whole body. Further, landmarks continue to have utility as anchor points for analyses involving the interface of a product with a model (virtual try-on), and for analyses in which traditional measurements and 3D models are used together.

As a direction for further research, we plan to examine the distances between the landmarks placed on the scan, and the equivalent location of the landmark on the model. Both the standard deviations of those distances, as well as the mean distance over the sample will be of interest.
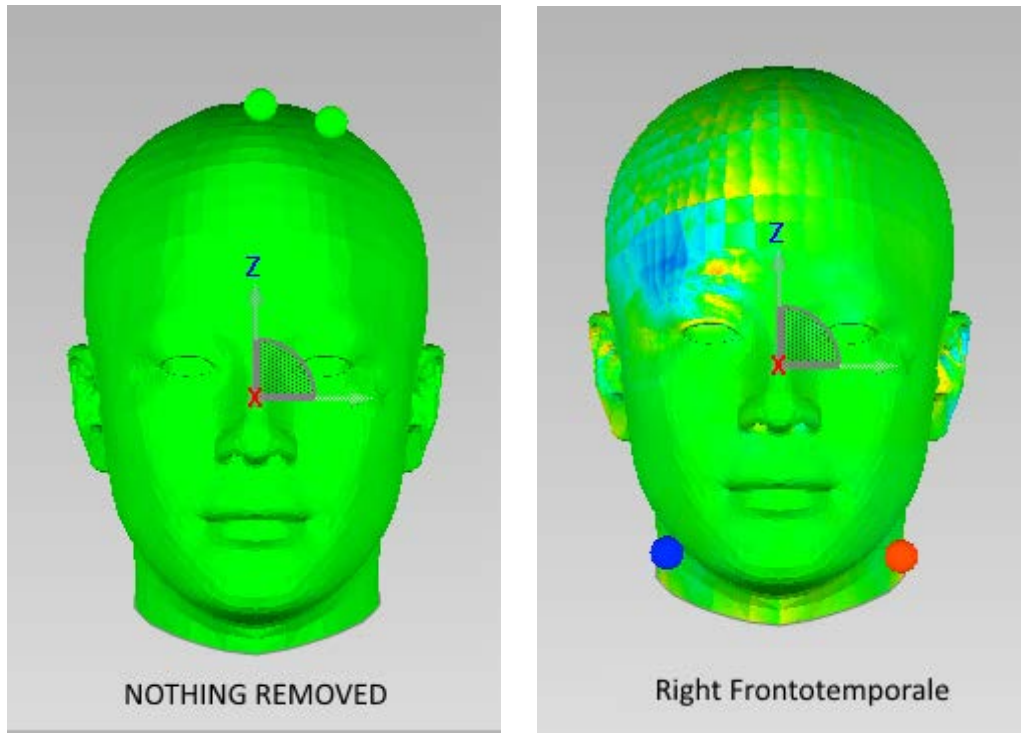
Fig. 5.1   Model with all landmarks (left); model missing right frontotemporale (right)
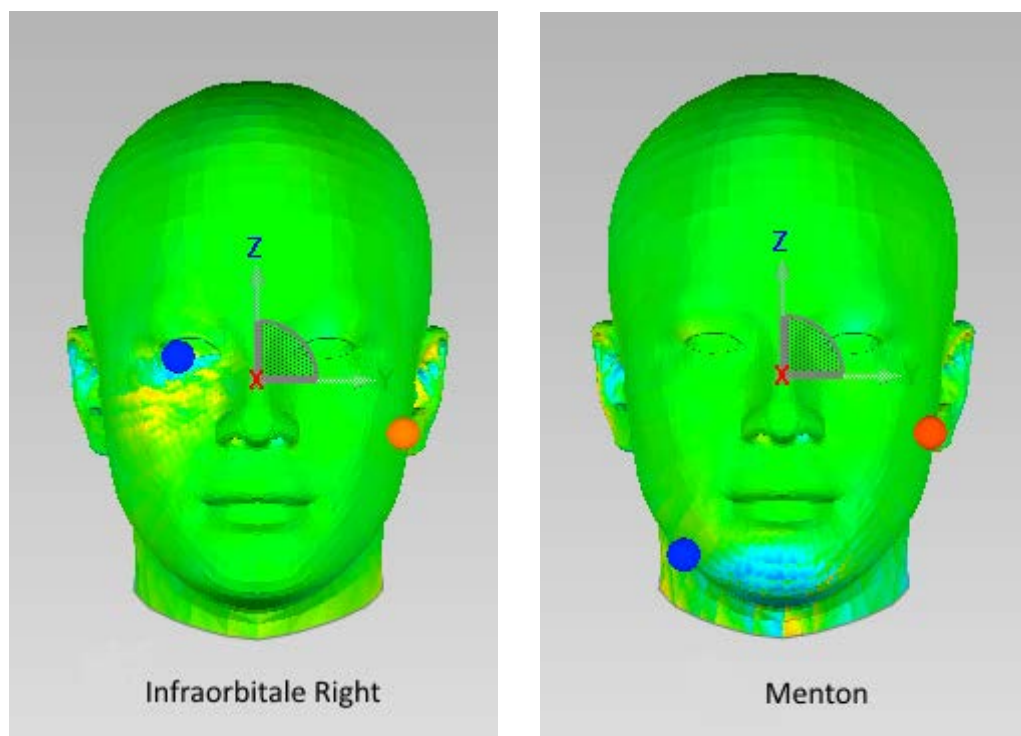
Fig. 5.2   Model missing right infraorbitale (left); model missing menton (right)

List of references

Ben Azouz, Z.; Shu, C.; Mantel, A.: Automatic Locating of Anthropometric Landmarks on 3D Human Models. Third International Symposium on 3D Data Processing, Visualization, and Transmission, IEEE DOI: 10.1109/3DPVT.2006.34.

Kouchi, M.; Mochimaru, M.; Bradtmiller, B.; Daanen, H.; Li, P.; Nacher, B.; Nam, Y.: A protocol for evaluating the accuracy of 3D body scanners. Work 41 (2012):4010-4017 DOI: 10.3233/WOR-2012-0064-4010.

Kouchi, M.; Mochimaru, M.: Errors in landmarking and the evaluation of the accuracy of traditional and 3D anthropometry. Applied Ergonomics 42:518-527, 2011.

Ramakrishna, V.; Kanade, T.; Sheikh, Y.: Reconstructing 3D Human Pose from 2D Image Landmarks. In: Fitzgibbon A, Lazebnik S, Perona P, Sato Y, Schmid C (eds) Computer Vision – ECCV 2012. ECCV 2012. Lecture Notes in Computer Science, vol 7575. Springer, Berlin, Heidelberg DOI: 10.1007/978-3-642-33765-9_41, 2012.

Toma, A.; Zhurov, A.; Playle, R.; Ong, E.; Richmond, S.: Reproducibility of facial soft tissue landmarks on 3D laser-scanned facial images. Orthodontics & Craniofacial Research 12: 33–42. DOI:10.1111/j.1601-6343.2008.01435, 2009.

Yu, Y.; Benson, S.; Cheng, W.; Hsiao, J.; Liu, Y.; Zhuang, Z.; Chen, W.: Digital 3-D Headforms Representative of Chinese Workers. Annals of Occupational Hygiene 56:113–122, 2012.

Technical Session 2 – Motion Capture reconstruction & posture and motion simulation

Regazzoni et al.:
Low cost motion capture for wheelchair posture evaluation in patients with spinal cord injury

Regazzoni, D., Rizzi, C., Vitali, A.

Università degli Studi di Bergamo, Italy

Abstract

Physician and physiotherapists assess patients with reduced mobility mainly through ob-servational tests. The direct interaction with the patient permits to evaluate many parame-ters, some of which are related to general health and psychological condition while some others refers to the level of muscular strength and control in doing specific tasks. This work refers to the research area of virtualization of the observational analysis performed by capturing patient's movements and elaborating data according to medical needs. The pa-per shows the use of commercial low-cost motion capture devices to record human motion, the transfer of acquired data to a digital human model and the extraction of desired infor-mation according to medical purpose. Moreover, raw data are elaborated and presented in a domain dependent form to be effective for physicians and caregivers. The method has been applied to the specific case of people who had a Spinal Cord Injury (SCI) that caused a paraplegic condition. Being seated for a long time on a wheelchair requires a correct static posture for a number of reasons including ease of transfers, mobility and skin pro-tection. Similarly, dynamic analysis of how pushes are performed can ease the correction of wrong habits with the goal of minimizing effort and preventing musculoskeletal diseases. A test with 7 male volunteer patients with SCI at different height has been performed. Motion analysis and data elaboration has been performed and is shown in the paper.

Key words:

Motion Capture, Digital Human Model, Rehabilitation, Spinal Cord Injury, wheelchair

1   Introduction

Human motion tracking for medical analysis is creating new frontiers for potential clinical and home applications (JARDIM et.al., 2016; BLUMROSEN et.al., 2016; KAMAL et.al., 2016; HAJIBOZORGI and ARJMAND, 2016). The state of the art of patient assessment con-cerning their walking progress or postural analysis after a major event occurred (e.g., neurologic or traumatic) is nowadays based on observational analysis. This is effective on stand-alone assessment, but it is highly subjective, results are qualitative and they highly depend on the physician performing the evaluation (FAY et.al., 2004; CHOW et.al., 2009).

Low-cost and easy to use hardware and software solutions are available for both track-ing and analyzing human body movements (COLOMBO et.al., 2013). What is still pre-venting their broad diffusion in hospitals and rehabilitation institutions is the last step of data analysis that is specific to each final application. Actually, general-purpose Digital Human Modeling (DHM) tools for analyzing human condition and behavior while performing a task are not specialized to any of the specific clinical need.

This may be due to the fact that developing this last step requires a considerable amount of work and deeply involves the collaboration of the medical staff. Specialized domain knowledge on the way to perform patients' assessment, together with the pa-rameters to be taken into account and empiric rules, need to be extracted. Some infor-mation can be found in literature, but most of the material is obtained with interviews to physicians and therapists and by observing their everyday common practices.

Once the required information is formalized and validated, it is possible to define the algorithms to extract the required parameters from the motion acquired and to use them to calculate physician-friendly output data, graphs or indexes.

2   Proposed method

This research work presents a method to evaluate the posture of patients on wheel-chair due to Spinal Cord Injuries (SCI) (ALM et.al., 2003) by means low-cost marker-less motion capture systems and further data analysis. A motion capture system allows tracking human motion in space and analyzing acquired data for detecting key-features useful during the wheelchair seating evaluation. We consider marker-less MOCAP so-lution by using multiple low-cost RGB-D camera (KRZESZOWSKI et.al, 2013), such as Microsoft Kinect v2.

Proposed solution is based on a MOCAP system exploiting two Microsoft Kinect v2 to track SCI patients while they move on a straight path within the acquisition volume of Kinect devices. The disposition of sensors has been optimized to provide the longest useful path while correctly capturing patient's movements.

The Kinects have been positioned at a distance of about 6 meters. The straight segment defined by the Kinects defines an angle of 40 degrees with respect to the direction orthogonal to the path, as shown in Figure 2.1.

This allowed a better capture also the front side of the patient, especially crucial for patients with spinal cord injuries who have an important occlusion due to the presence of the wheelchair hiding the back part of the legs. To optimize the acquisition of visible parts some empirical attempts have been performed related to the height of the Ki-nects.

The chosen configuration with the sensors positioned at a height from the ground of 1200 mm allows a complete acquisition of the patient, thus avoiding the wheelchair occlusion problem. The acquisition is in fact optimal: the extrapolated point cloud appears to be very dense, making even the stage of data processing much easier.
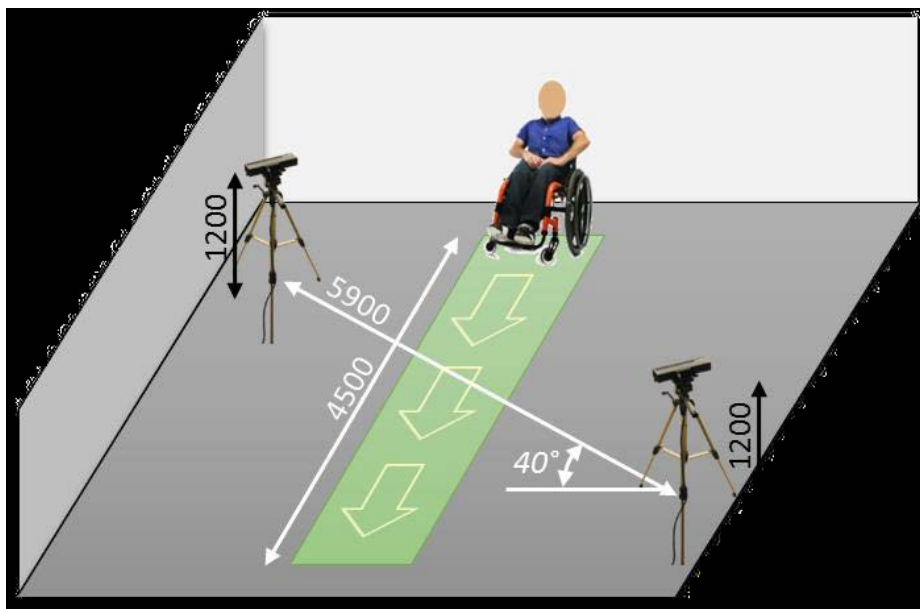
Fig. 2.1   Positioning of MOCAP system

iPiSoft (http://ipisoft.com/) has been used as software for virtual creation of acquired motion. This commercial application detects and tracks human motion of the patient. Figure 2 shows the two depth color map gathered at the same time frame from the two sides of the path. On the base of RGB-D data, iPiSoft automatically reconstructs the virtual skeleton of the tracked human body as for the one shown in Figure 2.3 related to the same reference time frame of Figure 2.2. Afterwards, it is possible to export the ac-quired motion in several file formats, including BVH. Furthermore, the iPiSoft BioMech Add-On allows obtaining some data relative to cinematics, such as translation, rotation and angular velocity of each virtual human segment. Kinematic data can be exported in CSV file format for further analysis in other applications.
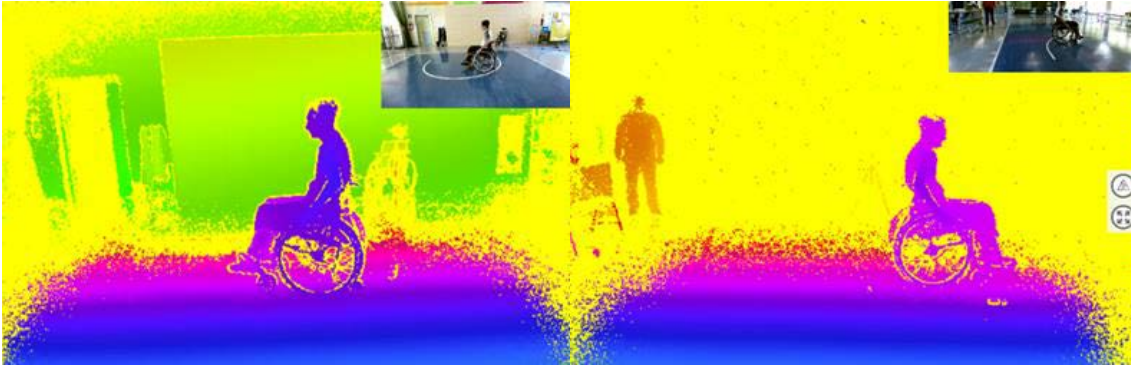
Fig. 2.2   RGB-D data acquired by both Kinect v2 sensors using iPiSoft
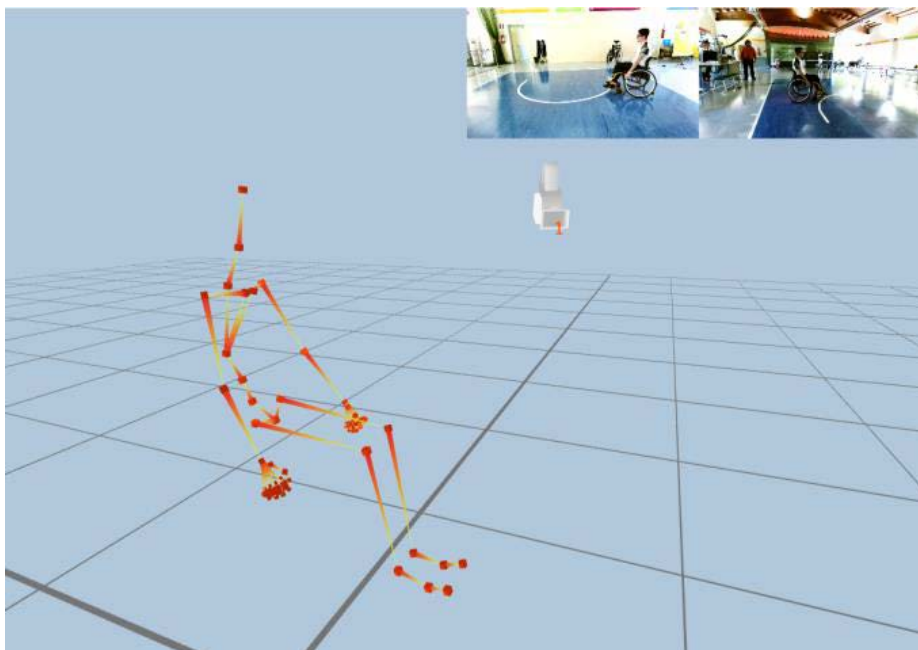
Fig. 2.3   Virtual animated skeleton of the tracked patient

Data have been used in a developed in-house application, which permits to evaluate the acquired motion of each segment and combine the motion of several body segments to evaluate the quality of the seating on the wheelchair. The application has been developed by using VTK (http://www.vtk.org/) and Qt (https://www.qt.io/), which are open source software development kits in C++ programming language. The application imports both BVH file and CSV file. BVH file allows us to view the motion of the patient on the wheelchair in a 3D scene and CSV file has been used to plot graphs relative to static and cinematic behaviors. Before starting the animation, the user can select the interesting virtual joints on an interactive skeleton to visualize the related data plotted on the graphs (Figure 2.4 and Figure 2.5).
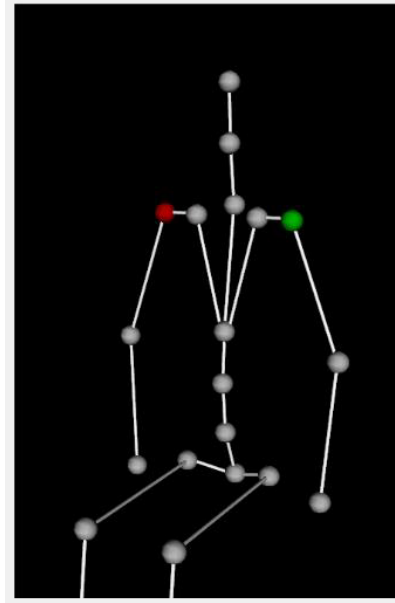
Fig. 2.4 Interactive skeleton used to select joint for analysis; in the example shoulders are selected and associated with a color
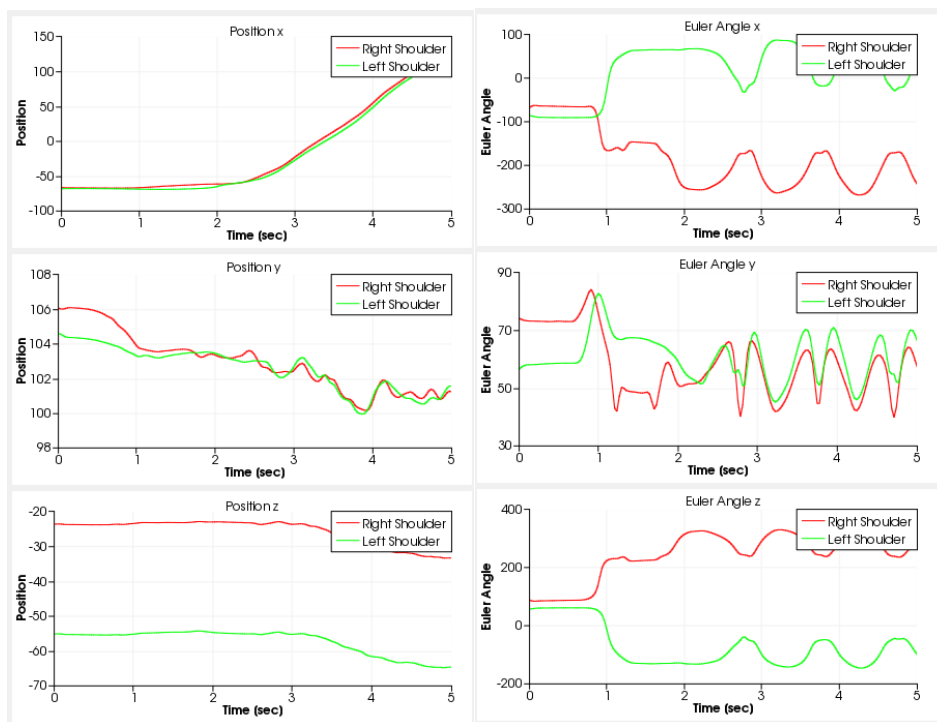
Fig. 2.5 Comparison of both position and rotations of selected joint during motion; in the example shoulders motion is plotted with the same color of the interactive skeleton

2.1 Static evaluation

A further software module has been developed to assess the position of the patient on the wheelchair. The module extrapolates key information relative to wrong postures and dynamic asymmetry during push phase. The strict collaboration with a high professional medical staff composed by physicians and physiotherapists was necessary to determine which are the most influencing parameters defining patient condition in terms of posture and motion. The following list is the result of this part of the work:

- Flexion of torso.
- Extension of hip and femur.
- Flexion of knees.
- Flexion of ankle.
- Lateral flexion of the pelvis.
- Lateral deflection of torso.
- Lateral deflection of shoulders.
- Abduction of hip and knees.
- Twisting of shoulders.
- Alignment of knees and ankles.

It may be noticed that some parameters refers to legs of the paraplegic patients. This may seem odd but it is actually crucial to assess legs posture to prevent issues such as a wrong seating posture or bad blood circulation.

By starting from the analysis of these parameters, the software module is able to get information useful for medical personnel relative to the static position of the patient on the wheelchair.

2.2 Dynamic evaluation

As to perform a gait analysis the physiological walking cycle is divided into a number of phases, in the same way the repeated action of pushing the wheelchair is broke down into phases.

A pushing cycle is composed of two main parts: the real pushing part in which handrail are moved to impress a force to the wheelchair and the return part in which hands are freely moved back in position for the following push. The push part is characterized by three key instants, as shown in Figure 2.6:

- First contact: instant in which the hands of the subject grasp the handrail of the wheel to start pushing.
- Top: instance in which the hand is at the highest vertical position.
- End of push: correspond to the instance in which the hands are detached from the handrail.
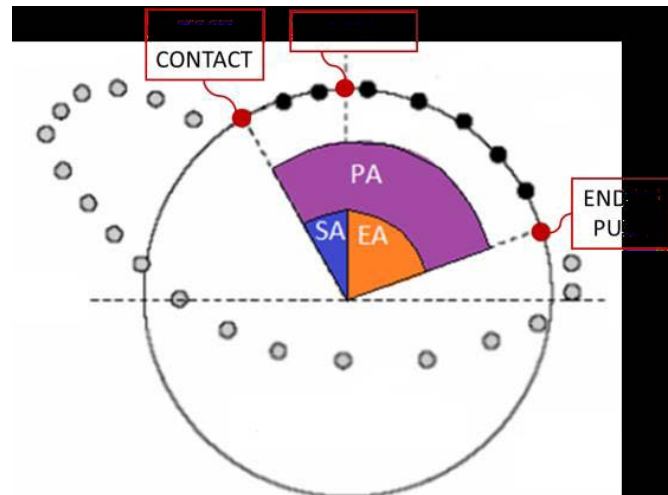
Fig. 2.6   Scheme and phases of the push cycle; SA is the angle between the first contact and the top, EA is the angle between top and end of push, PA is the sum of SA and EA

Three algorithms have been defined to automatically identify the three key instants selecting the proper frame from the entire acquisition. The software module is able to track the angle of the pushing part during which the patient is in contact with the hand-rails of the wheels. Analogously to the static analysis, the interaction with the medical staff has been crucial to determine what to extract from the raw data of the acquisition. The most relevant quantities are related to elbow, shoulder and torso. Due to the complexity of these articulations, the parameters are decomposed in their contribution on the three anatomical planes (i.e., sagittal, frontal and transverse).

The detailed analysis of the push cycle plays a central role in the rehabilitation of paraplegic patients. Actually, on one hand, it allows defining a custom physical exercise plan to improve muscle tonicity and control for a better use of the wheelchair; on the other hand, it provides a quantitative approach also for the set-up and tuning of the wheelchair regulations to compensate or correct patient's condition.

3   Application and test with patients

The whole solution has been run and tested in collaboration with a rehabilitation department of the ASST Papa Giovanni XXIII Hospital in Bergamo, in the Lombardy region. As shown in Table 3.1, seven male SCI patients with lesion of the spine at different levels and different Asia indexes (DITUNNO JF Jr, 1994) have been involved to evaluate their posture and motion skills. Three trials have been done for each of them in a scene configured as in Figure 2.2 and the tracked motions have been evaluated by the physi-cians with the aim to understand the quality and reliability of the tracked motions.

Table 3.1 Medical data of the patients involved in clinical test

# Patient	Date of Birth	Date of Event	Height of the Lesion	ASIA index	Gender	Height
1	27.08.74	28.05.08	T7	D	M	1.72
2	17.01.68	24.09.09	T12	D	M	1.72
3	17.11.75	13.10.09	C7	A	M	1.78
4	08.04.72	14.08.11	T8	A	M	1.85
5	08.06.79	29.08.09	C7	A	M	1.80
6	24.04.80	17.08.05	T7	A	M	1.78
7	27.01.62	21.09.68	L2	A	M	1.70

The proposed method and the software tool developed allows creating the reports without any user's intervention.

Reports have been produced by the application for evaluating both static posture and dynamic push cycle after the mocap acquisition with iPiSoft (Figure 3.1).
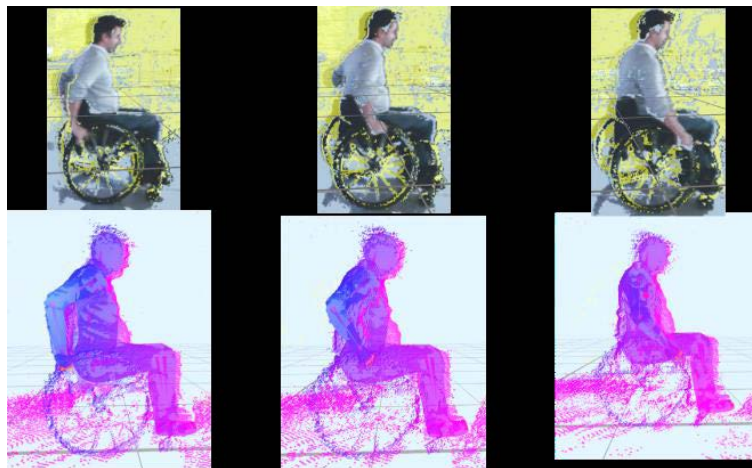
Fig. 3.1   Mocap acquisition of the first patient

Concerning postures, Table 3.2 shows some angles for assessing static posture with respect to sagittal plane of Patient #1. In particular, Table 3.2 highlights the differences between left and right side so that asymmetry can be assessed.

Table 3.2 Featured angles with respect to sagittal plane.

Posture	Sagittal Plane		
Flex-extension Torso [°]	3		
Flex-extension Hip [°]	Left	right	diff
	6	7	1
Flex-extension Knees [°]	Left	right	diff
	90	85	5
Flex-extension Ankles [°]	Left	right	diff
	90	90	0

The dynamic analysis of push cycle has been executed by the application and each parameter of interest has been detected. Table 3.3 shows angles of selected body dis-tricts in the front plane during two cycles of push. Also in this case, the report allows comparing the potential differences between left and right sides of the body.

Table 3.3 Report of push cycle analysis with respect to front plane

Push Cycle	Front Plane					
		1st Cycle			2nd Cycle	
Lateral Inclination of Torso[°]	1st Contact	-1			2	
	Top	-1			2	
	End of push	-1			-1	
		left	right	diff	left	right	diff
Abduction of arm[°]	1st Contact	67	58	9	66	60	6
	Top	58	47	11	58	46	12
	End of push	61	58	3	66	58	8
Flex-extension of elbow[°]	1st Contact	159	134	25	156	143	13
	Top	128	101	27	135	112	23
	End of push	150	136	14	153	146	7

The analysis of the quantities reported in the tables confirm the fact that the measure and elaboration errors are not relevant to the final aim of the evaluation. Actually, small angles (i.e., minor than 2 degrees) are generally neglectable for assessment of patients' conditions.

4 Conclusion

The research work introduces a procedural method to assess the posture of SCI patients by means of low-cost marker-less motion capture systems. A developed in-house application allows reporting several information according to the needs of med-ical staff. A test has been done in which seven SCI patients have been involved. The reports make available analysis of data that have been considered very interesting from the medical personnel following the test. The overall procedure has demonstrated to be effective in evaluating the posture in a very simple way and detecting posture anomaly as a starting point for further wheelchair set-up and tuning. Future develop-ments and tests have been planned in collaboration with the rehabilitation department of the ASST Papa Giovanni XXIII Hospital in Bergamo to refine the procedure and to extend it to patients having different health conditions.

Acknowledgement

List of references

Jardim, D.; Nunes, L.; Dias, M.: Human Activity Recognition from automatically labeled data in RGB-D videos, IEEE 8th Computer Science and Electronic Engineering (CEEC) 2016, pp. 89-94.

Blumrosen, G.; Miron, Y.: Intrator, N.; Plotnik, M.: A Real-Time Kinect Signature-Based Patient Home Monitoring System. Sensors 2016, 16 (11), art. no. 1965.

Kamal, S.; Jalal, A.; Kim, D.: Depth images-based human detection, tracking and activity recognition using spatiotemporal features and modified HMM. Journal of Electrical Engineering and Technology 2016, 11(3), pp.1921-1926.

Hajibozorgi, M.; Arjmand, N.: Sagittal range of motion of the thoracic spine using iner-tial tracking device and effect of measurement errors on model predictions. Journal of biomechanics 2016, 49(6), pp.913-918.

Fay, B. T.; Boninger, M. L.; Fitzgerald, S. G.; Souza, A. L.; Cooper, R. A.; Koontz, A. M.: Manual wheelchair pushrim dynamics in people with multiple sclerosis, Archives of physical medicine and rehabilitation 2004, 85(6), pp.935-942.

Chow, J. W.; Millikan, T. A.; Carlton, L. G.; Chae, W. S.; Lim, Y. T.; Morse, M. I.: Kinematic and electromyographic analysis of wheelchair propulsion on ramps of different slopes for young men with paraplegia, Archives of Physical Medicine and Rehabilita-tion 2009, 90(2), pp.271-278.

Colombo, G.; Regazzoni, D.; Rizzi, C.: Markerless motion capture integrated with human modeling for virtual ergonomics, International Conference on Digital Human Mod-eling and Applications in Health, Safety, Ergonomics and Risk Management, Springer Berlin Heidelberg 2013, pp.314-323.

Krzeszowski, T.; Michalczuk, A.; Kwolek, B.; Switonski, A.; Josinski, H.: Gait recognition based on marker-less 3D motion capture, IEEE Advanced Video and Signal Based Surveillance (AVSS) 2013, pp. 232-237.

Alm, M.; Gutierrez, E.; Hultling, C.; Saraste, H.: Clinical evaluation of seating in persons with complete thoracic spinal cord injury, Spinal Cord 2003, 41(10), pp.563-571.

Ditunno, J. F. Jr.; Young, W.; Donovan, W. H.; Creasey G.: The international standards book-let for neurological and functional classification of spinal cord injury. American Spinal Injury Association Paraplegia 1994, 32(2) pp.70-80.

Li et al.:
Visualization of part surfaces for identifying feasible assembly grasp locations

Li, Y., Kressin, J., Vajedi, S., Carlson, J. S.

Fraunhofer-Chalmers Research Centre for Industrial Mathematics, Gothenburg, Sweden

Abstract

As the first step toward automatic grasp planning in the IPS (Industrial Path Solutions) platform with a DHM (Digital Human Modeling) tool called IMMA (Intelligently Moving Manikins), two methods named Pointwise Shortest Distance and Environment Clearance are presented in this paper to color part surfaces by taking environmental constraints into account so that a DHM tool user can easily identify feasible grasp locations for a manikin. The implementation of these two methods are robust enough to handle triangle meshes with common geometric flaws such as cracks and gaps. In fact, with the help of Visual Shell algorithm implemented on Graphics Processing Unit (GPU), even meshes with inconsistently oriented normal vectors can be handled. Currently, we are planning to conduct an industrial user study, where assembly simulation experts will be asked to specify manikin's hand grips using IMMA with and without the help of the proposed methods, to prove that the proposed methods indeed enhance the flexibility and hence the usability for the assembly simulation experts.

Key words:

Assembly Simulation, Digital Human Model, Ergonomics, Grasping, Visualization

1   Introduction

Digital Human Modeling (DHM) is frequently used, for example, within automotive industry to analyze human postures and motions in order to evaluate both human-product interactions and human-production system interactions before a physical prototype is available. With the addition of a DHM tool called IMMA (Intelligently Moving Manikins) (HÖGBERG et al., 2016) to the IPS (Industrial Path Solutions) platform, it is now possible to use IPS for ergonomic verification. Given a manikin and a part to be assembled such as the Central Electronic Module (CEM) box shown in Figure 1.1, the manikin must grasp the part first before he/she can place it at the correct configuration (i.e., both location and pose). In the field of robotics, many researchers have worked on grasp planning under the assumption that the part to be grasped is alone (LI et al., 2015) in the environment. Furthermore, the kinematics of the robot are often not taken into account (MILLER et al., 2015) by the researchers in the field (i.e., the manipulator is assumed to be disembodied). Consequently, most DHM tools still rely on teleoperation or hand scripted grasps.
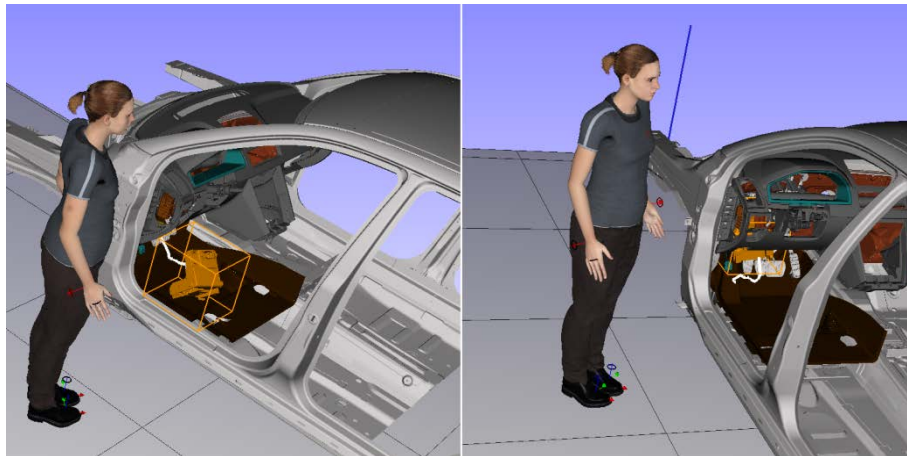
Fig. 1.1   The manikin has to install the Central Electronic Module (CEM) box by moving it from its start configuration shown in the left subfigure to its goal configuration shown in the right subfigure while following the path shown in white.

In this paper, two methods called Pointwise Shortest Distance and Environment Clearance are presented to color part surfaces by taking environmental constraints into account so that a DHM tool user can easily identify feasible grasp locations for a manikin. It is assumed that both the part to be assembled and the environment are represented by triangle meshes in this paper. Unfortunately, these triangle meshes are not always consistently oriented (i.e., the normal vectors sometimes point in the "wrong" directions). In addition, many meshes contain other geometric flaws such as cracks and gaps. The two methods we presented here are robust enough to handle triangle meshes with these geometric flaws. In BERENSON et al. (2007), the surfaces of the part are sampled by casting rays from every point in the six fine-resolution grids, one on each side of the part. The first intersection point between each ray and the part becomes a sample point. The surface normal vector at the sample point is simply the negative of the ray's approach direction. However, this approach cannot be applied to parts of complex shapes such as car rims. Instead,

our GPU-based algorithm called Visual Shell is applied to flip inconsistently oriented normal vectors.

The objective of this paper is to introduce methods to visualize part surfaces so that best collision-free grasp locations can be easily identified. This can be seen as the first step towards autonomous grasp planning in IPS with IMMA. Consequently, this paper does not contain a grasp planner that chooses the best grasp location; computes the corresponding grasp points for all fingers of a manikin hand; computes the optimal path the hand must follow in order to reach the grasp points while avoiding collisions.

This paper is organized as follows. Methods Pointwise Shortest Distance and Environment Clearance are presented in Section 2. Our contributions are then illustrated with a couple of relevant industrial examples in Section 3. These examples demonstrate that the proposed methods can be applied to enhance the flexibility and hence the usability for a DHM tool user who wants to specify manikin's hand grips on a part by highlight areas on the surfaces of the part that are suitable locations for hand grips. Currently, we are planning to conduct an industrial user study where assembly simulation experts will be asked to specify manikin's hand grips using IMMA with and without the help of the proposed methods. Our validation study proposal is presented in Section 4. Finally, the paper is concluded in Section 5.

2 Visualization of Part Surfaces

In this section, methods Pointwise Shortest Distance and Environment Clearance for coloring part surfaces by taking environmental constraints into account are presented. The aim is to enhance the flexibility and hence the usability for the DHM tool user who specifies manikin's hand grips on a part. It is assumed that the part to be assembled and the environment are represented by triangle meshes. During the preprocessing stage, inconsistently oriented normal vectors are flipped using our GPU-based algorithm called Visual Shell.

2.1 Pointwise Shortest Distance

Pointwise Shortest Distance is designed so that surfaces of a part can be colored as fast as possible (i.e., at a low computational cost), because the color at each vertex is simply determined by the shortest distance between it and the environment. In fact, it is fast enough to allow a DHM tool user to interactively manipulate part with hundreds of thousands of triangles.

With Pointwise Shortest Distance, a point model is constructed for each vertex position on the part surfaces (as shown in the left subfigure of Figure 2.1) and then the shortest distance between the point model and the triangle meshes representing the environment is computed. Next, the part mesh is rendered after mapping the shortest distances to vertex colors, where all vertices with the same position (and hence the same distance to the environment) are assigned the same color. If the part is manipulated (i.e., moved and/or rotated) manually by the user or automatically in order to follow a precomputed path, then the shortest distances are recomputed and

the part surfaces are re-rendered at each step. This is the so-called *Instant mode*. For example, the CEM box shown in the right subfigure of Figure 2.1 is rendered in Instant mode, where the environment is comprised of the chassis, the dashboard, the pedals, and the rest of the car. Alternatively, the user can choose *Accumulative mode* if he/she wants to map the minimum accumulated shortest distance between each vertex position on the part surfaces and the environment to a vertex color.
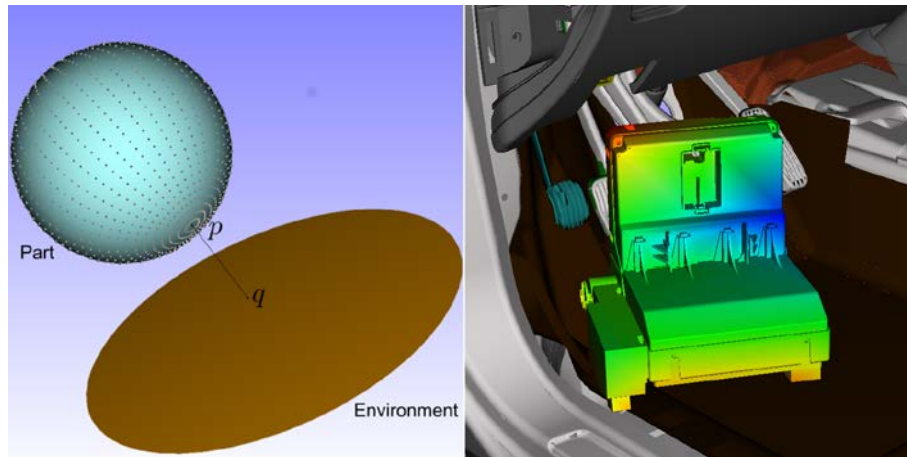
Fig. 2.1 A spherical part is shown in the left subfigure, where each point represents a triangle vertex on the surface of the sphere. Given triangle vertex p on the surface of the part, the closest point on the surface of the environment is represented by q. The CEM box shown in Instant mode in the right subfigure was rendered by mapping the shortest distance between each triangle vertex on its surfaces and the environment to a vertex color.

2.2 Environment Clearance

For a part with complex shape, Environment Clearance (BERENSON et al., 2007) can be used instead of Pointwise Shortest Distance. For example, cavities and holes on the surfaces of the part may be feasible assembly grasp locations even if the surfaces of these pockets are located very close to the environment, because an assembly operator can access these pockets as long as their openings are not blocked. To color the part surfaces with method Environment Clearance, the clearance along the normal vector at each vertex has to be calculated. Consequently, Environment Clearance is much more computationally expensive, but it is also much better at isolating/highlighting potential grasp locations than Pointwise Shortest Distance.

Before Environment Clearance is computed, algorithm Visual Shell is applied to find a consistent normal orientation over the surfaces of the part. Visual Shell is similar to the algorithm presented in BORODIN et al. (2004). However, Visual Shell has been implemented on GPU and hence it runs much faster. To speed up the computation even further, Visual Shell ignores all triangles that are invisible from the outside of the part.

Environment Clearance prefers triangle vertices with high clearance in the directions of the corresponding vertex normal vectors. From each vertex p on the part surfaces,

rays are cast inside a (right circular) cone with aperture θ, its apex located at p, and its alignment defined by the vertex normal vector n, as shown in Figure 2.2. The Environment Clearance at p is then defined as:

$$EC(p, \theta) = \min_{r:r\cdot n\leq\cos(\theta/2)} Dist(p, r) \qquad\qquad \text{(2.1)}$$

where $Dist(p, r)$ is the shortest distance between p and the nearest point ray originated from p with direction r hits either the part itself (although not at p) or the environment. Our implementation allows the user to choose between (i) ray-to-part collision detection, (ii) ray-to-environment collision detection, and (iii) ray-to-environment-and-part collision detection, as shown in Figure 2.2. The third collision detection mode is the default one. However, the first two modes are faster to compute and are more appropriate for certain types of analysis. For example, to visualize clearance of cylinder walls of a cylinder/engine block, there is no need to compute the distances between the cylinder walls and the environment around the engine and hence the first mode is the best choice. Moreover, both the distance range and the color range can be adjusted by the user. Furthermore, the user can vary the cone aperture in order to cover a smaller or bigger region of the environment. In BERENSON et al. (2007), the default value for angle θ is $\pi/12$. Finally, the user can choose the number of rays to be casted inside each cone. Given the number of rays, the positions of the intersection points between the rays and the cone's flat base can be obtained from SPECHT (2017). These positions are the centres of the best known packings of equal circles in a circle, where the number of rays is equal to the number of circles to be packed. The default number of rays is set to 9 (PIRL, 1969).
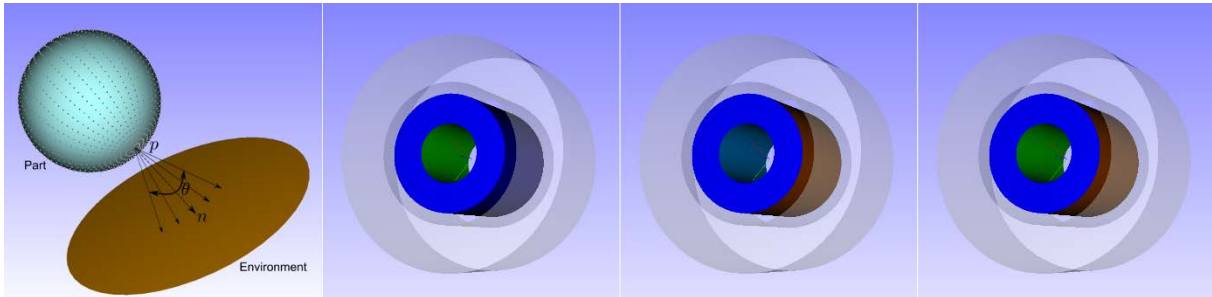
Fig. 2.2 In subfigure (a), a (right circular) cone with apex $\boldsymbol{p}$, aperture $\boldsymbol{\theta}$, and axis $\boldsymbol{n}$, where $\boldsymbol{n}$ is the surface normal vector at triangle vertex $\boldsymbol{p}$ on the surface of the spherical part. In the other three subfigures, the cylinder in the middle and the transparent cylinder represent the part to be assembled and the environment, respectively, and distance in a range from 0 mm to 200 mm is mapped to color in a range from red to blue. Subfigures (b), (c), and (d) are rendered using (i) ray-to-part collision detection, (ii) ray-to-environment collision detection, and (iii) ray-to-environment-and-part collision detection, respectively. The order of the subfigures is left-right.

3   Results

In order to demonstrate the applicability of the two methods we presented in this paper (i.e., Pointwise Shortest Distance and Environment Clearance), two relevant test cases from the automotive industry are presented in this section. As mentioned before, we have yet to conduct a study with assembly simulation experts to validate the degree of usability of these two methods for them; however, our validation proposal is listed in Section 4. The results of the validation study will be presented in future work.

Firstly, a CEM box needs to be installed in a dashboard. In Figure 3.1, the CEM box colored in Accumulative mode had to follow a precomputed path in order to be installed. Clearly, the surface patches covered by green and blue are potential feasible grasp locations, whereas the surface patches covered by red correspond to the parts of the CEM box that came too close to the dashboard. Efficient distance computation in IPS enables us to compute shortest distances from a part modeled by a mesh containing a large number of triangles and render it interactively. For example, a Center Console model (as shown in Figure 3.2) that is frequently used at FCC for testing contains 155646 vertices and 233489 triangles.
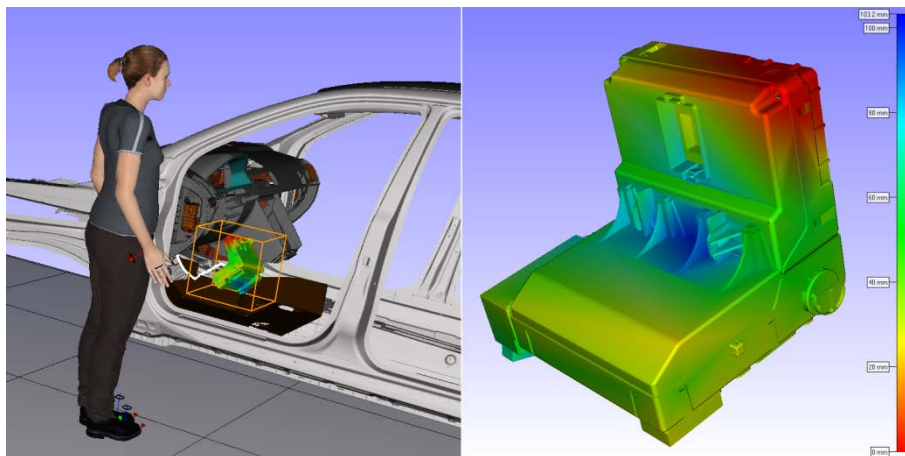
Fig. 3.1 The CEM box located at its start configuration is shown in Accumulative mode. To color the vertices on the CEM box surfaces, the CEM box traced the path from its start configuration to its goal configuration.

Secondly, as shown in Figure 3.2, a gear stick and a handbrake are covered by a Center Console, which is the part that has to be removed. In addition to the gear box and the handbrake, the environment also contains a dashboard and a roof. Both Pointwise Shortest Distance and Environment Clearance are used to color the surfaces of the Center Console and the results are shown in Figure 3.2. Environment Clearance is more computational expensive than Pointwise Shortest Distance, but it does provide additional information about the surfaces of the part beyond the shortest distance between each vertex on the surfaces of the part and the environment. For example, as shown in subfigure (a) of Figure 3.2, several surface patches on the left side of the Center Console are colored red using Pointwise Shortest Distance (in Instant mode), because triangle vertices on these patches are located very close to either the gear stick or the handbrake, even though these

patches can be easily accessed by a manikin hand tracing a high clearance path. However, as shown in subfigure (b), these surface patches are rendered in blue. Furthermore, the edges of the Center Console's storage boxes are rendered in green in the right subfigure. Clearly, Environment Clearance is better at distinguishing potential feasible grasp locations from locations that cannot be easily accessed. Finally, in subfigure (c), a manikin grasps the edges, which are classified as feasible grasp locations by Environment Clearance, of the Center Console's storage boxes with both hands.
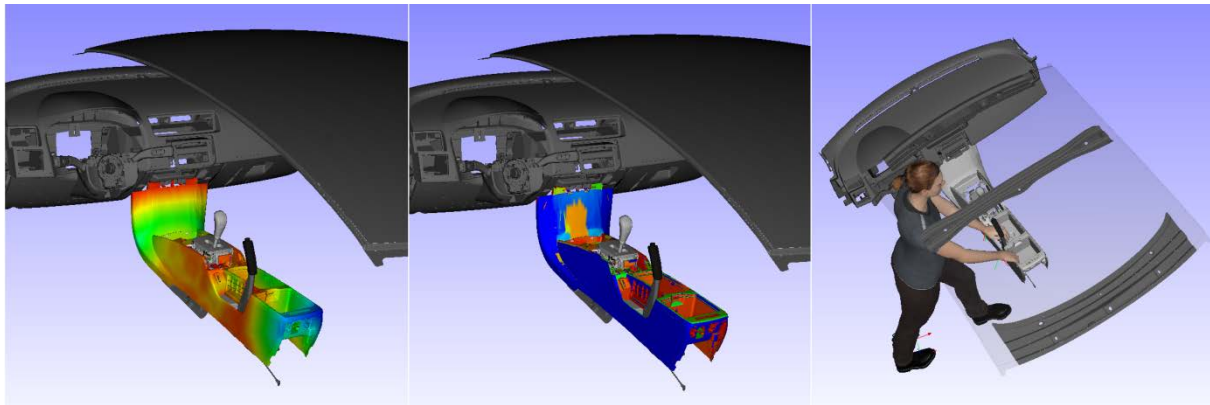
Fig. 3.2 The Center Console is colored using Pointwise Shortest Distance (in Instant mode) in subfigure (a), whereas Environment Clearance (also in Instant mode) is used to color the surfaces of the Center Console in subfigure (b). To synthesize the figure in subfigure (b), ray-to-environment-and-part collision detection was chosen over ray-to-environment collision detection and ray-to-part collision detection. In subfigure (a), distance in a range from 0 m to 2.6 m is mapped to color in a range from red to blue, whereas the maximum distance is 2 m in subfigure (b). In Subfigure (c), a manikin grasps the center console with both hands. The roof is rendered as a semi-transparent object in the subfigure. The order of the subfigures is left-right.

4 Discussion

Methods Pointwise Shortest Distance and Environment Clearance enable a DHM tool user to color part surfaces by taking environmental constraints into account so that he/she can easily identify potential feasible grasp locations for a manikin. However, these two methods do not identify the best grasp location nor the correponsindg grasp points for a manikin hand. In order to identify these grasp points, additional part parameters such as weight and material properties must be taken into account by a grasp planner. Furthermore, as the last step, the grasp planner is required to bring the fingers of the hand to the grasp points. Such a grasp planner is not presented in this paper.

In BERENSON et al. (2007), Environment Clearance enables an automatic grasp planner to find stable and collision-free grasps faster in cluttered environments. In the future, we intend to integrate these two methods with a grasp planner to enable automatic fast planning of grasp actions in IMMA.

Another direction for future work is to enable two-arm cooperation (i.e., exchanging and regrasping assembly parts using manikin's two arms). By divining a precomputed assembly path for a part into multiple subpaths, either manually or automatically, Pointwise Shortest Distance and Environment Clearance can be applied to color the part surfaces so that feasible grasp locations for each subpath can be easily identified. By taking the feasible grasp locations for all subpaths as input, a motion planner will be able to return a plan that coordinates the motions of manikin's two arms.

Moreover, we apply at moment both Pointwise Shortest Distance and Environment Clearance to meshes we have obtained from our customers without a resampling step. Since the running time of the two methods is proportional to the number of mesh vertices and the shapes of mesh triangles affect the shapes of the potential grasp locations rendered by IPS on mesh surfaces, we are considering to add a resampling step in order to generate a new discretization of the original geometry with a mesh that exhibits the uniform sampling property. For an overview of recent advances in remeshing of surfaces, we refer to ALLIEZ et al. (2008).

Furthermore, we are planning to conduct an industrial user study to demonstrate that the proposed methods indeed enhance the flexibility and hence the usability for the DHM tool user who wants to specify the manikin's hand grips. As for assembly simulation experts, we intend to invite at least 8 engineers from four Swedish vehicle OEMs (2 from each company). All study participants are then randomly divided into two groups. We will also prepare 10 test cases. The first group will be assigned the first 5 test cases where each participant has to specify a grasp for each case with IMMA without access to neither Pointwise Shortest Distance nor Environment Clearance, whereas the second group will be assigned to the same test cases where each participant has to use both Pointwise Shortest Distance and Environment Clearance before specifying a grasp for each case with IMMA. Next, the two groups are assigned the remaining 5 test cases. But this time, the first group has to use both Pointwise Shortest Distance and Environment Clearance, whereas the second group is not allowed to use them. Moreover, the study participants will be asked to respond to a questionnaire to find out whether they think that Pointwise Shortest Distance and Environment Clearance have enhanced the flexibility and hence the usability for them. Furthermore, the study participants will be asked to score each grasp he/she specified with IMMA. Specifically, we want to find out whether Pointwise Shortest Distance and Environment Clearance enable the study participants to find better grasps. Finally, to find out whether Pointwise Shortest Distance and Environment Clearance enable the study participants to find good grasps faster, all test runs will be timed.

5   Conclusions

We have presented two methods called Pointwise Shortest Distance and Environment Clearance for coloring part surfaces by taking environmental constraints into account. The implementation of these two methods are robust enough to handle triangle meshes with common geometric flaws such as cracks, gaps, and even inconsistently oriented normal vectors. The goal of the proposed methods is to enhance the flexibility and hence the usability for a DHM tool user who wants to specify manikin's hand grips on a part by highlight areas on the surfaces of the part that are suitable for hand grips. These two methods constitute the first step toward automatic grasp planning in IPS IMMA DHM tool. Currently, we are planning to conduct an industrial study in order to demonstrate the benefits of these two methods.

List of references

Alliez, P.; Ucelli, G.; Gotsman, C.; Attene, M.: Recent Advances in Remeshing of Surfaces, Recent advances in remeshing of surfaces, Shape Analysis and Structuring 2008, pp. 53-82.

Berenson, D.; Diankov, R.; Nishiwaki, K.; Kagami, S.; Kuffner, J.: Grasp planning in complex scenes, Proceedings of the 7th IEEE-RAS International Conference on Humanoid Robots (Humanoids 2017), pp. 42-48.

Borodin, P.; Zachmann, G.; Klein, R.: Consistent normal orientation for polygonal meshes, Proceedings of the Computer Graphics International (CGI 2004), pp. 18-25.

Högberg, D.; Hanson, L.; Bohlin. R.; Carlson, J. S.: Creating and shaping the DHM tool IMMA for ergonomic product and production design, International Journal of the Digital Human 2016, Vol. 1, No. 2, pp. 132-152.

Li, Y.; Saut, J. P.; Pettré, J.; Sahbani, A.; Multon, F.: Fast Grasp Planning Using Cord Geometry, IEEE Transactions on Robotics 2015, Vol. 31, No. 6, pp. 1393-1403.

Miller, A.; Allen, P. K.: Graspit!: A Versatile Simulator for Robotic Grasping, IEEE Robotics and Automation Magazine 2004, Vol. 11, No.4, pp. 110-122.

Pirl, U.: Der Mindestabstand von n in der Einheitskreisscheibe gelegenen Punkten, Mathematische Nachrichten 1969, Vol. 40, pp. 111-124.

Specht, E.: The best known packings of equal circles in a circle (complete up to N = 2600) [Online], Available: http://hydra.nat.uni-magdeburg.de/packing/cci/. [Accessed: 15-Mar-2017].

Miyajima et al.:
Optimal Arrangement of Inertial Sensors on a Motion Measurement Suit for On-site Working Posture Assessment

Miyajima, S.[1], Miyata, N.[2], Tada, M.[2], Tanaka, T.[1], Mochimaru, M.[2]

[1] Human-Centric Engineering Laboratory Graduate School of Information Science and Technology, Hokkaido University, Japan

[2] National Institute of Advanced Industrial Science and Technology (AIST), Japan

Abstract

Digital human models can be used to estimate workloads on the body when actual work motions are input correctly and interactive musculoskeletal simulations are carried out. To measure the motion of workers in the workplace, we have been developing motion measurement suits that are equipped with inertial sensors for ease of use. We describe the optimization of the arrangement of inertial sensors on the suits for measuring waist posture by using digital human models. To verify the usefulness of optimized sensor positions, a motion measurement experiment was performed with three male participants.

Key words:

Motion Capture, Inertial Sensor, Sensor Arrangement, Posture Estimation, Occupational Health

1   Introduction

Labor shortages caused by an aging population have made it more common to manage workloads to extend healthy work life. To prevent work-related injuries and to make work more sustainable, it is important to analyze the actual motion of workers. We are currently developing a system for evaluating workloads and the effect of a wearable assistive device using a digital human model (DHM). In this system, work motion in a real environment is measured by inertial sensors. Each sensor comprises a three-axis accelerometer and a three-axis gyroscope which are less affected by surrounding environment unlike optimal motion capture systems. When measuring motion in a real workplace, it is desirable to avoid disturbing the work process and to minimize the setup time. Thus, motion measurement suits equipped with inertial sensors have been developed to capture the working motion regardless of the work environment. When inertial sensors are used to obtain motion data for a DHM, measured angles need to be converted into bone inclination angles to give motion information. This conversion involves relationship between the inclination of bones and sensors. However, fixing sensors on the suit decreases its adaptability owing to the individual differences in physique, which means that the relative positions between the sensors and the body change from the expected position. In the case of multi-linked parts, such as the trunk, these changes in position affect the result of a measurement.

In this study, we determined the optimal arrangement of inertial sensors on sensor suits used to estimate workloads based on musculoskeletal dynamic calculations by using a DHM and the actual motion of the subjects during work. The optimal sensor position was defined as the one that measures body motions without being affected by the deviation of the sensor position and individual differences in the body surface. The optimization used the relationship between body surface shape that the sensors were placed on and the posture of the DHM's bones. DHMs with various physiques were used instead of the actual human.

2   Sensor arrangement optimization

2.1   Optimization procedure

The optimization was performed on capturing the back posture to determine the workload on the waist. Small (S), medium (M), and large (L) sensor suits were created. It was assumed that the suit fitted the body. The target motion in this study was bending the waist without twisting the torso. Body motion refers to the time-series joint angle, θ_j, that was input into the DHM. The method to determine the optimal sensor position consisted of the following procedures.

1. Inputting primitive motions to the evaluation DHMs and getting joint angle θ_j ($j = p, l, t$) of the motion.
2. Obtaining inclination angle ψ_n of the sensor at candidate point P_n.
3. Producing a formula converting ψ_n to θ_j for each suit size.
4. Substituting the converted angle into the evaluation function.

2.2   DHM "Dhaiba"

A DHM called "Dhaiba" (ENDO et al., 2014) was used in this research. Dhaiba model was developed by the Digital Human Research Group in the National Institute of Advanced Industrial Science and Technology, Japan. The Dhaiba model (Figure 2.1), consists of a linkage model armature composed of bones and a skin mesh model that forms the body surface shape. Feature points can be arranged anywhere on the body surface. The Dhaiba model deforms and can reproduce the body surface shape according to the change in the posture of the bones. The Dhaiba model can also model arbitrary physiques. In this paper, the model was individualized by using a small number of dimensions according to NOHARA et al. (2016).

2.3   Definition of the DHM posture and sensor inclination angles

The trunk of the Dhaiba model, which was the measurement target of this study, was modeled by three links: pelvis (PELVIS), lumbar vertebrae (SPINE), and thoracic vertebrae (STERNUM). Each link had a local coordinate system based on its proximal link coordinate system (Figure **2.2**). The root of all the bones was PELVIS. The coordinate system of PELVIS, written as (X_P, Y_P, Z_P), was set in the same direction as the global coordinate system, (X_W, Y_W, Z_W), and all the bones' *X*-axes were parallel to X_W. The joint angle of PELVIS, SPINE, and STERNUM links was defined as that with respect to the direction of gravity (X_W axis), written as

$$\boldsymbol{\theta}_j = \begin{bmatrix} \theta_j^x \\ \theta_j^y \end{bmatrix} \ (j = p, l, t) \tag{2.1}$$

where θ_j^x is the angle on the sagittal (Y_W-Z_W) plane and θ_j^y is the angle on the coronal (X_W-Z_W) plane.
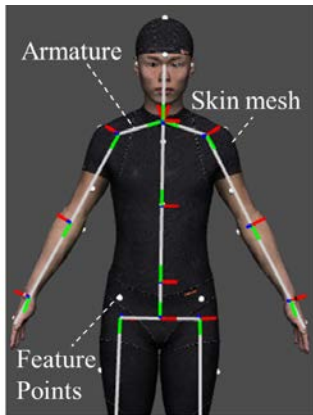
Fig. 2.1 Dhaiba model
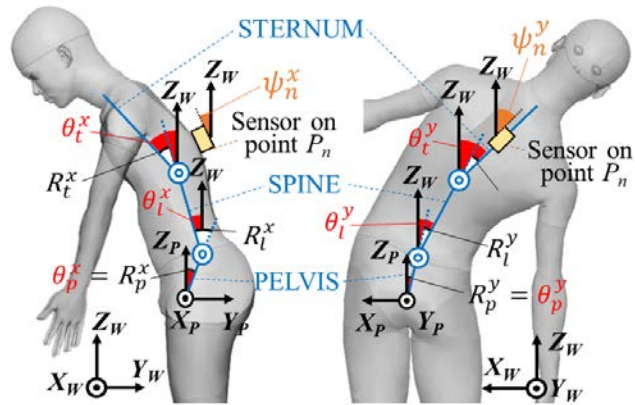
Fig. 2.2 Schematic of elements

The sensor attachment position was set on the spine at the center of the back. The candidate area was defined by dividing the curve of the spine from the seventh cervical vertebrae (C7) to the sacral bone into 10 equal sections. Each position was separated by feature points, which were arranged on a skin mesh. The center point of each divided curve was set as candidate point P_n and the points were numbered in ascending order from the C7 side following the format P_1, P_2, P_3, …, P_{10} (Figure 2.3). The actual inertial sensor could not be put on the DHM's body surface. The

inclination of the sensor placed on the candidate position was defined with the vector connecting feature points above and below the position. The coordinates of upper and lower marker of P_n were written as $(^u x_n, ^u y_n, ^u z_n)$ and $(^d x_n, ^d y_n, ^d z_n)$, respectively. The angle $\boldsymbol{\psi}_n = [\psi_n^x \quad \psi_n^y]^T$ was expressed by equations (2.2) and (2.3).

$$\psi_n^x = \tan^{-1} \frac{\left(^u z_n - ^d z_n\right)}{\left(^u y_n - ^d y_n\right)} \tag{2.2}$$

$$\psi_n^y = \tan^{-1} \frac{\left(^u z_n - ^d z_n\right)}{\left(^u x_n - ^d x_n\right)} \tag{2.3}$$

The joint angle θ_j^r around the r axis $(r = x, y)$ was obtained by the sensor inclination angle $\psi_n^r (r = x, y)$. Although the spine is a structure made of multiple links, each candidate area can be considered as a rigid body due to its division into 10 parts. Therefore, the relationship between ψ_n^r and θ_j^r was assumed to be linear. A linear conversion was used to convert angle ψ_n^i (equation (2.4)).

$$\widehat{\boldsymbol{\theta}}_j = {}_n^d h_j(\boldsymbol{\psi}_n) = {}_n^d \boldsymbol{a}_j \boldsymbol{\psi}_n + {}_n^d \boldsymbol{b}_j = \begin{bmatrix} {}_n^d a_j^x & 0 \\ 0 & {}_n^d a_j^y \end{bmatrix} \begin{bmatrix} \psi_n^x \\ \psi_n^y \end{bmatrix} + \begin{bmatrix} {}_n^d b_j^x \\ {}_n^d b_j^y \end{bmatrix} \tag{2.4}$$

Coefficients ${}_n^d \boldsymbol{a}_j$ and ${}_n^d \boldsymbol{b}_j$ were composed of real-valued constants and calculated by linear regression analysis for each size d (d = S, M, L) using $\boldsymbol{\psi}_n$ and $\boldsymbol{\theta}_j$ of motions used in the optimization.

2.4   Physique of evaluation DHMs

DHMs used in the optimization had physiques corresponding to the S, M, and L suits. The physique was defined by the height and chest measurements in the Japanese Industrial Standards (JIS) L4004. Five evaluation DHMs were generated for each size and were used as the evaluation DHM. The height and chest measurements of the evaluation DHM, k_i, for size k (k = S, M, L) are shown in Figure 2.4. However, circumferences, such as chest circumference, cannot be used to designate the physique of the Dhaiba model. Thus, the length of the bust breadth and bust depth were used to generate DHMs instead of chest circumference. These dimensions were calculated for the chest using the linear regression equation created by the body database collected by the Research Institute of Human Engineering for Quality Life in size-JPN project (2004-2006).
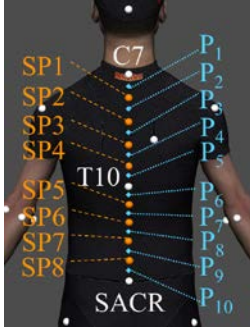
Fig. 2.3 Candidate points
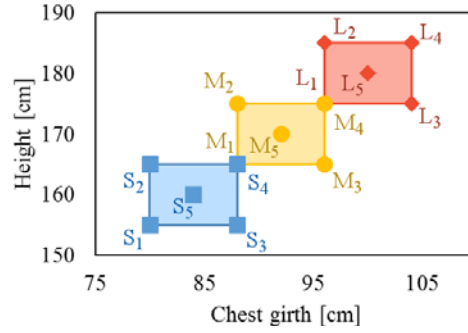
Fig. 2.4 Height and chest girth of each model

2.5 Primitive motions used in the optimization

The measurement target was the posture of the waist during motion without twisting the torso. Two primitive motions of bending the trunk forward and laterally at the waist were used. The motions were obtained by measuring 1 actual human's motions with an optical motion capture system (VICON; 10 MX-13 cameras and five T-160 cameras). Input motions for evaluating DHMs were expressed by time-series full-body joint angles, which were acquired by fitting motion capture data to the DHM, which realized the subjects' individual physique (ENDO et al., 2012).

2.6 Evaluation index for sensor position

It was assumed that sensors placed in the optimal position would measure the joint angle that was the least affected by the individual differences and the least affected by the deviation of the sensor position. Thus, these two requirements were considered in choosing the sensor position.

Individual differences

The effect of individual differences was assessed by angle conversion error using same converting formula, ${}_n^d h_j(\boldsymbol{\psi}_n)$, for all models d_1, d_2, …, d_5 generated for the same size d ($d = \mathrm{S}, \mathrm{M}, \mathrm{L}$). The error value was expressed by the root-mean-square error (RMSE) of all elements for each size. The number of frames of motion used in the optimization was F, and ${}^{d_i}\boldsymbol{\psi}_n(f)$ defined the angle of the sensor at P_n of evaluation DHM d_i at frame f ($0 \le f \le F$). The joint angle, ${}_n^{d_i}\widehat{\boldsymbol{\theta}}_j(f)$, expressed the angle conversion, ${}^{d_i}\boldsymbol{\psi}_n(f)$, by formula ${}_n^d h_j$. RMSE value ${}^d E_j(n)$, which was the conversion error of ${}_n^{d_i}\widehat{\boldsymbol{\theta}}_j(f)$ of M models for size d, was calculated by equation (2.5).

$$
{}^d E_j(n) = \sum_r^{x,y} \sqrt{\frac{1}{FM} \sum_{i=1}^M \sum_{f=0}^F \left({}_n^{d_i}\widehat{\theta}_j^r(f) - \theta_j^r(f) \right)^2} \tag{2.5}
$$

Misregistration of the sensing position

Owing to individual differences, a sensor on the suit can be located at different places on the wearer. The deviation from the assumed sensing position was assumed to fall within the adjacent sensing positions. It was also assumed that the more the sensor slipped, the more the angle conversion error increased. Measuring motion with the sensor slipped δ mm from the assumed position along the backbone, the angle converting error was written as $^dE_j(n, \delta)$ by using equation (2.5). If the deviation affected motion measurement, the value of $^dE_j(n, \delta)$ would change greatly owing to δ. Hence, the variation of $^dE_j(n, \delta)$ was used to assess the effect of the deviation. Considering a sensor at P_n, RMSE value $^dE_j(n, \delta)$ was calculated for measuring motion with a sensor that had slipped to an upper adjacent position $P_{n-1}\left(\delta = z_{P_{n-1}} - z_{P_n}\right)$, to a lower adjacent position $P_{n+1}\left(\delta = z_{P_{n+1}} - z_{P_n}\right)$, and without slipping ($\delta = 0$). Next, a curve passing through the three points, $\left(\delta, {^dE_j(n, \delta)}\right)$, was approximated by the least squares method to determine $^d_ne^r_j(\delta)$, which was a quadratic curve of δ. Evaluation index $^dD_j(n)$ was defined as

$$^dD_j(n) = \sum_r^{x,y} \int_{\delta_d}^{\delta_u} \left| \frac{\partial\, ^d_ne^r_j(\delta)}{\partial \delta} \right| d\delta \tag{2.6}$$

where $\delta_u = z_{P_{n-1}} - z_{P_n}$ and $\delta_d = z_{P_{n+1}} - z_{P_n}$. Accordingly, evaluation function $^dX_j(n)$ for sensor position was composed of $^dE_j(n)$ and $^dD_j(n)$ as

$$^dX_j(n) = \alpha\, ^dE_j(n, \delta = 0) + \beta\, ^dD_j(n) . \tag{2.7}$$

Point P_n, which minimized $^dX_j(n)$, was chosen as the optimal sensor position.

3   Optimization results

The optimal sensor position was determined by the method in Section 2 by using sensor inclination angle $\boldsymbol{\psi}_n$ and target joint angle $\boldsymbol{\theta}_j$ in two primitive motions. The results of calculating evaluation function $^dX_j(n)$ for size M are shown in Figure 3.1. The value of the evaluation function of the SPINE angle, $^dX_l(n)$, and that of the STERNUM angle, $^dX_t(n)$, differed greatly owing to the position. In contrast, the value of the evaluation function of PELVIS angle, $^dX_p(n)$, was altered less by position P_n. The relationships between $^dX_j(n)$ and P_n for sizes S and L were similar to that for size M. $^dX_l(n)$ reached its minimum value at P_7, $^dX_t(n)$ reached its minimum value at P_4, and $^dX_p(n)$ reached its minimum value at P_{10}. The optimal sensor position was determined for each target joint angle in each size.
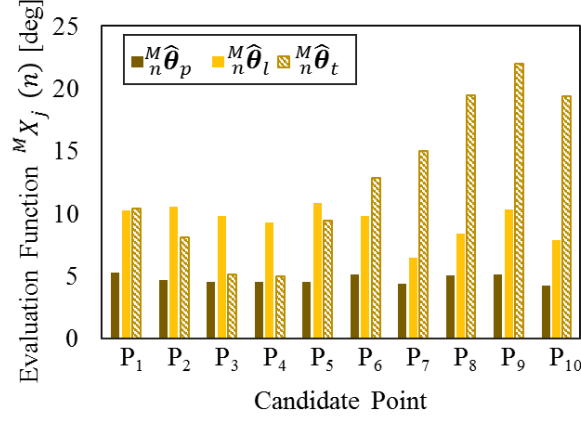
Fig. 3.1 Results for Evaluation Function $^M X_t(n)$

4   Verification of the optimization result

The optimization in Sections 2 and 3 was performed using a DHM. To verify the applicability of the result for measuring the motion of actual humans, an experiment was performed with three male subjects (A, B, and C), shown in Figure 4.1, classified as size M. The back surface shape and posture during motions bending the trunk forward and laterally at the waist were measured.

The optimal sensor position determined by the method above was not always the one that measured the joint angle with the smallest RMSE value. However, using the obtained sensor position and converting formula enabled us to avoid positions with the worst conversion accuracy. The result suggests that our method works effectively.

Next, we consider why the optimal position was not the one with the highest measurement accuracy. Figure 4.2 shows the curvature of the spine of subject A and the DHM with the subjects' dimensions. The spinal shape of the subject was measured with 11 markers arranged along the spine. The difference in the shape between the DHM and the human during the motions was expressed by RMSE value $E(\psi_n^x)$ for each sensor position (Figure 4.3) with SPINE angle conversion error $^{M_A}E_l(n)$. These results confirm that the difference in the surface shape caused a conversion error and affected the feasibility of the method. To deal with this difference, the conversion formula was corrected by using the measured sensor angle of the standing posture. When all joint angles of standing posture were set as 0 and all measured sensor angles of same posture were defined as $\boldsymbol{\psi}_n(0)$, the conversion formula for joint angle $\widetilde{\boldsymbol{\theta}}_j$ was redefined using $\boldsymbol{\psi}_n(0)$ by equation (4.1).

$$\widetilde{\boldsymbol{\theta}}_j = {}_n^d\widetilde{h}_j(\boldsymbol{\psi}_n) = {}_n^d\boldsymbol{a}_j\boldsymbol{\psi}_n - {}_n^d\boldsymbol{a}_j\boldsymbol{\psi}_n(0) \tag{4.1}$$

Figure 4.4 shows the result of rectifying the SPINE angle conversion formula of subject B. According to the Figure, SPINE angle conversion error $^{M_A}E_l(n)$ was decreased at most positions after correcting the formula.
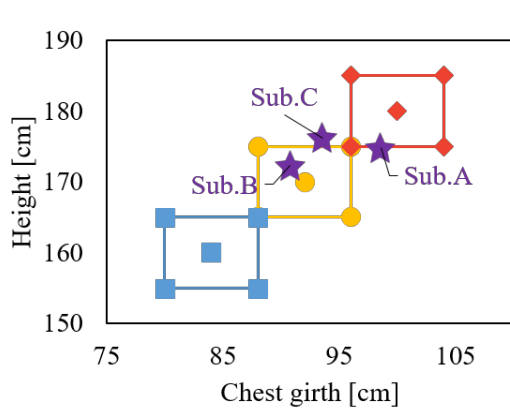
Fig. 4.1 Physiques of each subject
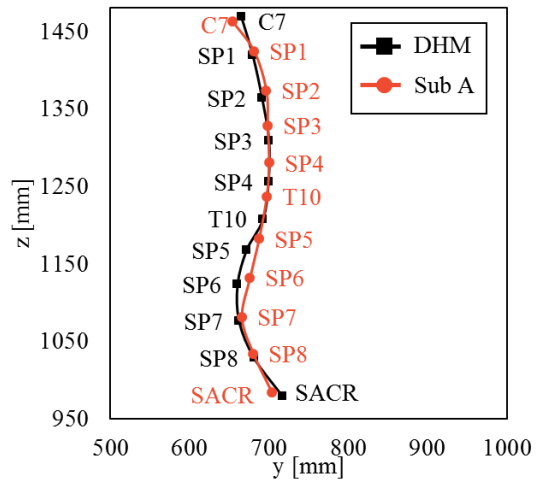
Fig. 4.2 Difference in back surface shape
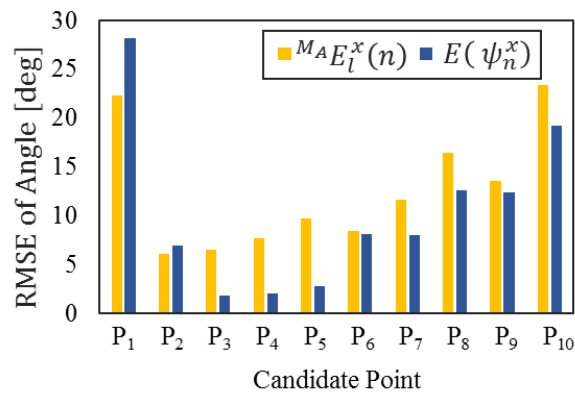
Fig. 4.3 Difference in ψ_n^x during motion between the DHM and the human subject
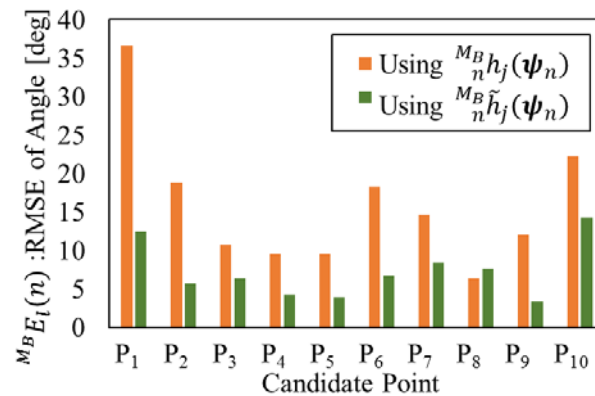
Fig. 4.4 Change in $^{M_B}E_l(n)$ after correcting the conversion formula

5   Conclusion

We have developed a method for optimizing the inertial sensor position on a motion capture suit to reproduce human motions on a DHM, the Dhaiba model, by using the body surface inclination of DHM. The optimal position was defined as the position of the joint angle that was the least affected by individual differences and the deviation of the sensor position. The results revealed that the optimal sensor position for each target joint angle for the S, M, and L suit sizes. The feasibility of the method was verified by applying the optimized sensor position and estimation formula to three human subjects. We increased the accuracy of the estimation by measuring some poses before the motion measurements. Future studies should focus on the optimal sensor arrangement to identify the type of work or the state of workers.

List of references

Endo, Y.; Tada, M.; Mochimaru, M.: Dhaiba: Development of Virtual Ergonomic Assessment System with Human Models, in Proceedings of the 3rd International Digital Human Modeling Symposium, Tokyo, May 2014, Paper #58

Nohara, R.; Endo, Y.; Murai, A.; Takemura, H.; Kouchi, M.; Tada, M.: Multiple Regression based Imputation for Individualizing Template Human Model from a Small Number of Measured Dimensions, in Proceedings of the 38th Annual International Conference of the IEEE Engineering in Medicine and Biology Society, Orlando, Aug. 2016, pp.2188-2193

Research Institute of Human Engineering for Quality Life: size-JPN 2004-2006, http://www.hql.jp/database/size2004/ (in Japanese)

Endo, Y.; Miyata, N.; Tada, M.; Kouchi, M.; Mochimaru, M.: Reconstruction of Skin Surface Models for Individual Subjects, Advances in Applied Human Modeling and Simulation, 2012, pp.392-400

Björkenstam et al.:
A framework for motion planning of digital humans using discrete mechanics and optimal control

Björkenstam, S.[1], Nyström, J.[1], Carlson, J. S.[1], Roller, M.[2], Linn, J.[2], Hanson, L.[3], Högberg, D.[4], Leyendecker, S.[5]

[1] Geometry and Motion Planning group, Fraunhofer-Chalmers Center, Göteborg, Sweden
[2] Department of Mathematical Methods in Dynamics and Durability, Fraunhofer Institute for Industrial Mathematics, Kaiserslautern, Germany
[3] Scania AB, Södertälje, Sweden
[4] School of Engineering Science, University of Skövde, Sweden
[5] Chair of Applied Dynamics, University of Erlangen-Nuremberg, Germany

Abstract

In this paper we present a framework for digital human modelling using discrete mechanics and optimal control. Discrete mechanics is particularly well suited for modelling the dynamics of constrained mechanical systems, which is almost always the case when considering complex human models interacting with the environment. We demonstrate that, by using recently developed recursive dynamics algorithms, it is possible to efficiently use discrete mechanics in direct optimal control methods to plan for complex motions. Besides a proper mechanical model, an appropriate objective function is paramount to achieve realistic motions as a solution to an optimal control problem. Hence, several different objective functions, such as for example minimum time or minimum applied torque over the joints, are compared, and the resulting motions are analyzed and evaluated. To further improve the model, we include basic muscular models for the muscles of the shoulder, arm and wrist, and examine how this affects the motions.

Key words:

Optimal control, discrete mechanics, human motion planning

1   Introduction

Although the degree of automation is increasing in manufacturing industries, many assembly operations are performed manually. To avoid injuries and to reach sustainable production of high quality, comfortable environments for the operators are vital, see FALCK et al. (2010) and FALCK et al. (2014). Poor station layouts, poor product designs or badly chosen assembly sequences are common sources leading to unfavorable poses and motions. To keep costs low, preventive actions should be taken early in a project, raising the need for feasibility and ergonomics studies in virtual environments long before physical prototypes are available.

Today, in the automotive industries, such studies are conducted to some extent. The full potential, however, is far from reached due to limited software support in terms of capability for realistic pose prediction, motion generation and collision avoidance. As a consequence, ergonomics studies are time consuming and are mostly done for static poses, not for full assembly motions. Furthermore, these ergonomic studies, even though performed by a small group of highly specialized simulation engineers, show low reproducibility within the group (LÄMKULL et al., 2008).

To describe operations and facilitate motion generation, it is common to equip the manikin with coordinate frames attached to end-effectors like hands and feet. The inverse kinematic problem is to find joint values such that the position and orientation of hands and feet matches certain target frames. For the quasi-static inverse kinematics this leads to an underdetermined system of equations since the number of joints exceeds the end-effectors' constraints. Due to this redundancy there exist a set of solutions, allowing us to consider ergonomics aspects, collision avoidance, and maximizing comfort when choosing one solution (BOHLIN et al., 2011).

The dynamic motion planning problem is stated as an optimal control problem, which we discretize using discrete mechanics. This results in a nonlinear constrained optimization problem, which can be solved using standard nonlinear programming solvers. Furthermore, this general problem formulation makes it straight forward to include very general constraints and objectives.

In this paper we work with the DHM tool IMMA (HANSON et al., 2011), and the paper extends the work presented in BOHLIN et al. (2011) and DELFS et al. (2014), and is a part of the CROMM (Creation of Muscle Manikins) (HÖGBERG et al., 2016) and EMMA-CC (Ergo-Dynamic Moving Manikin with Cognitive Control) (LINN, 2016) projects.

2   Human motion planning

Here we describe the kinematical model of the manikin in the DHM tool IMMA. We also describe how we introduce dynamics and optimal control in the model, and finally how we actuate the manikin using muscular forces.

Kinematics

The manikin model is a tree of rigid bodies connected by joints. Each body has a fixed reference frame, and we describe its position relative to its parent body by a rigid transformation $T(q)$, where q is the coordinate of the joint.
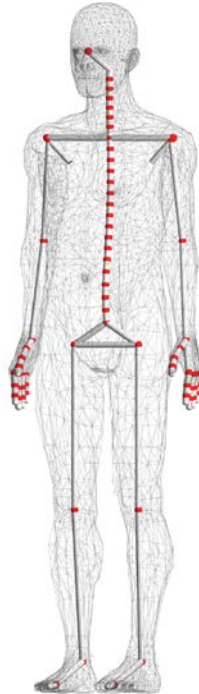
Fig. 2.1 The current mechanical manikin model in IMMA, with 192 degrees of freedom**.**

To position the manikin in space, with respect to some global coordinate system, it has an exterior joint positioning the manikin relative to a fixed inertial frame – as opposed to the interior links representing the manikin itself (Figure 2.1), see BOHLIN et al. (2011). The exterior joint is modeled as a rigid transformation that completely specifies the position of the lower lumbar in the world. In turn, the lower lumbar represents an interior root, i.e. it is the ancestor of all interior joints. Note that the choice of the lower lumbar is not critical. In principal, any link can be the interior root, and the point is that the same root can be used through a complete simulation. No re-rooting or change of tree hierarchy is needed.

For a given configuration of each joint, collected in the joint vector $q = [q_1^T, \ldots, q_n^T]^T$, we can calculate all the relative transformations $T_1, \ldots, T_n$, traverse the tree beginning at the root and propagate the transformations to get the global position of each body. We say that the manikin is placed in a pose, and the mapping from a joint vector into a pose is called forward kinematics. Furthermore, a continuous mapping $q(t)$, where $t \in R$, is called a motion, or a trajectory of the system.

Dynamics and optimal control

Traditionally, human simulation tools use quasi-static poses to emulate motion, which severely limits the possible set of motions which can be produced. Furthermore, the current version of the IMMA tool does not include muscles, which are necessary to make detailed assessments of work related musculoskeletal disorders. Our goal is to extend the model in IMMA to be able to generate dynamically feasible motions for the manikin based on a performance index, which could typically include quantities such as comfort, muscle strain, and cycle time. Furthermore, we want to be able to realistically simulate highly dynamic motions, where modelling of inertial effects become crucial. To do this, we model the manikin as a dynamical system, and use optimal control methods to compute the motions. Optimal control is the problem of determining a control function for a dynamical system in order to minimize a given performance index.

In order to solve the optimal control problem on a computer, we discretize the continuous problem into a nonlinear programming problem using discrete mechanics. In discrete mechanics, the variational principle is directly discretized into a set of nonlinear equations known as the discrete Euler-Lagrange equations. The discrete equations of motions derived in this way have been shown to be superior compared to standard discretizations since they preserve characteristics of the continuous system such as conservation of momentum and a good energy behavior (MARSDEN et al., 2001). This results in very stable integrators, which in practice allows us to use large time steps when solving our problems.

In order to efficiently use the discrete equations for these potentially high dimensional systems in a direct optimal control method, it is important to exploit both the structure of the optimal control problem as well as the structure of the dynamics. This was accomplished by exploiting the partial separability of the discrete equations, and applying sparse finite differencing techniques (BJÖRKENSTAM et al., 2015).

Muscle modelling

The method described thus is able to produce realistically looking human motions if joint torques are used as control actuators. For the assessment of ergonomic risk factors, due to for instance high muscular loads, repeated work or rapid muscle activation, it seems however natural to apply a model that directly includes muscular elements. A wide range of such muscle models, ranging from simple mass-spring systems to highly detailed finite element models, have been proposed in the literature, see LEE et al. (2010) for a survey. In our work, have utilize a Hill-type force model coupled with a piecewise line segment representation of the muscles of the shoulder, arm and wrist. In total, 35 muscles are included in the model as shown in Figure 2.2.

$$F = \underbrace{A \cdot f_l \cdot f_v \cdot F_M}_{\text{Active part}} + \underbrace{k \cdot l_m}_{\text{Passive part}}$$
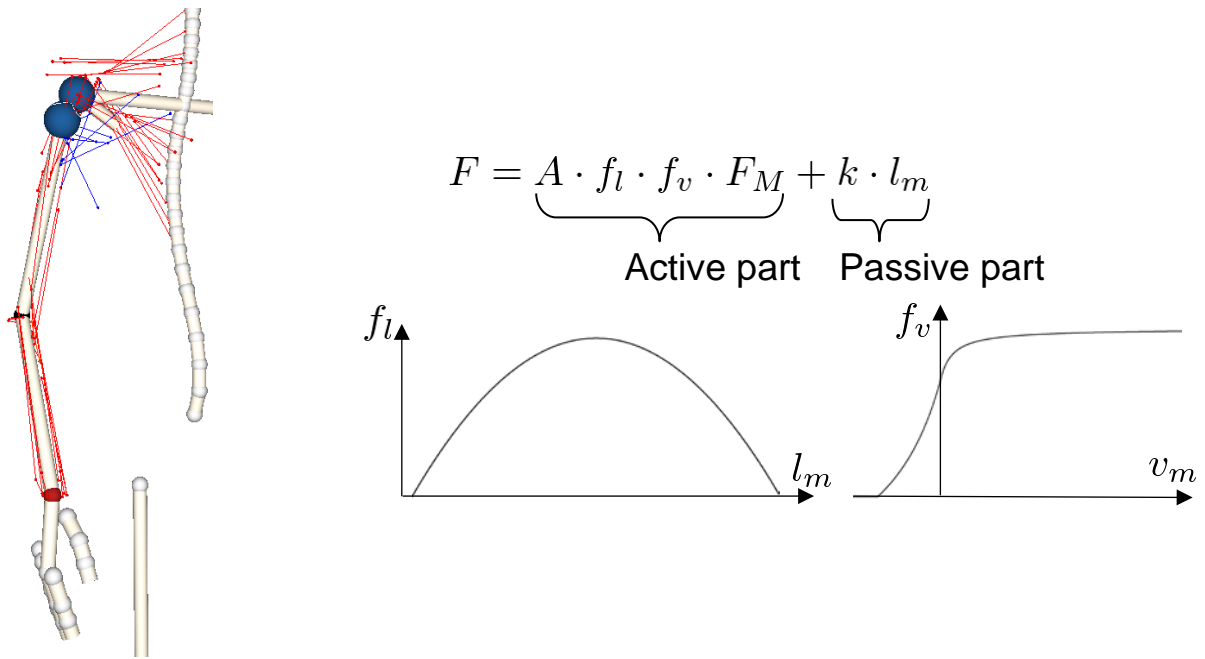
Fig. 2.2 35 Hill-type muscles are present in the manikin model and serve as actuation in the optimal control problem. For these optimizations, only the shoulder, arm and wrist were active, with the remaining manikin joints locked. Muscle activation signals are treated as control signals in the optimal control problem. Hill-type muscle models phenomenologically describe muscle forces. The models typically contain force-length and force-velocity relationships, together with an excitation-contraction coupling.

Hill models phenomenologically capture the force-length and force-velocity dependencies observed in real muscles and typically include both active and passive contributions to the total muscle contraction force. The specific Hill model used in this work is the nonlinear Hill-type muscle actuation from MAAS et al. (2013), which presents a trade-off between low computational cost needed for the optimal control and enough parameters to fit the behavior of the model to measurement data or more detailed simulation models.

The activation signals – values between 0 and 1 – for each muscle are used as control signals for the optimal control problem, and the task of the optimization is to produce muscle activations for lifting a box of specified weight, as shown in Figure *2.3*. The parameters of the objective function are set to give a compromise between low muscle activation signals and short motion time. As a result, the heavy box is lifted closer to the body, reducing the forces needed to perform the motion at the cost of longer motion time.
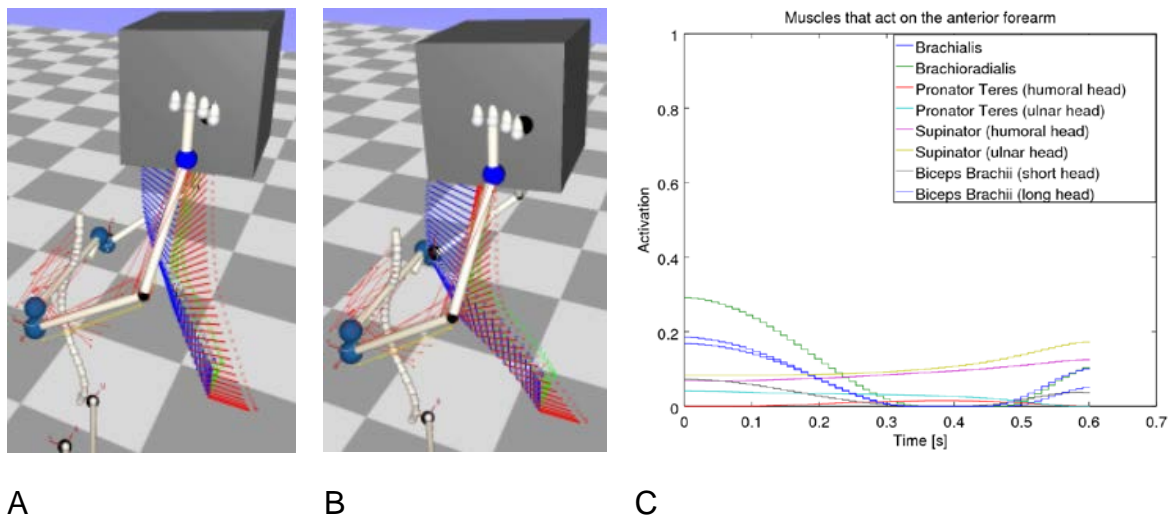
Fig. 2.3 Optimizations of muscle activations for the muscles of the shoulder, arm and wrist are performed for the task of lifting a box. As the box weight is increased (low weight in A and large weight in B) the path follows by the center of mass of the box is clearly adapted; a result following from the objective function to minimize muscle activations at the same time as minimizing the time of moving the box between specified start and end positions. In C are examples of activation signals (control signals from the optimal control problem) for the muscles that act on the anterior forearm. Similar types of signals for all muscles included in the model are the output of the optimization procedure.

The optimal control solution to this task was computed in close to real time and demonstrates the capabilities of the approach. Future work includes research in automatized ways to tune the approximately 1000 model parameters used for the 35 simulated muscles, based either on measurement data or models, and to extend the model to simulate larger parts of the human body, as done in LEE et al. (2009). The muscle model may be extended by rate equations describing the fractions of muscle fibers that are active, exhausted or in recovery, to capture fatigue effects due to repetitive loading (LIU et al., 2002). A framework for automatically adjusting muscle parameters to simulate individuals that are strong/weak, tall/short, with long/short arms etc. is the long term challenge, where the plan is to associate the framework development to the work presented in BROLIN et al. (2016). With this in place the goal is to give input in the process of designing ergonomically better work places and work procedures, leading to sustainable production with increased human well-being and overall system performance.

3   Conclusions

By introducing dynamic simulation capabilities to the IMMA software and adding muscles to the manikin, the aim of this work was to take the digital human modelling tool to a new level, where not only static loads on different joints in the body can be analyzed, but where also musculoskeletal dose-response based evaluations can be made with more precision. This has been achieved using a Hill-type muscle model,

simulating both active and passive components of muscle contraction, in combination with the framework for dynamical manikin simulations.

Muscle activation was modelled as an activation signal – a value between 0 and 1 – very similar to the MVC (maximum voluntary contraction) concept used to assess muscular loads (GARG et al., 2002). The activation signal is found by the optimal control optimization algorithm and gives rise to forces on the muscle attachment points, which are converted to joint torques that result in manikin motion. Each activation signal can control multiple muscles, allowing for simulation of broader muscles by having several single line segment muscles controlled by the same signal.

The fact that paths generated by the DHM tool are now dynamic and have a time stamp for each manikin position allows for extended comparisons between simulation results and measures made in the physical world, something we view as one of the great benefits added to the IMMA software. Output from the software now includes time dependent muscle activations and muscle forces, which can be used for instance when analyzing the benefits and disadvantages of performing a task in different alternative ways.

Acknowledgements

List of references

Björkenstam, S.; Carlson, J. S.; Lennartson, B.: Exploiting sparsity in the discrete mechanics and optimal control method with application to human motion planning. In: Automation Science and Engineering (CASE), 2015 IEEE International Conference on IEEE (2015), S. 769–774

Bohlin, R.; Delfs, N.; Hanson, L.; Högberg, D.; Carlson, J. S.: Unified solution of manikin physics and positioning - Exterior root by introduction of extra parameters. In: Proceedings of DHM, First International Symposium on Digital Human Modeling (2011)

Brolin, E.; Högberg, D.; Hanson, L.; Örtengren, R.: Generation and evaluation of distributed cases by clustering of diverse anthropometric data. In: International Journal of Human Factors Modelling and Simulation 5 (2016), Nr. 3, S. 210–229

Delfs, N.; Bohlin, R.; Gustafsson, S.; Mårdberg, P.; Carlson, J. S.: Automatic Creation of Manikin Motions Affected by Cable Forces. In: Procedia CIRP 23 (2014), S. 35–40

Falck, A. C.; Örtengren, R.; Högberg, D.: The impact of poor assembly ergonomics on product quality: A cost-benefit analysis in car manufacturing. In: Human Factors and Ergonomics in Manufacturing & Service Industries 20 (2010), Nr. 1, S. 24–41

Falck, A. C.; Rosenqvist, M.: A model for calculation of the costs of poor assembly ergonomics (part 1). In: International Journal of Industrial Ergonomics 44 (2014), Nr. 1, S. 140–147

Garg, A.; Hegmann, K. T.; Schwoerer, B. J.; Kapellusch, J. M.: The effect of maximum voluntary contraction on endurance times for the shoulder girdle. In: International Journal of Industrial Ergonomics 30 (2002), Nr. 2, S. 103–113

Hanson, L.; Högberg, D.; Bohlin, R.; Carlson, J. S.: IMMA–Intelligently Moving Manikins–Project Status 2011. In: Proceedings of the 1st International Symposium on Digital Human Modeling, Lyon, France, June Université Claude Bernard Lyon, 2011

Högberg, D.; Hanson, L.; Bohlin, R.; Carlson, J. S.: Creating and shaping the DHM tool IMMA for user-centred product and production design. In: International Journal of the Digital Human (2016), Nr. 2, S. 132–152

Lämkull, D.; Hanson, L.; Örtengren, R.: Uniformity in manikin posturing: A comparison between posture prediction and manual joint manipulation. In: International Journal of Human Factors Modelling and Simulation 1 (2008), S. 225–243

Lee, D.; Glueck, M.; Khan, A.; Fiume, E.; Jackson, K.: A survey of modeling and simulation of skeletal muscle. In: ACM Transactions on Graphics 28 (2010), Nr. 4, S. 1–13

Lee, S. H.; Sifakis, E.; Terzopoulos, D.: Comprehensive biomechanical modeling and simulation of the upper body. In: ACM Transactions on Graphics (TOG) 28 (2009), Nr. 4, S. 99

Linn, J.: EMMA-CC: Ergo-Dynamic Moving Manikin with Cognitive Control. In: Human Modeling and Simulation in Automotive Engineering, 6th International Symposium, Heidelberg, Germany, Oct. 20-21 (2016)

Liu, J. Z.; Brown, R. W.; Yue, G. H.: A dynamical model of muscle activation, fatigue, and recovery. In: Biophysical journal 82 (2002), Nr. 5, S. 2344–2359

Maas, R.; Leyendecker, S.: Muscle paths in biomechanical multibody simulations. In: ECCOMAS Multibody Dynamics Conference, Zagreb, Croatia, 2013

Marsden, J. E.; West, M.: Discrete mechanics and variational integrators. In: Acta Numerica 2001 10 (2001), S. 357–514

Ivaldi et al.:
Anticipatory models of human movements and dynamics: the roadmap of the AnDy project

Ivaldi, S.[1], Fritzsche, L.[2], Babic, J.[3], Stulp, F.[4], Damsgaard, M.[5], Graimann, B.[6], Luinge, H.[7], Nori, F.[8]

[1] INRIA Nancy Grand-Est, France.
[2] IMK automotive GmbH, Germany.
[3] Institut Jozef Stefan, Slovenia.
[4] DLR, Germany.
[5] AnyBody Technology A/S, Denmark.
[6] Otto Bock HealthCare GmbH, Germany.
[7] XSens Technologies BV, Netherlands.
[8] IIT, Italy.

Abstract

Future robots will need more and more anticipation capabilities, to properly react to human actions and provide efficient collaboration. To achieve this goal, we need new technologies that not only estimate the motion of the humans, but that fully describe the whole-body dynamics of the interaction and that can also predict its outcome. These hardware and software technologies are the goal of the European project AnDy.

In this paper, we describe the roadmap of AnDy, which leverages existing technologies to endow robots with the ability to control physical collaboration through intentional interaction. To achieve this goal, AnDy relies on three technological and scientific breakthroughs. First, AnDy will innovate the way of measuring human whole-body motions by developing the wearable AnDySuit, which tracks motions and records forces. Second, AnDy will develop the AnDyModel, which combines ergonomic models with cognitive predictive models of human dynamic behavior in collaborative tasks, learned from data acquired with the AnDySuit. Third, AnDy will propose AnDyControl, an innovative technology for assisting humans through predictive physical control, based on AnDyModel.

By measuring and modeling human whole-body dynamics, AnDy will provide robots with a new level of awareness about human intentions and ergonomy. By incorporating this awareness on-line in the robot's controllers, AnDy paves the way for novel applications of physical human-robot collaboration in manufacturing, health-care, and assisted living.

Key words:

robotics, wearable sensors, ergonomics, machine learning, prediction, anticipation, MSD, human movement, cobots, exoskeletons, humanoids

1   Introduction

In modern societies, the demand for physical assistance to humans is increasing. In factories, for example, production workers execute repetitive tasks in non-ergonomic postures that, on the long run, often cause musculo-skeletal diseases. The increasing age of the workers poses additional risks for muscolo-skeletal accidents in physically demanding tasks. Many workstations are now equipped with co-bots sharing the workspace with workers. Despite the fact that the low-level control of these machines allows the humans to physically interact with them in a safe way, most workstations actually implement the concept of "human-robot co-existence", that is the robot and the human share the space, work side by side, but have very few limited interactions. Particularly, there is little "collaboration", that literally means "working together". If robots want to go beyond the mere "act" in a shared space, they must not only be proficient in physical interaction, but also in physical collaboration.

Not all (physical) interactions necessarily are collaborations. Collaboration is a higher and more cognitive form of interaction, where the two partners mutually understand each other, mutually predict and control the exchanged forces, posture and movements while being able to anticipate those of the other partner.

To fully describe the whole-body dynamics of humans collaborating with other humans, and humans collaborating with robots, we need new technologies that allow us to not only estimate the motion, but also to predict its outcome, so that the robots can properly react to the human actions and provide efficient collaboration. These hardware and software technologies are the goals of the H2020 European project AnDy (www.andy-project.eu).

The aim of this paper is to present the roadmap of the AnDy project, presenting the key methodologies and technologies that we will develop for tackling our ambitious objectives.
In AnDy, our requirement is to develop safe dependable robotic systems that are able to collaborate with people by predicting and anticipating their movements.
Having such skills requires understanding the biomechanics of collaboration, to have models that we can use to integrate cognition in the robot. To develop these models, we need to track and model the human whole-body dynamics motions.

However, current robotic technologies are not yet able to provide these measures in real-time: therefore robots have a blind spot. To predict the future forces and postures of the human, we need first a sensing device that can measure the human whole-body dynamics, which makes the robot aware of the entire human body posture. This is very different from the current cases where the robot only controls the physical interaction with the human, and is thus aware of the human only at the contact level.
In other terms, the current limitations of robots in observing human dynamics makes them blind to the human dynamics, and "unaware" of the human effort, which leads to inefficient and non-ergonomic collaboration.

In AnDy, our first milestone is to resolve this blind spot, by developing a novel sensor suit, the AnDySuit, capable of measuring human whole body dynamics in real-time.

The big data sets collected with the AnDySuit will be used to generate ergonomic and anticipatory models. Those models will be used online by the robots to adapt their on-line control and make collaboration more efficient and ergonomic. It will combine wearable sensing technologies based on inertial sensors, EMG, tactile and force/torque sensors.

To evaluate the AnDySuit and its application for ergonomic human-robot collaboration, we devised three validation scenarios covering a wide spectrum of technical challenges in a crescendo of complexity. In the first validation scenario, the robot is an industrial cobot, which tailors its controllers to individual workers to improve ergonomy. In the second, the robot is an assistive exoskeleton that optimizes human comfort by reducing physical stress. In the third, the robot is a humanoid, which offers assistance to a human while maintaining the balance of both.In all three cases the robot leverages the measurements of the AnDySuit and the models to predict the intention, action and efforts of the human. This knowledge is the basis to develop novel controllers for efficient human-robot collaboration.

Further, the three scenarios with the three different robots (cobot, exoskeleton and humanoid) allow us to investigate the collaborative action and strategies of the robot in different contexts of manufacturing and industry, which increases the impact of our research.

2 Methods

The ability to collaborate with humans requires that the robots have the ability to provide physical assistance to people that needs help in performing a certain task. The fundamental assumption is that physical collaboration requires the robot to understand what the partner is doing and predict what the partner is going to do. This requires a model of the partner, and since we are not only interested in the motion but also in the effort, we need a comprehensive model that contains kinematics and dynamics information of the human.
Developing models requires observations, and to make appropriate observations to study a phenomenon often we need to create new tools. This paradigm is recurrent in our history since centuries: for example, the Newtonian telescope was used to observe celestial orbits, which led to the universal gravitation law. In a similar way, to develop anticipatory controllers that enable robots to collaborate with human partners (AnDyControl) we need predictive models of the human motion and dynamics (AnDyModel); to create these models, we need to collect observations of collaborating partners (AnDyDataset), with a novel tool (AnDySuit) that allows us to fully measure the kinematics and dynamics of the humans.

2.1 Key technologies

Methodologically, the concept above translates into four sequentially enabling objectives, which define our roadmap:

— The AnDySuit: this is going to be a breakthrough technology that allows us to fill the blind spot of measuring human-robot physical interaction. The AnDySuit is a wearable device that monitors in real-time the kinematics (position, velocity, acceleration at the joints/limbs) and dynamics of the human (contact forces, joint torques and muscle activations): that is, it provides the whole-body posture and whole-body dynamics. By processing the kinematics and dynamics measures, it allows retrieving important variables for collaboration, such as the contact stiffness, the gaze direction (here approximated by head direction), and for ergonomics, such as the body posture.

— The AnDyDataset: the AnDySuit will enable us to record the motion and dynamics of a human performing different tasks, of two humans collaborating, and of a human collaborating with the robot. The kind of recordings we will do are unique in their kind, as we will mix wearable inertial measures, force/torque measures, EMG, motion capture, etc. This will allow us to record kinematics descriptors of the actions (e.g., marker placement, estimated joint angles) as well as dynamics descriptors (e.g., contact force at the hands and feet, arm stiffness). Data collection will take place both in research labs and in real manufacturing scenarios. Experimental protocols with ethics committee approval will be obtained by the partners leading the data collection.

— The AnDyModel: the AnDyDataset will enable the development of models of human motion and dynamics and human collaboration. Accurate dynamics models will rely on the musculo-skeletal models of AnyBody, but model reduction and strong optimization will be obtain real-time signals. We aim at three different types of models: ergonomics models, that are used to retrieve relevant metrics for assessing the ergonomics impact of the motions, based on the metrics of the standard evaluation tools (e.g., EAWS, OCRA) (GLAESER et al., 2014); classification models, that are used to recognize the current activity of the human; and predictive models, that are used to predict the future evolution of the dynamics and motion of the human (e.g., the goal position of a reaching action, as well as the joint torques that are necessary to accomplish the movement). For the latter, we will explore different machine learning tools, ranging from probabilistic movement primitives to deep neural networks (DRONIOU et al., 2015).

— The AnDyControl: the final objective is to develop online control strategies for physical human-robot collaboration. Thanks to the AnDySuit, we can measure the human motion and its dynamics in real-time. These observations can be used to make predictions using the prior information provided by the AnDyModel, for example predicting the goal of a human movement, which forces or trajectories to expect. The AnDyControl here has the goal to adapt the robot control strategy in real-time, taking into account such predictions, with the purpose to optimize the collaboration, particularly the ergonomics criteria of the human movement.

The four objectives are summarized in Figure 3.1, which also represents the logical and temporal structure of the project and the interconnection between the objectives. The development of the AnDySuit is the first goal of the project, as it defines the main dependency for the dataset collection. Since it is mostly based on wearable sensing

technologies that are already available on the market, it is reasonable to expect a high TRL (*technology readiness level*) for this device.

All the other objectives have a lower expected TRL, with the most ambitious predictive models and controllers for collaboration being those with the lowest.

The development of models and controllers will basically proceed in parallel, in a crescendo of complexity. In order to reduce the risks of a purely sequential methodology, we defined a number of sub-objectives at incremental levels of difficulty with respect to two main metrics that are particularly relevant for collaborative tasks: mutual-care and anticipation.

Mutual-care is related to the amount of care for the partner, i.e., the concern that the actor has for the partner (e.g., partner's equilibrium, partner's posture, partner's effort) in the collaborative task execution. In a situation of minimal care, the robot does not particularly care about the forces and postures that the human assumes during the collaboration. If the robot starts "caring" about the human, it means it takes into account human-related variables in the design of its control action. For example, it evaluates the ergonomics postures of the human during the collaborative task, to adapt its action to maximize the comfort of the human. To show better "care", the robot must then monitor the posture and forces in real-time, all along the collaboration, to react and optimize the collaborative action.

Anticipation is related to the amount of synchronization needed to successfully complete the collaborative task, and it is strongly related to the prediction capabilities of the robot. In a situation of minimal anticipation, the robot does not need to anticipate the human partner's positions or forces to perform the collaborative task. If the robot is capable of classifying and recognizing the current action performed by the human, it can choose appropriate control settings to adapt to each action/task. If it can recognize the goal of a reaching movement, or the intent of motion, it can proactively provide a support control action. If it is able to predict the positions and forces that the human partner will do, it can use this information to choose its future control actions and postures as well.

A sketch of the collaborative objectives in terms of the increasing levels of anticipation and mutual-care is shown in Figure 3.2. Interestingly, the complexity of models and controllers is reflected also in the type of robots used for demonstrating the collaborative tasks.

We stress on the fact that the collaborative scenarios will use the AnDySuit, which provides the online measurements of the human motion and forces, the AnDyModels to extract ergonomics metrics, predict the intentions and motions, and the AnDyController to provide suitable *human-careful* controllers.

The key difference with respect to previous projects is to provide technologies for human-aware and human-careful physical collaboration. *Human-awareness* refers to the fact that robot should be able to monitor human motions and forces. Human-care refers to the robot ability to provide a collaborative interaction that takes into account the human needs (e.g. ergonomic posture, minimal fatigue, equilibrium maintenance). In the literature, most prior works dealing with collaboration provide

prediction (i.e. human-awareness) but often with limited human monitoring. Very often human-robot interaction is modeled as an exchange of forces, without explicitly modeling neither the human posture, nor the human joint torques. For example, in the manufacturing domain often only the contact forces or the forces at the end-effector are considered. In the healthcare domain, exoskeletons typically access the human posture and exchanged forces (eventually projected into joint-torques) but this information is always local (i.e. limited to body parts where the exoskeleton is attached); the remaining body postures and forces are often neglected. Few projects have been focused on the importance of monitoring human body posture, typically measured with depth sensors (e.g. kinect) or wearable devices (e.g. the Xsens MVN). In this sense, in AnDy we put forward the concept of "*human-careful*", as opposed to simple "*human-aware*", meaning that the robot takes into account the whole body measures from the human in the synthesis of its collaborative strategies.

In this sense, the AnDySuit is going to be a breakthrough technology that allows us to fill the blind spot of measuring human-robot physical interaction. This wearable device that monitors in real-time the kinematics (position, velocity, acceleration at the joints/limbs) and dynamics of the human (contact forces, joint torques and muscle activations): that is, it provides the whole-body posture and whole-body dynamics. By processing the kinematics and dynamics measures, it allows retrieving important variables for collaboration, such as the contact stiffness, the gaze direction (here approximated by head direction), and for ergonomics, such as the body posture. These quantities will be used by the robots to optimize their control strategies, with the aim to provide ergonomically safe actions for the human partners. By optimizing human-related metrics, we will realize a human-careful control.

3   Results

The achievements of the project will be experimentally evaluated on different robotic platforms, addressing different collaborative scenarios.

Three types of robots are addressed in AnDy: collaborative robotic manipulators, or "cobots", exoskeletons and humanoid robots.

Cobots are already diffused in manufacturing, and so far have been mostly used in co-existance scenario where human operators share the same workspace of the robot, working side-by-side or performing tasks in coordination. For these robots, performing more collaborative tasks is an innovation requiring the online ergonomics estimation of the human partner. The main cobots we will use in AnDy are the KUKA iiwa and LWR.

For exoskeletons, the main problem we will address is how to adapt control settings to the action of the human operator in a smooth and automatic way. An interesting research is the quantification of the effects of the action of the exoskeleton on the human body, which requires the measure of kinematics and dynamics of the human thanks to the AnDySuit. The main platform we will use in AnDy is an exoskeleton for overhead work by Ottobock.

Humanoids robots, especially legged robots, are still research prototypes. However, in the future it is reasonable to expect that humanoids will find their use in manufacturing, in applications where *cobots* or even manipulators mounted on a mobile base would not be able to perform the desired tasks.
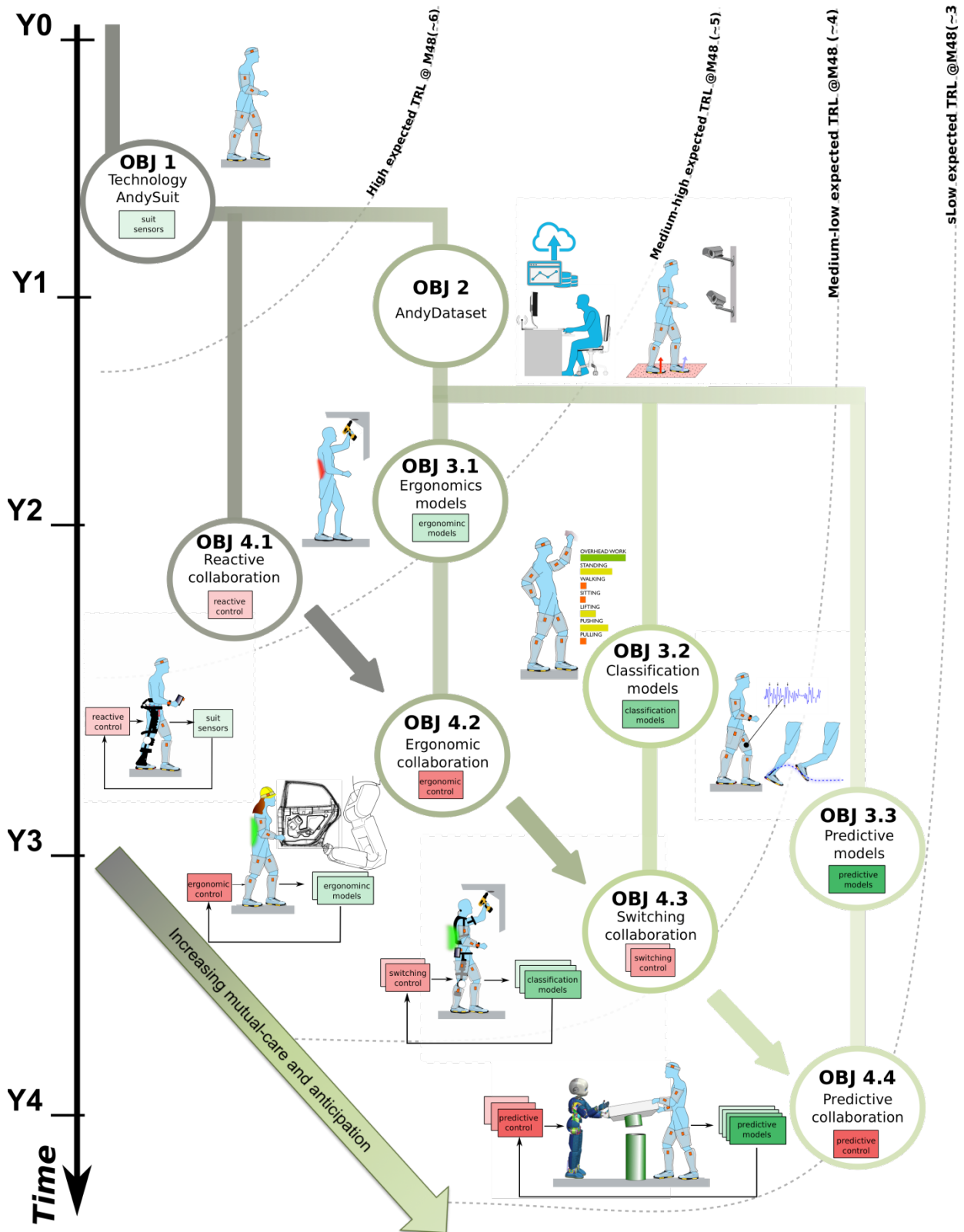
Fig. 3.1 [Notice: this figure may be difficult to interpret if not printed/visualized in colors] A sketch of the roadmap of the AnDy project and its objectives.
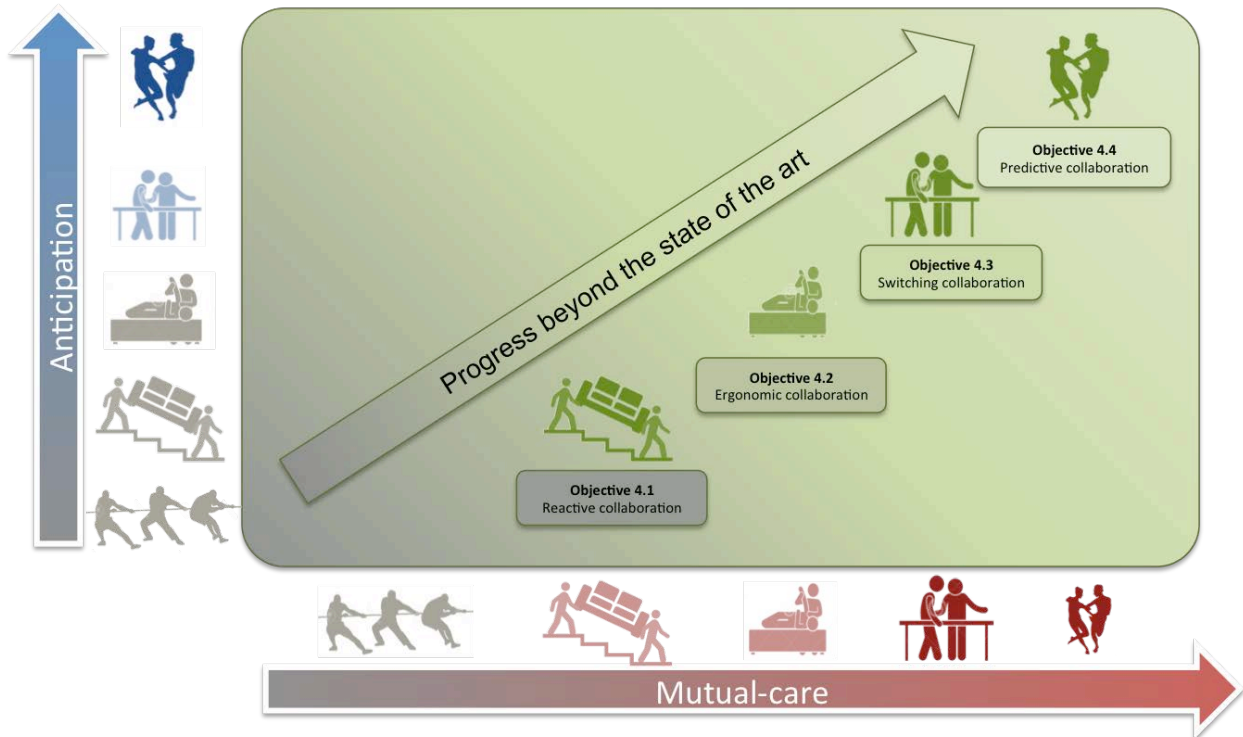
Fig. 3.2 [Notice: this figure may be difficult to interpret if not printed/visualized in colors]. A sketch of the collaborative control objectives, with respect to the different levels of mutual-care and anticipation, used as metrics for collaboration.

The three collaborative scenarios with the three types of robots are represented in Figure 3.3.
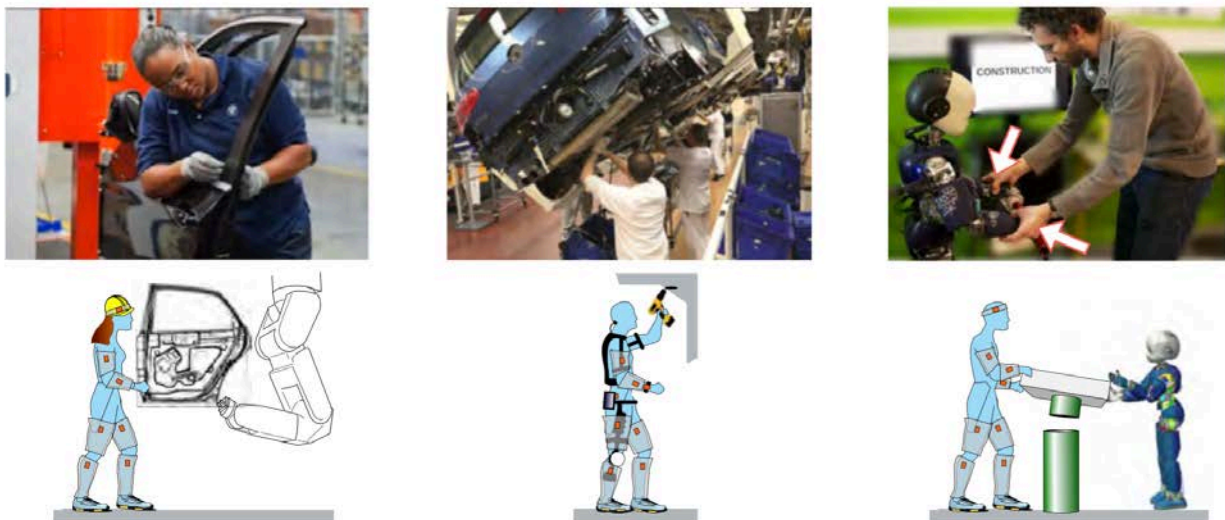
Fig. 3.3 the three collaboration scenarios with the three different robot types: cobot or robotic manipulator, exoskeleton and humanoid robot.

Some European projects are currently focused on producing new humanoids for aircraft manufacturing (H2020 COMANOID – http://comanoid.cnrs.fr) and for technical support (H2020 SECOND HANDS – http://secondhands.eu). In our project, we will use the humanoid robot iCub, which is equipped with force and tactile sensing and allows us to tackle the scientific challenges of collaborative human-humanoid interaction.

3.1 Scenario 1 (cobots)

A key feature of collaborative robots / cobots in assembly is that they share a workspace with human workers. Important distinctions between different types of cobots are whether they avoid or exploit contact with humans, and whether they are purely reactive or also predictive (HADDADIN et al., 2008; HADDADIN et al., 2012). In contrast, SISBOT et al. (2010) generate motion plans that take human social rules into account. DRAGAN et al. (2013) plan motions such that they become easier for humans to interpret. Kinesthetic teaching exploits human-robot physical contact by enabling humans to demonstrate motions to robots by physically moving the (passive) robot (STULP et al., 2013). Virtual guides also enable human-robot contact, by constraining the motion to certain pre-defined trajectories or regions (RAIOLA et al., 2015).

Dynamic, active physical interaction between a human and a robot is particularly challenging. AnDy enables this by 1) giving direct, on-line measurements of the human posture and forces exerted by the human through AnDySuit; 2) by not only reacting to, but also predicting human motion with AnDyModel by analyzing previous executions of tasks stored in AnDyDataset; 3) by taking the ergonomy of the human into account whilst generating motions. Monitoring humans with the AnDySuit will also facilitate the task of programming force-controlled robots for complex assembly tasks. At present the cost of cobots and associated programming is not cost-effective for small production lots (e.g. SMEs) and to flexible and customized productions. ANDY will enable force-controlled assemblies through collaborative human-cobot assemblies that will be more flexible, easier to customize and in the end more cost effective and suitable for SMEs.

3.2 Scenario 2 (exoskeletons)

Robotic assistive devices (i.e. exoskeletons) are being developed to either augment the abilities of able-bodied humans or to improve the condition of the people with impaired physical abilities (RAHMAN et al., 2006). Such devices assist movement abilities of different body parts (reviewed by DOLLAR et al., 2008). The purpose of such devices is to provide useful mechanical power by operating synchronously with the person that is wearing it (GAMS et al., 2013). The human robot interface is crucial for a safe and comfortable interaction with an exoskeleton device (de ROSSI et al., 2011).

From the technical perspective there are two branches of exoskeleton development: passive power assist devices and active power assist devices. In general, active power assist devices are more powerful, but require actuators and power source,

which make them quite heavy; they can be found mostly in rehabilitation, orthopedics, assistive devices (YAMAMOTO et al., 2004; KAWAMOTO et al., 2005). On the other hand, passive power assist devices are mainly used to reduce the burden of the user rather than to amplify their forces (IMAMURA et al., 2011; WALSH et al., 2007).

One of the crucial elements of active assistive robots and exoskeletons are the actuators. A promising alternative to conventional stiff actuators is the use of elastic elements to create an intrinsic compliant behavior. This allows a safer human-robot interaction, shock absorbance, and leads to a greater energy efficiency than stiff actuators (VANDERBORGHT et al., 2012). An expansion of compliant actuators is variable stiffness actuators (VSAs) that allow changing the stiffness of the driven joint. These actuators fit the requirements of certain bio-inspired robots, since humans use the ability of changing joint stiffness to change, for example, the walking speed (KIM et al., 2011), and to accommodate changes in surface stiffness during walking (FERRIS et al., 1998). VSAs can, in principle, be used to extend the versatility of spinal support systems.

Today, especially for the assembly of heavy or bulky parts, weight compensators/balancers are used. Since these systems do not compensate for inertial forces, even small mistakes lead to work-related injuries (lower back pain, spine injuries) (KROEGER et al., 2009). In this context, AnDy will establish a novel paradigm for ergonomic interventions through a combination of the four interrelated technologies (AnDySuit, AnDyDataset, AnDymodel and AnDyControl). With AnDy the workers working in human-unfriendly environments will get a valuable assistant that will make their job safe from the possible injuries. The solutions in AnDy also have high potential to become an indispensable diagnostic tool for specialists working in physical medicine and rehabilitation, occupational medicine, and others. A driving force behind the efforts in this scenario is the fact that musculoskeletal problems account for the largest part of work incapacities and that there is a clear demand for solutions that would mitigate these problems. Our project will utilize such sensory solutions (i) to develop models for studying loading of the human joints and then (ii) to leverage exoskeleton control principles and create solutions that will allow a natural merge of exoskeleton technology with the vast spectrum of available sensory solutions.

Moreover, the control strategy developed in AnDy for the exoskeletal system will smooth the breakthrough of human-exoskeletal interaction in the field of wearable/assistive robots that support workers in a variety of tasks. Our goal is to improve working ergonomics with prevention of muscle skeletal disease, which will have a direct influence on improving the quality of manufacturing and related processes with special attention given to the ageing workforce. To make sure that the innovation potential of this scenario is as high as possible, user-acceptance and cost-effectiveness will be also addressed.

3.3   Scenario 3 (humanoid robots)

In the human-humanoid interaction experiments with the iCub performing collaborative assembly with 56 adults, IVALDI et al. (2017) gained a lot of knowledge about the dynamics of social signals and physical signals (e.g., contact forces). However, in these experiments switching control strategies to adapt the compliance were controlled by the human and there was no prediction of human intent. On the other hand, in the CoDyCo project there have been numerous advancements in the whole-body interaction of the iCub with its environment (NORI et al., 2015), also with humans perturbing the robot equilibrium. There is a need to make the two research streams converge for the case of collaboration. This convergence should happen at several levels: first at the control level, as the robot should be able to cope with the contact forces; second, at the prediction level, as the robot should extract information from the haptic exchange. The first problem is about how to switch between controllers where contact forces must be rejected or followed, which are about functional roles. Traditionally, many works adopted a conservative approach of assigning the robot a passive follower role, e.g. implemented with a low-level impedance control loop in pHRI. Based on fixed roles (master/slave, leader/follower), the robot can easily estimate the human intention and improve the collaboration (GROTEN et al., 2010). Extracting information from haptic signals has been addressed in several papers using local force/torque sensing (BUSSY et al., 2012; BERGER et al., 2013); however, DUMORA et al. (2012) noted that wrench measurements provide incomplete information to detect the operator's intent of motion, which was confirmed by REED (2012). Haptic feedback can temporarily be sufficient to achieve sub-tasks, if contextual information about the task phase is provided. However, more non-verbal cues, e.g., gaze, may be necessary to recognize the partner intent during collaborative tasks and synchronize the dyadic activity (IVALDI et al., 2014). Humanoid robots such as the iCub are well poised to investigate these issues.

In AnDy, we want to exploit the humanoid to push further the complexity of the collaboration. First, the humanoid will be balancing on its feet, therefore it will have to carefully control the exchanged forces and anticipate the human forces to prevent falling; there will be a bilateral control action in place, and the robot will need to balance the control strategy between leader and follower, predicting the human action. Finally, the human and the humanoid will have to realize a complex assembly action, for example a collaborative carrying or a snap-fit. As in the other scenarios, the AnDySuit provides the human posture and dynamics, AnDyModel provides models of human motion: the AnDyControl here is pushed to a bigger level of complexity. From the robot control point of view, this task explores the trade-off between physical interaction and postural tasks when the robot balance is at stake. Control strategies mixing soft and hard priorities will be considered and combined with suitable learning strategies to cope with uncertainties, following previous results (NAVA et al., 2017; MODUGNO et al., 2016). Furthermore, this task allows studying whole-body control strategies for humanoid robots with several tasks and several constraints (some from the human, some from the humanoid, some originated by the closed-loop chain formed during their collaboration) in presence of partial and noisy observations of the state.

4   Conclusion

The H2020 European Project AnDy started in January 2017 and lasts 4 years. The goal of AnDy is to endow robots with the ability to control physical collaboration through intentional interaction. To achieve this goal, AnDy relies on three technological pillars: a wearable sensing device, called AnDySuit, which tracks the human motions and forces; AnDyModel, that is ergonomic and human movement models that also provide prediction of movement in collaborative tasks; AnDyControl, which combines ergonomic models with cognitive predictive models of human dynamic behavior in collaborative tasks, learned from data acquired with the AnDySuit.

In this paper, we described the roadmap of the project, its motivation and its objectives. As described in the previous section, the research outlined in the roadmap builds on prior results from the different partners, such as the learning and control frameworks developed in the last years in the framework of the European Projects CoDyCo (https://www.codyco.eu/) and Spexor (http://www.spexor.eu/), for humanoid robots, cobots and exoskeletons.

Acknowledgment

List of references

Berger, E.; Vogt, D.; Haji-Ghassemi, N.; Jung, B.; Ben Amor, H.: Inferring guidance Information in Cooperative Human-Robot Tasks. In: HUMANOIDS 2013.

Bussy, A.; Kheddar, A.; Crosnier, A.; Keith, F.: Human-humanoid haptic joint object transportation case study. In: IROS 2012, pp. 3633–3638.

De Rossi, S. M. M.; Vitiello, N.; et al.: Sensing pressure distribution on a lower-limb exoskeleton physical human-machine interface. In: Sensors, 2011, vol. 11 n.1, pp. 207–227.

Dollar, A. D.; Herr, H.: Lower extremity exoskeletons and active orthoses: Challenges and state-of-the-art. IEEE Transactions on Robotics, 2008, vol. 24, pp. 144–158.

Dragan, A.; Srinivasa, S.: Generating Legible Motion. Robotics: Science and Systems, 2013.

Droniou, A.; Ivaldi, S.; Sigaud, O.: Deep unsupervised network for multimodal perception, representation and classification. Robotics and Autonomous Systems, 2015, vol. 71, pp. 83-98.

Dumora, J.; Geffard, F.; Bidard, C.; Brouillet, T.; Fraisse, P.: Experimental study on haptic communication of a human in a shared human-robot collaborative task. In: IROS 2012, pp. 5137–5144.

Ferris, D. P.; Louie, M.; Farley, C. T.: Running in the real world: adjusting leg stiffness for different surfaces. In: Proceedings. Biological sciences / The Royal Society 265.1400 (1998), pp. 989–994.

Gams, A.; Petric, T.; Debevec, T.; Babic, J.: Effects of robotic knee exoskeleton on human energy expenditure. In: IEEE transactions on bio-medical engineering, 2013, vol. 60, n.6, pp. 1636–44.

Glaeser, D.; Fritzsche, L.; Bauer, S.; Leidholdt, W.: The Quest to Validate Human Motion for Digital Ergonomic Assessment – Biomechanical Studies to Improve the Human-Like Behavior of the Human Model EMA. In: Proceedings of the 5th International Conference on Applied Human Factors and Ergonomics AHFE 2014, Krakow, Poland.

Groten, R.; Feth, D.; Peer, A.; Buss, M.: Shared decision making in a collaborative task with reciprocal haptic feedback: an efficiency analysis. In: ICRA 2010, pp. 1834–1839.

Haddadin, S., Albu-Schaffer, A.; De Luca, A.; Hirzinger, G.: Collision detection and reaction: A contribution to safe physical human-robot interaction. IROS, 2008.

Haddadin, S.; Khoury, A.; Rokahr, T.; Parusel, S.; Burgkart, R.; Bicchi, A.; Albu-Schaeffer, A.: "On making robots understand safety: Embedding injury knowledge into control". International Journal of Robotics Research, 2012.

http://comanoid.cnrs.fr

https://secondhands.eu

Imamura, Y.; Tanaka, T.; Suzuki, Y.; Takizawa, K.; Yamanaka, M.: Motion-Based-Design of Elastic Material for Passive Assistive Device Using Musculoskeletal Model. In: Journal of Robotics and Mechatronics, 2011, vol. 23 n.6, pp. 978–990.

Ivaldi, S.; Anzalone, S. M.; Rousseau, W.; Sigaud, O.; Chetouani, M.: "Robot initiative in a team learning task increases the rhythm of interaction but not the perceived engagement". In: Frontiers in Neurorobotics 8.5, 2014.

Ivaldi, S.; Lefort, S.; Peters, J.; Chetouani, M.; Provasi, J.; Zibetti, E.: Towards engagement models that consider individual factors in HRI: on the relation of extroversion and negative attitude towards robots to gaze and speech during a human-robot assembly task. International Journal of Social Robotics, 2017, Vol 9, No 1, Pages 63-86.

Kawamoto, H.; Sankai, Y.: Power assist method based on Phase Sequence and muscle force condition for HAL. In: Advanced Robotics, 2005, vol. 19, pp. 717–734.

Kim, S.; Park, S.: Leg stiffness increases with speed to modulate gait frequency and propulsion energy. In: Journal of Biomechanics 44.7 (2011), pp. 1253–1258.

Kroeger, J.; Lien, T.; Verl, A.: Cooperation of human and machines in assembly lines. In: CIRP Annals - Manufacturing Technology, 2009, pp. 628 –646.

Modugno, V.; Chervet, U.; Oriolo, G.; Ivaldi, S.: Learning soft task priorities for safe control of humanoid robots with constrained stochastic optimization. In: HUMANOIDS, 2016.

Nava, G.; Pucci, D.; Nori, F.: Momentum Control of Humanoid Robots with Series Elastic Actuators. arXiv preprint arXiv:1703.01882, 2017.

Nori, F.; Traversaro, S.; Eljaik, J.; Romano, F.; Del Prete, A.; Pucci, D.: iCub Whole-body Control through Force Regulation on Rigid Noncoplanar Contacts. In: Frontiers in Robotics and AI, 2015.

Rahman, T.; Sample, W.; et al.: Passive exoskeletons for assisting limb movement. Journal of rehabilitation research and development, 2006, vol. 43 n.5, pp. 583–590.

Raiola, G.; Lamy, X.; Stulp, F.: Co-manipulation with Multiple Probabilistic Virtual Guides. In: International Conference on Intelligent Robots and Systems. IROS, 2015.

Reed, K. B.: Cooperative Physical Human-Human and Human-Robot Interaction. In: Immersive Multimodal Interactive Presence. Ed. by A. Peer and C. Giachritsis. Springer Series on Touch and Haptic Systems, 2012.

Sisbot, E. A.; Marin-Urias, L. F.; Broquere, X.; Sidobre, D.; Alami, R.: Synthesizing robot motions adapted to human presence. International Journal of Social Robotics, 2010.

Stulp, F.; Raiola, G.; Hoarau, A.; Ivaldi, S.; Sigaud, O.: Learning Compact Parameterized Skills with a Single Regression. In: HUMANOIDS, 2013.

Vanderborght, B. et al.: Variable impedance actuators: Moving the robots of tomorrow. In: IROS. 2012, pp. 5454–5455.

Walsh, C. J.; Endo, K.; Herr, H.: A quasi-passive leg exoskeleton for load-carrying augmentation. In: International Journal of Humanoid Robotics, 2007, vol 4, pp. 487–506.

Yamamoto, K.; Ishii, M.; Noborisaka, H.; Hyodo, K.: Stand alone wearable power assisting suit - sensing and control systems. In: RO-MAN, 2004.

Technical Session 3 – Elderly, Disabled and other special populations, Impact and deformation analysis

Gabrielli et al.:
New finite element human models representing elderly, disabled and overweight people for aircraft seat comfort simulation

Gabrielli, F.[1], Pudlo, P.[1], Beaugonin, M.[2], Borot, C.[2]

[1] Laboratory of Industrial and Human Automation control, Mechanical engineering and Computer Science (LAMIH UMR CNRS 8201), Université de Valenciennes et du Hainaut-Cambrésis, Valenciennes France

[2] ESI Group, Biomechanics R&D and Product Management, France

Abstract

In the growing but highly competitive market of the airline industry, airliners have to differentiate themselves from their competitors while increasing or maintaining their profitability. They request innovations in aircraft interior design to increase aircraft capacity, reduce airplane turn time through fast boarding and unloading operations, improve passenger comfort and living space, lighten aircrafts and meet safety requirements. So many necessary yet conflicting expectations, which make aircraft interior and seat design very challenging. In this context, it is easier to only manage average standard passenger population in product development phase. But morphology of passengers is evolving, as our population ages and increases in size and weight. More and more elderly people travel, and the senior market cannot be neglected by airliners. Regulations prevent also discrimination and airliners must now cater to all types of passengers, whatever their age, weight or disability.

While standard passengers can board an airplane, walk in the cabin and sit without difficulties, overweight, age and disability are usually associated with lower mobility, which raises difficulties and lowers the air travel experience. If seat access is one certain issue, seat comfort is somehow more important, especially for long range flight. The more severe is the impairment or the higher is the weight, the least is the satisfaction for the aircraft seat. That highlights the need for adapted design of aircraft seat for overweighted, senior passengers as well as the ones with severe mobility impairment, such as passengers that rely on permanent seating posture. Such design investigation, fitting to these populations, is not easy, request lots of difficult experimental tests with large group of volunteers. One alternative solution is the use of digital human model, more specifically finite element models, representing all these different populations, during the conception and development phases of aircraft seat.

The present paper will describe the development methodology of new finite human models, adapted to non-standard population of passengers, such as elderly, overweighted and disabled people. These models have been developed starting from an existing human model representing standard aircraft population as reference

model, and based on literature review. These models have been then used in seating simulations for the evaluation of aircraft seat comfort and comparison for different postures.

For severe mobility impairment passengers, there is a need of accurate figures for morphometric modification on the lower limb and lower trunk, as those segments may not be fully functional and are the most stressed segments during sitting. In order to identify morphometric modifications induced by permanent sitting posture, methodologies and methods of the reviewed process are presented and focused on permanent wheelchair users. Proposed modifications concern mainly bone, muscle, fat, and skin tissues. The most of those changes are applied to the reference finite element human model at pelvis region and lower extremities. That consists of the adaptation of muscle and fat distribution as well as the modification of radius of ischial apex curvature. Then, bony properties of these segments are updated.

For the senior and overweighted human models, an equivalent modification process has been applied for the whole body, based on the available data and specificities of the reference model. It concerns the adaptation of morphology as well as muscle and fat distribution. For the senior model, bone properties are also modified.

Seating simulations have been then performed with these dedicated models to evaluate their capabilities to highlight comfort problems encountered by these passenger population with respect to the reference standard passenger population. Three different postures, taxi, take-off and landing, inclined and relaxed ones, have been evaluated and compared.

Key words:

Virtual Seat Prototype, Comfort, Simulation, Design, Human Model, Elderly, Overweighted, Disabled

1   Introduction

The present paper describes the development of new finite human models, adapted to non-standard population of passengers, such as elderly, overweighted and disabled people. Based on a literature review, a methodology of human model development was defined, and applied to an existing human model representing standard aircraft population as reference model.

For each new human model, representing an average disabled, elderly and overweight person, a literature review has been first performed to define average values and figures for morphometric modifications, mainly for bone, muscle, fat, and skin tissue. The results of the literature studies were compiled and expressed thereafter in percentage of reduction/augmentation compared to control subjects, as the purpose is to modify a reference finite element model of a regular human. In order to offer as many modification possibilities as possible, morphometric variations were given in volume, mass and section area, depending on availability within selected literature. In the case of section area, the data are only pertinent for the corresponding body segment.The corresponding modifications have been then applied to a reference finite element model of a regular human The final part presents an application of that model as a comparison between the reference model and the modified models on sitting position.

2   Disabled/paraplegic finite element human model

At first, one of ESI human models from Virtual Seat Solution has been adapted to the H2020 Standard of AIR France for its long-haul flights, as an average representative of passengers adult population, in terms of standing height and weight.Then, changes encountered by a permanent wheelchair user, e.g. paraplegic person, have been applied to human model, to build a so called 'ESI PP model', hereafter.

The choice of the modifications are dependent on the available data in the literature which provides average values and the specific modelling of ESI human models dedicated to comfort applications.Therefore changes have been focused on pelvis and lower extremities, and have concerned adaptation of muscle and fat distribution, of radius of ischial apex curvature, and of bony properties.

2.1   Geometry modifications

2.1.1   Adaption of muscle and fat distribution

Permanent sitting position produces three major body modifications on muscle and fat tissue: muscle get thinner with both decrease of muscle fiber number and size. Several clinical studies focused on those body modifications. Thigh can show a decrease in section area from 20% to 39% (GORGEY et al, 2008) with a decrease in mass of 42% (MODLESKI et al, 2004). Calf can show a decrease in section area up to 70% (SHERK et al., 2010).

In order to match those modification, external morphology has been changed as well as the muscle and fat distribution. Based on the literature review the change has been applied to the maximum circumference of these biological components:-25% for thigh fat and muscle and -45% for calf fat and muscle.

Figure 2.1 gives a comparison between the H2020 and PP ESI human models.

ESI H2020 Standard model   ESI PP model
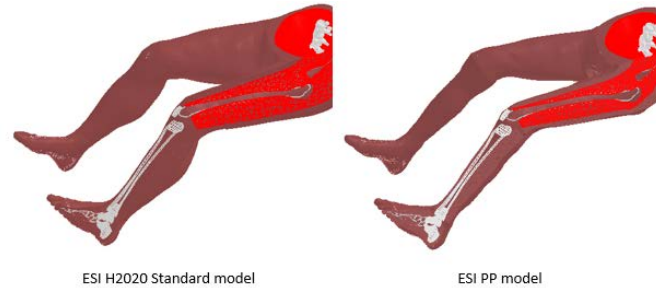
Fig. 2.1   Decrease of lower extremities circumferences**.**

External Skin   Muscles
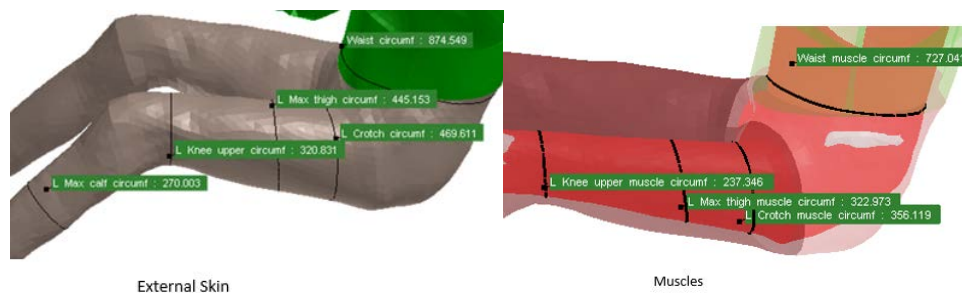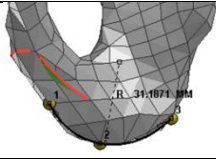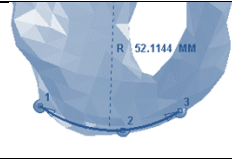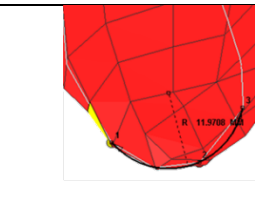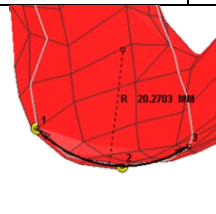
Fig. 2.2   ESI PP model – Pelvis and lower extremities circumferences

These morphological changes are important and result on big local deformation of concerned meshes. For these fat and muscles components, it has been mandatory to create new 2D and 3D meshes to ensure the mandatory quality requested by static comfort applications.

2.1.2   Adaption of radius of ischial apex curvature

Two clinical investigation reported that severe mobility impairment persons suffer for a change of their ischial apex due to permanent sitting position (LINDER-GANZ et al., 2008; LINDER-GANZ et al., 2007), resulting in an increase of their curvature radius by 70%. Ischial apex geometry has been modified in this sense, as presented in Table 2.1.

Table 2.1 Modification of radius of ischial apex curvature

Lateral view			
Curvature radius (mm)	31	52	**+68%**
Frontal Section			
Curvature radius (mm)	12	20	+70%
	ESI H2020 Standard model	ESI PP model	Difference

2.2   Bony properties modifications

The lack of muscle activity and permanent sitting posture also brought modification to bone structures. Literature reported a decrease of the thickness of cortical bone and density of both cortical and trabecular bones. Decrease for the pelvis ranged from 35% (BAUMANN et al., 1999) to 54% (DAUTY et al., 2000), for the femur 34% (MODLESKI et al., 2005) to 70% (DAUTY et al., 2000), and for the tibia from 46% (GIANGREGORIO et al., 2005) to 73% (ESER et al., 2004). Modifications in Table 2.2 have been applied to ESI PP model.

Table 2.2 Changes applied to bony structure of pelvis and lower extremities

Lower extremities : Cortical bone thickness	-35%
Bone density	
Pelvic bone	-45%
Femur	-53%
Tibia/Fibula/Foot bones	-55%

3   Elderly finite element human model

As for the paraplegic model, the elderly is an adaption of the H2020 standard European 50 percentile. In addition, literature shows that elderly usually exhibit a decrease in muscle mass (JANSSEN et al., 2000; VANDERVOORT et al., 2002; POWER et al., 2013) and some bone modification (RUFF et al., 1984; BLECK et al., 2000; MARSHALL et al., 2006). Therefore, the following changes have been done: Global morphology adaption in order to fit the dimensions of a subject selected in the CAESAR database, adaptation of muscle and fat distribution in the lower limbs, adaptation of bony properties, and adaption of the thoracic-lumbar spine (length and curvature).

3.1 Global morphology adaption

The external shape has been modified in order to take into account the increase of the adipose mass at the level of the abdomen. The subject CSR4692 from the CAESAR database is used as a target (see Figure 3.1).
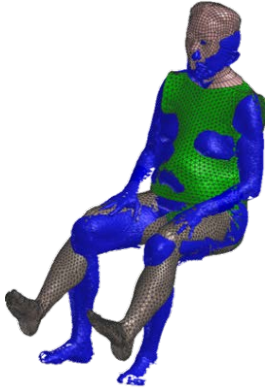
Fig. 3.1 Comparison between model (green) and targeted shape (blue

Fig. 3.2 Elderly human mode

3.2 Adaption of muscle and fat distribution

Based on literature review, a muscular atrophy is represented in the model for lower limbs of approximately 20% for 70 years old people and 40% for 80 years old people. The targeted age for the elderly model being 65 years, an atrophy of 15% is considered.

Fig. 3.3 Circumferences at the level of the skin and at the level of the muscles

3.3 Adaption of the bony properties

Age has also some impact on the bony properties. The cortical bone section decreases of approximately 25%, the external one remaining constant. The cortical thickness of lower limb bones has been modified in such extents.

3.4   Adaption of the thoracic-lumbar spine
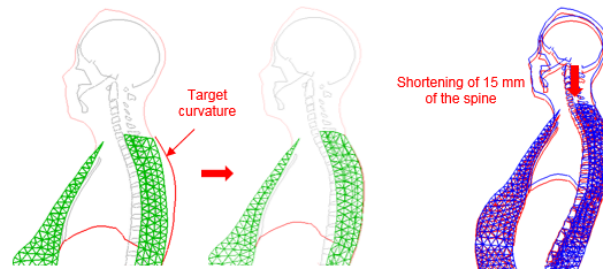
Fig. 3.4   Curvature and length of the thoracic-lumbar spine

The spine curvature is modified in order to fit the one of the CAESAR database, which is more consistent with the expected kyphosis increase at this age (MIAS et al., 1997).

4   Overweight human model

For its economic class, Air France indicates that seats are designed with an armrests distance of about 40 to 45 cm, which permits a comfortable sitting to a passenger waist size limit to 1,35 m. Therefore the target anthropometry for the overweight model is defined in this study by a waist of 1,40 m.

For the overweight model, a targeted anthropometry is selected in the CAESAR database : CSR4520, 1.4 m for the waist size. In order to produce this model, the closest one in ESI database (American 95th percentile) is taken as starting point. A litterature review has been performed (ZSFR-IFSTTAR, 2014) to study the evolution of the proportion between fat and muscle. The conclusions are an increase of the fat proportion with Body Mass Index and a decrease of the muscle density with no significant impact on comfort prediction. As a conclusion, only the external shape of the base model is modified with addition of fat tissues.

Fig. 4.1 CSR4520 CAESAR scan

Fig. 4.2 ESI American 95th human model

Fig. 4.3 ESI overweight human model

5 Human models seating on aircraft passenger seats

5.1 Pressure distribution measurements

As defined in EN 4723, comfort measurement is a set of measures related to the seat itself (such as armrest top height over seat bottom cushion, cushion height above cabin floor level or average bed angle in full recline position), but also pressure distribution for several occupant postures. Usually volunteers are used to measure them.

But pressure mapping measurements performed with volunteers lead to two mains issues. The first one is the repeatability aspect of such experiment. Indeed, a pressure distribution is highly dependent on the anthropometry and weight, as well as the characteristics in terms of muscle tonus (flesh stiffness). As a consequence, the same individual should perform the tests in order to enable comparisons between seats. Additionally, for a given individual, a change in posture will dramatically affect the pressure distribution.

The second main issue regarding tests with volunteers is the subjectivity. The comfort/discomfort notion is highly subjective and such subjectivity doesn't leave the possibility to do fair benchmarking between seats. It is therefore necessary to relate the objective pressure distribution measurement to this subjective feeling. Such connection has been established (MERGL et al., 2006).

5.2 Seating simulation of human models

The human models previously described (disabled, elderly and overweight human models), are used to simulate their seating in aircraft economic class seat, and to compare the induced pressure map. First a virtual seat model of a Zodiac seat Z301 is build, as shown in Fig 4.1, published in AEGATS2016_37 paper (BOROT et al., 2016).

Fig. 5.1   Zodiac Seat Z301 Virtual Prototype published in Aegats publication

Then, the human models are seated by simulation on this seat with a standard and repeatable seating procedure in three different postures:

— TTL (Taxi / Take off / Landing) where the backrest is in its straight position, and the main support is brought to the human by the bottom cushion,

— Reclined where the backrest is reclined and the support of the bottom cushion is diminished,

— Relaxed where the backrest is in its straight position and the occupant bends his spine laterally in order to position one of his arms on the armrest.

Fig. 5.2   Postures used for comfort evaluation in Zodiac Seat Z301

5.3   Pressure Mapping simulation results

5.3.1   Overweight human model

The maximum pressure is reduced under the ischions, leading from a non-comfortable situation (red cells from the Mergl criteria) to a comfortable one (green cells from the Mergl criteria) (see Figure 5.3.).

Fig. 5.3   Mergl criterion applied to the two postures of the overweighted individual

5.3.2   Eldery human model

For the elderly person, in the TTL position, the peaks under the ischions have higher values than for the standard person. It may be due to less muscular tonus and/or reduced flesh thickness. The same trends are observed between TTL and reclined postures (see Figure 5.4).
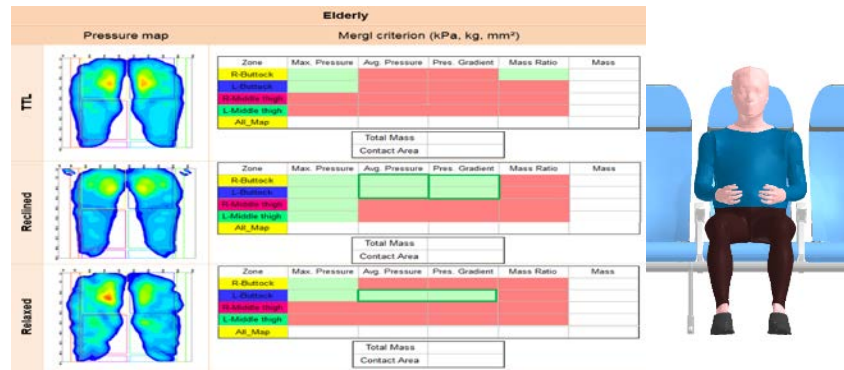
Fig. 5.4   Mergl criterion applied to the three postures of the elderly individual

5.3.3   Disable human model
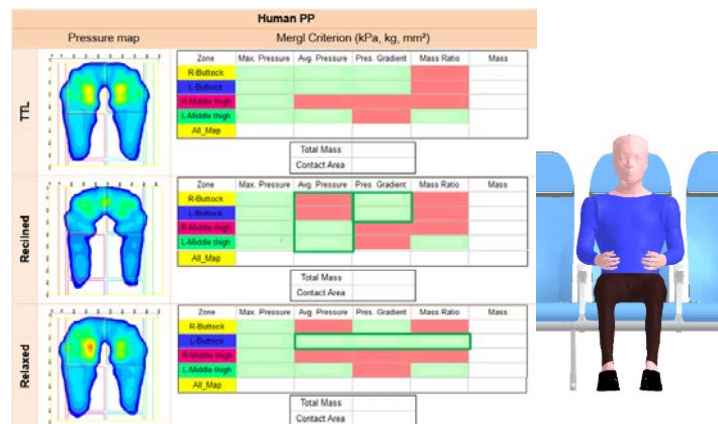
Fig. 5.5   Mergl criterion applied to the three postures of the disabled human model

For the paraplecix human midel, the average pressure is very weak in reclined position, under the discomfort limit; additionnaly to the instability issues.

6   Conclusion

Human models have been developed in order to represent overweight, elderly and paraplegic people. Those models have been used on aircraft seats in order to evaluate discomfort for those populations. Next steps of the project consist in using this simulation capability in order to propose new seat design enabling a better accomodation for all passengers types.

Acknowledgements

List of references

Aerospace series - Standardized measurement methods for comfort and living space criteria for aircraft passenger seats; German and English version EN 4723:2015

Bauman, W. A.; Spungen, A. M.; Wang, J.; Pierson, R. N.; Schwartz, E.: Continuous loss of bone during chronic immobilization: a monozygotic twin study. Osteoporos. Int. J. Establ. Result Coop. Eur. Found. Osteoporos. Natl. Osteoporos. Found. USA, 1999, vol. 10, nb. 2, pp. 123–127.

Beck, T. J.; Looker, A. C.; Ruff, C. B.; Sievanen, H.; Wahner, H. W.: Structural Trends in the Aging Femoral Neck and Proximal Shaft: Analysis of the Third National Health and Nutrition Examination Survey Dual-Energy X-Ray Absorptiometry Data. Journal of Bone and Mineral Research, Dec. 2000, vol. 15, nb. 12, pp. 2297–2304.

Borot, C.; Marca, C.; Jammet-Reynal, O.: Predict Passenger Comfort in Aircraft Cabin to improve seat design, AEGATS2016_37, 2016.

Dauty, M., Perrouin Verbe, B.; Maugars, Y.; Dubois, C.; Mathe, J. F.: Supralesional and sublesional bone mineral density in spinal cord-injured patients, Bone, Aug. 2000, vol. 27, nb. 2, pp. 305–309.

Eser, P.; Frotzler, A.; Zehnder, Y.; Wick, L.; Knecht, H.; Denoth, J.; Schiessl, H.: Relationship between the duration of paralysis and bone structure: a pQCT study of spinal cord injured individuals. Bone, May 2004, vol. 34, nb. 5, pp. 869–880.

Giangregorio, Lora M., Craven, Berley C.; Webber, Colin E.: Musculoskeletal Changes in Women With Spinal Cord Injury. Journal of Clinical Densitometry, 2005, vol. 8, nb. 3, pp. 347–351.

Gorgey, A. S.; Dudley, G. A.: Spasticity may defend skeletal muscle size and composition after incomplete spinal cord injury. Spinal Cord, Feb. 2008, vol. 46, nb. 2.

Janssen, I.; Heymsfield, S. B.; Wang, Z. M., Ross, R.: Skeletal muscle mass and distribution in 468 men and women aged 18-88 yr. Journal of Applied Physiology. Bethesda Md 1985, July 2000, vol. 89, nb. 1, pp. 81–88.

Linder-Ganz, E.; Shabshin, N.; Itzchak, Y.; Yizhar, Z.; Siev-Ner, I.; Gefen, A.: Strains and stresses in sub-dermal tissues of the buttocks are greater in paraplegics than in healthy during sitting. Journal of Biomechanical, 2008, vol. 41, no. 3, pp. 567–580.

Linder-Ganz, E.; Shabshin, N.; Itzchak, Y.; Gefen, A.: Assessment of mechanical conditions in sub-dermal tissues during sitting: A combined experimental-MRI and finite element approach. Journal of Biomechanics, 2007, vol. 40, nb. 7, pp. 1443–1454.

Marshall, L. M.; Lang, T.; Lambert, L. C.; Zmuda, J.; Ensrud, K. E.; Orwoll, E.: Dimensions and Volumetric BMD of the Proximal Femur and Their Relation to Age

Among Older U.S. Men. Journal of Bone and Mineral Research, Aug. 2006, vol. 21, nb. 8, pp. 1197–1206.

Mergl, C.; Klendauer, M.; Mangen, C.; Bubb, H.: Predicting long term riding comfort in cars by contact forces. Lehrstuhl für Ergonomie, Technische Universität München, Germany, 2005.

Modlesky, C. M.; Slade, J. M.; Bickel, C. S.; Meyer, R. A.; Dudley, G. A.: Deteriorated geometric structure and strength of the midfemur in men with complete spinal cord injury. Bone, February 2005, vol. 36, nb. 2, pp. 331–339.

Modlesky, C. M.; Bickel, C. S.; Slade, J. M.; Meyer, R. A.; Cureton, Kirk J.; Dudley, G. A.: Assessment of skeletal muscle mass in men with spinal cord injury using dual-energy X-ray absorptiometry and magnetic resonance imaging. Journal of Applied Physiology, Jan. 2004, vol. 96, nb. 2, pp. 561–565.

Power, G. A.; Dalton, B. H.; Rice, C. L.: Human neuromuscular structure and function in old age: A brief review. Journal of Sport and Health Science, December 2013, vol. 2, nb. 4, pp. 215–226.

Ruff, C. B.; Hayes, W. C.: Age changes in geometry and mineral content of the lower limb bones. Annals of Biomedical. Engineering, Nov. 1984, vol. 12, nb. 6, pp. 573–584.

Sherk, V. D.; Bemben, M. G.; Bemben, D.: Interlimb muscle and fat comparisons in persons with lower-limb amputation. Archives of Physical Medicine and Rehabilitation, vol. 91, July 2010, nb. 7, pp. 1077–1081.

Vandervoort, A. A.: Aging of the human neuromuscular system. Muscle Nerve, Jan. 2002, vol. 25, nb. 1.

Ullmann & Fritzsche:
Ergonomic work design for older and performance-restricted workers using digital human models

Ullmann, S., Fritzsche, L.

imk automotive GmbH, Chemnitz, Germany

Abstract

Technical and functional demands on digital human models (DHM) are rising, due to the demographic change and related challenges in ergonomic work place design. The increasing relevance and importance of age-specific parameters in DHM were the motivation to start the research project "Virtual Aging", funded by the German federal ministry of education and research. The project aims on enhancing DHM functions by incorporating criteria of impaired abilities and age-related parameters in order to provide better possibilities for user-centered product and work process design. One of the selected DHM is the "Editor for Manual Work Activities" (EMA). This 3D planning method and software tool allows the dynamic simulation of manual work processes, the layout design of workstations, the performance of feasibility studies as wells as the analysis of ergonomic risks (EAWS, Ergonomic Assessment Worksheet) and expected production time (MTM, Method Time Measurement).

The incorporation of age-related parameters in digital human models is the next step towards an integrated model for holistic ergonomic work place design. Furthermore, the integration of variable human performance abilities provides enhanced functionalities for analyzing possibilities to design work for people with restricted physical capabilities. Such new functions in digital human models also need new workflows for the virtual planning of workstations and production processes as well as new methods for the interpretation of simulation results.

This article describes the current approach of integrating age-specific parameters and performance abilities into the digital human model EMA and gives examples for the practical use towards an appropriate design of work places for worker's needs.

Key words:

Ergonomics, work place design, process planning, older workers, employees with disabilities or special needs, capability-appropriate design

1   Introduction

The aging labor force is becoming a difficult challenge for companies around the globe, due to the associated effects on health and performance of workers. In particular, the share of people with musculoskeletal diseases strongly grows with higher average age (REINHART et al., 2012). In addition, companies face a high increase of employees with physical impairments (GRIFFITH, 1997). This special group of workers cannot perform their regular work tasks anymore, which often results in productivity losses. Moreover, there are many different types of restrictions that mostly occur in combinations, which makes appropriate work design even more difficult (RUDOW et al., 2007; MENGES, 1998). Analysis of work forces has shown that not only older workers have restrictions of capabilities, but also younger workers can have impairments of their performance (SCHELLER et al., 2015; KESKIN et al., 2010).

Especially the industry sector needs highly efficient production processes to secure competitiveness. To ensure a value-adding work task, it is necessary to provide older and performance-restricted employees with a job and work place that is adapted to their specific abilities and needs. Digital human models (DHM) could be used to support this task, because they provide functionalities for prospective ergonomic work place design and for early validation of feasibility, process time and physical strain.

Technical demands on DHMs increase with such new use cases, particularly if they are going to be applied for the design of age- and capability-appropriate work places. Current DHMs are mostly adjustable to gender, body height and somatotype (MÜHLSTEDT, 2012). Integration of age-related anthropometric parameters and other human performance abilities are mentioned in some studies (e.g., PORTER et al., 2003). However, these functions are not yet part of digital simulations with DHMs, especially not for designing manual work processes (MÜHLSTEDT et al., 2008).

Motivated by the challenge of integrating older workers into production processes and the lack of age-specific parameters in DHMs used for designing such processes, the research project "Virtual Aging" was initiated. It is funded by the German federal ministry of education and research and includes the Technical University of Chemnitz, Human Solutions GmbH and imk automotive GmbH. The research project mainly focuses on the advancement of DHMs by implementing age-related parameters that should be considered for the user-centered design of products and work processes.

DHMs can help to visualize and analyze products, manufacturing processes and manual workstations, especially in early phases of production planning. The Editor for Manual Work Activities (EMA) is a planning method used for the dynamic simulation and analysis of manual work processes based on an autonomously acting DHM (FRITZSCHE et al., 2011; ILLMANN et al., 2013). EMA automatically interprets and executes assigned tasks using a natural job description language. As results, EMA computes the standard production time based on Method Time Measurement (MTM; BOKRANZ et al., 2006) and a physical risk assessment based on the Ergonomic Assessment Worksheet (EAWS; SCHAUB et al., 2013). Moreover, it can be used to perform feasibility studies of assembly and production processes.

Incorporating parameters of individual human performance abilities and age-related changes is the next step to a holistic ergonomic work place design with DHMs and EMA in particular.

2 Method

The analysis of age-related and disease-related performance restrictions and the selection of criteria for a possible implementation in DHMs is the first step to generate a database for age-specific restrictions like changes in anthropometrics, vision, range of motion and physical strength. First of all, it is necessary to identify differences in body-height, corpulence and proportion in connection with gender and defined age groups. A detailed analysis of age-specific range of motion is also essential for the integration of age-specific factors into DHMs. This work was mainly completed by the University of Chemnitz, Professorship for Ergonomics and Innovation Management.

For mapping impaired abilities into DHMs it is required to define criteria of restricted performances. Therefore, existent assessment systems for classifying impaired abilities (e.g. Integration von Menschen mit Behinderung in die Arbeitswelt (IMBA), MODZANOWSKI et al., 2013) were analyzed and factors for impaired abilities were identified and grouped in a universal classification system. It includes physical capabilities like kneeling or working above shoulder level as well as psychological criteria and categories for work organization like shift-system.

3 Results

Results of a literature review shows the change of anthropometrics in the defined age groups of 20, 40 and 60 years old (see Figure 3.1). With an increasing age, body height is reduced, the corpulence increased and the overall proportion is nearly the same. These conclusions are the first part to be implemented into the DHMs.
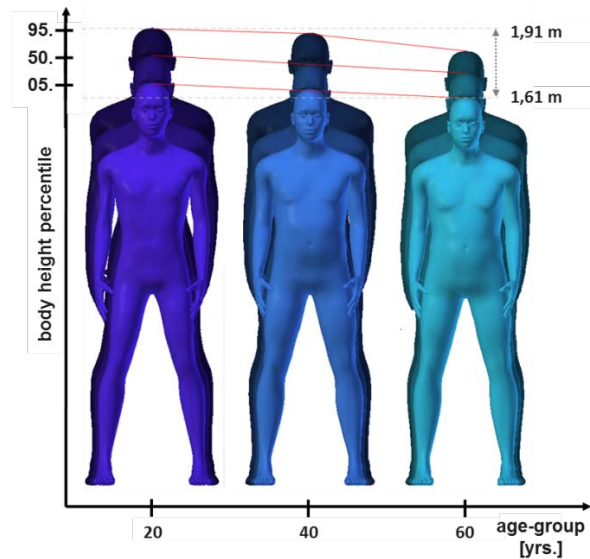
Fig. 3.1 Anthropometric data in different age groups. Source: ULLMANN et al., 2016

Another result were age-related data of varied range of motion of upper and lower limbs which will be also included in the DHM for each age group. For this purpose, the University of Chemnitz performed a large meta-analysis (results will be published by Spitzhirn et al). The first tests with this data showed, that the particular combination of multiple restricted joint angles can be a limitation for completing a work task and makes it necessary to simulate work processes with age-specified parameters.

Based on another literature review for critical values and definitions of impaired abilities, each capability was precisely defined (e.g. trunk bent forward > 60°), grouped in time slices, and transferred into an employee-capability-profile (see Figure 3.2).

The enlarged portion shows:

Employee-capability-profile

plant			analyst		
personal-No./personal identification			date		

category	capability	time slice per cycle/shift (8h)				
		never	occasionally bis 10%	frequently 11-50%	mainly 51-90%	constantly 91-100%
basic body postures	standing/walking in alteration	O	O	O	O	⊗
	standing (space of movement <1sqm)	O	O	O	O	⊗
	permanent sitting	O	O	O	O	⊗
	alternating body postures standing/walking/sitting	O	O	O	O	⊗
body postures / range of motion — upper limbs	movement head/cervical spine	O	O	O	O	⊗
	working above head level	O	O	⊗	O	O
	working above shoulder level	O	O	⊗	O	O
	arms in far reach	O	O	O	O	⊗
	range of motion ellbow/wrist	O	O	O	O	⊗
trunk	bent forward 20° - 60°	⊗	O	O	O	O
	strongly bent forward > 60°	⊗	O	O	O	O
	lateral bending/trunk rotation > 10°	⊗	O	O	O	O
lower limbs	kneeling	O	⊗	O	O	O
	squatting	O	⊗	O	O	O
	climbing	O	⊗	O	O	O
	lying on back, chest or side	O	⊗	O	O	O

Fig. 3.2   Prototype of employee-capability-profile. Source: ULLMANN et al., 2017

The software implementation of these impairments needs a synthesis of a model to transfer human capabilities into interpretable parameters for the DHM. For example, joint-movement-restrictions due to musculoskeletal diseases can affect the range of motions in the DHM. This impairment can automatically influence joint movements or block the execution of entire work tasks. Such enhanced functionalities for simulating special cases of individual impairment need new workflows and outputs for DHMs.

4   Workflow

Using digital planning tools for the prospective ergonomic design of work places needs a systematic procedure. Normally, work places would be virtually designed with default standard-work processes and default DHM properties (in terms of anthropometrics, range of motion etc.). Similar to the standard EMA version, results might be an ergonomic assessment based on EAWS and a standard time analyses with MTM-UAS. With the implementation of specific human performance capabilities, it is now possible to generate an additional work place profile that can be used for matching individual abilities with work requirements based on the classification scheme mentioned above.

However, the new function will explicitly consider requirements of workers with special needs that may be age- and/or disease-related for the design of new or the redesign of existing work places. The software users (e.g., production planers or ergonomists) can also create workstations with a "design for all" approach. Therefore, DHM ability restrictions can be selected on a newly developed user interface in EMA. Furthermore, it is possible to import existing profiles of workers based on the universal classification scheme (e.g. profiles previously recorded by doctors). Both workflows finally lead to the generation of an ability-restricted DHM for further simulation and analysis (Figure 4.1).
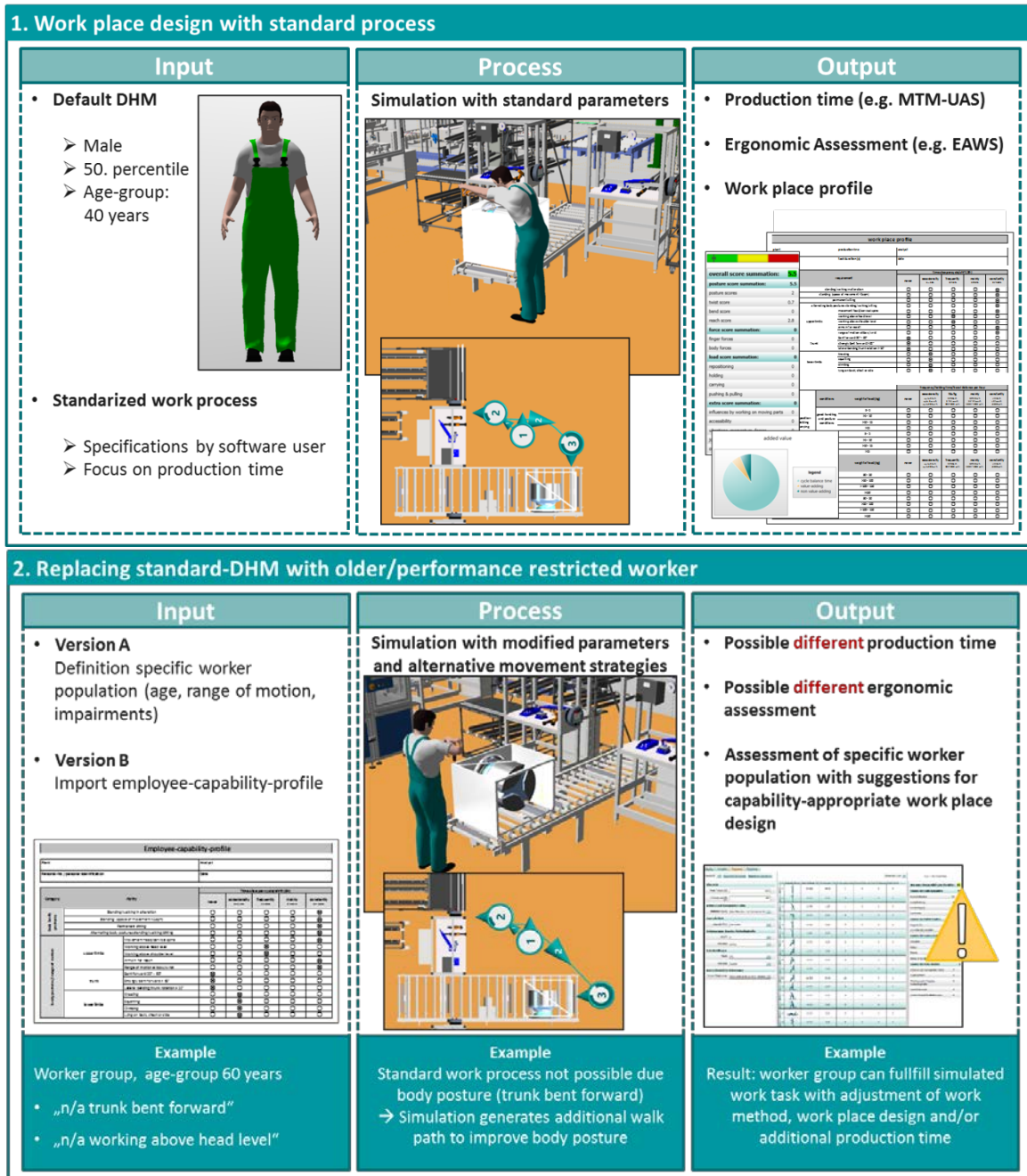
Fig. 4.1   Workflow for digital planning and simulation (standard and altered process).

There are two possible ways how the use of the restricted DHM may influence the EMA simulation. Firstly, ideally no differences occur compared to the standard simulation with the standard DHM. This means that the restricted worker population should be able to carry out the work task in the given work environment and work process. Secondly, the restricted DHM could also lead to new requirements for the work design and the work process. Due to age-related restrictions like reduced range of motion or specific impairments, it can be necessary that the DHM must vary the execution of a task like adding additional walk paths or use alternative movement strategies. In some cases, EMA will be able to automatically generate such

adaptations. In other cases, the software user might be requested to change the work process manually.

The changes in the simulation induced by the restricted DHM also lead to different analysis results. In addition to the automatically updated results in ergonomics and time assessment based on different ways of completing the work, the future system will be able to provide an assessment of the specific work ability for the simulated worker group. Changes like production time, ergonomic parameters and walking paths will be shown displayed in an overview in order to support the EMA software user in redesigning the workstation according to the worker requirements. It is also planned to provide hints and advices based on the simulation, such as design proposals and warnings (e.g. for exceeding age-related weight limits). It should be noted, however, that the MTM standard time will not be changed with a global age-factor on working speed because research and practice did not provide evidence for such modifications.

5 Example

EMA can now be used to design work places with ergonomic and efficient restrictions for a purposeful appropriate assignment of workers with special needs. Figure 5.1 shows an example of a pre-assembly line that has been designed with EMA. These work places were designed for employees with restricted abilities, who can participate at a value-added production, regardless of their individual physical restrictions. The assessment with EAWS shows overall a very low risk score at each station.
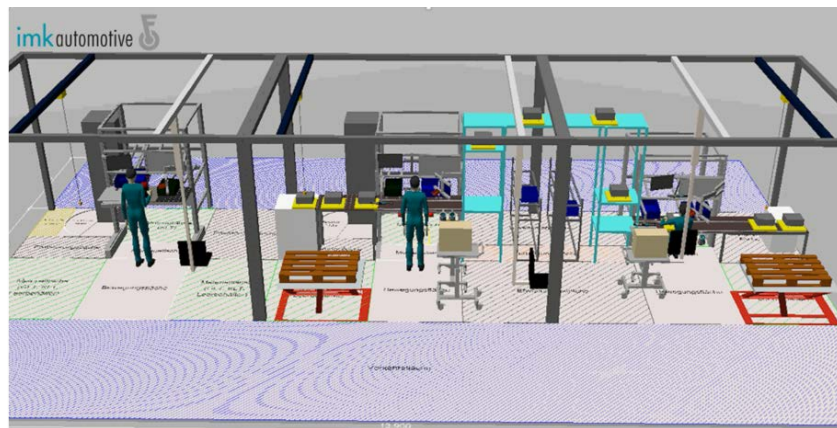
Fig. 5.1 Example of workstations with a low-risk for physical strain. Source: ULLMANN et al., 2016

6 Discussion

This report shows that the integration of age-related and individual performance attributes as an add-on for DHM simulations is an opportunity to consider the special needs of specific populations in virtual production planning and ergonomic design.

The incorporation of age-related parameters is the next step towards an integrated model for holistic ergonomic work place design. Moreover, the consideration of specific human performance abilities in DHMs provides a possibility to integrate workers with specific abilities in regular work places. In general, prospective ergonomic work design can avoid the aggravation of existing diseases as well as the development of new work-related diseases for all employees. Therefore, digital planning needs new workflows and interpretation of simulation results according to specific use cases. Developing this part of the software is still ongoing. Next step will be an analysis of the impact of alternative movement strategies on the simulation. Finally, a validation study with ergonomic experts will focus on use-cases comparing a task done by real persons vs. simulated DHM movements, similar to the approach used in FRITZSCHE (2010).

List of references

Bokranz, R.; Landau, K.: Produktivitätsmanagement von Arbeitssystemen, Stuttgart: Schäffer-Poeschel.

Fritzsche, L.: Ergonomics risk assessment with digital human models in car assembly: Simulation versus real-life. Human Factors and Ergonomics in Manufacturing & Service Industries 2010, Vol. 20, pp. 287-299.

Fritzsche, L.; Wegge, J.; Schmauder, M.; Kliegel, M.; Schmidt, K.-H.: Good ergonomics and team diversity reduce absenteeism and errors in car manufacturing, Ergonomics 2014, Vol. 57 No. 2, pp.148-161.

Fritzsche, L., Jendrusch, R., Leidholdt, W.; Bauer, S.; Jäckel, T.; Pirger, A.: Introducing ema (Editor for Manual Work Activities) – A New Tool for Enhancing Accuracy and Efficiency of Human Simulations in Digital Production Planning. In: Duffy, Vincent G. (Ed.): Digital Human Modeling, HCII 2011, LNCS 6777. Berlin, Heidelberg: Springer, pp. 272–281.

Griffiths, A.: Ageing, health and productivity: A challenge for the new millennium, Work & Stress 1997, Vol. 11 No. 3, pp. 197-214.

Illmann, B.; Fritzsche, L.; Leidholdt, W.; Bauer, S.; Dietrich, M.: Application and Future Developments of ema in Digital Production Planning and Ergonomics. In: Duffy, Vincent G. (Ed.): Digital Human Modeling and Applications in Health, Safety, Ergonomics, and Risk Management, DHM/HCII 2013, Held as Part of HCI International, Springer: Berlin, Heidelberg, 2013, pp.66–75.

Keskin M.-C.; Stork, J.: Der chronisch Kranke im Betrieb: Erkenntnisse aus dem Audi Checkup, http://www.bgm-bielefeld.de/downloads/ ws101012bgm0008.pdf, 2010.

Menges, R.: Rechnerunterstützte Planung manueller Montage. In: Lotter, Bruno; Hartel, Marko; Menges, Raimund (Ed.): Manuelle Montage – wirtschaftlich gestalten: Neuzeitliche Analysen und Planungsmethoden zur Montagerationalisierung. Renningen-Malmsheim: expert-Verlag, 1998, pp.169-192.

Mozdzanowski, M.; Glatz, A.: Das Profilvergleichssystem IMBA als Instrument im betrieblichen Eingliederungsmanagement, Bewegungstherapie & Gesundheitssport 2013, Vol. 29 No. 2, pp.55-61.

Mühlstedt, J.: Entwicklung eines Modells dynamisch-muskulärer Arbeitsbeanspruchungen auf Basis digitaler Menschmodelle. 2012, Münster: Monsenstein und Vannerdat, pp.41-43.

Mühlstedt, J.; Scherf, C.; Spanner-Ulmer, B.: Alles beim Alten? Digitale Menschmodelle und die Simulation des Alters. BGAG - Institut Arbeit und Gesundheit der Deutschen Gesetzlichen Unfallversicherung e.V Tagungsband Produktdesign für alle: FÜR JUNGE = FÜR ALTE? 15.-16.05.2008. Dresden: BGAG, pp.119-124.

Porter, M. J.; Marschall, R.; Sims, R.; Gyi, D.; Case, K.: HADRIAN: a human modelling CAD tool to promote design for all. In: Proceedings of Inclusive Design for Society and Business, INCLUDE 2003, Royal College of Art, London, 23rd-26th March 2003, vol. 6, pp.222-228.

Reinhart, G.; Egbers, J.: Integrating Ability Limitations into Assembly System Design. In: ElMaraghy, Hoda (Ed.): Enabling Manufacturing Competitiveness and Economic Sustainability - Proceedings of the 4th International Conference on Changeable, Agile, Reconfigurable and Virtual Production (CARV2011), pp. 35-40, Montreal, October 2011, Springer, Berlin, Heidelberg, 2012.

Rudow, B.; Neubauer, W.; Krüger, W.; Bürmann, C.; Paeth, L.: Die betriebliche Integration leistungsgewandelter Mitarbeiter – ein Arbeits- und Personalprojekt aus der Automobilindustrie, Arbeit: Zeitschrift für Arbeitsforschung, Arbeitsgestaltung und Arbeitspolitik 2007, Vol. 2 No. 16, pp.118-131.

Schaub, K. H.; Caragnano, G.; Britzke, B.; Bruder, R.: The European assembly worksheet, Theoretical Issues in Ergonomics Science 2013, Vol. 14 No. 6, pp.616-639.

Scheller, K.; Wittemann, P.; Müglich, D.; Sinn-Behrendt, A.; Pirger, A.; Bruder, R.: Auswertung altersdifferenzierter Fähigkeitsdaten zur Entwicklung von ergonomischen Gestaltungsansätzen in der Produktion, Zeitschrift für Arbeitswissenschaft 2015, Vol. 69 No. 3, pp.137-145.

Ullmann, S.; Fritzsche, L.: Virtual Aging: Einsatz von 3D-Technologien zur präventiven Gestaltung von demografiefesten Arbeitsplätzen, 2016, Tagungsband innteract 2016. Chemnitz.

Ullmann, S.; Fritzsche, L.: Designing ergonomic workstations for people with restricted abilities using EMA simulation software, Book of Proceedings of the 6th International Ergonomics Conference: Ergonomics 2016 – Focus on Synergy, Zagreb: Croatian Ergonomics Society, pp.361-364.

Ullmann, S.; Fritzsche, L.: Arbeitsgestaltung für leistungsgewandelte Mitarbeiter mit digitalen Planungstools. Bericht zum 63. Arbeitswissenschaftlichen Kongress vom 15. – 17. Februar 2017, Gesellschaft für Arbeitswissenschaft e.V. (Hrsg.), Dortmund: GfA-Press, 2017.

Jones et al.:
Tracking Occupant Head Movements During Braking Events

Jones, M. L. H.[1], Miller, C. S.[1], Ebert, S.[1], Bonifas, A.[1], Byoung-Keon, D. P.[1], Reed, M. P.[1], Hallman, J.[2], Sherony, R.[2]

[1] University of Michigan Transportation Research Institute, USA
[2] Toyota Collaborative Safety Research Center, USA

Abstract

Accurate tracking of occupant head movements in response to abrupt vehicle maneuvers, such as emergency braking, may provide information useful to evaluate the performance of vehicle safety systems. Driver and passenger response to hard braking have been investigated in previous studies. Methodologically, participants were typically well aware of the purpose of the testing and/or instrumented extensively. The effects of these rapid vehicle motions on unaware vehicle occupants have not been well quantified. In a pilot study, data were gathered from 7 adults (3 female and 4 male), ranging in age from 18 to 58 years, stature from 1574 to 1885 mm, and BMI from 18 to 38 kg/m^2. Surface geometry of the occupant's head was recorded using hand-held scanners. A midsize sedan equipped with an inertial measurement unit was used to conduct vehicle maneuvers on a closed test track facility. Video cameras in the test vehicle recorded passenger movements. The camera system was spatially calibrated using a FARO Arm coordinate digitizer. Head surface data were aligned with 3D kinematic trajectory data computed from camera images and peak excursions were quantified. The results demonstrated reliable tracking of head position and orientation through the movement. These data have value for validating computational simulations of pre-crash responses.

1   Introduction

Analysis of the National Motor Vehicle Crash Causation Survey (NMVCCS), a dataset of on-scene information about the events and associated factors leading up to crashes involving light vehicles, determined that up to 40% of crashes were preceded by a vehicle maneuver. Braking was the most common pre-crash maneuver, followed by steering and steering with braking. Pre-crash maneuvers may become more common with the introduction of crash avoidance technologies such as automatic emergency braking. While the frequency of occupants being unaware of an impending maneuver or crash is unknown, the effects of rapid vehicle motions on unaware vehicle occupant kinematics currently are not well understood.

Several previous studies have gathered data on occupant responses to aggressive vehicle maneuvers. Testing methodologies have varied from simulated or impact sled test conditions (EJIMA et al. 2009; HAULT-DUBRULLE 2011) to in-vehicle testing (MORRIS and CROSS 2005; CARLSSON and DAVIDSSON 2011; ÖSTH et al. 2013; ÓLAFSDÓTTIR et al. 2013; KIRCHBICHLER et al. 2014; HUBER et al. 2015). Methodologically, participants were typically well aware of the purpose of the testing and/or instrumented extensively. As a result of the test preparation, the initial state of the participant may have been different from a typical vehicle occupant. The available data demonstrate that awareness reduces excursions, so the boundary cases for restraint system design are not meaningfully represented in the responses of unaware occupants. The current pilot study aimed to develop an experimental approach and platform for studying vehicle passenger responses to abrupt vehicle maneuvers. Accurate tracking of head location is one critical aspect of the needed methodology. This paper demonstrates that 3D head geometry aligned to 3D kinematic data can be used to produce useful estimates of occupant head movement in response to a braking event.

2   Methods

The study protocol was approved by the University of Michigan Institutional Review Board (IRB) for Health Behavior and Health Sciences (IRB # HUM00120296). Participants were recruited through online postings. Each participant was briefed that they are participating in a study of vehicle ride and handling and that they might experience rapid braking or vehicle maneuvers typical of automated vehicles of the future. Written consent was obtained prior to commencing the study.

Four women and five men were tested in this pilot study. Anthropometric data were gathered from each participant to characterize overall body size and shape. The standard anthropometry measures listed in Table 1 were obtained using manual measurements. All measurements were obtained from the participants in their own clothing. The participants ranged in age from 18 to 58 years, stature from 1574 to 1885 mm, and BMI from 18 to 38 kg/m^2.

Table 2.1 Participant Characteristics (N=9)

Measurement	Min	Max	Mean
Age (yr)	18	58	33
BMI (kg/m^2)	18	38	25
Weight (kg)	47	126	77
Stature	1574	1885	1751

2.1 Vehicle Instrumentation

The in-vehicle test was performed with an instrumented 2008 Honda Accord. The vehicle was equipped with a high-end inertial measurement unit (IMU) near the mass center of the vehicle that recorded acceleration and angular rate along three axes. Three Point Grey Blackfly S cameras were rigidly mounted to the vehicle interior to collect images at 60 Hz. Cameras viewed the passenger from three different angles and locations within the vehicle space. Figure 2.1 illustrates the camera placement within the test vehicle. Custom software was developed to synch the camera images with the inertial measurement unit.

Fig. 2.1 Test vehicle exterior (left) and interior camera placement (right)

Prior to beginning participant testing, the camera system was spatially calibrated using a FARO Arm coordinate digitizer to record calibration target locations placed throughout the data capture volume space. Quadrant target stickers were placed at different locations in the vehicle interior that could be viewed by multiple cameras. Three-dimensional coordinate locations were collected for each point with respect to the vehicle coordinate system. These quadrant targets remained in the vehicle during testing and were tracked along with the participant landmarks. The optical images were calibrated and processed using TEMA Automotive version 4.1-003 by Image Systems Motion Analysis. The orientation and location of each camera relative to the quadrant targets was computed for each frame to correct for small camera movements that may result during vehicle test maneuvers due to imperfections in the camera mounts. A lens distortion correction was also calculated prior to participant testing using a calibration board containing a grid with known point distances and TEMA software.

2.2   3D Surface Head Geometry

A hand-held infrared scanner (Cubify Sense) and a structured light Artec scanner were used to record contours of each participant's head. Surface contour data were merged and post-processed in Geomagic Studio software. The locations of surface landmarks on the participants were recorded via skin targets stamped on the skin prior to scanning and manually extracted from surface scan data using a custom script in Meshlab software (meshlab.org). Figure 2.2 shows a representative head scan and corresponding landmarks.

Fig. 2.2   Representative head scan and illustration of digitizing points and extracting anatomically derived landmarks in MeshLab.

2.3   Protocol

In-vehicle testing was conducted on the University of Michigan Mcity facility, which is a closed test track that enabled the use of scripted routes to achieve consistent acceleration levels under the driver's control. In each test drive the participant was seated in the front passenger seat with the seat placed in the most rearward position. The participant adjusted the seat back angle to achieve a comfortable posture and donned the seat belt. The investigator ensured that the belt was reasonably snug and appropriately positioned. A FARO Arm coordinate digitizer was used to record the initial three-dimensional locations of landmarks on the participant's body and on the vehicle, seat, and belt. In addition, a stream of points with approximately 5-mm spacing was recorded along the edges of lap and shoulder portions of the belt between the anchorages and latch plate. Throughout each test drive participants were asked to sit with feet translated forward until they were resting on heels and hands on thighs to avoid any bracing or leaning against the floor, door, or armrests.

Because the purpose of this research study was to obtain "unaware" vehicle passenger motions in response to vehicle maneuvers, a dummy questionnaire intended to distract attention from the primary objective was administered to employ some obfuscation. After a five-minute acclimation period, the driver reached a speed of approximately 50 km/hr and applied sudden, maximum braking to a stop. Following this trial, the investigator performed a second run with a rapid, rightward lane change. Data was recorded continuously from the cameras and the inertial measurement unit that quantified vehicle movements.

2.4   Digitizing Head Kinematic Data

Kinematic tracking of the movement of head landmarks during the braking event was performed using TEMA software. In addition to the vehicle quadrant targets, nine participant landmarks were digitized frame by frame (60 frames per second) from the three camera views of the participant in the passenger seat: six reference landmarks were tracked on the head, and three on the belt at the clavicle, sternum, and the latch plate (Figure 2.3).
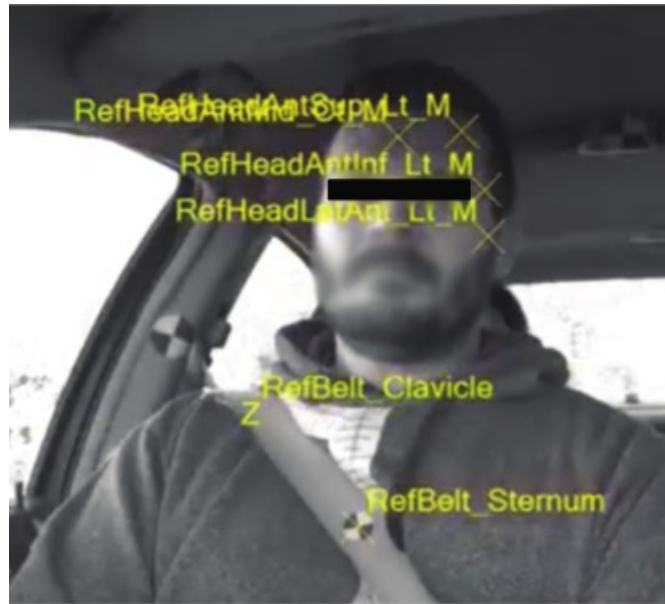
Fig. 2.3 Points tracked in TEMA software.

To collect 3D kinematics, each point needed to be tracked by only two cameras at any given point in time, but three cameras were used to reduce the data loss due to points being obscured by passenger motion. Vehicle quadrant targets were tracked using the quadrant symmetry function, which calculates the intersection of the light and dark regions of the target within a search area and calculation area set by the user. Because quadrant targets are tracked using a calculation of pixel intensity over a set area, the tracked data has high accuracy. Participant points were tracked using both the circular symmetry or correlation functions. The circular symmetry function searched each successive image for the circular target contained within the size of the target square over the search area. When a point became partially obscured or moved significantly out of the plane of the camera, the point was tracked using the correlation option, which searches each successive frame for the part of the image contained within the correlation circle over the search area.

2.5   Aligning 3D Surface Head Geometry with Head Kinematic Data

Manually extracted landmarks and vertex data from the surface contour of the participant's head were aligned to the TEMA extracted digitized head kinematic data using a least-squares fit on landmark locations. The maximum forward displacement of the head (the change in distance between the initial posture and the most forward translated location that occurred in the initial response to the evasive vehicle maneuver) was determined using the aligned landmarks (Figure 3.2).

3   Results

Figure 3.1 illustrates a passenger's head kinematics in response to the abrupt braking maneuver for a representative participant. The maximum head excursion was predominantly aligned with the principal direction of the acceleration. Figure 3.3 shows the result of aligning the 3D surface head geometry to the 3D head kinematic trajectory at both the starting position and maximum head displacement.
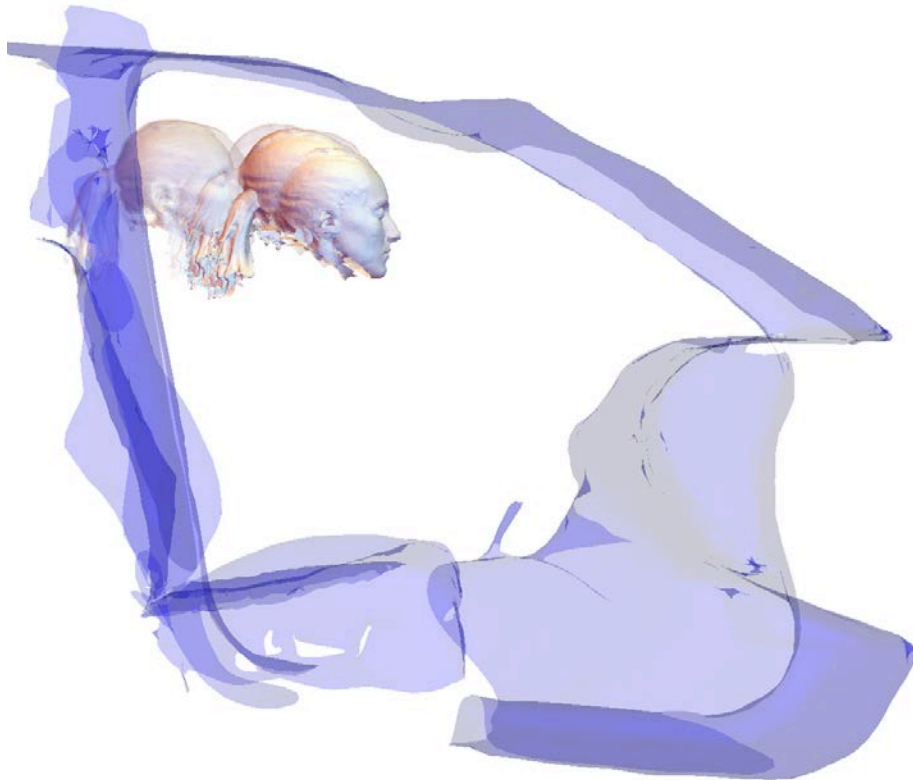
Fig. 3.1   Mapping aligned landmarks and head scan to 3D head kinematic trajectories during braking.

Head excursions measured at the glabella landmark ranging from 166 to 270 mm (mean = 210 mm; SD = 43 mm) along the axis of acceleration were observed. Figure 3.5 shows the trajectory of the head (defined by the glabella landmark) in response to the abrupt braking event across all participants. Data were aligned on the starting point of the braking event [t = 0].
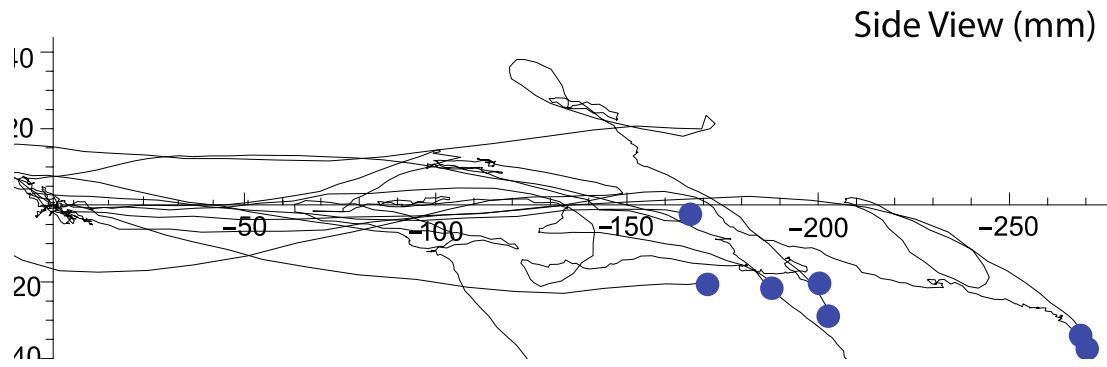
Fig. 3.2 Plot of the maximum forward and vertical displacement of the head during abrupt braking maneuver.
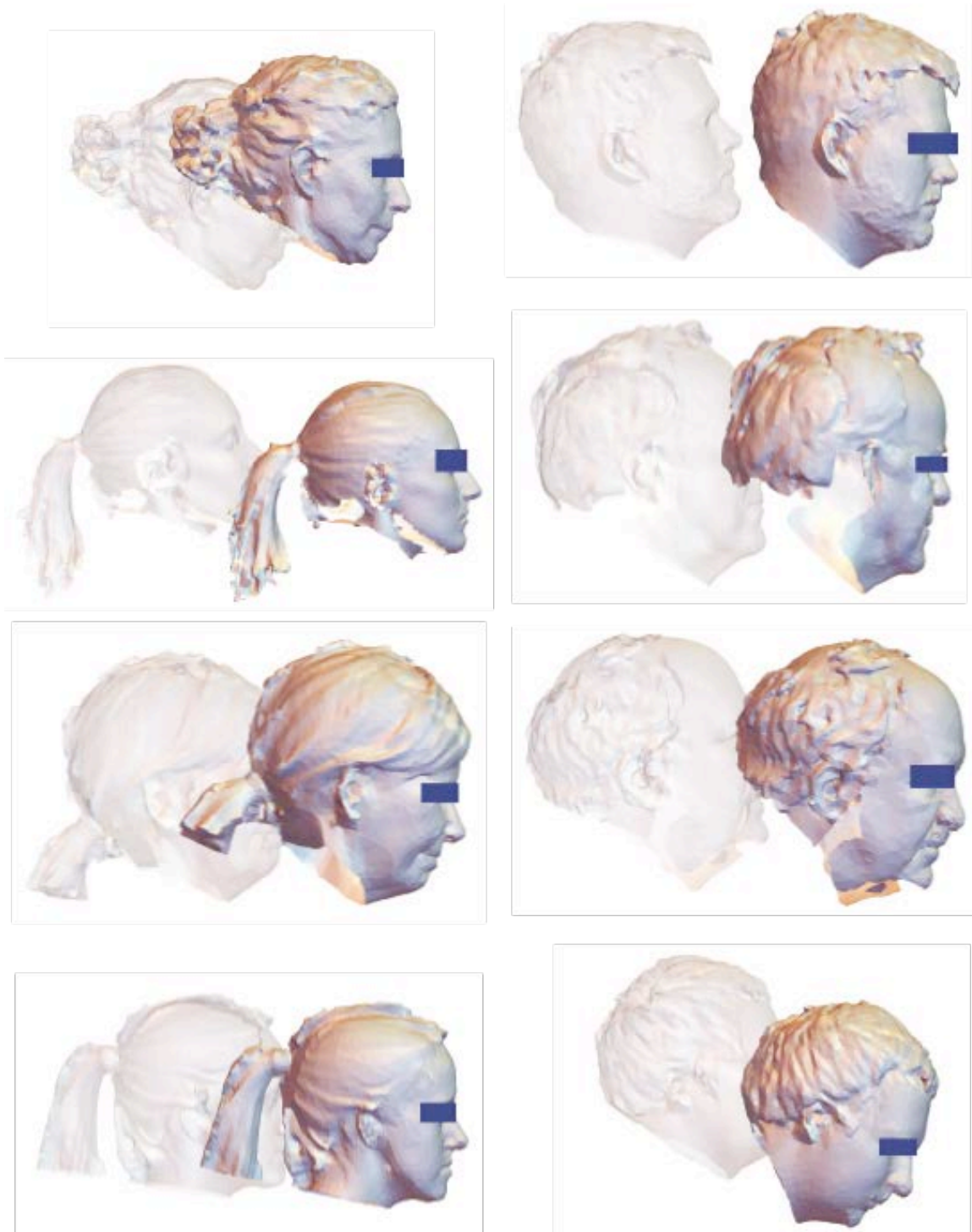
Fig. 3.3 Aligned 3D head surface geometry in the starting position (transparent) and final maximal forward excursion (opaque).

4 Discussion

This pilot study demonstrated the combination of 3D surface scanning and landmark-tracking methods to obtain full 3D head location during a vehicle maneuver. The method allows post-hoc measurement of clearances to the vehicle header, which is otherwise difficult to measure. A limitation of this approach is that landmark occlusion can compromise tracking. Additional cameras can help to reduce that possibility.

Future research will expand the number of subjects to enable evaluation of the associations with passenger covariates, such as age and body size. These data may be used to develop and tune models of pre-crash occupant motions.

Computational human body models that are capable of representing the effects of human muscle activations and occupant kinematics may help enhance future restraint systems and crash avoidance technology. The outcome of this research will be quantification of occupant motions as a function of vehicle accelerations and occupant characteristics. This information may provide further validation data and support human model development and application to understand the potential consequences of such motions for occupant protection if the system is not successful in avoiding a crash.

Acknowledgement

List of references

Carlsson, S.; Davidsson, J.: Volunteer occupant kinematics during driver initiated and autonomous braking when driving in real traffic environments. Proceeding of the 2011 International Research Council on Biomechanics of Injury Conference, 2011. Ejima, S.; Zama, Y.; Ono, K.; Kaneoka, K.; Shiina, I.; Asada, H.: Prediction of pre-impact occupant kinematic behavior based on the muscle activity during frontal collision. Proceeding of the 2009 Enhanced Safety of Vehicles Conference, 2009.

Hault-Dubrullea, A.; Robachea, F.; Pacauxa, M. P.; Morvana, H.: Determination of pre-impact occupant postures and analysis of consequences on injury outcome. Part I: A driving simulator study. Accident Analysis and Prevention 43: 66–74, 2011.

Huber, P.; Kirschbichler, S.; Prüggler, A.; Steidl, T.: Passenger kinematics in braking, lane change and oblique driving maneuvers. Proceeding of the 2015 International Research Council on Biomechanics of Injury Conference, 2015

Kirschbichler, S.; Huber, P.; Prüggler, A.; Steidl, T.; Sinz, W.; Mayer, C.; D`Addetta, G. A.: Factors influencing occupant kinematics during braking and lane change maneuvers in a passenger vehicle. Proceeding of the 2014 International Research Council on Biomechanics of Injury Conference, 2014.

Morris, R.; Cross, G.: Improved understanding of passenger behavior during pre-impact events to aid smart restraint development. Proceeding of the 2004 Enhanced Safety of Vehicles Conference, 2005.

Ólafsdóttir, J. M.; Östh, J. K.; Davidsson, J.; Brolin, K. B.: Passenger kinematics and muscle responses in autonomous braking events with standard and reversible pre-tensioned restraints. Proceeding of the 2013 International Research Council on Biomechanics of Injury Conference, 2013.

Östh, J.; Ólafsdóttir, J. M.; Davidsson, J.; Brolin, K.: Driver kinematic and muscle responses in braking events with standard and reversible pre-tensioned restraints: Validation data for human models. Stapp Car Crash Journal, 57, 2013.

Technical Session 4 – Anthropometry and Biomechanics

Xu et al.:
Fatigue Life Prediction of Pedicle-Screw-Bone Connection in Human Lumbar Spine: Finite Element Preliminary Study

Xu, M.[1], Yang, J.[1], Lieberman, I.[2], Haddas, R.[3]

[1] Human-Centric Design Research Laboratory Mechanical Engineering, Texas Tech University, Lubbock, TX, USA
[2] Texas Back Institute, Plano, TX, USA
[3] Texas Back Institute Research Foundation, Plano, TX, USA

Abstract

Pedicle-screw-based spinal fusion surgery is a standard technique to restore spinal stability in spines with disease such as scoliosis and spondylolisthesis. However, the screw breakage and loosening have been reported in the post-surgical subjects, and therefore revision surgery is required. The fatigue-related failure of the screw-bone connection is one main reason for the failure of the pedicle screw. Due to the high cost of the revision surgery, there are great clinical interests to study the fatigue behavior of the pedicle screw-bone connection. In the literature, extensive biomechanical tests have been conducted to study the fatigue performance of the pedicle screws under the cyclic loading. The biomechanical tests have complications in experimental setting, high cost, and lack of prediction for internal parameters such as stress distributions in the cancellous bone. As an alternative option to the biomechanical tests, finite element (FE) study has been proved to be an effective tool to study spine biomechanics and spinal implants. In the literature, no FE study has been conducted to predict the fatigue behavior of the screw-bone connection. This study is to utilize the FE models to investigate the fatigue life of the pedicle-screw connection under cyclic loading, which required the predictions of fatigue life cycles in both the screw and the adjacent bony tissues. To validate the FE modeling methods, FE models of pedicle screws inserted in a polyethylene cylinder were developed and subjected to identical cyclic loadings in the literature. The simulation results in this study were compared with the experimental results in the literature. After validation of the modeling method through pedicle screw and polyethylene cylinder connection, FE model of one spinal vertebra was developed based on in vivo computerized tomography (CT) scans. The FE vertebra model was inserted with two types of pedicle screws separately. The cyclic loads were applied on the pedicle screws and the fatigue behaviors of the vertebra and the pedicle screws were predicted using FE method. Based on this pilot study, future work will be to extend the simulation method to predict the fatigue performance of the screw-bone connection under realistic spinal loading environment.

Key words:

Pedicle screw, lumbar spine, fatigue life, finite element method, cyclic load

1   Introduction

Pedicle-screw (PS)-based spinal fusion surgery (FS) is a common treatment for several spinal diseases such as scoliosis and spondylolisthesis, which aims to restore the spinal stability (BRASILIENSE et al., 2013). However, despite of the continuous advances in the PS design and FS technique during the last two decades, failures of PS, such as screw breakage and loosening, haven't been fully eliminated in post-surgical fused spines (AMARITSAKUL et al., 2014; ELDER et al., 2015). In clinical observations, the fatigue failure is more common than the immediate damage (AKPOLAT et al., 2016; BRASILIENSE et al., 2013). The failure of PS requires revision surgeries for the patients, which associate with high costs (MARTIN et al., 2014). There is a great clinical interest to understand the failure mechanisms of the PS and the screw-bone interactions (ELDER et al., 2015) to improve the PS design and the surgery protocols. Immediate holding capability and long-term fatigue behavior are two important factors to gauge the performance of the PS (BRASILIENSE et al., 2013). To test the immediate holding capability of the PSs, pullout tests are constantly performed in previous studies using both biomechanical material tests and computational techniques such as finite element (FE) analysis (AMARISSAKUL et al., 2014; CHAO et al., 2008; AKPOLAT et al., 2016; BRASILIENSE et al., 2013; SHIH et al., 2015). Fatigue strength of the PS has also been investigated by the biomechanical tests in the literature (AMARISSAKUL et al., 2014; BRASILIENSE et al., 2013; AKPOLAT et al., 2016). Cyclic loading has been proved to contribute severe damage to the bone and the spinal implants under complex loading environments (FATIHHI et al., 2015). However, it remains challenging for the biomechanical testing equipment to provide complex cyclic loading conditions to represent the physiological spinal loads which constantly includes axial-torsional or multi axial loading (FATIHHI et al., 2015). As results, to predict the fatigue performance of the screw-bone connection, most researchers only perform experimental tests on single cadaveric vertebra (AKPOLAT et al., 2016; BRASILIENSE et al., 2013) or single piece of synthetic polyethylene material (AMARISSAKUL et al., 2014) by applying single-axis loads on the PS due to the limitations of the testing equipment. Furthermore, strict protocols are required to perform the biomechanical tests especially the in vitro cadaveric tests, which greatly increase the complications of the biomechanical tests. Compared to the experimental approach, FE studies have advantages of low cost, high efficiency, and capability of predicting internal biomechanical parameter such as stress which is difficult to be measured through experiments (DRESCHARF et al., 2014). In fatigue tests, FE methods are useful to prevent possible fracture initiation and to optimize the treatment of the bony tissues while the experimental tests could be complicated (FATIHHI et al., 2015). Although FE simulations have been employed to predict the fatigue behavior of the trabecular bone (FATIHHI et al., 2015), to our best knowledge no computational studies have been reported to study the fatigue life of the screw-bone connection. The aims of this pilot study are to: (1) develop one feasible FE approach to predict the fatigue behavior of the screw-bone connection; (2) validate the FE models against the experimental data in the literature; (3) based on the validated FE method predict the fatigue life and failure behavior of screw-bone connection with single vertebra and different types of PS.

2   Methods

2.1   PS design

One conical PS (COPS) and one cylindrical PS (CYPS) are tested in this study (Fig 2.1). The computer aided design (CAD) models of the PSs are developed based on the dimensions and design variables reported by CHAO et al. (2008). These two PSs have an identical length of 45 mm, inner diameter of 4.9 mm and outer diameter of 6.5 mm. Other design variables (Fig 2.2) of these two PSs are summarized in Table 2.1. The CAD models of the PSs are imported into Hypermesh® (Altair Engineering, Troy, MI, USA) for FE mesh generation. The PSs were simulated as homogeneous linear-elastic material with a Young's modulus of 114 GPa and a poison's ratio of 0.3 (AMARISSAKUL et al., 2014).

Conical PS
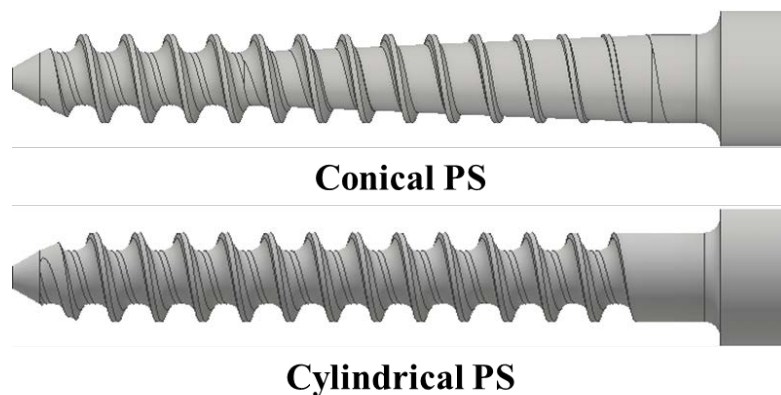
Cylindrical PS

Fig 2.1 Conical and cylindrical pedicle screw
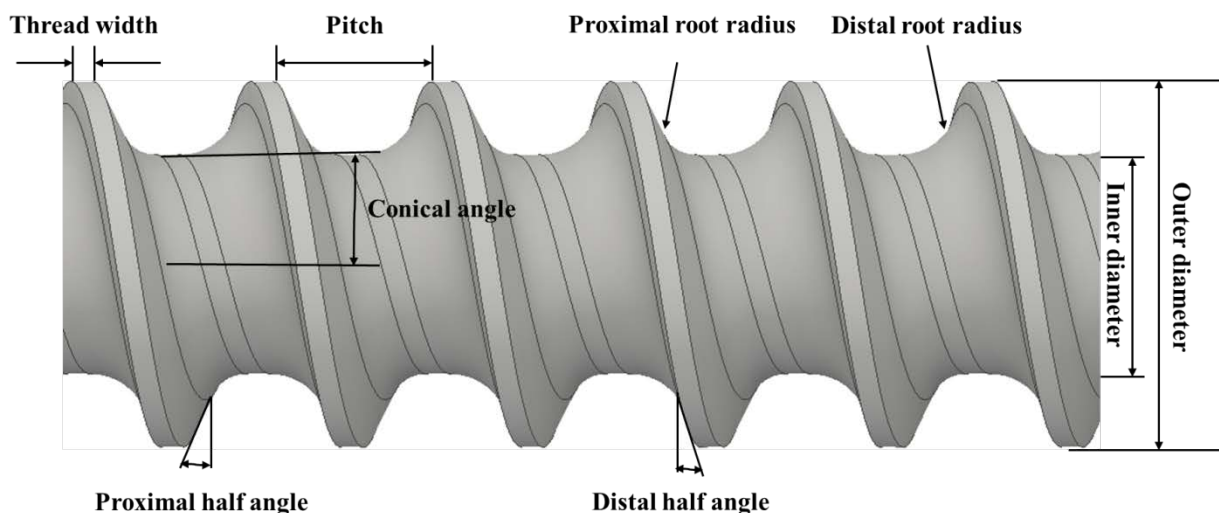
Fig 2.2 Design variables of PS (CHAO et al., 2008)

Two types of bending tests were simulated for both of the two PSs in this study: (1) cantilever bending test with polyurethane (CHAO et al., 2008) and (2) bending test with lumbar spine vertebra (BRASILIENSE et al., 2016).

Table 2.1 Design variable values of PS (CHAO et al., 2008)

Design variables	Conical PS	Cylindrical PS
Conical angle (degree)	2.481	
Beginning point of conical angle (mm)	15	
Thread-shank junction	No step	Deep step
Pitch (mm)	2.8	
Proximal root radius (mm)	0.8	
Distal root radius (mm)	1.2	
Proximal half angle (degree)	14	
Distal half angle (degree)	25	
Thread width (mm)	0.2	

2.2 Cantilever bending test with polyurethane foam

In the cantilever bending test, the PS FE models are inserted into a cylinder model (Fig 2.3). The cylinder model with a diameter of 20 mm and a height of 45 mm is created to simulate the polyurethane foam from the fatigue test performed by CHAO et al. (2008): the PS head is fully constrained (bonded connection) (XU et al., 2016 submitted) and vertical force is applied at 45 mm from the PS head-body junction in longitudinal direction (Fig 2.3).
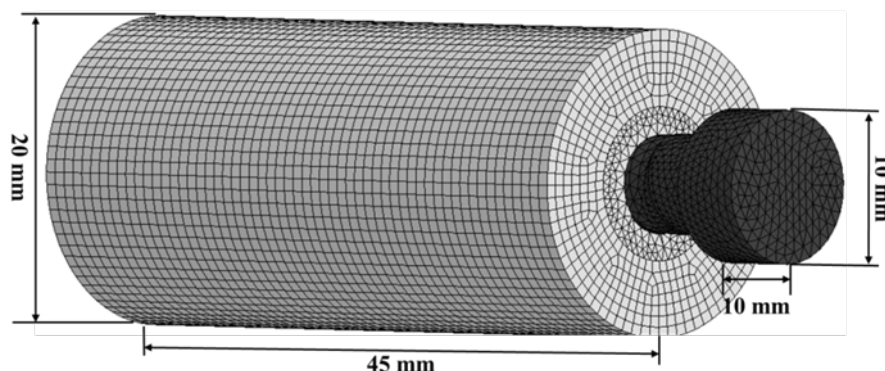
Fig 2.3 FE model configuration of the screw-cylinder simulations (XU et al., 2016 submitted)

2.2.1 Quasi-static loading and FE model validation

In the first step, quasi-static bending test with a vertical force of 220 N or 330 N is simulated for each of the two PSs tested in this study (CHAO et al., 2008). The polyurethane foam is modeled with a Young's modulus of 2.6 GPa and a poison's ratio of 0.3 (CHAO et al., 2008). Mesh refinement is tested to determine an appropriate mesh resolution to ensure both the calculation accuracy and efficiency in our previous study (XU et al., 2016 submitted). The final element numbers selected for the screw-cylinder combinations range from 127,837 to 178,275 in our previous study (XU et al., 2016 submitted). The meshed FE models are imported into LS-DYNA ® (Livermore Software Technology Corp, Livermore, CA, USA) for FE simulation. The predicted maximum von Mises stress of the PS in the cantilever

bending test is compared with the experimental results in the literature (CHAO et al., 2008) for validation purpose.

2.2.2   Cyclic loading and fatigue analysis

In the second step, cyclic vertical forces of 400 N and 600 N are applied with a frequency of 10 Hz using the same FE models for each of the PSs. For each of the four cyclic loading tests performed, one loading cycle simulated in LS-DYNA lasts 100 ms. Then, the stress/strain history of FE elements from the one-cycle simulation is exported into a virtual proving ground (VPG) ® (Engineering Technology Associates, Troy, MI, USA) for fatigue analysis. VPG uses strain-based Smith-Watson-Topper (SWT) equation for fatigue life prediction, which suggests that fatigue life is a function of the strain amplitude and maximum stress (KANG et al., 2010). The SWT equation is explained as follows (KANG et al., 2010):

$$\sigma_{max}\varepsilon_{\alpha} = \frac{\sigma_f}{E}(2N_f)^{2b} + \varepsilon_f\sigma_f(2N_f)^{b+c}$$

where σ_{max} is maximum stress, ε_{α} is amplitude of strain, E is elastic modulus, b is fatigue strength exponent, c is fatigue ductility exponent, ε_f is fatigue ductility coefficient, σ_f is fatigue ductility coefficient, N_f is the fatigue life. The fatigue life cycles of the PSs predicted in this study are compared with the experimental results reported by CHAO et al. (2008).

2.3   Bending test with lumbar spine vertebra

In the vertebra bending test, the FE PS models are inserted into the FE model of one vertebra (Fig 2.4), which utilizes the L_3 vertebra FE model from our previously-validated FE lumbar spine model of one healthy 47-year old male (XU et al., 2016). It has been demonstrated that there exists a circular effective region surrounding the PS in the screw-bone interaction where the stress is considerably higher than the rest of the vertebra (LIU et al., 2014). Thus, the effective region is of greater importance in the fatigue analysis. Fine mesh is created for the effective region on the vertebra tested in this study. The cortical bone of the vertebra is modeled as shell elements with a thickness of 1 mm surrounding the cancellous core (ZANDER et al., 2009). After the insertion of the PS in the vertebra, the superior and inferior endplates of the vertebra body are fully constrained and vertical loads are applied on the PS head to produce bending moments. For each PS, four vertical cyclic forces (75 N, 100 N, 125 N, and 150 N) were applied with a frequency of 2.5 Hz. 75 N of vertical force applied on one PS is considered to be the lower boundary of physiologic loading for walking (ROHLMANN et al., 1997). Identical computational process with the PS-cylinder cantilever bending test is utilized for this fatigue analysis. For each simulation trial, the fatigue life cycles for both the PS and the vertebra are predicted.

(a)

(b)

(c)
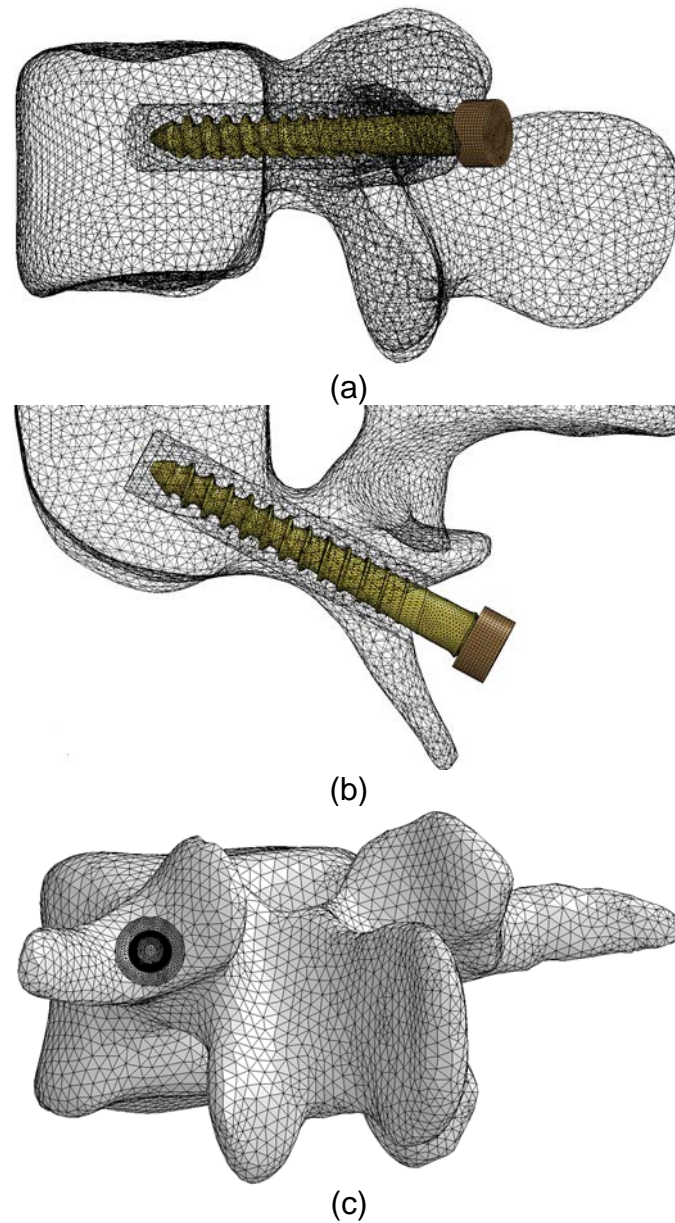
Fig 2.4 FE model configuration of the screw-vertebra simulations: (a) Side view of vertebra with pedicle screw; (b) top view of vertebra with pedicle screw; and (c) view of screw hole

The input parameters in this study are obtained from the experimental data in the literature (FATIHHI et al., 2015; HIGHT and BRANDEAU, 1983) and summarized in Table 2.2. The material properties assigned to the FE models were summarized in Table 2.3.

Table 2.2 Input parameters for fatigue analysis (FATIHHI et al., 2015)

Fatigue parameters	Titanium PS	Cancellous bone
Fatigue strength coefficient	7790	0.0035
Fatigue strength exponent	-0.0887	-0.096
Fatigue ductility coefficient	0.4098	0.352
Fatigue ductility exponent	-0.6637	-0.98

Table 2.3 Material properties assigned in this study

Material	Elastic modulus (MPa)	Poisson's ratio	Reference
Cortical bone	12,000	0.3	Dreischarf et al. (2014)
Cancellous bone	100	0.2	Dreischarf et al., (2014)
Posterior bony elements	3500	0.25	Dreischarf et al., (2014)
Polyurethane foam	2600	0.3	Chao et al. (2008)
Titanium PS	114000	0.3	Chao et al. (2008)

3 Results

3.1 Cantilever bending test with polyurethane foam

3.1.1 Quasi-static loading

The maximum values of von Mises stress and deflection of the COPS and CYPS under bending forces of 220 N and 330 N predicted in this study were compared with the results reported by Chao et al. (2008) (Fig 5). According to Fig 3.1 (a), the maximum von Mises stress values predicted in CYPS are considerably larger than those predicted in COPS under both bending forces of 220 N and 330 N. Under bending forces of 220 N and 330 N, the maximum von Mises stress predicted in

CYPS were 1670 MPa and 2538 MPa respectively, whereas those predicted in COPS were 413 MPa and 629 MPa. According to Fig 3.1 (b), the deflection values of CYPS were also significantly larger than those of COPS. Both the maximum von Mises stress and the maximum deflection predicted in this study were well consistent with those reported by CHAO et al. (2008). Linear regressions were calculated between the predicted values in this study and those reported by CHAO et al. (2008) (maximum von Mises stress: R^2=0.999907, maximum deflection: R^2=0.996334). Thus, the FE models of the PSs utilized in this study were considered to be validated.
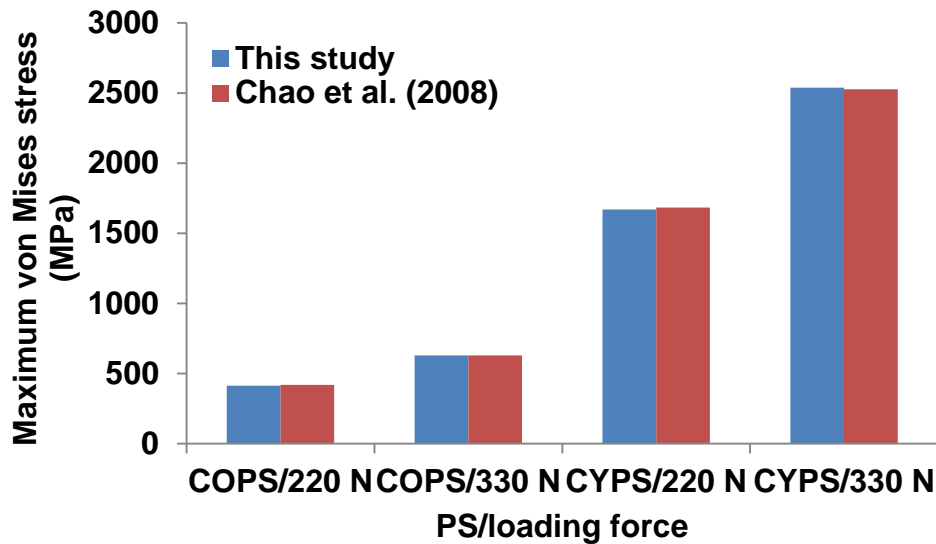
(a)
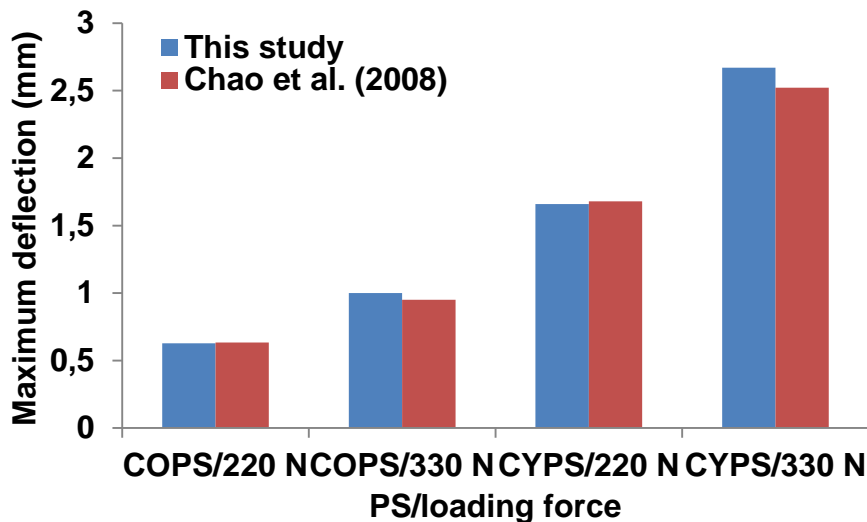
(b)

Fig 3.1 Comparison of the maximum von Mises stress and deflection of the PSs predicted in this study and by CHAO et al. (2008): (a) Maximum von Mises stress; and (b) maximum deflection

3.1.2 Cyclic loading and fatigue analysis

The fatigue life cycles for COPS and CYPS under cyclic bending forces of 400 N and 600 N predicted in this study were compared with those reported by CHAO et al. (2008) in Fig 3.2. Fatigue analysis was not conducted for CYPS subjected to 600 N

bending force since immediate breakage occurred within one loading cycle, which was also observed in experimental study (CHAO et al., 2008). Exact values of the fatigue life cycles of COPS under bending forces of 400 N and 600 N were not reported by CHAO et al. (2008) since the fatigue failure didn't occur within 10^6 loading cycles, which was the measurement limit set by CHAO et al. (2008). As shown in Fig 3.2, fatigue life cycles predicted in COPS were 6.2396×10^6 and 1.5654×10^6 under bending forces of 400 N and 600 N respectively while CYPS withheld only 265 loading cycles before fatigue failure. The fatigue life cycle of CYPS under 400 N bending force predicted in this study was within the range of the experimental value (290 ± 35) reported by CHAO et al. (2008). Thus, the fatigue life of the PS predicted in this study was considered within reasonable range from the experimental results.
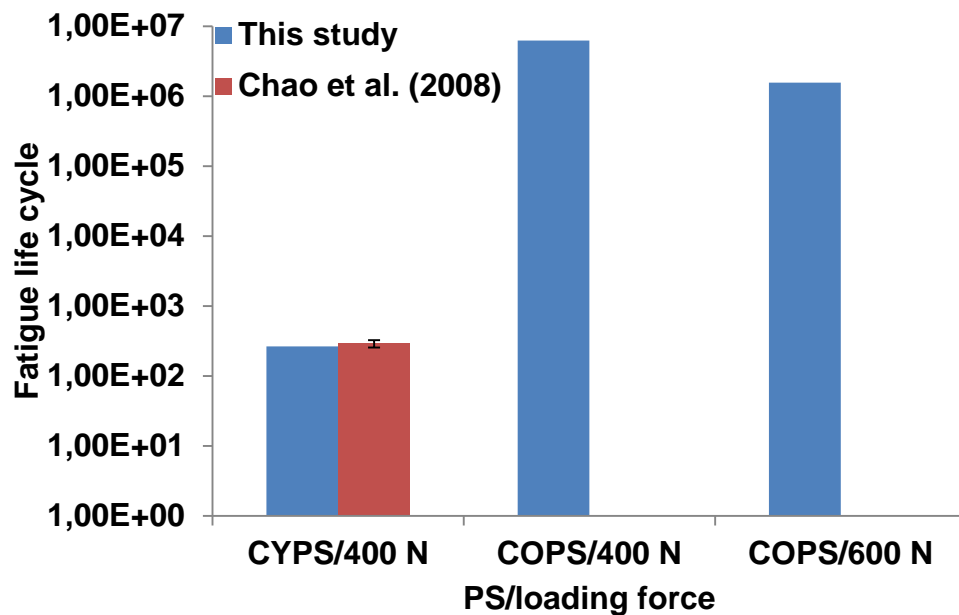
Fig 3.2 Comparison of the fatigue life cycles of CYPS under cyclic bending forces of 400 N and 600 N predicted in this study and CHAO et al. (2008)

3.2 Bending test with lumbar spine vertebra

The predicted contour plots of fatigue life cycles of the vertebra bony tissues under different bending forces (75 N, 100 N, 125 N, and 150 N) were shown in Fig 3.3. Under cyclic bending of 150 N when inserted in the vertebra, COPS had fatigue life cycles of 9.0183×10^8 loading cycles and CYPS was able to withhold 1.1201×10^7 loading cycles shown in Fig 3.4, which were significantly larger than the vertebral bony tissues. Thus, in this test, fatigue failure of the PS-vertebra connection occurred when the vertebral bony tissues approached fatigue limit. According to Fig 3.3, as the bending force increase from 75 N to 150 N, the fatigue life (number of loading cycles before the failure) of the bony tissues considerably decreased in both PSs. The bony tissues in vertebra inserted with COPS had larger fatigue life cycles than those in vertebra inserted with CYPS.
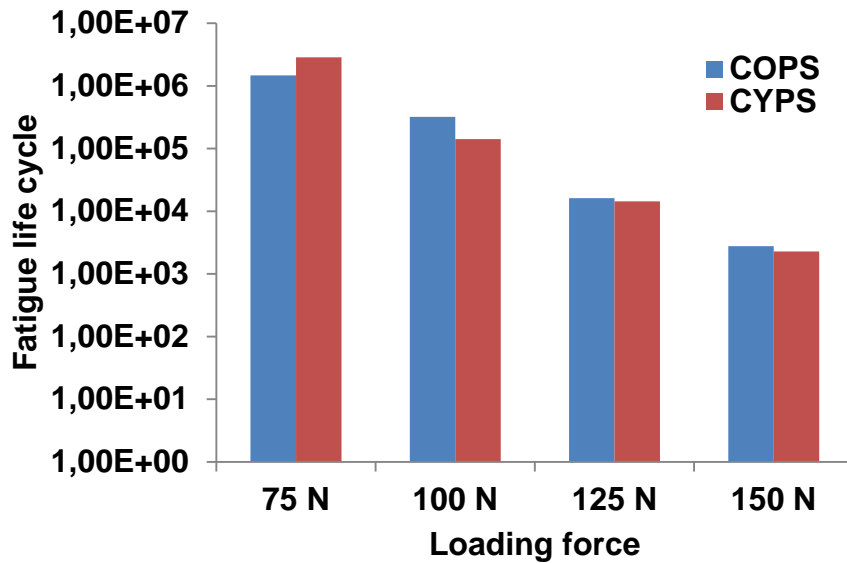
Fig 3.3 Comparison of fatigue life cycles of vertebra when inserted with COPS and CYPS under cyclic bending forces from 75 N to 150 N
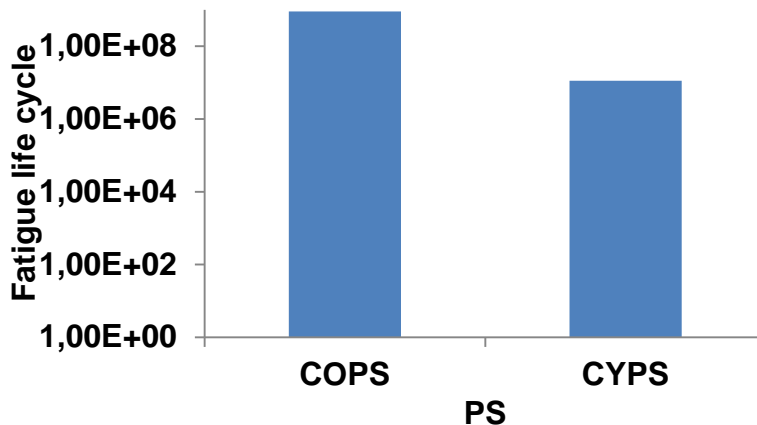
Fig 3.4 Fatigue life cycles of COPS and CYPS under cyclic bending force of 150 N

4   Discussion

In this study, an innovative-developed feasible computational approach was introduced to study the fatigue life of the interactions between the PS and vertebral bony tissues (or synthetic bony tissues). Compared with the traditional experimental approaches, the computational approach introduced in this study had advantages of lower cost and higher efficiency. It is challenging to validate the fatigue prediction method introduced in this study because great inter-subject variations exist in the material properties and anatomies of spinal bony tissues (DREISCHARF et al., 2014). Thus, the modeling method in this study was validated against experimental results obtained from polyurethane foam with known and stable material properties instead of the cadaveric vertebra sample. Since the fatigue calculation was based on the stress/strain history of FE elements obtained from the FE analysis, the accuracy of the FE model is critical. Validated FE models of the vertebra and the PSs from our

previous study were employed in this study. Besides, SWT fatigue equation indicated that the fatigue life of the material is related with the mean stress in the material during the entire loading process instead of the maximum stress at any particular time point. The magnitude of the loading condition alone is not sufficient to accurately predict the fatigue life of one type of material. The frequency of the loading and the loading history during the entire loading process are required for fatigue analysis as well.

In the quasi-static cantilever bending test between the PS and the polyurethane foam, the von Mises stress and deflection of the PSs predicted in this study were consistent with the results reported by CHAO et al. (2008). Under identical loading conditions, COPS had significantly smaller von Mises stress and deflection. In order to test the fatigue life predicting capability of the proposed method, fatigue life cycles of the validated PS-foam FE models were calculated under identical loading condition with mechanical tests performed by CHAO et al. (2008). The immediate failure of the PS is related to the von Mises stress at failing time point whereas the fatigue failure of the PS is related to the mean stress the PS withhold (CHAO et al., 2008). Thus, it is possible that the immediate failure and the fatigue failure will occur at different sites on the PS under certain type of loading. To illustrate this point, von Mises stress contour plot of CYPS under bending force of 400 N and fatigue damage contour plot of CYPS under cyclic bending force of 400 N are shown in Fig 4.1. The sites with maximum von Mises stress and the sites with least fatigue life cycles were close yet not identical. This suggested that fatigue behavior of the PS should be studied separately from the immediate holding capability, which should be thoroughly considered in the design process of PS. In light of the fact that fatigue damage of PS could not be fully eliminated in the post-surgical subjects, fatigue failure of the PS should also be considered during clinical practice (CHAO et al., 2008). In clinical observations, fatigue damage of the PS commonly occurred at the body-head junction of the PS (CHAO et al., 2008; BRASILIENSE et al., 2013). The fatigue life cycles of PS predicted in this study were within one standard deviation range of the mean value of those obtained from mechanical tests (CHAO et al., 2008). However, it is worth noticing that the fatigue life cycles predicted in this study (fatigue life cycle of CYPS under cyclic bending force of 400 N is 265) was close to the lower boundary of the range (290±35) reported by CHAO et al. (2008). The reason might be due to the difference between the fatigue failure criteria applied in this study and in the mechanical test (CHAO et al., 2008). CHAO et al. (2008) considered fatigue failure of PS when the displacement of the actuator was beyond 10 mm or when the number of testing cycles was more than one million whereas the fatigue life cycles of PS predicted in this study was the fatigue life cycle of the first failing element. If the fatigue failure process could not finish within short period of time, considerable difference would exist between the simulation result in this study and the experimental observation. However, based on experimental data reported by CHAO et al. (2008), no plastic deformation of the PS was observed and after certain amount of loading cycle, sudden fatigue damage was able to finish within short period of time, which explained why the fatigue life predicted in this study was still reasonably close to the experimental result.

(a)

(b)
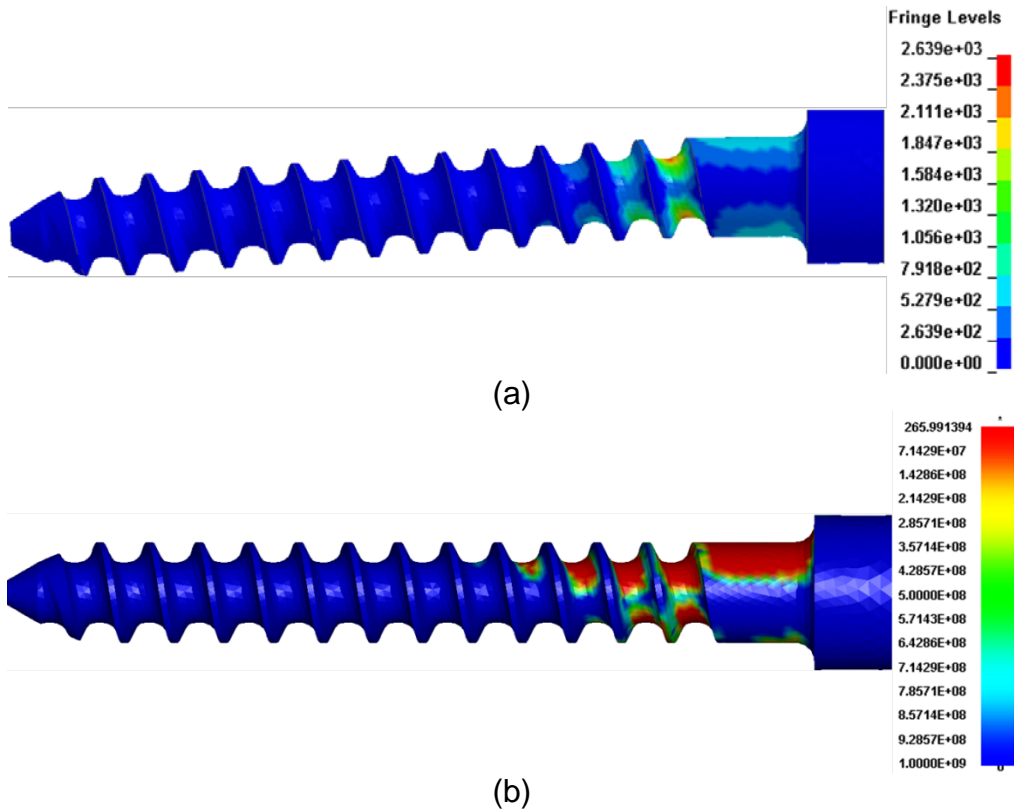
Fig 4.1 CYPS Contour plots: (a) von Mises stress (MPa) under static bending force of 400 N; and (b) fatigue life cycles under cyclic bending force of 400 N

In the PS-vertebra bending test, since the fatigue life cycles of the bony tissues were significantly smaller than those of the PS, fatigue failure of the PS-bone interaction was considered to be the bony tissues. As the magnitude of cyclic bending load linearly increased, the fatigue life of the bony tissues exponentially reduced. This suggested that long-term high loads on post-surgical spine would greatly reduce the fatigue life of the PS-bone bond, which increased the risks of PS loosening and even fatigue breakage.   As shown in Fig 4.2, the fatigue failure occurred first at the elements around the outer edge of the screw hole in the vertebra for both COPS and CYPS. Fatigue life cycles of the elements in vertebra tend to be more uniformly distributed along the outer edge when inserted with COPS than those when inserted with CYPS, which might be the potential reason for the better fatigue performance of COPS.

Cyclic bending force75 N Cyclic bending force 100 N

Cyclic bending force 125 N Cyclic bending force 150 N

(a)

Cyclic bending force75 N Cyclic bending force100 N

Cyclic bending force125 N Cyclic bending force150 N

(b)

Fig 4.2 Contour plots of fatigue life cycles under cyclic bending forces of 75 N, 100 N, 125 N, and 150 N: (a) COPS; and (b) CYPS

One limitation of this pilot study was that deterministic FE model of vertebra was utilized. To better predict the realistic fatigue behavior of the PS-bone interaction, subject-specific material properties are recommended (DREISCHARF et al., 2014), which could be partially obtained from the medical image. The computational approach introduced in this study matched well with the experimental study for the PS, where the sudden fatigue occurred after certain amount of loading cycles. Greater error was assumed when gradual fatigue failure took place. However, in the literature, most experimental fatigue studies for the PS-vertebra interactions were designed to reach fatigue failure in a short period of time. Thus, the computational approach introduced in this study was able to act as a reasonable alternative for the experimental study. Due to errors introduced by the inter-subject variations in the material properties of the spinal tissues, the exact values of the fatigue life cycles of the vertebra might not necessarily apply to all the subjects. However, the method introduced in this study was able to provide general trend of the fatigue performance of the PS-bone interaction, which was also the main objective of this method. In this study, only one vertebra inserted with one PS was tested under simplified uniaxial loading conditions to study the fatigue life of PS-vertebra interaction, which was set to be identical with the experimental study in the literatures (CHAO et al., 2008; BRASILIENSE et al., 2013; AKPOLAT et al., 2016). However, PS was subjected to complex multiaxial loading conditions including both force and bending moment during physiologic spinal loading environment. In this study, the only one set of deterministic input parameters were 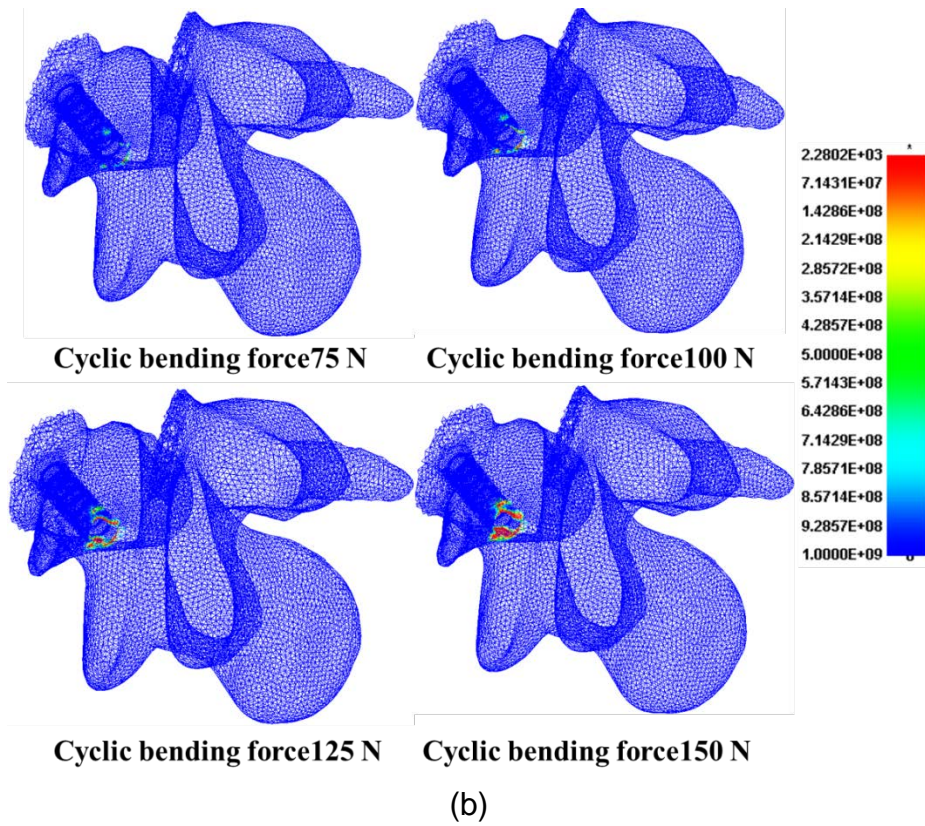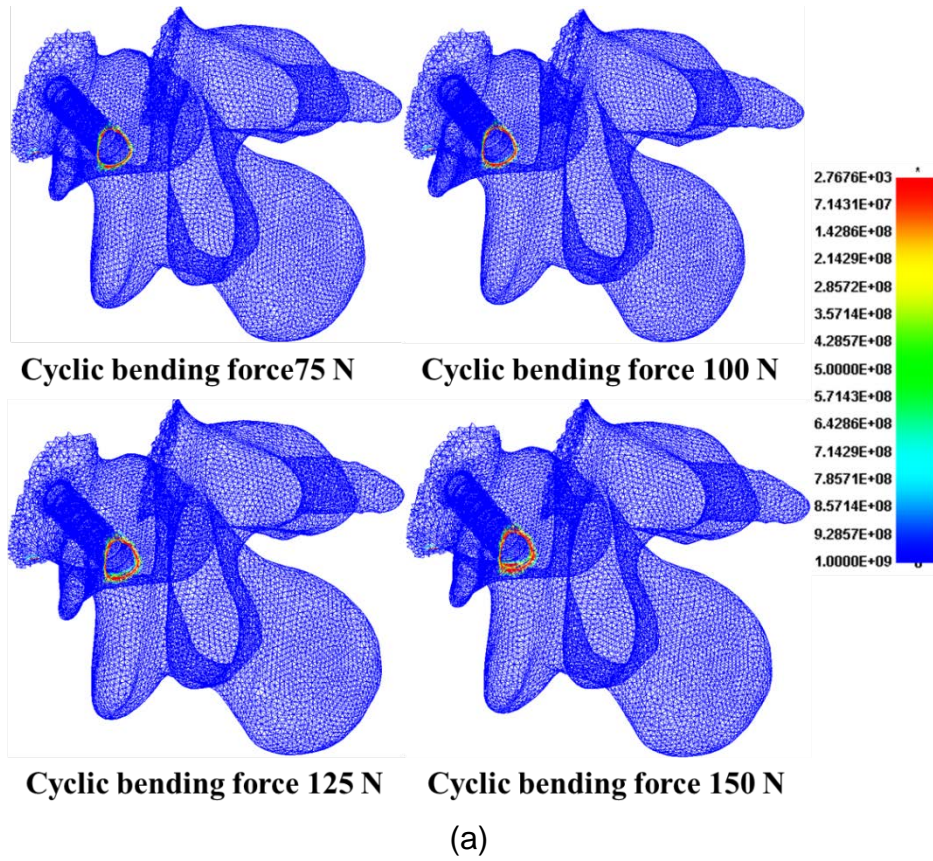employed for the fatigue analysis. In the future study, sensitivity analysis will be performed for the fatigue analysis input parameters. Furthermore, the fatigue analysis method introduced in this study will be utilized to study the fatigue behavior of PS-bone interaction within multi-segment spine FE models under physiological spinal movements. It is of clinical value to compare the fatigue behaviors of the PS-bone interaction with different surgical plans and under different types of spinal movements.

5   Conclusion

This study introduced one feasible computational approach to predict the fatigue behavior of the screw-bone interactions. The predicted fatigue life cycles in this study were validated against the experimental data in the literature. The fatigue life prediction method introduced in this study is a reasonable alternative for the screw-bone experimental test. By comparing the contour plots of the von Mises stress and fatigue life cycles on the PS, this study suggested that the sites with maximum von Mises stress and most likely fatigue failure are not consistent. Thus, fatigue damage of PS should be studied separately from the immediate breakage of the PS. In the PS-vertebra bending test, small amount of loading increase will exponentially reduce the fatigue life of the screw-bone bond, which suggested that post-surgical patient should avoid applying high load on the spine for a longer serving life of the spinal implant. In the future work, the modeling method validated in this study will be utilized to study the fatigue behaviors of the screw-bone interaction under physiological spinal loading environment within multi-segment spine FE models.

List of references

Akpolat, Y. T.; Inceoglu, S.; Kinne, N.; Hunt, D.; Cheng, W. K.: Fatigue performance of cortical bone trajectory screw compared with standard trajectory pedicle screw, Spine 2016, 41(6), pp.E335-E341.

Amaritsakul, Y.; Chao, C. K.; Lin, J.: Biomechanical evaluation of bending strength of spinal pedicle screws, including cylindrical, conical, dual core and double dual core designs using numerical simulations and mechanical tests, Medical Engineering & Physics 2014, 36(9), pp.1218-1223.

Brasiliense, L. B. C.; Lazaro, B. C. R.; Reyes, P. M.; Newcomb, A.; Turner, J. L.; Crandall, D. G.; Crawford, N. R. : Characteristics of immediate and fatigue strength of a dual-threaded pedicle screw in cadaveric spines, The Spine Journal 2013, 13(8), pp.947-956.

Chao, C.-K.; Hsu, C.-C.; Wang, J.-L.; Lin, J.: Increasing bending strength and pullout strength in conical pedicle screws: Biomechanical tests and finite element analyses, Journal of Spinal Disorders & Techniques 2008, 21(2), pp.130-138.

Dreischarf, M.; Zander, T.; Shirazi-Adl, A.; Puttlitz, C. M.; Adam, C. J.; Chen, C. S.; Goel, V. K.; Kiapour, A.; Kim, Y. H.; Labus, K. M.; Little, J. P.; Park, W. M.; Wang, Y. H.; Wilke, H. J.; Rohlmann, A.; Schmidt, H.: Comparison of eight published static finite element models of the intact lumbar spine: Predictive power of models improves when combined together, Journal of Biomechanics 2014, 47(8), pp.1757-1766.

Elder, B. D.; Holmes, S. L.; Goodwin, C.; Kosztowski, T. A.; Lina, I. A.; Locke, J. E.; Witham, T. F.: The biomechanics of pedicle screw augmentation with cement, The Spine Journal 2015, 15, pp.1432-1445.

Fatihhi, S. J.; Harun, M. N.; Kadir, M. R. A.; Abdullah, J.; Kamarul, T.; Ochsner, A.; Syahrom, A.: Uniaxial and Multiaxial Fatigue Life Prediction of the Trabecular Bone Based on Physiological Loading: A Comparative Study, Annals of Biomedical Engineering 2015, 43(10), pp.2487-2502.

Hight, T. K.; Brandeau, J. F.: Mathematical modeling of the stress-strain rate behavior of bone using the Ramberg-Osgood, Journal of Biomechanics 1983, 16(6), pp.445-450.

Kang, D. O.; Park, K.; Heo, S. J.; Ryu, Y. I.; Il Jeong, J.: Development and Application of VPG Simulation Technique based on Equivalent Virtual Road Profile, International Journal of Precision Engineering and Manufacturing 2010, 11(2), pp.265-272.

Liu, S.; Qi, W.; Zhang, Y.; Wu, Z.-X.; Yan, Y.-B.; Lei, W.: Effect of bone material properties on effective region in screw-bone model: an experimental and finite element study, Biomedical Engineering Online 2014, 13.

Martin, B. I.; Franklin, G. M.; Deyo, R. A.; Wickize, T. M.; Lurie, J. D.; Mirza, S. K.:

How do coverage policies influence practice patterns, safety, and cost of initial lumbar fusion surgery? A population-based comparison of workers' compensation systems', The Spine Journal 2014, 14(7), pp.1237-1246.

Rohlmann, A.; Bergmann, G.; Graichen, F.: Loads on an internal spinal fixation device during walking, Journal of Biomechanics 1997, 30(1), pp.41-47.

Shih, K. S.; Hsu, C. C.; Hou, S. M.; Yu, S. C.; Liaw, C. K.: Comparison of the bending performance of solid and cannulated spinal pedicle screws using finite element analyses and biomechanical tests, Medical Engineering & Physics 2015, 37(9), pp.879-84.

Xu, M.; Yang, J.; Lieberman, I. H.; Haddas, R.: Lumbar spine finite element model for healthy subjects: development and validation, Computer Methods in Biomechanics and Biomedical Engineering 2016, pp.1-15.

Xu, M.; Yang, J.; Lieberman, I. H.; Haddas, R.: Finite Element Method-Based Study of Pedicle Screw-Bone Interaction, Computer Methods in Biomechanics and Biomedical Engineering, submitted.

Zander, T.; Rohlmann, A.; Bergmann, G.: Influence of different artificial disc kinematics on spine biomechanics. Clinical Biomechanics 2009, 24, pp.135-142.

Shu et al.:
Extracting Traditional Anthropometric Measurements from 3-D Body Scans

Shu, C.[1], Xi, P.[1], Keefe, A.[2]

[1] National Research Council of Canada
[2] Defence Research and Development Canada

Abstract

Despite the prevalence of the 3-D body scans, traditional anthropometric measurement is still the dominate form of human body measurement used in the industry. Increasingly, however, traditional measurements are extracted from 3-D body scans. The traditional measurements are simple to use and are well-understood in the industry. In this paper, we introduce a new method for extracting measurements from body scans. Our method is based on accurately locating anthropometric landmarks using a machine learning approach. All of the measurements are defined according to the landmarks. Three types of measurement – linear distance, geodesic distance, and circumference – are considered. We validate the scan-extracted measurements against human measurements using the 2012 Canadian Forces Anthropometric Survey (CFAS) dataset, which consists of 2,200 full body scans.

Key words:

anthropometric landmark localization, measurement extraction, non-rigid registration, deep convolutional neural network

1   Introduction

Traditional anthropometric measurements are 1-D measurements defined on the surface of human body based on anthropometric landmarks. They are widely used in industry for product design and other ergonomic applications that concern the human body size and shape. Despite the prevalence of the 3-D body scans, traditional anthropometric measurement is still the dominate form of human body measurement used in the industry. This situation is expected to continue in the near future, because current methods and practice are deeply rooted in the 1-D measurement and 3-D anthropometry has not yet provided the necessary tools and methods for designers. Increasingly, however, traditional measurements are extracted from 3-D body scans. The advantage of doing this is that measurements can be taken repeatedly without the human subjects being present, and therefore, unlimited number of measurement can be taken.

A raw 3-D body scan consists of hundreds of thousands of 3-D points. They are unorganized, noisy, and incomplete due to the limitations of the imaging sensor. To extract body measurements from the 3-D scans, the raw scan data have to be processed to extract higher level information. Several methods have been proposed in the literature. NURRE (1997) analyzes the slices that are parallel to the ground and segments the whole body into parts representing limbs, torso, and head. Leong et al. (2007) and LU et al. (2008) study the geometric characteristics of the silhouette and extract features points and curves. The problem of these geometric methods is that they rely on rules to define landmarks and key features. Because of the complex nature of the body shape and the 3-D data, it is difficult to come up with a simple set of rules for this purpose and there are always exceptions, making the algorithm unreliable.

In some 3-D anthropometric surveys, for example, the CAESAR survey (ROBINETTE et al. 2002), anthropometrists marked the anthropometric landmarks on the subjects with photo reflective markers prior to the scanning process. The locations of the landmarks can then be identified on the scans manually or using software. Several authors make use of these landmarks to fit a template mesh to every scan (ALLEN et al., 2003; XI et al. 2007). This method establishes a correspondence or registration among the individual scans, and at the same time, smoothly fills the holes in the scans. The correspondence provides a foundation for statistical shape analysis and other applications including extracting body measurements.

However, landmarking the human subjects is a tedious task and requires expert knowledge of the human anatomy. Several authors proposed methods for locating the landmarks automatically (BEN AZOUZ, 2006; WUHRER, 2010; YAMAZKI, 2013) with moderate success. TSOLI et al. (2014) suggest a data-driven approach to predicting the body measurements by using a markerless registration method and establishing a statistical model between the measurements and the body shapes. However, this method can only predict the measurements that have been taken in the training data.

Since the traditional anthropometric measurements have long been standardized based on the landmarks, any useful system that extracts body measurements has to be able to locate the landmarks robustly. In this paper, we introduce a new method

for predicting landmarks based on deep neural networks (LECUN et al. 2015). All of the measurements are defined according to the landmarks. Three types of measurement – linear distance, geodesic distance, and circumference – are considered. We validate the scan-extracted measurements against human measurements using the 2012 Canadian Forces Anthropometric Survey (CFAS) dataset, which consists of 2,200 full body scans.

2 Landmark prediction

Anthropometric landmarks are stable corresponding positions on the human body that exist across the population. They are usually located on the human body where bones protrude. Therefore, many of them have visible features on the surface of the human body. This suggests that we can apply a Machine Learning approach to train a computer program using data from manually identified landmarks. In the past, geometric features and explicit models, such as the Markov Random Field model (BEN AZOUZ, 2006), has been used to learn the relationship between the landmarks and their surface features. The recent development in deep neural networks provides a much more flexible and expressive model. A set of tools, called convolutional neural networks (CNN), is particularly effective for solving the image classification problems (KRIZHEVSKY et al. 2012). In this section, we show that they can be adapted for the 3-D meshes and solving the landmarking problem.

2.1 Training

In order to use CNN, the data have to be in the form of a 2-D array, such as a color image. Converting the mesh models to images is a crucial step in applying CNN to solve the landmark prediction problem. Although a mesh model is a 3-D object, its surface is a 2-D manifold embedded in 3-space. Therefore, at any given point on the surface, we can extract a local 2-D image. One simple way of reducing the landmark identification problem to an image classification problem is to project the 3D model to an image plane, like taking a photograph of the model, and generate an image using the surface properties of the model. We consider three types of images.

1. Curvature map. At each vertex of the mesh, the two principal surface curvatures are computed and the mean or Gaussian curvature can be evaluated. This is a scalar that can be converted to a color value. We can render the mesh in color by interpolating the vertex colors for every triangle and thus obtain a curvature map. We then project the color model to a plane to generate a color image. Two projection planes were selected, one in front of and another one at the back of the model. Figure 2.1(a) shows an example of the curvature map. The curvature map completely defines the local surface properties of the mesh model.
2. Depth map. With the same front and back image planes chosen as above, we can generate two images in which each pixel value represents the distance from the image plane to the corresponding point on the mesh. These are grey-scale images (Figure 2.1 b), just like the ones obtained with 3-D scanners.
3. Appearance image. We can simulate a camera taking photographs of the 3-D model. An upper front light source is selected and the 3-D model is rendered

into the defined image plane. The shading on the model captured by the virtual camera represents the geometry of the 3-D model. Figure 2.1(c) shows examples of the appearance image.
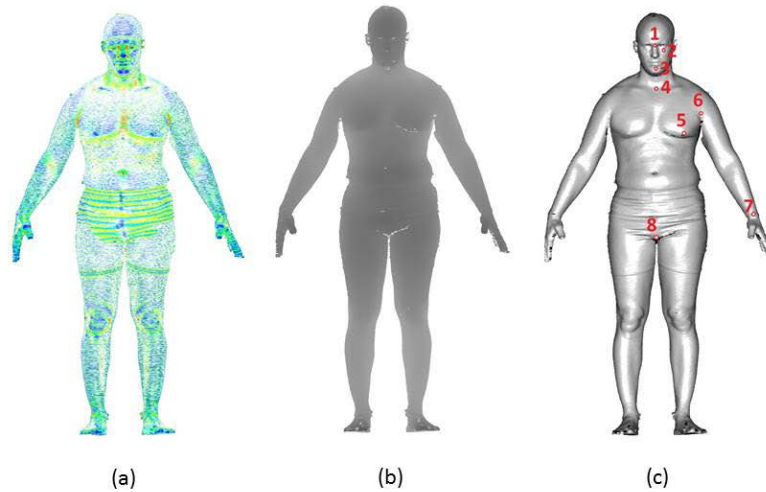
Fig. 2.1   Images generated from a mesh. (a) curvature map; (b) depth map; (c) appearance image.

2.2   Prediction

The most straightforward way of predicting landmarks is to formulate it as a regression problem. This approach trains a regression network that takes an image and outputs the coordinates of the landmarks. FAN and ZHOU (2016) used this approach to localize landmarks on face images and achieved good results. However, for identifying landmarks for the full body, this method cannot deliver sufficient accuracy because the image size that is feasible for CNN is limited. Nonetheless, we can use it as a first approximation of the landmark locations. Based on this approximation, we devise a classification CNN for each landmark.

In our implementation, we use the VGG network (CHATTFIELD et al., 2014), a publicly available network pre-trained with the ImageNet images. It consists of five convolutional layers followed by three fully-connected layers. We customize this network for solving our landmark localization problem. For the regression problem, we remove the last softmax layer and the change the output size of the last fully-connected layer to twice the number of selected landmarks. For computing the loss, we use least square error (L_2 norm) for forward and backward loss propagation.

To train a deep classification network, we need both the locations of the true landmarks and the locations for none landmarks. For this purpose, we select nearby pixels, called phantom landmarks, to train the classifier. Images of the phantom landmarks are generated as examples of none-landmarks (Figure 2.2).
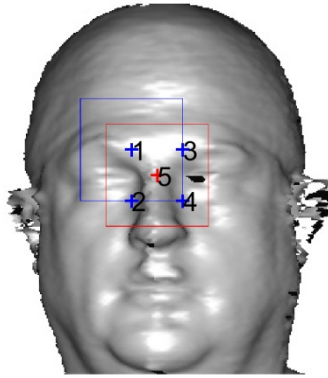
Fig. 2.2 Phantom landmarks

To modify the VGG network for classification, we first remove the output softmax layer and change the last convolution layer to reflect the size of the output, which is the number of classes for the new classifier. Then we add a new softmax loss layer for the classification of image patches.

When training the network, we keep all of the VGG parameters and weights, only changing the learning rate to ensure convergence. To predict a landmark, we search around the first approximation using a sliding window approach.

We use MatConNet, a MATLAB toolbox for Convolutional Neural Networks (CHATTFIELD et al., 2014) to customize the VGG network. The toolbox provides basic building blocks of a deep CNN, including convolution, pooling, and non-linear activations. It also supports multiple GPUs.

2.3 Validation

We use 200 manually landmarked models for training the deep CNN. We also set aside 50 manually landmarked models for validation. The validation dataset is also used for monitoring the learning processes to avoid over-fitting.

The resolution of the image initially generated from the mesh model is 2240x2240. Since VGG requires all images to be 224x224, we scale all the images to this size. The landmark coordinates are projected to the same sized image.

2.3.1 Deep regression and classification CNNs

The training of the customized deep regression CNN takes about 40 hours, running 16,000 epochs. The learning rate is set to 0.5e-4.

For each landmark, we train a deep CNN classifier. A square image of 80x80 centered at the landmark location is extracted for a positive example. Four other points that are 20 pixels away from the landmark are selected as *phantom landmarks*, to generate negative example images. The collection of both positive and negative example images is used to train the deep classification CNN.

Training the CNN takes about 2.5 hours for completing 12,000 epochs at a learning rate of 0.0002.

2.3.2 Prediction results and evaluation

Figure 2.3 illustrates the window-sweeping process for predicting the landmarks. The results are summarized in Table 2.1. We evaluate the maximal absolute difference (MAD) from the predicted landmark to the human marked landmark. We selected 25 landmarks that are important for measurements (Figure 2.4). The mean MAD and the 95% confidence for each landmark are computed. With the exception of the sacrum (landmark 11), the majority of the errors are within 15mm. Note that a landmark like the sacrum, where there is little local surface feature, is difficult to locate even for the human operators. KOUCHI and MOCHIMARU (2011) studied the accuracy of the anthropometrists with a small sample set and reported that the intra-observer errors range from 2mm to 26mm.
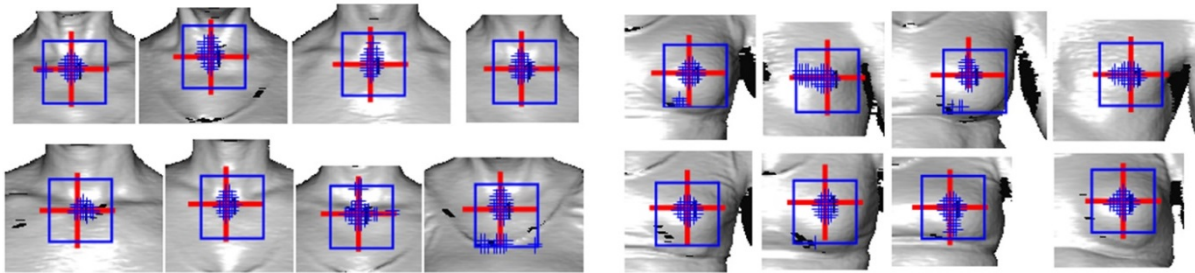
Fig. 2.3 Examples of the window-sweeping process.
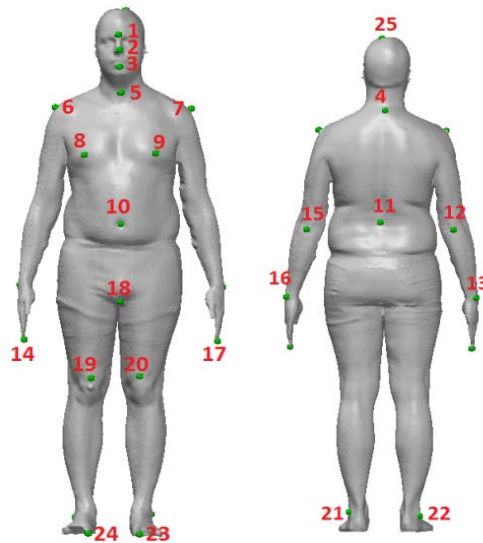
Fig. 2.4 Landmark index

Table 2.1 Landmark prediction errors

Landmark Name	MAD - mean	MAD - std	MAD-mean (95%)	MAD-std (95%)
1 Glabella	4.25	2.13	3.98	1.88
2 Most Anterior Point of Nose	3.99	2.02	3.71	1.67
3 Mentis	5.65	6.50	4.65	2.13
4 Cervicale	10.60	8.77	8.93	5.39
5 Anterior Neck	17.63	12.60	15.85	10.40
6 Acromion (left)	9.73	3.23	9.30	2.72
7 Acromion (right)	10.31	6.37	9.24	4.62
8 Bustpoint (left)	8.61	9.33	6.83	5.62
9 Bustpoint (right)	10.50	13.66	8.01	8.94
10 Omphalion (anterior)	5.27	4.35	4.52	2.17
11 Sacrum	62.61	32.80	59.22	30.40
12 Olecranon (left)	13.56	17.53	10.35	10.83
13 Ulnar Styloid (left)	14.52	17.77	11.07	8.88
14 Tip of middle finger (left)	11.59	4.98	10.83	3.88
15 Olecranon (right)	21.70	22.68	17.50	13.15
16 Ulnar Styloid (right)	12.18	10.28	10.36	5.45
17 Tip of middle finger (right)	13.09	22.69	9.16	4.38
18 Crotch/Groin	14.96	8.74	13.54	6.02
19 Suprapatella (left)	7.03	3.79	6.49	3.10
20 Suprapatella (right)	20.50	11.22	18.73	8.31
21 Lateral Malleolus (right)	10.74	7.35	9.62	4.74
22 Lateral Malleolus (left)	10.54	9.84	8.93	5.53
23 Left Most Anterior Metatarsal	7.63	10.11	5.34	2.68
24 Right Most Anterior Metatarsal	6.91	6.73	5.54	3.51
25 Vertex	22.44	10.19	21.24	9.10

3   Measurement Extraction

With the predicted the landmarks, we fit a template mesh to every scan. Dimensional measurements are extracted from the fitted models. This way, we can avoid the noisy surface and holes in the raw scans, which can cause errors in computing the measurements.

From a computational perspective, there are three types of measurements: linear distance, geodesic distance, and circumference, all related to the landmarks. The linear distance is the simplest to implement; it is just the Euclidean distance between two landmark points. Examples of linear distance are Cervicale Height, Ankle Height, and Chest Height.

The geodesic distance is the shortest path length from one point to another along the surface. It is equivalent to flatten the surface locally and connecting the two points with a straight line. This geometric procedure closely approximates the tape measure operation performed by a human operator. Examples of geodesic distance include the waist back length and the sleeve outstream.

Circumferences are computed by intersecting a plane with the model and calculating the length of the intersecting curve. Examples of circumference are Waist, Ankle, and Neck circumferences. Note that in general a cutting plane may result in multiple loops and the correct loop has to be selected. This can be done by pre-segmenting the body into parts and the cutting is only performed on the correct part. For some measurements, the cutting curve is not convex and is not the same as the tape measure. This can be compensated by computing the convex hull of the cutting curve. The convex hull of a set of points in the smallest convex polygon that encloses the point set.

3.1   Validation

In general, it is difficult to evaluate the accuracy of the extracted dimensions simply because there is no ground truth for these dimensions. The shape and size of a human are constantly changing due to breathing and posture variation. Different operators have slightly different interpretations of a definition of a measurement and therefore will obtain different results for the same person.

In traditional anthropometric surveys, human operators are often tested for consistency. A measurement is taken multiple times on a subject by the same operator during a day. The Mean Absolute Difference (MAD) is computed to gauge the operator's reliability (GORDON et al., 1989).

ROBINETTE and DAANEN (2006) studied the consistency of scan-extracted measurements by scanning a subject multiple times and extracting the measurements by software. They reported that the consistency of the scan-extracted measurements is comparable to that of expert anthropometrists.

As the goal of extracting traditional anthropometric measurements from 3-D models is to simulate a human operator performing the measurements, one reasonable validation is to compare with manual measurements for the likewise measurements.

BRADTMILLER and GROSS (1999) and PAQUETTE et al. (2000) evaluated proprietary software against human anthropometrists.

Table 3.1 Comparison with manual measurements (error in mm)

Measurement Names	Mean MAD	MAD Std
'Acromion-Radiale Length'	20.1	17.6
'Ankle Circumference'	25.5	10.0
'Axilla Height'	21.0	13.4
'Bitragion Breadth'	7.9	3.5
'Bustpoint/Thelion-Bustpoint/Thelion Breadth'	14.5	20.3
'Buttock Depth'	26.9	10.9
'Buttock Height'	24.6	15.8
'Calf Circumference'	8.0	6.9
'Calf Height'	15.3	13.4
'Cervicale Height'	27.9	20.5
'Chest Depth'	6.5	5.1
'Chest Height'	15.7	13.2
'Elbow Circumference'	15.2	9.7
'Head Length'	6.5	4.6
'Lateral Malleolus Height'	12.8	9.1
'Neck Circumference, Base'	22.8	24.2
'Radiale-Stylion Length'	21.1	20.1
'Stature'	21.5	8.2
'Suprasternale Height'	14.7	10.8
'Tenth Rib Height'	35.0	20.6
'Thigh Circumference'	38.1	41.8
'Trochanterion Height'	19.5	12.7
'Waist Back Length (Omphalion)'	32.3	26.0
'Waist Circumference (Omphalion)'	38.7	63.3
'Waist Depth'	11.2	9.0
'Waist Front Length (Omphalion)'	39.1	39.4
'Waist Height (Omphalion)'	24.7	25.9
'Sleeve Outseam'	34.1	28.1
'Knee Circumference'	21.4	14.3
'Neck-Bustpoint/Thelion Length'	16.5	24.9
'Shoulder Length'	10.0	6.4

We conduct a preliminary test that compares the machine extracted results to those obtained by traditional anthropometry using 30 subjects. Table 2 shows the statistics of these comparisons. Note that the MADs are significantly higher than the ISO 20685 (2010) specified allowable errors, which are less than 1 cm for all measurements. This shows that our measurement extraction process has significant differences with the human operators in terms of interpreting the definitions of the measurements, given that we have relative accurate prediction of the landmarks. We have also analyzed the positive / negative bias of the results and found that most

computed measurements are larger than the manual measurements. This may be due to the fact that the human operators apply a tension to the measuring tape. The results can be improved by calibrating the machine computed dimensions with those obtained by the anthropometrists. Further investigation is necessary using more data.

4   Conclusions

Physical measurement extraction allows measurements to be taken from the scans at any time and an extended range of measurements to include those that have not been considered at the time of the survey. It is also possible to perform measurements more consistently, as demonstrated by ROBINETTE and DAANEN (2006). The key issue is to find the landmarks accurately. In this paper, we have shown that the deep convolutional neural network can be used effectively to solve this problem. Once we have a reasonable set of landmarks, we can fit a template mesh to each scan, and from there, we can compute the measurements using standard geometric algorithms.

Comparing to the human measurements, certain scan-extracted measurements are more accurate. For example, the calf circumference, defined as the maximal circumference of the lower leg, can be computed precisely by a search algorithm, while human operators can only estimate.

It is necessary to note that the machine measurements will always be different from the manual measurements, because many different factors are involved in the two processes. However, as we train the computer to identify landmarks like the human exports, we will be more confident to extract reliable body dimensions from the scans automatically.

List of references

Allen, B.; Curless, B.; Popovic, Z.: The space of human body shapes: reconstruction and parameterization from range scans, ACM Transactions on Graphics, 22(3): 587-594, 2003.

Ben Azouz, Z.; Shu, C.; Mantel, A.: Automatic Locating of Anthropometric Landmarks on 3D Human Models, Third International Symposium on 3D Data Processing, Visualization and Transmission (3DPVT 2006). Chapel Hill, North Carolina, USA. June 13-16, 2006.

Bradtmiller, B.; Gross, M.: 3D Whole Body Scans: Measurement Extraction Software Validation, SAE Technical Paper 1999-01-1892, 1999.
Chatfield, K.; Simonyan, K.; Vedaldi, A.; Zisserman, A.: Return of the devil in the details: Delving deep into convolutional nets. In British Machine Vision Conference, 2014.

Fan, H.; Zhou, E.: Approaching human level facial landmark localization by deep learning, Image and Vision Computing, 47:27-35, 2016. 300W, the First Automatic Facial Landmark Detection in-the-wild Challenge.

Gordon, C. C.; Bradmiller, B.; Clausen, C. E.; Churchill, T.; McConville, J. T.; Tebbetts, I.; Walker, R. A.: 1987-1988 Anthropometric survey of US Army personnel. Methods and summary statistics. Natick/TR-89-044. US Army Natick Research Development and Engineering Center, Natic, MA.; 1989.

ISO 20685:2010, 3-D scanning methologies for internationally compatible anthropometric databases.

Kouchi, M.; Mochimaru, M.: Errors in landmarking and the evaluation of the accuracy of traditional and 3D anthropometry, Applied Ergonomics, 42:518-527, 2011.

Krizhevsky, A.; Sutskever, I.; Hinton, G. E.: ImageNet classification with deep convolutional neural networks, Advances in Neural Information Processing Systems (NIPS), 2012.

LeCun, Y.; Bengio, Y.; Hinton, G.: Deep learning, Nature, 2015.

Leong, I.; Fang, J.; Tsai, M.: Automatic body feature extraction from a marker-less scanned human body, Computer-Aided Design, 39:568-582, 2007.

Lu, J.; Wang, M.: Automated anthropometric data collection using 3D whole body scanners, Expert Systems with Applications, 35:407-414, 2008.

Nurre, J. H.: Locating landmarks on human body scan data, International Conference on Recent Advances in 3-D digital imaging and modeling, pp. 289-295, 1997.

Paquette, S.; Brantley, J. D.; Corner, B.; Li, P.; Oliver, T.: Automated extraction of anthropometric data from 3D images, Proceedings of the IEA 2000 / HFES 2000 Congress.

Robinette, K.; Daanen, H.: Precision of the CAESAR scan-extracted measurements, Applied Ergonomics, 37(3):259-265, 2006.

Robinette, K.; Blackwell, S.; Daanen, H.; Fleming, S.; Boehmer, M.; Brill, T.; Hoeferlin, D.; Burnsides, D.: Civilian American and European surface anthropometry resource (CAESAR), Final Report, Summary, vol. 1. AFRL-HE-WP-2002-0169, 2002.

Aggeliki, T.; Loper, M.; Black, M. J.: Model-based Anthropometry: Predicting Measurements from 3D Human Scans in Multiple Poses, IEEE Winter Conference on Applications of Computer Vision (WACV), 2014.

Wuhrer, S.; Azouz, Z. B.; Shu, C.: Posture invariant surface description and feature extraction. In Computer Vision and Pattern Recognition (CVPR), pages 374–381, June 2010.

Xi, P.; Lee, W.-S.; Shu, C.: Analysis of segmented human body scans. In Proceedings of Graphics Interface 2007, GI'07, pages 19–26, New York, NY, USA, 2007.

Yamazaki, S.; Kouchi, M.; Mochimaru, M.: Markerless landmark localization on body shape scans by non-rigid model fitting, 2nd International Digital Human Modeling Symposium, 2013.

Lee et al.:
A Shape-based Sizing System for Facial Wearable Product Design

Lee, W., Goto, L., Molenbroek, J. F. M., Goossens, R. H. M., Wang, C. C. C.

Faculty of Industrial Design Engineering, Delft University of Technology, Delft, The Netherlands

Abstract

A sizing system of a multiple-size product have been conventionally generated based on anthropometric size of a human body part. But a product which fit to a complex-shaped body part such as the face need to have a sizing system generated with consideration of body shape characteristics. This study applied template registration and machine learning clustering methods in order to make a sizing system which can consider variations of size and shape of the face. A hybrid approach using the bounded biharmonic weights (BBW) and non-rigid iterative closet point (ICP) registration methods was applied in this study to generate template-registered face images. Then, the Self-Organizing Map (SOM), a type of artificial neural network model for large-data clustering was used in order to cluster the template-registered face images into multiple shape categories. The proposed methods can be usefully applied in design of a facial wearable product such as face mask.

Key words:

Sizing system, Template registration, Machine learning clustering, Self-Organizing Map, Facial wearable product

1   Introduction

A sizing system which is generated based on anthropometric data is commonly used to determine sizing strategy in design of a multiple-size product. A sizing system needs to be properly created to accommodate various anthropometric characteristics of a target population in various sizes of a product with good fit (LEE et al., 2013a, WINKS, 1997). A sizing system have conventionally generated through a decision making process of a panel of experts based on several practical considerations including selection of target population, selection of key anthropometric dimensions related to design dimensions, statistics for sizing system generation (e.g., factor analysis, principal component analysis, clustering analysis), accommodation percentage of a sizing system, the number of sizing categories, tolerance of each sizing category, and costs for design and manufacturing of a product (JUNG et al., 2010, LEE et al., 2013a, LEE, 2013). The appropriateness of a sizing system can be varied by those considerations in product design process.

Various methods and techniques which intend to create a more appropriate sizing system for a product design have been proposed. Factor analysis or principal component analysis (PCA) are frequently used to select body dimensions which are highly relevant to specific design of a product. The variation of human body shape (e.g., face shape) is systematically considered using the first and second principal components (PCs) as key dimensions in a sizing system. A sizing system generated using two PCs (LEE et al., 2013a, XI et al., 2009, YU et al., 2012, ZHUANG et al., 2010) can show better representativeness in the human body shape (CHEN et al., 2009, GOTO et al., 2015, ZHUANG et al., 2007) than a sizing system created based on two anthropometric dimensions. However, the PCA-based sizing system has still a lack of consideration about body shape, because it is derived using a few anthropometric measurements which represent only body sizes.

This study aimed to develop methods to generation of a shape-based sizing system which can be used to designing a facial wearable product. A hybrid approach using the bounded biharmonic weights (BBW) and non-rigid iterative closet point (ICP) registration methods was applied to generate template-registered face images. Then, the Self-Organizing Map (SOM), a type of artificial neural network model for large-data clustering was used in order to cluster the template-registered face images into multiple shape categories.

2 Methods

2.1 Dataset

3D head scan images of Dutch children collected by GOTO et al. (2015) were used in this study. 302 children heads (male: 174, female: 128; age: 0.5 to 6) were scanned using the 3dMD face scanner (3dMD Ltd., London, UK).

2.2 Pre-Processing of the 3D data

Landmarking and alignment were applied on 3D head images. 19 anthropometric landmarks were identified on the 3D face area to measure 13 facial dimensions related to designing the medical face mask. All 3D heads were aligned with the origin point at the sellion landmark, then aligned with two vectors (one vertical vector parallel to the Y axis and passing through sellion and supramentale and one horizontal vector parallel to the X axis and passing through left and right tragion) (LEE et al., in press). Only face area was used in this study and the number of vertex point of the face area was 2,372.

2.3 Hybrid template-registration method

Method of deformation and non-rigid template model registration to individual 3D head scans was applied to earn template-registered head models. Three-step of a hybrid approach using the bounded biharmonic weights (BBW) and non-rigid iterative closet point (ICP) registration methods was applied in the present study as illustrated in Figure 2.1. First, one of the head having the average size was selected. The selected head was edited as a template face model by applying the symmetry-shaped mesh topology. 19 facial landmarks were identified on the template face. Second, BBW proposed by JACOBSON et al. (2014) were applied to the template model for global registration by matching the location of landmarks of the template face to the location of landmarks of a target face. In the BBW method, weight values are assigned to each vertex point of the 3D image by considering distant relationships between a vertex and landmark points. When the landmarks of template face are matched to the landmarks of target face, all template face's vertex points around each landmark were also relocated with the weight. Third, a non-rigid ICP registration method were applied for local registration by matching the location of all vertex points of the template face to surface of a target face. Through the template registration, all 3D face images in the database got same number of vertex points and consistent structure of mesh topology (ALLEN et al., 2003, BALL et al., 2010, LUXIMON et al., 2012, TSOLI et al., 2014, XI et al., 2009, ZHUANG et al., 2013). The hybrid registration approach which consider landmark's location by the BBW and non-rigid ICP registration methods could provide the accurate correspondence of mesh topology across all template-registered faces. Edge vectors (a linear link between two vertexes) of the parametric face model were used as a shape descriptor.
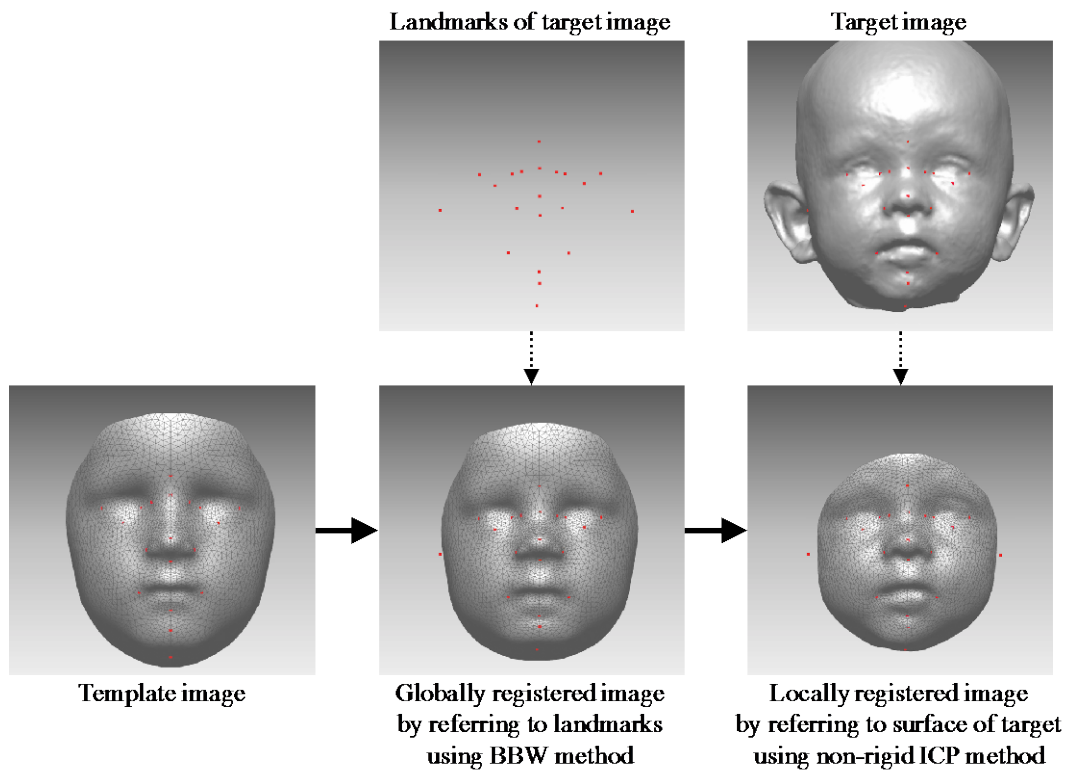
Fig. 2.1 Hybrid approach of template registration

2.4 Machine learning clustering

This study used a machine learning clustering technique to segment face shapes in a few categories. X, Y, Z values of corresponded edge vectors in all template-registered faces were used as inputs of the machine learning algorithm. The Self-Organizing Map (SOM), a type of artificial neural network model (KOHONEN, 2001, VESANTO et al., 2000) which is broadly used in large-data clustering was used in this study. The clustering of the face shape was performed using the SOM Toolbox supported by MATLAB 2016a (Mathwork, Inc., Natick, MA, USA). Two by one (2 × 1) SOM matrix was applied to simply cluster data into two categories. After the clustering was iteratively performed 100 times, the performance of clustering showed that 293 out of 302 faces (97 %) were clustered as the same category with over 80 % of repeatability (cluster A: 132, cluster B: 162, not clustered: 9). The average shapes in each category shows that the cluster A (yellow face in Figure 2.2) is longer, wider, and flatter than the cluster B (blue face in Figure 2.2). Then, the principal component analysis was applied on X, Y, Z positions of all correspond vertex points of template-registered 3D face images to see shape variations (BALL et al., 2010, GOTO et al., 2015, LEE et al., in press, MEUNIER et al., 2009, ZHUANG et al., 2007). Figure 2.3 shows difference between two clusters. Black (cluster A) or blue (cluster B) lines in the figure represent eigenvector x ± 50 SD applied on each vertex point.
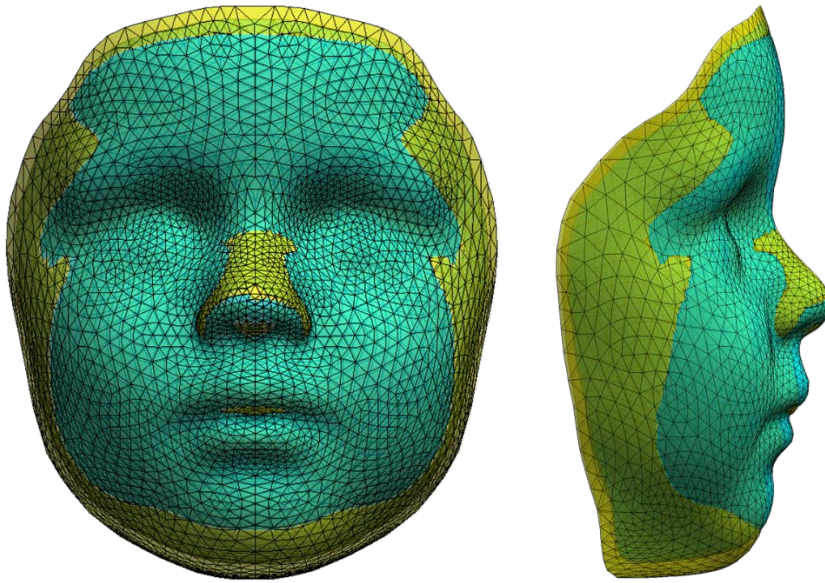
Fig. 2.2 Difference between average shapes of each cluster
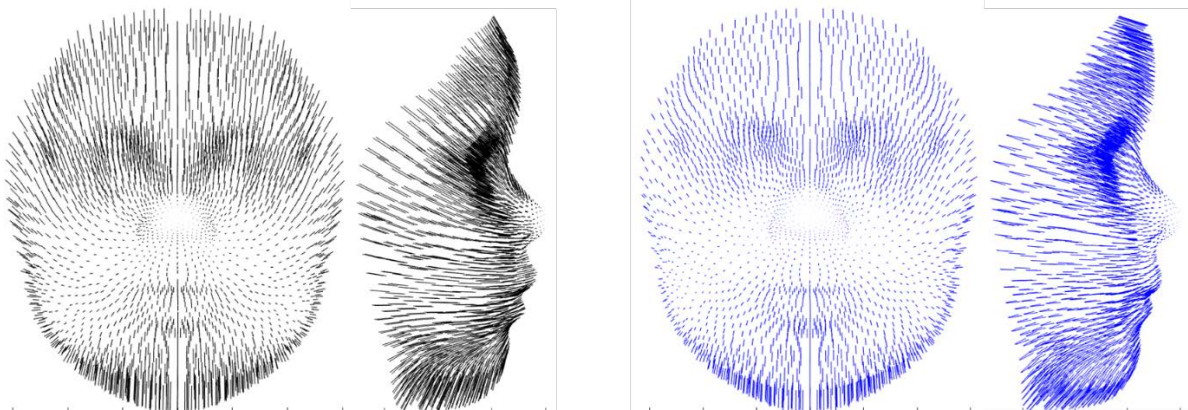
Fig. 2.3 Differece of PCA's eigenvectors between two clusters

2.5 Forming sizing system

This study clustered the face shape of Dutch children into two groups through the machine learning clustering; thus, the number of designs of the facial mask also can be two. However, the shape clusters found based on edge vectors do not consider the size variation of the face, so that the size of faces varies within each cluster due to the variation of their ages (0.5 to 6 years old). Therefore, after the clustering using the shape descriptor, this study re-segmented each cluster into two sizes (small and large) based on anthropometric measurements of two facial dimensions. This study selected face length, the most commonly used as key anthropometric dimensions in facial mask design by referring to existing study (GROSS et al., 1997, HAN et al., 2003, LEE, 2013, LEE et al., 2013b, OESTENSTAD et al., 1992, ZHUANG et al., 2005). Two sizing categories clustered based on the SOM clustering method were segmented into two sizes (short & long) using the face length measurements.

Through the 2-step procedure of sizing system creation, the number of facial mask designs could be found as four (two shape-based clusters × two sizes). Table 2.1 shows the distribution of population in each sizing category.

Table 2.1 Distribution of population in each sizing category

	Shape cluster A	Shape cluster B
Short (< average face length)	64	68
Long (≥ average face length)	75	87

3 Discussion

This study proposed a novel approach for generation of sizing system using both size and shape of human face, which can be usefully applied in facial product design. The machine learning clustering with the SOM, a type of artificial neural network was applied to cluster the shape of faces. The edge vectors of template-registered models were proposed as the shape descriptor in this study. This study clustered the facial shape of children into two categories. Those two clusters showed differences in terms of average shape of each cluster. Technical understanding of the SOM clustering as well as technical methods for comparison of shape differences between clusters need to be further considered in clustering study of body shape with good accuracy and performance.

A hybrid template-registration method consisting of the BBW and non-rigid ICP algorithms was applied in this study. This hybrid method can show more accurate results regarding anthropometric dimensions compared to the results taken through the non-rigid ICP method (without applying the BBW, because the template model was first globally registered to a target model based on location of landmarks using the BBW algorithm. Through global registration using landmarks, the mesh topology surrounding each landmark shows high correspondence across all template-registered models.

Further study regarding analysis of performance of the shape-based sizing system is needed. The shape-based sizing system proposed in this study need to be compared to conventional sizing systems generated based on anthropometric sizes. Conventionally, a sizing system is generated by a decision making process of a panel of experts (e.g., ergonomists, product designers) based on several practical considerations including selection of target population, selection of key anthropometric dimensions which are mostly related to design dimensions, sizing system generation methods (e.g., lattice method, clustering method, optimization method), accommodation percentage of the sizing system, the number of sizing categories, tolerance of each sizing category, and costs for design and manufacturing of the product (JUNG et al., 2010, LEE et al., 2013a, LEE, 2013, LEE et al., in press). The performance between different sizing systems can be assessed by comparison of such as accommodation, size and shape variability of population in each sizing category, and appropriateness of the sizing system in product design.

As the conclusion, the shape-based sizing system using edge vectors of the parametric model can be applied to create more appropriate sizing systems for

product design, which intend to provide good fit and comfort to users. Future study such as a quantitative comparison between sizing system creation methods, and a usability evaluation of product (e.g., facial mask) designs are needed to validate the effectiveness of the proposed method.

Acknowledgement

List of references

Allen, B.; Curless, B.; Popović, Z.: The space of human body shapes: reconstruction and parameterization from range scans, ACM Transactions on Graphics 2003, 22(3), pp.587-594.

Ball, R.; Shu, C.; Xi, P.; Rioux, M.; Luximon, Y.; Molenbroek, J. F. M.: A comparison between Chinese and Caucasian head shapes, Applied Ergonomics 2010, 41(6), pp.832-9.

Chen, W.; Zhuang, Z.; Benson, S.; Du, L.; Yu, D.; Landsittel, D.; Wang, L.; Viscusi, D.; Shaffer, R. E.: New respirator fit test panels representing the current Chinese civilian workers, Annals of Occupational Hygiene 2009, 53(3), pp.297-305.

Goto, L.; Lee, W.; Song, Y.; Molenbroek, J. F. M.; Goossens, R. H. M.: Analysis of a 3D anthropometric data set of children for design applications". Proceedings of the 19th Triennial Congress of the International Ergonomics Association (IEA), 2015.

Gross, M. E.; Taylor, S. E.; Mountjoy, D. N.; Hoffmeister, Jeff: Antropometric Research on the Sizing of the MBU-20/P. Wright-Patterson Air Force Base, OH: Human Effectiveness Directorate, Crew System Interface Division, AFRL-HE-WP-TR-2002-0181, 1997.

Han, D.-H.; Choi, K.-L.: Facial dimensions and predictors of fit for half-mask respirators in Koreans, American Industrial Hygiene Association Journal 2003, 64(6), pp.815-822.

Jacobson, A.; Baran, I.; Popović, J.; Sorkine-Hornung, O.: Bounded biharmonic weights for real-time deformation, Communications of the Acm 2014, 57(4), pp.99-106.

Jung, K.; Kwon, O.; You, H.: Evaluation of the multivariate accommodation performance of the grid method, Applied Ergonomics 2010, 42(1), pp.156-161.

Kohonen, T.: Self-Organizing Maps. Heidelberg: Springer, 2001.

Lee, B.; Jung, K.; You, H.: Development of a distributed representative human model (DRHM) generation and analysis system for multiple-size product design". Proceedings of the Human Factors and Ergonomics Society 57th Annual Meeting, 2013a.

Lee, W.: Development of a design methodology of pilot oxygen mask using 3D facial scan data. (Doctoral dissertation). Pohang University of Science and Technology 2013, Pohang, South Korea. Retrieved from http://postech.dcollection.net/jsp/common/DcLoOrgPer.jsp?sItemId=000001628149.

Lee, W.; Kim, H.; Jung, D.; Park, S.; You, H.: Ergonomic design and evaluation of a pilot oxygen mask". Proceedings of the Human Factors and Ergonomics Society 57th Annual Meeting, 2013b.

Lee, W.; Yang, X.; Jung, H.; You, H.; Goto, L.; Molenbroek, J. F. M.; Goossens, Richard H. M.: Application of massive 3D head and facial scan datasets in ergonomic head-product design, The International Journal of the Digital Human in press.

Luximon, Y.; Ball, R.; Justice, L.: The 3D Chinese head and face modeling, Computer-Aided Design 2012, 44(1), pp.40-47.

Meunier, P.; Shu, C.; Xi, P.: Revealing the internal structure of human variability for design purposes". Proceedings of the 17th Triennial Congress of the International Ergonomics Association, 2009.

Oestenstad, R. K.; Perkins, L. L.: An assessment of critical anthropometric dimensions for predicting the fit of a half-mask respirator, American Industrial Hygiene Association Journal 1992, 53(10), pp.639-44.

Tsoli, A.; Loper, M.; Black, M. J.: Model-based anthropometry: Predicting measurements from 3D human scans in multiple poses". Proceedings of the IEEE Winter Conference on Applications of Computer Vision (WACV), 2014.

Vesanto, J.; Alhoniemi, E.: Clustering of the self-organizing map, IEEE Transactions on Neural Networks 2000, 11(3), pp.586-600.

Winks, J. M: Clothing Sizes: International Standardization Manchester, UK: The Textile Institute, 1997.

Xi, P.; Shu, C.: Consistent parameterization and statistical analysis of human head scans, Visual Computer 2009, 25(9), pp.863-871.

Yu, Y.; Benson, S.; Cheng, W.; Hsiao, J.; Liu, Y.; Zhuang, Z.; Chen, W.: Digital 3-d headforms representative of chinese workers, The Annals of Occupational Hygiene 2012, 56(1), pp.113-22.

Zhuang, Z.; Benson, S.; Viscusi, D.: Digital 3-D headforms with facial features representative of the current U.S. workforce, Ergonomics 2010, 53(5), pp.661-671.

Zhuang, Z.; Bradtmiller, B.; Shaffer, R. E.: New respirator fit test panels representing the current U.S. civilian work force, Journal of Occupational and Environmental Hygiene 2007, 4(9), pp.647-659.

Zhuang, Z.; Coffey, C. C.; Ann, Roland B.: The effects of subject characteristics and respirator features on respirator fit, Journal of Occupational and Environmental Hygiene 2005, 2(12), pp.641-649.

Zhuang, Z.; Shu, C.; Xi, P.; Bergman, M.; Joseph, M.: Head-and-face shape variations of U.S. civilian workers, Applied Ergonomics 2013, 44(5), pp.775-84.

Lecomte et al.:
Fusion of anthropometric data and principal component analysis of the bones for generating a personalized skeleton: case of the lower limb

Lecomte, C.[1], Wang, X.[2]

[1] University of Southampton, Computational and Engineering Design Group,
   United Kingdom
[2] Université de Lyon, IFSTTAR, France

Abstract

An approach is presented and evaluated here to provide realistic internal and external dimensions of Human Body Models for a broad range of predictor values, such as, for example, to estimate the dimensions of a slightly overweight 11 year old of height 1m40. The difficulty due to lack of sufficient internal and external data is alleviated by combining widely available anthropometric measurements with more sparse databases of surface meshes of bones. Assuming that the external anthropometric measurements are estimated from the predictors through a regression, the link with the internal shape dimensions is made through the subset of target "skeletal" measurements that can be closely estimated from skeletal landmarks. The matching of internal dimensions then proceeds as follows. First the set of surface meshes of bones is aligned and a Principal Component Analysis (PCA) model of their variance compared to their mean shape is evaluated. This is done by aligning the bones, body part by body part, in such a way that the effect of posture is removed, and by evaluating the variance for the whole skeleton, so that the covariance of shapes between different bones is captured. Any subject sampled from this PCA model consists in a set of bones loosely positioned compared to each other, for particular values of the Principal Component (PC) modal magnitudes or scores. In a second step, values of these modal magnitudes are estimated in such a way that the corresponding sampled subject skeleton has dimensions that estimate closely the target skeletal anthropometric measurements. In this last step, a direct kinematic approach and a sequential quadratic programming method are used to reposition the sampled bones in an appropriate posture and to evaluate the most appropriate PC scores. The whole approach is successfully applied and evaluated on a three segment model of the lower limb.

Key words:

Internal-external, Anthropometric measurements. PCA model, skeleton mesh, lower limb

1 Introduction

Accurate geometric and mechanical models of human bodies for a wide range of types of occupants and other road users are required for vehicle crash simulation. However, while the shape of human body parts can be obtained from images of medical scans, the amount of such data available to represent any chosen human population is limited due to two main reasons. First, medical scans of a full body may not be publicly available for a wide range of the population - this is a particularly acute problem for children, and, second, the process of segmentation into body parts is currently so time consuming that a large database may only contain data concerning shapes for a few tens of partial bodies.

Due to their complexity and cost, it is not realistic to generate a full finite element human body model (HBM) that include material properties for each subject. The strategy chosen in the EU funded PIPER project (PIPER, 2017) consists of deforming one of the very few existing HBMs to match some dimensional targets. As part of that project, the work presented here consists of generating personalised target skeletal shapes that are accurately representative of a wide range of predictors within the human population.

Information from two resources is combined here in order to reach this goal. First, publicly available databases are used to estimate the anthropometric dimensions of a target subject or population. Since these measurements have been made in relatively large numbers and for a wide range of the population, estimated anthropometric dimensions can be trusted to be realistic. For example, a slightly overweight 13 year old female passenger can be sampled from a female population regression using predictors such as age and body mass index (BMI). However anthropometric measurements only represent limited information such as length and breadth of body parts. The internal skeleton remains difficult to be predicted from external measurements. One way to alleviate this issue is to use principal component (PC) analysis of the bone shape data which can be used as a second source of information.

The objective of the paper is to present such an approach of fusion of anthropometric data and principal component analysis of the bones that consists in generating a realistic personalised skeleton to match sampled external body dimensions. Here this is illustrated for the lower limb. The methods used are presented in section 2, and the application to the lower limb in section 3. This is followed by discussion and conclusion in section 4.

2   Methods

2.1   PC model of the skeleton

In the present work, the PC model of the skeleton is built from bone surface meshes segmented with the Anatoreg tools (MOREAU et al., 2016), following a semi-automatic segmentation approach adopted within the PIPER project. With data having been generated this way, the meshes of the bones are already in correspondence, meaning that they have the same number and connectivity of nodes. Anthropometric features on the same bone from different subjects can be estimated using the same nodes for all the subjects. In order to evaluate the mean shape mean and the variance of a group of bones, the bones of interest are individually aligned between all the subjects via generalized Procrustes analysis, so that the sum of all squares of distance between equivalent nodes is minimized. Grouping some bones together, such as the tibia and the fibula, allows to bypass the modelling of their relative articulation. Alignments are reached by two steps, as follows: each group of bones is first centered so that the average spatial coordinates of its mesh nodes, for any particular subject, is at the origin. These groups of bones are then aligned by generalized Procrustes (iterating one to one Procrustes of one subject's bones from the current group to the average of the corresponding bones of all other subjects).

After alignment, principal component analysis is performed by considering the mean and covariance matrices for all the aligned bones considered together, and extracting the main modes of the covariance matrix. A single covariance matrix, $\mathbf{C}$, is thus evaluated for all vertices coordinates of all bones, independent of whether they share the same group, or not. The modes or eigenvectors of this matrix with non-zero eigenvalues are the modes or principal components of shape variation. They are then normalized. Expressed in the basis of these modes, the modal magnitudes or PC scores, $\mathbf{c} = [c_1 \quad c_2 \quad ... \quad c_m]^T$, of the difference of the aligned meshes compared to the mean mesh differ for each subject. The variance of these modal magnitudes among the subjects is equal to the eigenvalues of the covariance matrix, $\mathbf{C}$, while the standard deviation, σj, of each modal magnitude, $j = 1,..., m$, is defined as the square root of its variance divided by the number m of non-zero PC scores.

The mean, modes, and standard deviation define a statistical shape model, from which sampled skeleton can be drawn, for example by estimating that the modal magnitudes are normally distributed. Due to the translations and rotations that occur during alignment, the resulting mean bones and any sampled bones from the statistical model are generally in a loose posture, as illustrated in Fig 2.1, in the sense that the relative location and orientation of the bones is relatively random and is not corresponding to a particular realistic human posture. The mean or sampled bones must therefore be assembled or positioned in a particular posture, based on positioning landmarks. This is done by using the direct kinematic model discussed in the next section.
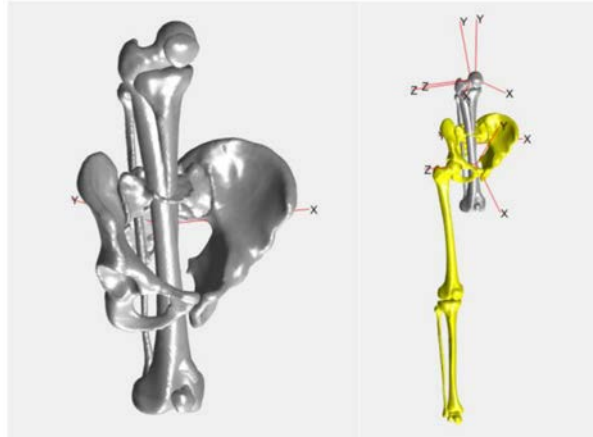
Fig 2.1 Illustration of sampled bones, before (grey) and after (yellow) articulation.

2.2   Articulated skeleton and its repositioning

The articulation of the sampled bones is necessary not only because the bones of the sampled skeletons are in a loose position, but also because most of the anthropometric dimensions are measured in a reference standing or sitting posture. For each value of the PC scores, the corresponding sampled skeletons are, therefore, assembled and articulated so that identical standing and sitting reference postures can be imposed, as illustrated in Fig 2.2. Here, this is done through a direct kinematic model whose joint and bone coordinate systems are mainly based on the ISB recommendations (WU et al., 2002, WU et al. 2005). Anthropometric dimensions can then be evaluated and compared to the target set of anthropometric dimensions, using landmarks on the bones similarly as for an actual human subject. The PC scores may then be searched as explained in section 2.4, so that the estimated skeletal anthropometric measurements approach or match the target anthropometric dimensions.

In practice, the landmarks used to measure the dimensions, as well as those used to define the coordinate systems are identified beforehand and integrated in the PC model. The details about the chosen skeletal anthropometric dimensions and landmarks for the right lower limb are described in the next section.
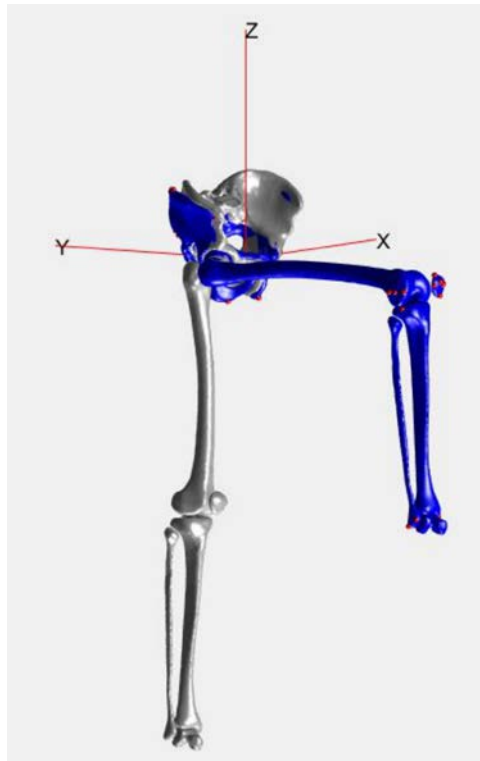
Fig 2.2 Illustration of the lower limb bone segments articulated in standing (in grey) and seated (in blue) positions

2.3 Skeletal anthropometric dimensions

As mentioned, the "skeletal measurements" are those among the external anthropometric measurements that can, in principle, be evaluated accurately on the

skeleton. For example, the stature of a standing subject could be estimated from the head vertex as far as a correct standing posture is defined, or the bispinous breadth is the width separating the right and left anterior spinous landmarks on the pelvis bone.

For the ANSUR anthropometric database (GORDON et al., 1989), selected candidate skeletal measurements for the right lower limb are presented in Table 2.1, together with the formulae to evaluate them. The skeletal landmark used in these formulae are themselves described in Table 2.2.

The postures are also reported in Table 2.1 for each measurement. Those are related to the general orientation of the subject body for which the lateral, vertical, and frontal directions are denoted respectively $\mathbf{d}_{lateral}$, $\mathbf{d}_{vertical}$, and $\mathbf{d}_{frontal}$. Since the foot bone meshes are not used, the lateral malleolar height is subtracted from measurements including the foot. For example "Crotch Height minus Lateral Malleolar Height" refers to the difference between the crotch and lateral malleolar heights.

Table 2.1 Skeletal anthropometric measurements selected from the ANSUR database and their estimation for the right lower limb. The numbers in parentheses are the measurement numbers in the ANSUR report (GORDON et al., 1989). The formulae, and posture of reference used to evaluate the measurements on a sampled subject's skeleton are also reported. The operations abs(.), norm(.), dot(.,.) indicate absolute value, two-norm, and inner product.

Skeletal Measurements	(No)	Posture	Formula
Bimalleolar Breadth	(13)	Standing	$abs(dot(\mathbf{d}_{lateral}, TMM\_R - FIML\_R))$
Bispinous Breadth	(14)	Standing	$norm(ASIS\_R - ASIS\_L)$
Crotch Height minus Lateral Malleolar Height	(38) & (75)	Standing	$abs(dot(\mathbf{d}_{vertical}, (ISTL\_R - FIML\_R)))$
Iliocristale Height minus Lateral Malleolar Height	(67)	Standing	$abs(dot(\mathbf{d}_{vertical}, IC\_R - FIML\_R)))$
Knee Height, midpatella minus Lateral Malleolar Height	(72) & (75)	Standing	$abs(dot(\mathbf{d}_{vertical}, (PCE\_R - FIML\_R)))$
Lateral Femoral Epicondyle Height minus Lateral Malleolar Height	(74) & (75)	Standing	$abs(dot(\mathbf{d}_{vertical}, (FLE\_R - FIML\_R)))$
Trochanterion Height minus Lateral Malleolar Height	(107) & (75)	Standing	$abs(dot(\mathbf{d}_{vertical}, (FTRION\_R - FIML\_R)))$
Buttock-Knee Length	(26)	Seated	$abs(dot(\mathbf{d}_{frontal}, (PSP\_R - PASA\_R)))$
Buttock-Popliteal Length	(27)	Seated	$abs(dot(\mathbf{d}_{frontal}, (PSP\_R - TPOPS\_R)))$
Knee Height, Sitting minus Lateral Malleolar Height	(73) & (75)	Seated	$abs(dot(\mathbf{d}_{vertical}, (PSUP\_R - FIML\_R)))$
Popliteal Height minus Lateral Malleolar Height	(86) & (75)	Seated	$abs(dot(\mathbf{d}_{vertical}, TPOPS\_R - FIML\_R)))$

Table 2.2 List of skeletal landmarks used to estimate the ANSUR anthropometric measurements described in Table 1.

Landmark	Body part	Description
TMM_R	(Tibia_R)	Most medial point of the right tibial malleolus
TPOPS_R	(Tibia_R)	Tibia point at the dorsal juncture of the right calf and thigh when sitting erect
ASIS_R	(Hip_R)	See(van Sint Jan,2007) p.106
ASIS_L	(Hip_L)	See(van Sint Jan,2007) p.106
ISTL_R	(Hip_R)	Lowest point of the right ilium in standing posture
ISTL_L	(Hip_L)	Lowest point of the left ilium in standing posture
ISTL_M	(Pelvis)	Average of ISTL_R & ISTL_L
ICR_R	(Hip_R)	Right iliocristale, the highest palpable point of the right iliac crest
FIML_R	(Fibula_R)	Most lateral point on the right fibular malleolus
FLE_R	(Femur_R)	Lateral-femoral-epicondyle landmark, Lateral point of the right femoral epicondyle (knee pivot point).
FTRION_R	(Femur_R)	Trochanterion, the superior point, of the greater trochanter of the right femur of a standing subject.
PSP_R	(Pelvis, Hip_R)	Most posterior point of right pelvis ilium in sitting posture
PASA_R	(Patella_R)	Most anterior point of right patella in sitting posture
PSUP_R	(Patella_R)	The superior point of the right patella. (kneecap).
PCE_R	(Patella_R)	Right midpatella, The anterior point halfway between the top and bottom of the right patella (the kneecap).
PME_R	(Patella_R)	Center of medial edge of right patella
PLE_R	(Patella_R)	Center of lateral edge of right patella
PAX_R	(Patella_R)	Apex of right patella

2.4   Matching PC scores to target anthropometric dimensions

The main step of the fusion presented here consists in matching those available target skeletal anthropometric measurements, $\mathbf{a}^{(skel)}$, to their estimation obtained from the PCA models.

The objective is thus to choose the PC scores or modal magnitudes, $\mathbf{c} = [c_1 \ c_2 \ ... \ c_m]^T$, so that, the corresponding skeletal model when repositioned in adequate posture, has estimated skeletal dimensions, $\tilde{\mathbf{a}}^{(skel)} = [\tilde{a}_1 \ \tilde{a}_2 \ ... \ \tilde{a}_s]^T$ that match closely their target values.

In loose posture, and for a specific value set of PC scores $\mathbf{c}$, the coordinates of the bones are the coefficients of the vector $\tilde{\mathbf{s}}_{(loose)}$, or simply $\tilde{\mathbf{s}} = \bar{\mathbf{t}} + \mathbf{M}\mathbf{c}$, where $\bar{\mathbf{t}}$ is the vector of mean coordinates and where each column of $\mathbf{M}$ contains the coefficients of a PC of shape variation. The direct kinematic operations (translations and rotations of the bones or groups of bones) allow to reposition the skeleton in standing or sitting postures, with coordinates $\tilde{\mathbf{s}}_{(standing)}$ and $\tilde{\mathbf{s}}_{(sitting)}$. The skeletal measurements $\tilde{\mathbf{a}}^{(skel)}_{(standing)}$ and $\tilde{\mathbf{a}}^{(skel)}_{(sitting)}$ can then be evaluated through the location of landmarks on

the skeleton placed respectively in standing and sitting postures (see section 2.2 and Table 3.1). The estimated full set of skeletal measurements, for particular values of **c**,

is therefore $\tilde{\mathbf{a}}^{(skel)} = \left[\tilde{\mathbf{a}}^{(skel)\ T}_{(standing)} \quad \tilde{\mathbf{a}}^{(skel)\ T}_{(sitting)}\right]^T$.

An optimisation approach is proposed that consists in iterating on the PC scores, so that the corresponding Euclidian distance of the estimated and target is minimised, so the optimization problem reads as:

Find **c** that minimizes $(\tilde{\mathbf{a}}^{(skel)} - \tilde{\mathbf{a}}^{(skel)^T})(\tilde{\mathbf{a}}^{(skel)} - \tilde{\mathbf{a}}^{(skel)})$ or equivalently, find **c** that

minimises $d(\boldsymbol{c}) = \sqrt{(\tilde{\mathbf{a}}^{(skel)} - \tilde{\mathbf{a}}^{(skel)^T})(\tilde{\mathbf{a}}^{(skel)} - \tilde{\mathbf{a}}^{(skel)})/s}$.

Several points are worth noting. First, the solution of this optimisation problem may not be unique if there are more PC scores to determine than the number of skeletal anthropometric measurements that one desires to match, i.e. if $m > s$. In order to remediate that, only the first $m_{opti} \leq s$ PC scores with highest standard deviation, σj, for $=1, ..., m_{opti}$, are allowed to change, while the other values are forced to be zero, $C_{m_{opti}+1} = \cdots = C_m = 0$. This is equivalent to working with the modes that are responsible for the most variance in the available shapes of bones, i.e. segmented surface meshes used to generate the PCA. Second, with this approach, information about the statistical distribution of the PC scores found in this available shape data is not really used, in the sense that a value of a PC score cj that is large relative to its standard deviation σj would be as likely as a smaller one. One knows however that larger relative values were less likely in the available data. To preserve plausibility of the PC scores, their relative values, $cj/\sigma j$ are limited between -3 and 3.

With these choices, a constraint Sequential Quadratic Programming (SQP) algorithm (NOCEDAL, 2006), as implemented in Matlab, is used to solve the constrained nonlinear minimisation problem:

Mimimise

$$d(\boldsymbol{c}) = \sqrt{(\tilde{\mathbf{a}}^{(skel)} - \tilde{\mathbf{a}}^{(skel)^T})(\tilde{\mathbf{a}}^{(skel)} - \tilde{\mathbf{a}}^{(skel)})/s} \qquad (2.1)$$

for $[c_1 \quad c_2 \quad ... \quad c_{m_{opti}}]^T$ In $\quad \mathbb{R}^{m_{opti}}$, $\qquad (2.2)$

and $c_{m_{opti}+1} = \cdots = c_m = 0,$ $\qquad (2.3)$

subject to $-3 \leq cj \leq 3$, for $j = 1, ..., m_{opti}.$ $\qquad (2.3)$

3   Application to the lower limb

The proposed fusion approach is now applied to the lower limb composed of three segments: pelvis, thigh, and lower leg (tibia, fibula, patella, and talus).

3.1   Data

The PC model of the six right lower limb bones was generated from the surface meshes of 22 subjects whose lower limb and thorax bones were segmented using Anatoreg (MOREAU et al., 2016). Altogether, the six meshes contain 88079 nodes (52109 for the Pelvis, and other 16899, 920, 11888, 3937 and 2326 respectively for the right femur, Patella, Tibia, Fibula and Talus). This resulted in the mean of the aligned three segments and in the m=21 modes of variance further described in section 3.2.

The meshes of a 23rd "LTE678" subject, segmented by the same approach and in correspondence with - but not included within - the set of 22 other subjects were also available. The bones of this subject "left-out" of the PCA model were used in the assessment of the behaviour of the fusion optimization approach, as described in section 3.3. This represents actual situations in which one would like to fit anthropometric measurements that cannot necessarily be exactly matched by samples from the PCA model. Nine skeletal anthropometric dimensions from the ANSUR database are considered. They are those described in Table 2.1, except the two popliteal measurements.

3.2   PCA of the lower limb bones

The modes, and mean, of the shape models are constructed from the 22 sets of six surface meshes. In the alignment, as well as in the articulation, the four bones below the knee are kept together in a single segment. Each of the pelvis and femur bones describes a single articulated segments. The values of the corresponding standard deviation, σj, $j = 1,\ldots, = 21$ are presented in Fig 3.1. This corresponds to 80% of the aligned meshes variance being covered by 7 modes, 90% by 11 modes, and 95% by 14 modes.
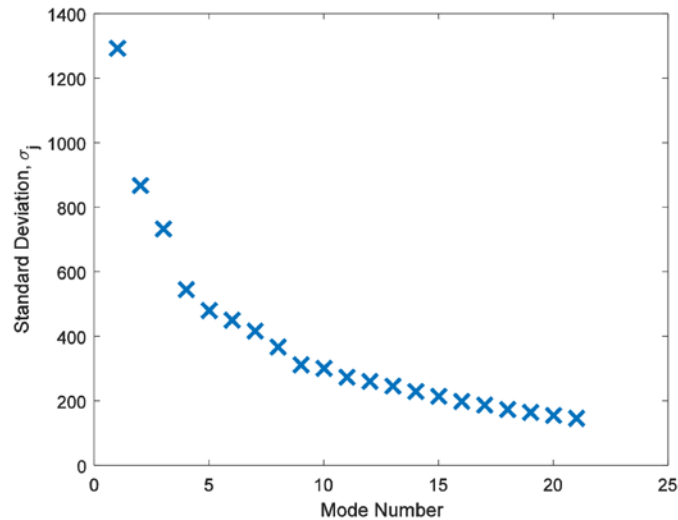
Fig 3.1 Standard deviation of the PC modes of the six bones/three segments of the Lower Limb model.

3.3 Assessment

The proposed fusion approach is now assessed. The nine LTE678 skeletal anthropometric dimensions are first evaluated. Their "exact" values are presented in Table 3.1 and compared to the corresponding values evaluated on the PCA mean subject. One can see that the lower limb (iliocristale) height of the LTE678 differs from that of the mean subject by about 7 cm.

This difference cannot be exactly reconciled by seeking an approximation of the LTE678 in the PCA model, since its shapes were not one of the 22 subjects used in the PCA model. The misfit of the LTE678 compared to the PCA models can be measured by first projecting the actual LTE678 meshes into the PCA space and by then evaluating the distance between the original and projected meshes.

Table 3.1 Anthopometric dimensions in [mm] of the LTE678 model, of its approximations though fusion, using 5 and 7 PCs ("F(5)" and "F(7)"), and those of the mean PCA model ("Mean")

Anthro. dimension	LTE678	F(5)	F(7)	Mean
Bimalleolar Breadth	57.54	60.8	58.8	60.8
Bispinous Breadth	241.58	243.1	241.0	245.7
Crotch Ht – MH.	692.07	691.2	687.8	748.3
Iliocr. Ht – MH.	887.12	895.0	889.2	954.8
Knee Ht - MH	380.26	372.7	376.4	402.5
F. Epic. Ht - MH	377.53	382.1	381.2	410.5
Troch. Ht – MH	754.65	758.0	760.3	821.7
Buttock-Knee Lth	548.88	541.0	546.3	579.4
Knee Ht – MH	403.56	397.0	399.1	426.4

The projection can be seen as the best match of the LTE678 subject in the PCA model. It can be evaluated by the algorithmic steps described in section 2.4. Most

noticeable is that one takes into consideration alignment and averaging that were used to generate the PCA models. For each mesh or group of meshes, the first step consists in the alignment of the shape with its current approximation within the PCA model, starting with the mean meshes. The mean PCA shape is then subtracted before projection in the space spanned by the modes (the LTE678 pelvis mesh is first aligned with the PCA mean pelvis mesh, etc.). The approach appears to converge quickly and to provide good approximation with a single iteration. The mean nodal distances between the aligned meshes of the projected meshes and those of LTE678 equals 3.8 [mm], and the minimal and maximal nodal distances are 0.1 and 13.6 [mm].
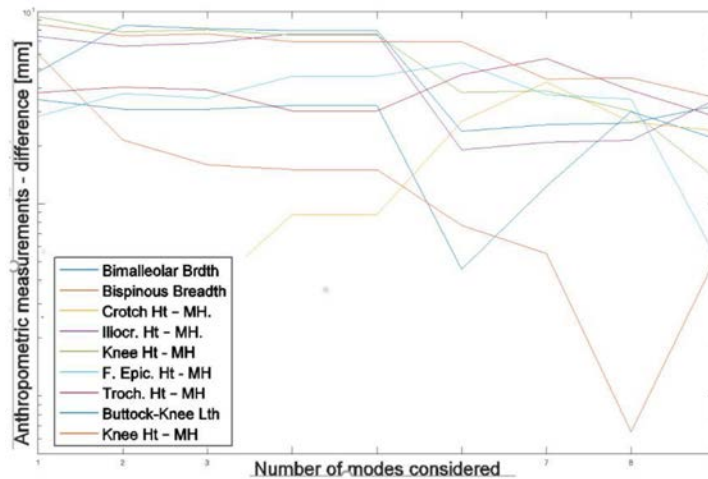

Fig 3.2 Evolution, for a varying number of PCs, of the distance between the LTE678 anthropometric dimensions and their approximation through fusion.

For the lower limb problem considered here, the optimization phase of the fusion approach takes the order of a couple minutes on a laptop. The distances between the exact LTE678 anthropometric dimensions and their approximation through fusion, using from $m_{opti} = 1$ to 9 PC scores, are presented in Figure 3.2. One can see that, by using a single PC, all differences are about 1 $[cm]$ and that these differences decrease by about one order of magnitude, when more PCs are considered. However, since there is necessarily a misfit between the LTE678 subject and the PCA model, increasing the quality of the match of the anthropometric dimensions may be at the cost of creating shapes that are unlikely and for which there exists excessive nodal distance between the original LTE678 meshes and their approximation. A moderate number, m_{opti}, of PCs compared to the number, m, of target skeletal anthropometric dimensions is therefore recommended.

The comparison of the original and approximated versions of the three lower limb segments are presented in Fig 3.5 for $m_{opti} = 7$ non-zero PC scores. The approximated shapes appear to be of reasonable quality for the purpose of crash simulation. One may nevertheless notice that some distances exist, for example, at the level of the patella. The mean and maximal differences between nodal distance of the approximations of the LTE678 meshes through fusion and either their through projection or the exact meshes are presented in Fig 3.3. Based on these metrics only, it appears that using the five first PCs provide the best approximations. Further study would be worth as the quality of the approximations might be improved by

using a larger dataset to generate the PCA model, more or better selected skeletal anthropometric dimensions. The jump in distances at $m_{opti} = 6$ might be due to the fact that an unlikely shape is being considered. This might be controlled by a better criteria in the selection of the PC scores. As a reminder, any of their values in the relative range $\sigma j = [-3,3]$ is equally allowed, while larger absolute values should be less likely based on the shape data statistics. This assumption seems to be confirmed by the values of the PC score values presented in for $m_{opti} = 1$ to 9. Looking at such plots (see Fig 3.4) also give an indication of the optimum value of $mopti$ that may be recommended. It appears nevertheless, as seen in Fig 3.5, that even results with $\sigma j = 3$ may provide reasonable models.
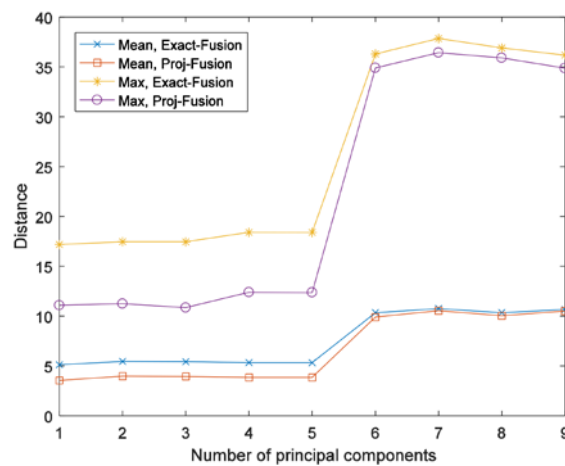

Fig 3.3 Mean and maximum nodal distances between the fusion and the exact and projected LTE678 meshes.

Additional bias may need to be considered, when dealing with anthropometric measurements coming from the ANSUR data, for example the fact that skeletal measurements are not exactly measured on the bones, and the difference between the actual human postures and their simulated versions.
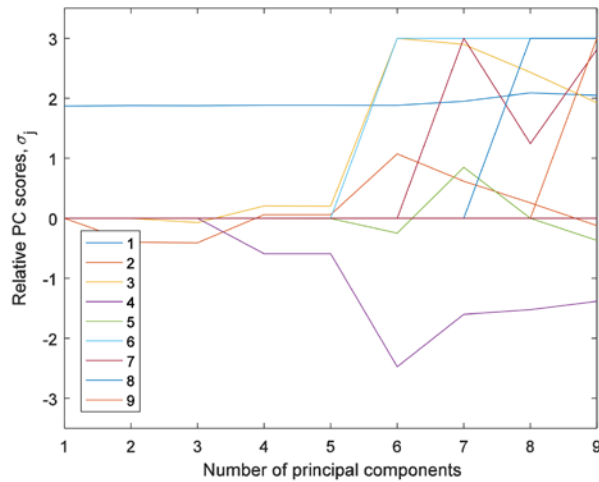
Fig 3.4 Relative PC scores for varying number of non-zero scores allowed.
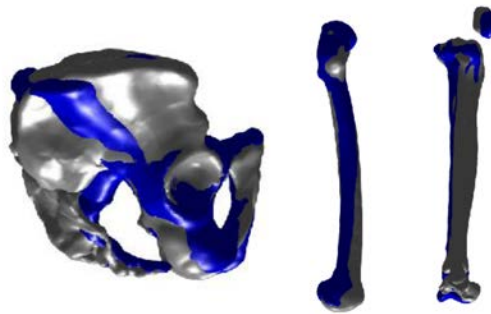
Fig 3.5 Comparison of the LTE678 Pelvis, Femur, and Leg meshes and their approximation through fusion, using 7 non-zero PC scores (in grey and blue).

4 Discussion and conclusions

The proposed fusion approach to combine external anthropometric dimensions of human body models with their internal skeletal dimensions has been successfully applied on the lower limb. The number of PC scores should be appropriately chosen, to make sure that their values stay likely. Other aspects may be worth studying, such as the effect of the quality of skeletal anthropometric measurements, and of the kinematic model used to reposition the skeleton standing and seated postures.

Acknowledgement

Jolivet and Baptiste Moreau for this, as well as Atul Bhaskar for edition of the manuscript.

List of references

Gordon, C. C.; Blackwell, C. L.; Bradtmiller, B.; Parham, J. L.; Barrientos, P.; Paquette, S. P.; Corner, B. D.; Carson, J. M.; Venezia, J. C.; Rockwell, B. M.: 2012 Anthropometric Survey of US Army Personnel: Methods and

Summary Statistics: DTIC Document. Natick/TR-89-044. US Army Natick Research Development and Engineering Center, Natick, MA. Available from the National Technical Information Service website, http://www.ntis.gov.

Moreau, B.; Dicko, A.-H.; Mailliez, P.; Portejoie, P.; Lecomte, C.; Bah, M.; Grenier, T.; Jolivet, E.; Petit, P.; Fréchède, B.: A segmentation pipeline for the creation of statistical shape models in the PIPER project. In: Proceedings of the 22nd Congress of the European Society of Biomechanics. Lyon, France (2016)

Nocedal, J.; Wright, S.: Sequential quadratic programming (pp. 529-562),.in: Numerical optimization: Springer Science & Business Media., Springer New York , 2006

Piper Project, EU PIPER project, under the European Union Seventh Framework Programme ([FP7/2007-2013]), grant agreement n°605544, www.piper-project.eu, 2104-2017. This has been followed up by the open source PIPER project, www.piper-project.org, 2017.

van Sint Jan, S.: Color atlas of skeletal landmark definitions: guidelines for reproducible manual and virtual palpations: Elsevier Health Sciences., 2007

Wu, G.; Siegler, S.; Allard, P.; Kirtley, C.; Leardini, A.; Rosenbaum, D.; Whittle, M.; D'Lima, D. D.; Cristofolini, L.; Witte, H.: ISB recommendation on definitions of joint coordinate system of various joints for the reporting of human joint motion–part I: ankle, hip, and spine. In: Journal of biomechanics 35 (2002), Nr. 4, S. 543--548

Wu, G; Van der Helm, F. C. T.; Veeger, H. E. J. D.; Makhsous, M.; Van Roy, P.; Anglin, C.; Nagels, J.; Karduna, A. R.; McQuade, K.; Wang, X.; Werner, F. W.; Buchholz, B.: ISB recommendation on definitions of joint coordinate systems of various joints for the reporting of human joint motion–Part II: shoulder, elbow, wrist and hand. In: Journal of biomechanics 38 (2005), Nr. 5, S. 981—992.

Kim et al.:
Underwater Assessments of Space Suit Reach Envelopes

Kim, H.[1], Benson, E.[2], Bernal, Y. [3], Jarvis, S.[2], Meginnis, I.[4], Rajulu, S.[4]

[1] Leidos, Inc.,
[2] MEI Technologies,
[3] Geologics, Inc.
[4] NASA Johnson Space Center

Abstract

Predicting the performance of a crewmember in an extravehicular activity (EVA) spacesuit presents unique challenges. The goal of this study is to develop a hardware and software system to evaluate the kinematic mobility of suited crewmembers, by measuring the 3-D reach envelope of the suit in an underwater environment. This study is aimed at developing quantitative metrics to compare the mobility of the existing extravehicular mobility unit (EMU) to a newly developed space suit, Z-2. Two configurations of the Z-2 space suit were evaluated: a configuration with the EMU lower torso assembly (ELTA) and a configuration with a mobile lower torso assembly (ZLTA). An underwater motion capture system was developed using commercial off-the-shelf cameras and open-source software tools. Subjects performed a prescribed set of reach motions in different suit configurations, while calibrated cameras optically triangulated the active markers held at the hand. An algorithm was developed to extract the maximal reach hand points and parametrically estimate reach envelopes. Thus far, in the preliminary analysis on a test subject in the ELTA and ZLTA configurations of Z-2, the fore-aft reach span is overall larger for ELTA as compared to the ZLTA configuration. However, the lateral reach span and horizontal rotation ranges are substantially larger in ZLTA, potentially suggesting an improved mobility and flexibility of the ZLTA configuration. Overall, the new motion capture system and reach envelope estimation methods provide usably accurate metrics to assess spacesuit mobility in the simulated microgravity environment.

Key words:

spacesuit, ergonomics, posture, biomechanics

1   Introduction

A space suit enables a crewmember to perform extravehicular activities (EVA), which typically require extensive use of the hands and upper torso. Thus decreasing the bulk of protective layers and improving kinematic flexibility and mobility are important considerations when designing a space suit. For the traditional space suit, including the extravehicular mobility unit (EMU; Figure 1.1A), which was developed in the 1980's and has been extensively used in the International Space Station and Space Shuttle programs, the design has been based on 1-D linear measurements of body shapes including stature, vertical trunk diameter, etc. With the newly developed Z-2 (Figure 1.1B), 3-D body scan and 3-D print prototyping technologies were used to improve suit fit (ROSS et al., 2014). The Z-2 suit design also includes   shoulder and lower torso joints that are intended to increase its mobility.
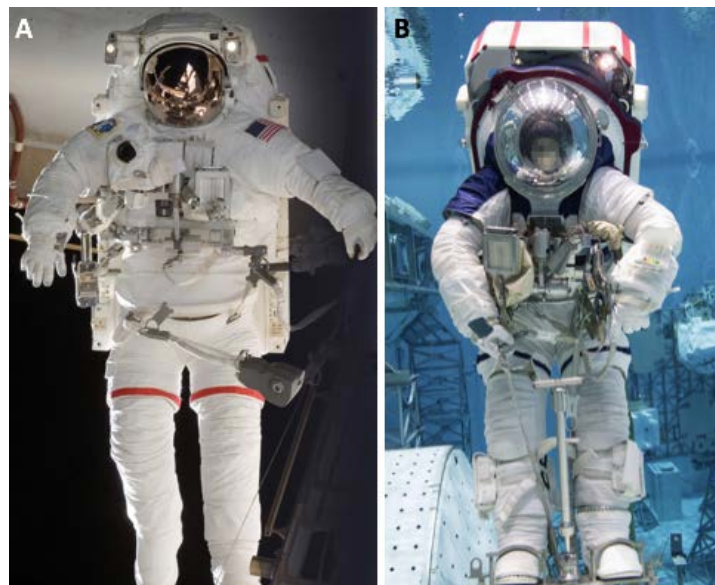
Fig. 1.1 A: Extravehicular Mobility Unit (EMU). B: Z-2

Understanding kinematic patterns and variations of motion is essential for quantifying what the suited crewmember is capable of performing in a suit. Reach boundaries and kinematics have been commonly used to assess suited and unsuited mobility (KIM et al., 2015; REED et al., 2003; WANG et al., 2011). However, the kinematic patterns in a space suit can be altered by a 1G environment, and need to be assessed in microgravity. While an underwater environment has been used for crewmembers' microgravity training, 3-D kinematics have been practically and technically difficult to quantify under water using a traditional motion capture system.

The goal of this work was to develop a hardware and software system to evaluate the kinematic mobility of suited crewmembers, by measuring the 3-D reach envelope of the suit in an underwater environment. This study was a part of the overarching work to compare the performances of the EMU and the Z-2 suit in a simulated microgravity environment at the Neutral Buoyancy Laboratory (NBL) at NASA's Johnson Space Center (JSC). The developed system provides quantitative metrics to compare the mobility performances of the suits.

2 Methods

2.1 Subjects

Seven test subjects for this study included NASA crewmembers. All subjects were familiar with pressurized suited testing, and had passed a U.S. Air Force Class III physical. Before testing, subjects signed the informed consent documents approved by the JSC's Institutional Review Board.

2.2 Equipment

The new system uses video images from multiple cameras to triangulate marker coordinates. Four off-the-shelf cameras (GoPro Hero 4, San Mateo, CA) were used, each of which was enclosed inside an underwater housing (Eye of Mine, Long Beach, CA). The cameras record video images at 1920 × 1080 resolution and at 30 frames per second. Each camera and housing combination was first calibrated to correct the optical distortions (intrinsic calibration). The images of a black-and-white checker board (122 cm × 91 cm, Figure 2.1A) were captured from a variety of perspectives underwater by a diver. The images were matched against the known geometry of the grid patterns to find the image center, focal length, and radial distortion parameters of the cameras (TSAI, 1987).
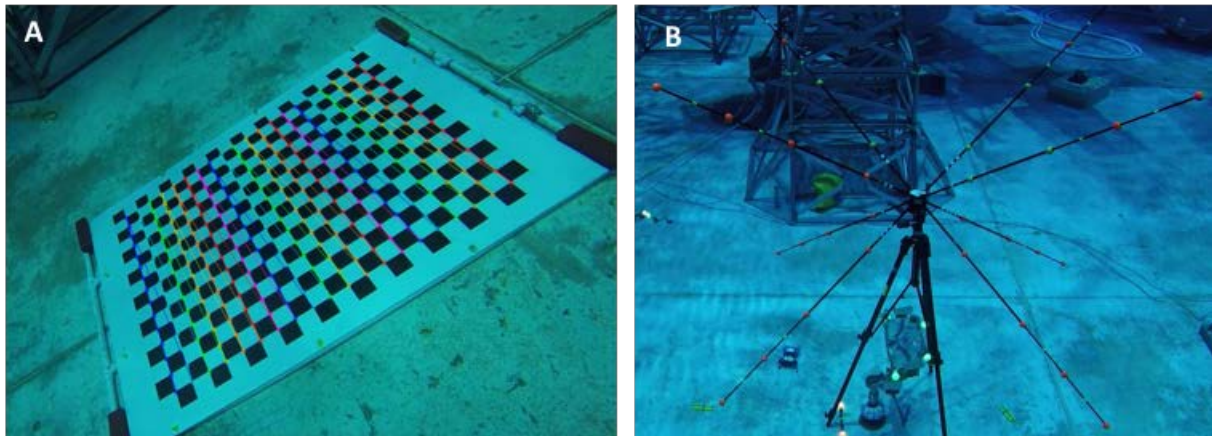
Fig. 2.1 A: Intrinsic calibration checkerboard. B: Global reference frame.

The system was deployed in the NBL, a 62 m × 31 m × 12.3 m diving tank at NASA. The cameras were mounted approximately 3.8 m above the floor of the capture volume (7.3 m × 6.7 m). The location and orientation of each camera was determined using a global coordinate reference system composed of a 1.7 m × 2.3 m × 2.0 m frame with 32 spherical markers (3.5-cm diameter each), which was placed in the capture volume center (Figure 2.1B). To synchronize all 4 cameras, a dive emergency strobe light was placed inside the capture volume.

2.3   Procedures

2.3.1   Suit Conditions

Each subject was tested in three different suit conditions including, EMU, Z-2 with EMU lower torso assembly (ELTA) and Z-2 with Z-2 lower torso assembly (ZLTA). Different suit conditions were tested on separate days. Suits were pressurized to 4 PSID. Only the Z-2 with ELTA and ZLTA configurations are considered in this report.

2.3.2   Reach Motions

The suited subject was placed on an articulating portable foot restraint (APFR), which secures the feet 80 cm above the floor. The subject was instructed to perform prescribed reach (sweep) motions as follows.

Isolated Arm Motions: The subject performed arm sweep motions at the shoulder. For each arm, vertical followed by horizontal sweeps across the body (Figure 2.2A).

Whole-Body Reach Motions:
— *Vertical sweeps* (Figure 2.2B): Sweeps from the maximum forward to the backward position with extended arms at horizontal angle 0°, 45° and maximum left and right.
— *Horizontal sweeps* (Figure 2.2C): Sweeps from the maximum right to the left position. The arms were positioned at the overhead, shoulder, waist, and below waist level.
— *Free motions* (Figure 2.2D): Subjects moved freely to cover any areas they may have missed during the previous motions.

While performing reach motions, the subject held wands (28-cm length) in one or both hands, depending on type of motion. At each end of the wand, a dive LED light was attached within a ping-pong ball diffuser (40-mm diameter). These "active" markers were to enhance visibility for pattern matching identification.
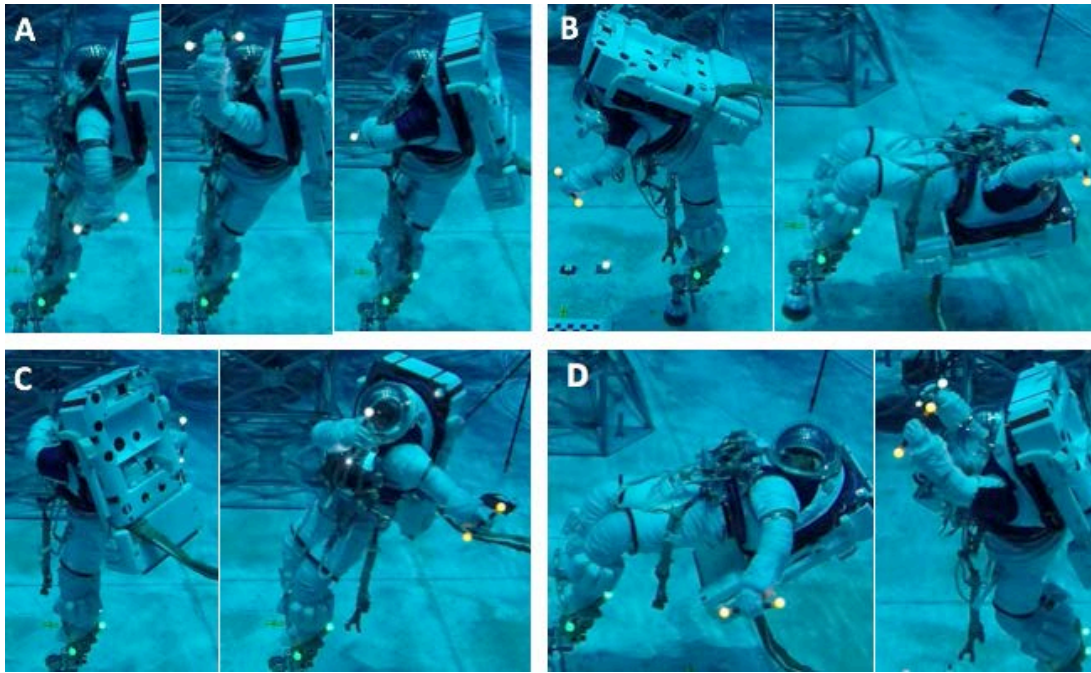
Fig. 2.2 Reach motion types. A: Isolated arm motions. B: Vertical whole-body sweep. C: Horizontal whole-body sweep. D: Free motions

2.4 Analysis and Modeling

2.4.1 Marker Tracking and Triangulation

The marker tracking algorithm was implemented on open-source software including a computer vision library OpenCV (OpenCV, 2017) and 3-D geometry authorizing tool Blender (BLENDER FOUNDATION, 2017). Specifically, the marker coordinates on the calibrated video images were identified using a pattern-matching and tracking algorithm on Blender. Then, the correspondence of 2-D image coordinates across multiple camera views triangulated the 3-D coordinates based on a Direct Linear Transform algorithm (HARLEY et al,. 2003).

2.4.2 Measurement Variables

— Hand Traces: The marker positions of the top and bottom end of the wand were averaged, representing a hand center position.
— Articulating Portable Foot Restraint (APFR): 4 LED markers placed underneath the APFR were used to triangulate the position and orientation.
— Primary Life Support System (PLSS) and Hard Upper Torso (HUT): Estimated the PLSS and HUT by the perspective and point algorithm (LEVENBERG, 1944), which estimate the pose of the rigid body object given a set of 2-D projection points in the image matched with the known 3-D coordinates.

2.4.3 Modeling

For the isolated arm motions (Figure 2.3A), hand traces in global coordinates were transformed into the PLSS/HUT-centered local coordinates. This process was done to isolate the hand traces from the accompanied PLSS/HUT motions (Figure 2.3A). For the whole-body reach motions (Figure 2.3B-D), the raw hand traces were used to

assess the maximum distances and span angles attained by the suited subjects (Figure 2.3B).

For reach envelopes, the raw hand reach traces alone do not provide point clouds that are dense enough for a reliable estimation. The hand traces were thus "permuted" by embedding isolated arm motions on the PLSS/HUT motions (Figure 2.3C). From the permuted hand point cloud (Figure 2.3D), the maximum reach points were extracted while rejecting the submaximal reach points. For this proces, the point cloud was sliced at a 5 cm horizontal (fore-aft) interval. With each slice, the points within were projected onto the frontal plane, and transformed into polar coordinates. Using an angular interval selected by a Freedman-Diaconis rule (FREEDMAN et al., 1981), the points of the maximum radial distances were determined. The resultant points constituted an outline of the maximum reach points for the given slice.

The maximum reach point outlines were then aggregated across the entire point cloud. A reach envelope was estimated by an icosphere parametrically deformed and scaled (Figure 2.3E). Specifically a finite set of control points in a radial basis function interpolation adjusted the geometry of the icosphere, in a way to minimize the surface-to-maximum reach point distances (Figure 2.3F). The vertical and horizontal sweeps and free motions were combined for reach envelope estimation. An envelope was estimated for the right and left hand separately. Only the right hand reach envelopes are considered in this report.
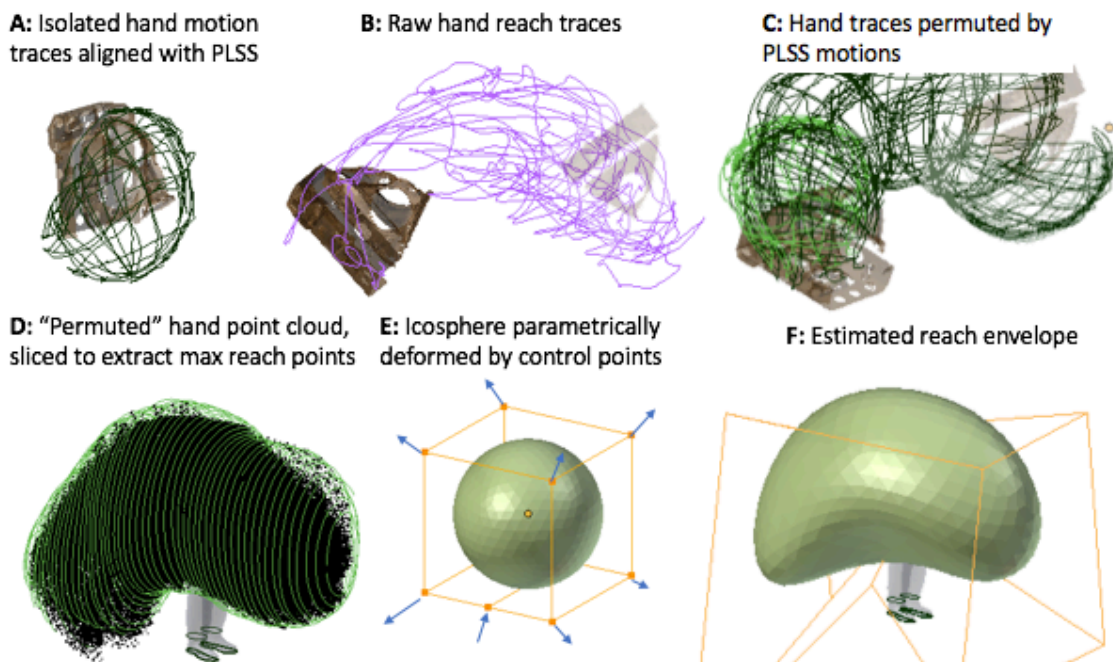
Fig. 2.3 Reach envelope estimation procedure.

3   Results

3.1   Hand Reach Traces

This report is based on the analysis on a single subject in the ELTA and ZLTA configurations of Z-2. In the whole-body vertical reach motions ("raw" traces before permutation or envelope estimation), the maximum fore-aft reach span angle is larger for the ELTA (129°) than ZLTA (119°) configuration (Figure 3.1). However, in the horizontal reaches, the lateral span is larger for the ZLTA (317°) than ELTA (255°).
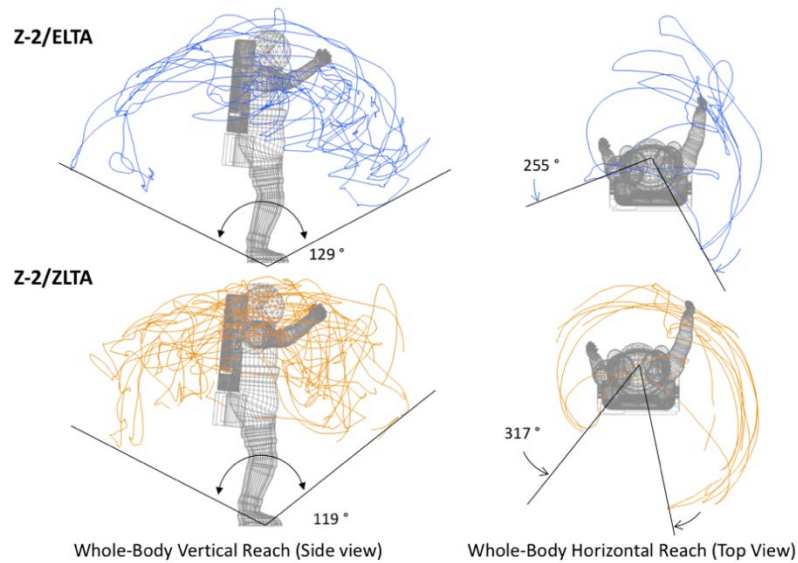
Fig. 3.1   Maximum reach span angles of the right hand. Data from one subject.

3.2   Reach Envelopes

The estimated reach envelopes of the corresponding subject (Figure 3.2; based on the permuted reach point cloud) show overall similar shapes between ELTA and ZLTA in the side view. However, the fore-aft reach span distance was larger for the ELTA (2.82 m) than ZLTA (2.47 m). In the top view, the ZLTA envelope for each arm is a round shape, while the ELTA envelope is elongated. The lateral width of the reach envelope is larger for ZLTA (2.11 m) than for the ELTA (1.95 m). Similarly, the front views show that the vertical reach spans are similar. The reach envelope volume is 3.42^3 m and 3.84 m^3 for ELTA and ZLTA, respectively. The overlap volume of the right and left hand envelopes is 1.77^3 m and 2.94 m^3 for ELTA and ZLTA.
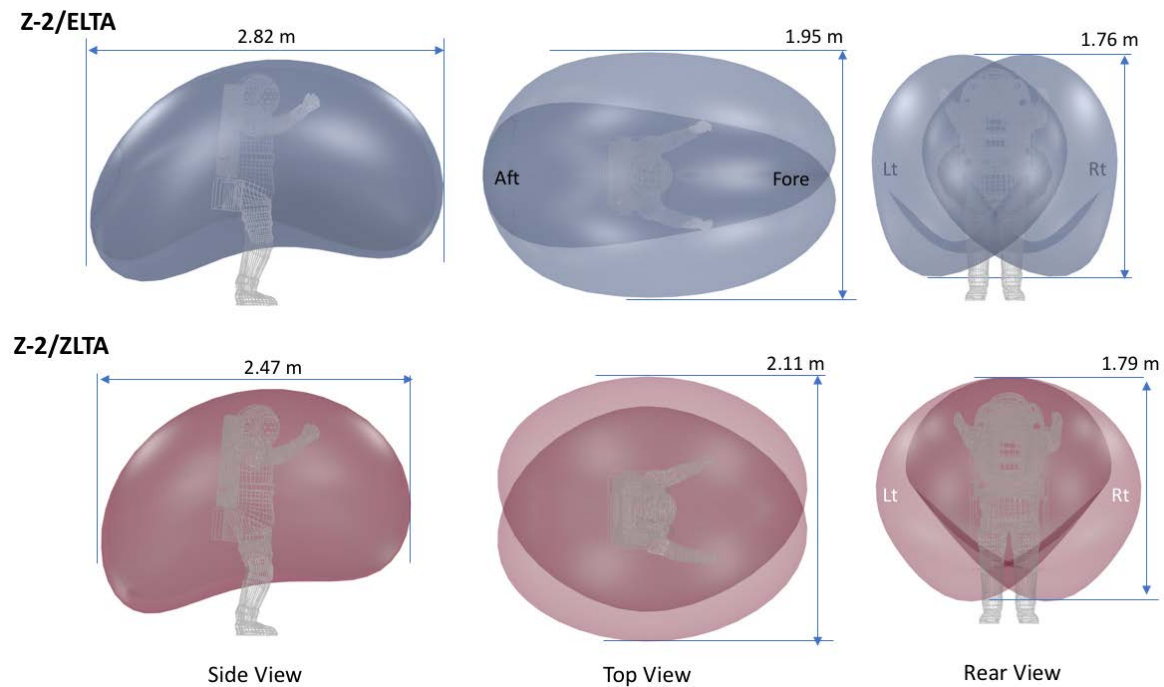
Fig. 3.2   Estimated reach envelopes of both hands. Data from one subject.

3.3   PLSS/HUT Orientation Ranges

The excursion ranges of PLSS/HUT orientations are listed in Table 3.1, as measured by the 97.5th and 2.5th percentile ranges. The sagittal flexion/extension range is larger for ELTA than ZLTA. However, ZLTA shows over two-fold larger ranges for the horizontal rotation and lateral bending angles.

Table 3.1 PLSS orientation excursion range. Data from one subject.

	Sagittal Flexion/Extension	Horizontal Rotation	Lateral Bending
ELTA	167 °	75 °	53 °
ZLTA	147 °	151 °	25 °

4   Discussion

The goal of this study was to develop a hardware and software system to evaluate the kinematic mobility of suited crewmembers, by measuring the 3-D whole-body reach envelopes in an underwater condition. Previously, a computer model generated simulated unsuited microgravity reach envelopes using the anthropometry samples of 192 male astronaut candidates measured in 1979 and 1980 (NASA, 1995). In a different study, underwater suit mobility assessments were performed by manually marking the hand traces on a 2-D grid board placed at intervals (KLAUS et al., 1989). However, with this new system, more naturalistic 3-D motions can be captured at reduced time and cost. Using this new motion capture method and assessment technique, the maximum reach capacity and reach envelopes of the space suit can be evaluated in a simulated microgravity environment.

An optical triangulation technique has been used for underwater archaeology (WEHKAMP et al., 2014) and marine biology survey (SHORTIS, 2015). Unlike common "dry land" motion capture systems, infrared lighting or structured-light based depth camera system may not be appropriate due to absorption and scattering in water (BIANCO et al., 2013; CHAPLIN, 2016). Thus, this system used an active LED marker system to improve detectability in the underwater environment, improving marker-tracking accuracy significantly. The system provides a level of accuracy adequate for the context of suit performance testing measuring "gross" motion trajectories, although different applications require a higher precision level. A separate study reported the measurement error of this system as 1.90 cm on average (BERNAL et al., 2017).

Reach envelope estimation in this study was based on a novel technique to permute the hand reach traces by the PLSS/HUT motions and suppress the sub-maximal reach points using a polar-histogram and cross-section outlining technique. The reach envelope estimated by a parametrically deformed icosphere provided a reasonably accurate representation of reach point cloud. However, the permuted point clouds (Figure 2.3) do not provide the information about kinematic characteristics inside the maximum reach volume. However, the "raw" reach traces (Figure 3.1) provide complementary information, including the reach span angle of the right hand in the horizontal plane.

The raw hand reach traces and estimated reach envelopes revealed the mobility differences between the suit conditions. Although the analysis is based on a single test subject, Z-2 with the ELTA configuration shows larger reach spans in the fore-aft direction, while the ZLTA configuration shows larger span distance in the lateral (left-right) direction and horizontal rotation angle. This observation is in agreement with the PLSS/HUT excursion ranges, which show the larger horizontal rotation and lateral bending angles in ZLTA. PLSS/HUT motions are largely determined by lower torso assembly flexibility and mobility, which potentially suggest more naturalistic kinematic patterns in torso and lower extremity motions for suited crewmembers in ZLTA.

Overall, the new method reported in this study can be used in different ergonomic environments using simple off-the-shelf equipment that are ready to use. The

validation of this new motion capture system proved it to be a usably accurate source for motion capture data collection and analysis.

List of references

Bernal, Y.; Kim, K. H.; Benson, E.; Jarvis, S.; Meginnis, I.; Rajulu, S.: Development of Underwater Motion Capture System for Space Suit Mobility Assessment, Human Factors and Ergonomics Society Conference, Manuscript accepted for publication, 2017.

Bianco, G.; Gallo, A.; Bruno, F; Muzzupappa, M: A comparative analysis between active and passive techniques for underwater 3D reconstruction of close-range objects, Sensors, 2013, 13(8), pp.11007–11031.

Blender Foundation: Blender - a 3D modelling and rendering package. URL https://www.blender.org/, 2017.

Chaplin, M: Water absorption spectrum. URL http://www1.lsbu.ac.uk, 2017.

Freedman, D.; Diaconis, P.: On the histogram as a density estimator:L 2 theory, Probability Theory and Related Fields 1981, 57(4), pp. 453–476.

Kim, K. H.; Jones, M. L. H.; Ebert, S.; Reed, M. P.: Effects of protective equipment and body borne gear on seated maximum reach envelopes, Proceedings 19th Triennial Congress of the IEA, 2015, 9(14).

Klaus, D. M. ; West, P. R.: Performance evaluation of advanced space suit concepts for Space Station, SAE Technical Paper, 1989, 89151.

Levenberg, K.: A method for the solution of certain non-linear problems in least squares, Quarterly Journal of Applied Mathmatics, 1944, 2(2), pp.164-168.

National Aeronautics And Space Administration: Man-System Integration Standards NASA-STD-3000, 1995, Rev B.

OpenCV: Open Source Computer Vision Library. URL http://opencv.org/ 2017.

Reed, M. P. ; Parkinson, M. B. ; Klinkenberger, A. L.: Assessing the validity of kinematically generated reach envelopes for simulations of vehicle operators, SAE Technical Paper, 2003.

Ross, A.; Rhodes, R.; Graziosi, D.; Jones, B.; Lee, R.; Haque, B. Z. ; Gillespie, J. W.: Z-2 Prototype Space Suit Development, 44th International Conference on Environmental Systems, 2014.

Shortis, M.: Calibration Techniques for Accurate Measurements by Underwater Camera Systems, Sensors 2015, 15(12), pp.30810–30826.

Tsai, R.: A versatile camera calibration technique for high-accuracy 3D machine vision metrology using off-the-shelf TV cameras and lenses, IEEE Journal on Robotics and Automation 1987, 3(4), pp.323-344.

Wang, X.; Trasbot, J.: Effects of target location, stature and hand grip type on in-vehicle reach discomfort, Ergonomics, 2011, 54(5), 466-476.

Wehkamp, M.; Fischer, P.: A practical guide to the use of consumer-level digital still cameras for precise stereogrammetric in situ assessments in aquatic environments, Underwater technology, 2014, 32(2), pp.111-128.

Miyata et al.:
An interactive assessment of robustness and comfort in human grasps

Miyata, N.[1], Honoki, T.[2], Sugiura, Y. [3], Maeda, Y.[2]

[1] Digital Human Research Group, Human Informatics Research Institute, National Institute of Advanced Industrial Science and Technology, Tokyo, JAPAN;
[2] Yokohama National University, Kanagawa, JAPAN;
[3] Keio University, Kanagawa, JAPAN

Abstract

This paper presents a system that interactively assesses the quality of grasping of an object while someone grasps the object in his/her bare hand. Many previous studies presented various methods for assessing grasps, but most are used for simulation and post-assessment. These methods are unsuitable for interactively assessing the usability of products. This report shows an interactive system that measures and assesses human grasps by a band sensor with distance sensors aligned in line. The proposed system assesses robustness and comfort of measured human grasps on-line. The effectiveness of the proposed system was verified in a simulation and a physical experiment.

Key words:

digital hand, grasp quality assessment

1   Introduction

To quantitatively assess usability of a handheld product, it is useful to measure the actual behavior of humans using the product and analyze reconstructed measured grasps with a digital hand model on a computer. By using commercially available systems, these processes (measurement, reconstruction, and analysis) can be executed one by one, which means it takes a while to reflect some findings from the measurement to change design. For example, an optical motion capture (MoCap) system is often used for measurement. The MoCap system is superior in terms of accurate measurement but requires many markers to be attached on the hand, which encumbers natural behavior. In addition, it requires time-consuming manual marker labeling, which is necessary to convert its position data into posture data to be assessed. However, if on-site natural behavior can be measured and grasp quality metrics can be used interactively then and there, the product design cycle is expected to be changed and accelerated: users of the product can freely try various way of grasping, and designers can test their ideas by observing actual users' reactions with quantitative assessment data.

This study, therefore, aims at developing an interactive assessment system for bare-hand grasping. To measure a grasp of an object by a bare hand, a "Wrap & Sense" system (MIYATA et al., 2016) is extended so that sensor density increases. To assess product usability, we focus on robustness and comfort of the grasp and implement indices that suit interactive calculation. The proposed system is validated through physical experiments.

2   Methods

2.1   Grasp measurement system: Wrap & Sense

For bare-hand grasp observation, several systems have been developed that use RGB-D camera(s) or color video images (e.g. WANG et al. 2013). As cameras are assumed to be fixed in the environment, such systems are not robust to environmental changes including changes in location of the user's body and the target object. Wrap & Sense can avoid this occlusion problem by attaching band-style sensor equipment on the object so that it detects the side edge of the hand.

A profile of the Wrap & Sense system used in this study is shown in Figure 2.1. The band-style sensor equipment was comprised of 16 infrared distance sensors. All the distance sensors were directed in parallel along the object surface, and each measured the distance between itself and a point on the side edge of the hand from the thumb tip to the index finger. By using a 3D model of the target object with the location and direction definition of each sensor, each distance was converted into a position of the detected point. The detected points were used to estimate the plausible location of each feature point defined on the hand model. The subject's hand model was generated by deforming a generic model through an optimization to satisfy 40 hand dimensions estimated from four directly measured dimensions: hand length, hand width, and breadth and a depth of the middle finger's proximal

interphalangeal joints (NOHARA et al., 2016). The whole hand posture was reconstructed by minimizing distances between corresponding points, resulting in the aligned hand model.

Compared with the original Wrap & Sense system, a smaller distance sensing module (Sharp Corporation, GP2Y0E02A) was used, and the number of sensors was increased for higher sensor density.
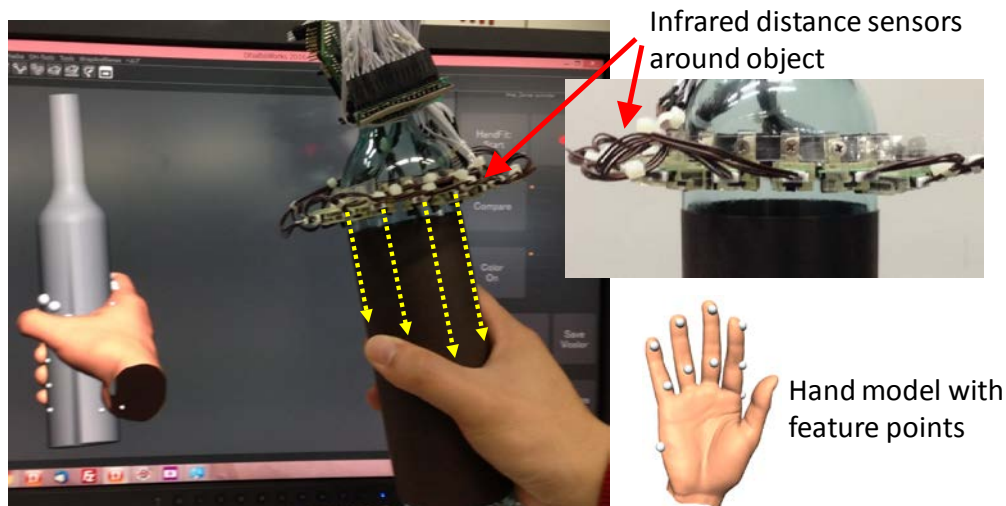

Fig. 2.1   Profile of Wrap & Sense system used in this study

2.2   Assessment indices for grasp: robustness and comfort

Grasp quality indices were originally developed in robotics (SHIMOGA, 1996) but have been gradually extended to human grasps (LEON et al., 2012; KANAI et al., 2014). As these metrics were for offline assessment and were not necessarily suitable for interactive assessment, two indices were developed and implemented here to assess robustness and comfort in human grasps. On implementation, contact between the hand and an object was modeled as a set of point-contacts with friction. The contact region was derived using surface vertices of a hand model and point clouds generated on an object model.

The robustness of the grasp was defined as the resistant capability of contact forces and known external forces (e.g. gravity) against unknown disturbing force and torque (MAEDA, et al., 1996). As shown in Figure 2.2, this corresponded to a derived radius of a six-dimensional inscribed hypersphere in the wrench space with its center located at the known external force and torque. At each contact point, the generable resistant force can be expressed as a friction cone assuming Coulomb friction. To reduce computational cost, each friction cone was approximated as a regular pyramid when considering wrench space, and the six-dimensional inscribed hypersphere was approximated as a hyperpolyhedron with a finite number of vertices. Then the robustness index (approximated radius of the inscribed hypersphere) was calculated by solving linear programming problems.

As for the grasp comfort index, we consider "maximum pain" by using the maximum contact pressure and "muscle load" by using the ratio of the generated force by each link to its maximum generable force. The comfort index was calculated by solving a linear programming problem that minimized the weighted summation of the maximum ache and muscle load terms.
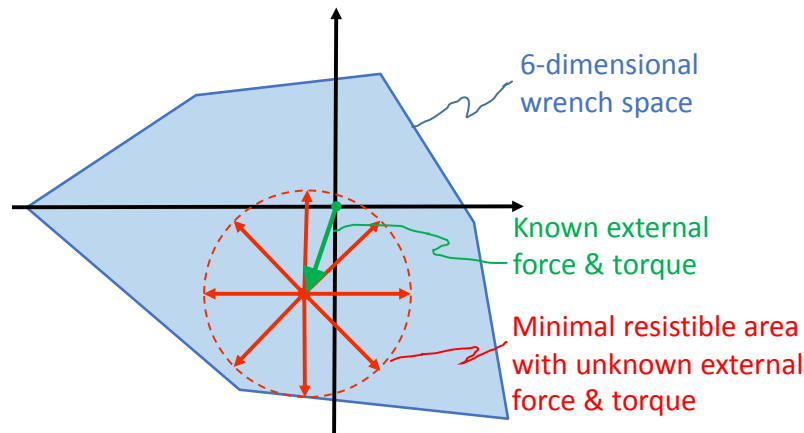
Fig. 2.2   Two-dimensional schematic view of proposed grasp robustness index

3   Experimental Results

The validity of the proposed system was tested through two experiments. The friction coefficient in both experiments was set to 0.3.

3.1   Assessment indices validation

First, a simulation experiment was conducted to test the validity of the implemented quality indices by showing the difference in accordance with the object shape. Seven different prisms shown along the top of Figure 3.1 were tested that had a cross-sectional shape (hexagram) with the same circumradius (30 mm) but different vertex angles from 0 deg (acutest hexagram) to 120 deg (hexagon). The same hand posture that was captured by the MoCap system was used for the grasp of all the objects. In the right side of Figure 3.1, the grasp of the prism with vertex angle at 100 deg is shown. A 5 N gravitational force along a longitudinal axis (downward to the wrist adduction direction) was given as a known external force.

Figure 3.1 shows the calculated indices' values. The robustness index is better when larger, and the comfort index is better when smaller. For the comfort index, better scores at obtuse vertex angles than at acute ones were considered to be natural in terms of the human preference to avoid aches. For the robustness, better scores at obtuse vertex angles were considered to be natural because they offer a larger contact area. These intuitively-natural tendency indicated the validity of the proposed indices for grasp assessment.

Fig. 3.1   Robustness and comfort indices according to object shape

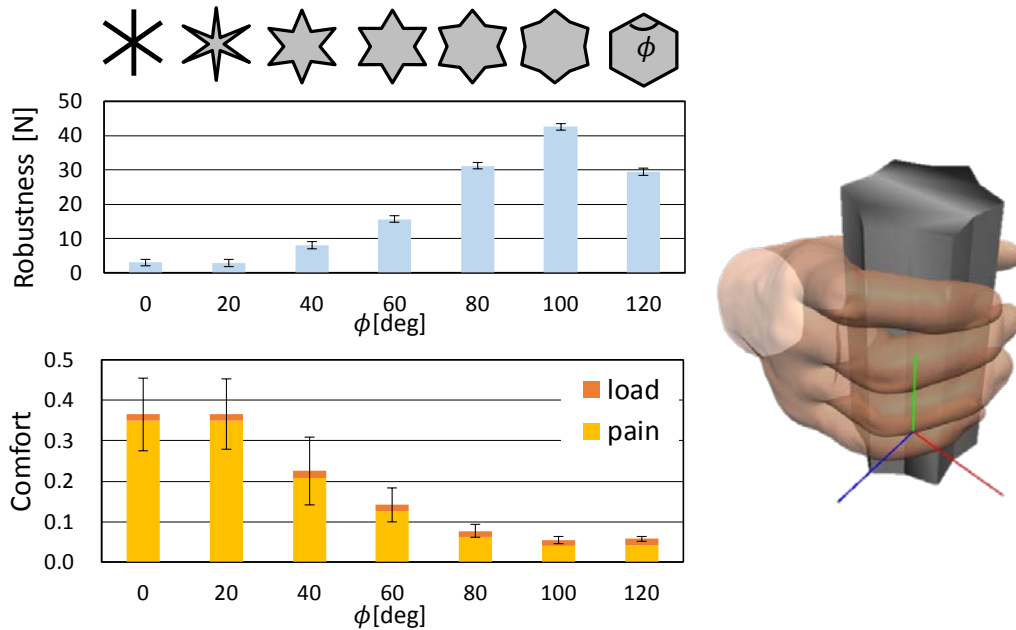## 3.2 Feasibility validation of interactive grasp assessment system

Feasibility of the proposed system in terms of interactivity was tested through a physical experiment to assess grasps of a bottle equipped with the Wrap & Sense sensor system. Two grasping locations (postures 1 and 2) in Figure 3.2 were captured and compared. In the indices calculation, 10 N force along a longitudinal axis of the object (downward to the wrist adduction direction) was given at the center of gravity of the object as a known external force (gravity).

In Figure 3.2 (a) and (b), reconstructed postures are shown in the right side, respectively. In each figure, a hand model in flesh color means a captured result by the proposed system and that in red means a result by a MoCap system. The proposed system reconstructed the actual system well.

According to the calculated indices shown in Figure 3.3 (a) and (b), posture 1 scored better in both indices. This was natural considering the relative configuration of the hand with the center of gravity of the object because posture 1 was closer to the center of gravity of the object than posture 2.

Figure 3.3 (c) shows the computation time consumed for each index. The proposed system was executed on a 64-bit personal computer (Intel® Core™ i7-3920XM 2.90GHz). The robustness index calculation sometimes took a rather long time, such as 3000 ms. This calculation time could be reduced by thinning the density of points generated on the object model for contact region derivation or decreasing the robustness estimation accuracy. The system could then be considered to be interactive.

(a) Posture 1   (b) Posture 2
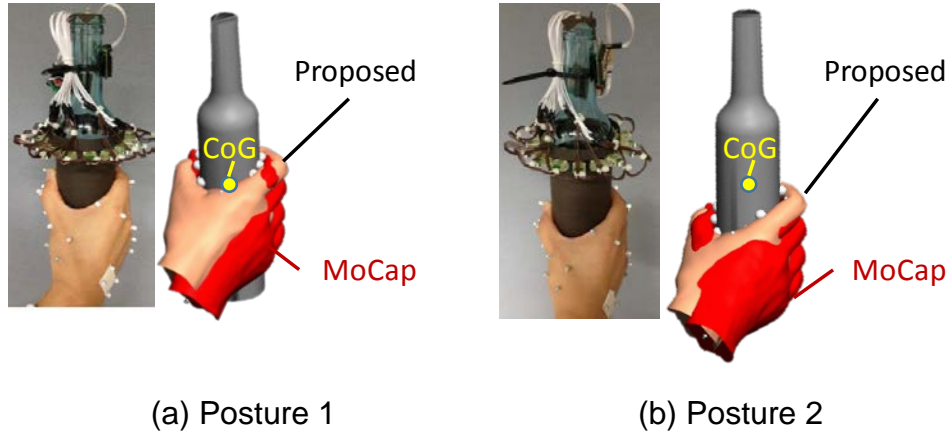
Fig. 3.2   Compared postures in system feasibility validation experiment

(a) Robustness   (b) Comfort   (c) Computation time
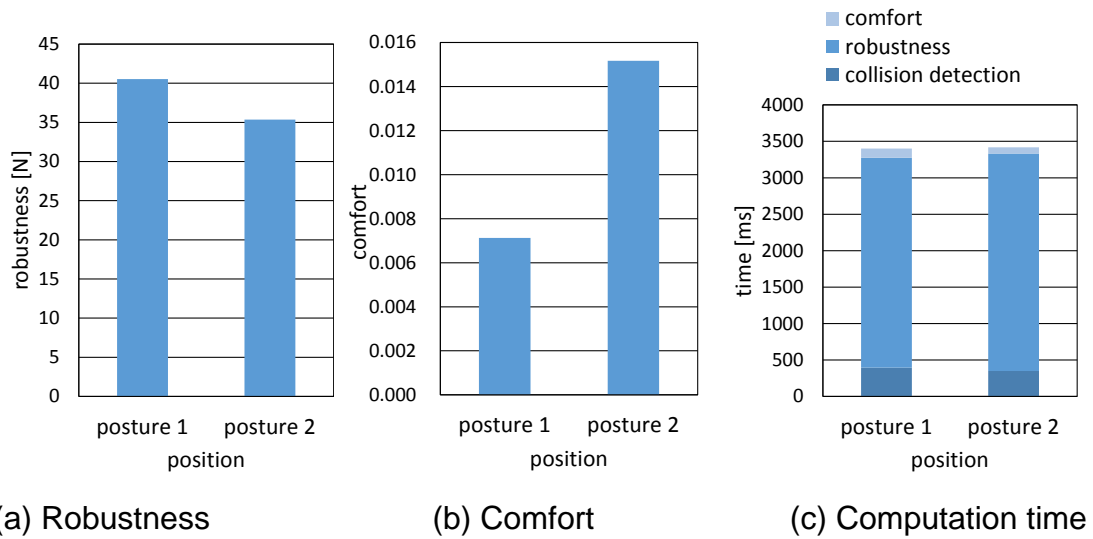
Fig. 3.3   Proposed assessment indices and computation time

4   Conclusion

This paper presented an interactive grasp assessment system. In addition to extending the previously developed Wrap & Sense measurement system by increasing the sensor disposition density, grasp robustness and comfort indices were developed and implemented with the system and validated through a simulation and a physical experiment.

List of references

Kanai, S.; Xie, Y.; Date, H.: Estimating Grasp Comfort using 3D Geometric and Musculoskeletal Models of the Human Hand, in Proceedings of the 3rd International Digital Human Modeling Symposium, Tokyo, May 2014, Paper #37.

León, B.; Sancho-Bru, J L.; Jarque-Bou, Néstor J.; Morales, Antonio; Roa, Máximo A.: Evaluation of Human Prehension Using Grasp Quality Measures, International Journal of Advanced Robotic Systems 2012, Vol. 9, Article Number 112.

Miyata, N.; Honoki, T.; Maeda, Y.; Endo, Y.; Tada, M.; Sugiura, Y.: Wrap & Sense: Grasp Capture by a Band Sensor, in Adjunct proceedings of the 29th Annual Symposium on User Interface Software and Technology, Oct. 2016, pp. 87-89.

Maeda, Y.; Aiyama, Y.; Arai, T.; Ozawa, T.: Analysis of Object-Stability and Internal Force in Robotic Contact Tasks, in Proceedings of IEEE/RSJ International Conference on Intelligent Robots and Systems, Nov. 1996, pp. 751-756.

Nohara, R.; Endo, Y.; Murai, A.; Takemura, H.; Kouchi, M.; Tada, M.: Multiple Regression based Imputation for Individualizing Template Human Model from a Small Number of Measured Dimensions, in Proceedings of the 38th Annual International Conference of the IEEE Engineering in Medicine and Biology Society 2016, Aug. 2016, pp.2188-2193.

Shimoga, K. B.: Robot Grasp Synthesis Algorithm: A Survey, The International Journal of Robotics Research, Vol. 15, No. 3, 1996, pp. 230-266.

Wang, Y.; Min, J.; Zhang, J.; Liu, Y.; Xu, F.; Dai, Q.; Chai, J.: Video-based Hand Manipulation Capture Through Composite Motion Control, ACM Transactions on Graphics (TOG) - SIGGRAPH 2013 Conference Proceedings 2013, Vol. 32, Issue 4, Article Number 43.

Technical Session 5 – Anthropometry and Biomechanics II & DHM validation methods

Lei et al.:
Application of Digital Human Modeling for Evaluating Loose-Fitting Powered Air-Purifying Respirators

Lei, Z., Zhuang, Z., Bergman, M.

National Institute for Occupational Safety and Health, National Personal Protective Technology Laboratory, Pittsburgh, PA 15236, USA

Abstract

Interest in loose-fitting powered air-purifying respirators (PAPRs) is increasing among healthcare workers, especially to reduce exposure to high-level respiratory pathogens and infectious body fluids. This study applied digital human modeling to evaluate loose-fitting PAPRs. Digital headform models were constructed with the biomechanics of breathing to simulate the performance of loose-fitting PAPRs on the headform using computational fluid dynamics (CFD) simulations.

The medium-size digital headform model, developed by the National Institute for Occupational Safety and Health, was used to simulate the wearer of a PAPR. To create a digital loose-fitting PAPR, a 3D-scanner captured the geometries of the components of a commonly-used PAPR. Cyclic breathing air flows (having both exhalation and inhalation) with minute ventilations of 35, 55, and 85 L/min were applied at the opening of the mouth, simulating light, moderate, and heavy workloads. For each of the three breathing workloads, PAPR supplied-air flow rates (85, 115, 145, 175, and 195 L/min), were introduced into the PAPR breathing zone at the supplied-air venting outlets located near the headform forehead. The challenge particles, which were the particles outside of the PAPR breathing zone, were introduced at the loose-fitting area where the PAPR loosely fits the headform. The particle concentration of the inhalation air flow at the opening of the mouth was calculated to derive the manikin protection factors (mPFs), the ratio of the challenge particle concentration to the inhalation particle concentration.

The smaller estimated mPFs were found at heavier workloads and lower supplied-air flow rates. At the moderate workload and supplied-air flow rate of 85 L/min, the estimated mPF was 31.8; at the heavy workload with supplied-air flow rates of 85, 115, and 145 L/min, the estimated mPFs were 6.6, 10.6, and 43.1, respectively. For the remaining 11 combinations of workloads and flow rates, the estimated mPFs were > 10,000. Simulation results indicate that the velocity distribution, pressure distributions, and streamlines changed instantaneously during breathing cycles. The particle distributions inside the inlet covering were not homogeneous (i.e., the majority of the leaking particles appeared in the region between the mouth and the loose-fitting area at the neck). This application can potentially assist respirator manufacturers for new product designs.

Key words:

powered air-purifying respirators, CFD, manikin protection factors

1 Introduction

Interest in loose-fitting powered air-purifying respirators (PAPRs) is increasing among healthcare workers, especially to reduce exposure to high-level respiratory pathogens and infectious body fluids. A loose-fitting PAPR uses a battery-operated blower and HEPA filters to provide the wearer with purified air through a loose-fitting hood or a helmet. Loose-fitting PAPRs are comfortable and are an attractive option because they do not require fit testing (ROBERGE 2008). Also, some loose-fitting PAPR hoods fully cover the wearer's head and neck to prevent contact with body fluids from an infected person. Hence, loose-fitting PAPRs are recommended for use by healthcare workers (HCWs) during high-risk aerosol-generating procedures. As summarized in a recent paper, use of PAPRs by HCWs is believed to be increasing (WIZNER et al. 2016).

The U.S. Occupational Safety and Health Administration (OSHA) requires that PAPRs used in regulated workplaces be approved by the National Institute for Occupational Safety and Health (NIOSH). The NIOSH approval requirements for loose-fitting PAPRs include an isoamyl acetate (IAA) fit test, a test of air flow, which measures the minimum air flow rate, maximal operational flow rate, and noise level (42 CFR Part 84). Loose-fitting PAPR models currently available on the market have some design limitations (to varying degrees), such as battery duration or overall bulkiness of the unit, which may limit their usability. PAPRs are still considered by some users to be too heavy and noisy, especially in healthcare settings. If PAPRs with lower flow rates could be designed to provide effective protection, they could use a smaller blower and battery to create a smaller pressure gradient, thus making them quieter and lighter (MCCOY et al. 2015), as long as the flow rate was adequate to provide for safe operation of the device.

The filtered air was supplied to a PAPR respiratory inlet covering (i.e., hood or helmet) to prevent the infiltration of contaminated ambient air. However, the PAPR may be over-breathed at heavy workloads (SINKULE et al., 2016). The supplied air flow rates of loose-fitting PAPRs are in the range of 170-206 L/min (MARTIN, MOYER, and JENSEN 2006), while peak inhalation flows of adults exercising at heavy workloads can be 255 L/min (ANDERSON et al. 2006). The PAPR user may require a higher inhalation flow rate than can be supplied, possibly resulting in a negative gauge pressure inside the face piece and a consequent of leakage of contaminants.

Limited studies have addressed the particle leakage in loose-fitting PAPRs. In (GAO et al. 2016), for example, the study investigated the protection levels offered by improperly sized PAPR hoods using various breathing conditions that included cyclic flows with mean inspiratory flows of 30, 55, 85, and 135 L/min for the light, medium, high, and strenuous workloads. Low protection factors were found at the high and strenuous workloads. None of these studies, however, investigated the effect of the supplied air flow rates on the performance of loose-fitting PAPRs.

Digital human modeling has provided an alternative approach to evaluating factors such as breathing rate and tidal volume on the performance of N95 filtering face piece respirator (e.g., LEI and YANG 2014; LEI et al. 2012). Using a Computational Fluid Dynamics (CFD) method, respirator performance can be simulated using digital

models of human head and respirator geometries. None of the existing literature on digital human modeling involved loose-fitting PAPRs.

This is the first study known to apply digital human modeling to evaluate loose-fitting PAPR performance. Digital headform models were constructed with the biomechanics of breathing to simulate the performance of loose-fitting PAPRs on a headform using CFD simulations. The effects of breathing workloads and supplied air flow rates on the PAPR's performance were determined.

2 Methods

The simulation-based study for loose-fitting PAPRs involved creating digital geometrical models of a headform and loose-fitting PAPR, defining a mathematical model for the headform and PAPR together, performing simulations to evaluate the PAPR at various conditions, and finally post-processing the resultant flow and pressure data.

2.1 Geometry Models

The medium-size digital headform, which was developed by NIOSH and represents approximately 50% of the current U.S. workforce (ZHUANG, BENSON, and VISCUSI 2010) (BERGMAN et al., 2014), was used to simulate the wearer of a PAPR. As a geometry model, the digital headform was a polygon surface containing thousands of small triangles to express geometrical features of the human face. We tailored the digital head form by constructing a breathing airway (simulated trachea) so that that breathing air would pass through the mouth and in and out of the airway during CFD simulations (Figure 2.1). The breathing airway was in the shape of a straight cylindrical tube with 2 cm diameter and 10 cm length; its one end was an opening, while its other end connected to the headform's mouth.
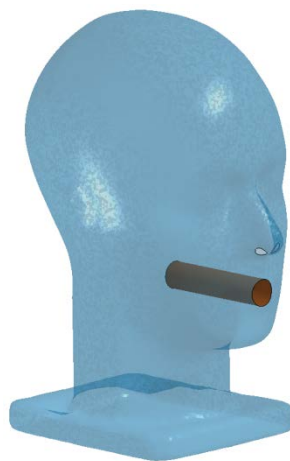

Fig. 2.1 Digital headform model having a breathing airway

For creating a digital loose-fitting PAPR, a 3D scanner captured the geometries of the components of a commonly-used PAPR (model: MaxAir® 78SP-36 cuff system, Bio-Medical Devices, Inc., Irvine, CA). The components included a helmet with a cuff fitting at the neck dam. The 3D scanner outputted the digital PAPR components as

polygon surfaces. However, it contained artifacts such as spurious holes in the digital model of the PAPR. Surface regions were repaired using the automated alignment of point clouds, reduction of overlap, intelligent filtering, and smoothing algorithms, which were geometrical processing functions provided in Polyworks software (InnovMetric Software Inc., Québec, QC Canada). The surface repairing was an iterative and time-consuming process. In each iteration of repair, we manually selected one problematic region and applied geometrical processing functions for improving surface quality. Finally, the PAPR components were assembled as a PAPR system and were virtually donned on the headform (Figure 2.2).

3D Scanning

Medium Size Headform Dons PAPR
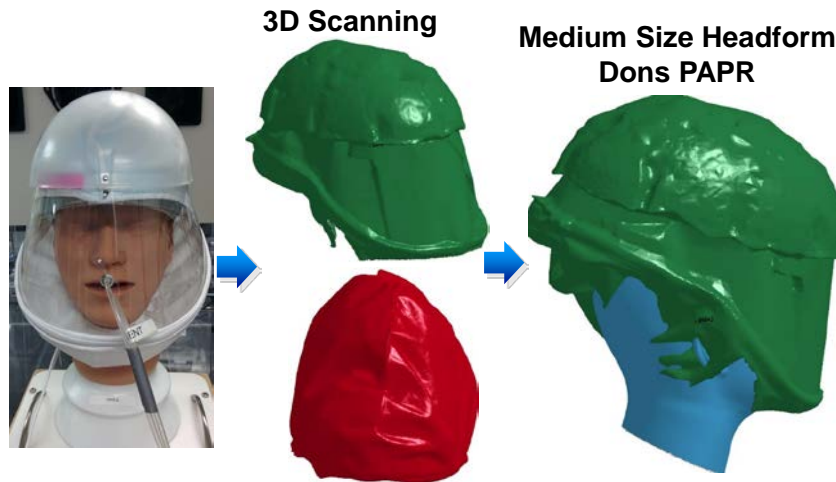
Photo Credit: NIOSH/NPPTL

Fig. 2.2   The process of the generation of a PAPR model

A CFD simulation for PAPR-headform simulated the flows of the breathing air and the supplied-air from the PAPR, both of which streamed inside the space between the headform and the loose-fitting PAPR. This region is known as the PAPR breathing zone and is the space modeled by CFD in this study. Additional geometry-processing work was done to trim and bridge the headform and PAPR surfaces, creating a closed surface for the PAPR breathing zone, as shown in Figure 2.3.

Supplied-Air Venting

Breathing airway
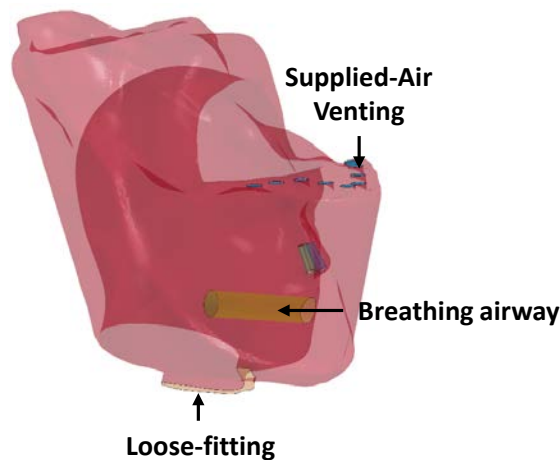
Loose-fitting

Fig. 2.3   The CFD model of headform-PAPR

The surface of the CFD model was split into different parts, including PAPR surface, headform surface, breathing airway wall, supplied-air venting holes, and loose-fitting

area. The supplied-air venting holes were the same number (10) and size (10 mm diameter) as the one in the PAPR prototype. The loose-fitting area where the PAPR loosely fits the headform had a gap with dimensions approximately 15 mm x 80 mm x 10 mm.

The CFD model of PAPR-headform was divided into 913,653 hexahedral cells using the tool Snappyhexmesh provided by OpenFOAM software (version 2.3, The OpenFOAM Foundation Ltd, London, United Kingdom). The Snappyhexmesh uses the adaptive mesh algorithm that iteratively splits hexahedrons into smaller hexahedrons until obtaining enough geometrical accuracy. In the CFD model, the cells with the minimum mesh size (0.5 mm) were at the regions near the supplied-air venting holes, the breathing airway, and the loose-fitting area.

2.2   Mathematical model

The interaction of the breathing air flow and supplied-air flow in the PAPR breathing zone is simplified as an unsteady incompressible flow problem. Hence, the mass continuity equation and the Navier-Stokes equations govern velocity and pressure fields in the PAPR breathing zone:

$$\nabla \cdot \mathbf{U} = 0 \tag{2.1}$$

$$\rho \frac{\partial \mathbf{U}}{\partial t} + \rho (\mathbf{U} \cdot \nabla \mathbf{U}) = -\nabla p + \mu \nabla^2 \mathbf{U} \tag{2.2}$$

where U is the velocity vector, ρ is the density, p is the pressure, and μ is the dynamic viscosity. The turbulent effect is determined using the k-epsilon turbulent model.

PAPR protection is related to the particles leaking into the PAPR breathing zone. The Lagrangian particle tracking technique is used to track particles in the velocity fields of the CFD model. We assume that only air drag force and gravity force influence the particle movement so that the governing equations for the movement of a particle are as follows:

$$m_p \frac{d\mathbf{U}_p}{dt} = F_D \tag{2.3}$$

$$\frac{d\mathbf{X_P}}{dt} = \mathbf{U}_p \tag{2.4}$$

where m_p is the particle mass, U_p is the particle velocity, F_D is the air drag force, and X_p is the particle position. F_D is dependent on the particle Reynolds number:

$$F_D = \frac{24v}{d} \frac{3\rho}{4d\rho_P} (1 + 0.15Re_P^{0.687}) \tag{2.5}$$

where v is the kinematic viscosity, d is the particle diameter, ρ_p is the particle density, and Re_p is the particle Reynolds number.

Because of turbulent fluctuations of the air flow, the particles appear in random motion, which is named particle dispersion. The particle dispersion can be modeled

using the discrete random walk (in OpenFOAM, it is called Stochastic Dispersion), in which an instantaneous fluid velocity is defined turbulent fluctuations in the air flow.

2.3 CFD simulations

The breathing air flow and the supplied-air flow were virtually generated by setting boundary surfaces of the CFD model with different conditions. A time-dependent flow rate with a sine wave shape was applied to the venting hole of the breathing airway to simulate the cyclic breathing pattern including both inhalation and exhalation. A constant flow rate with the direction inwards towards the PAPR breathing zone was applied at the supplied-air venting holes. In the subsequent section, CFD simulations using different flow rates at the breathing airway vent and the blower source are described and simulated in a series of CFD runs. The loose-fitting area is the pressure outlet boundary where air flow passed through the headform surface. The flow velocity at the surfaces of the headform, breathing airway and PAPR was held at zero (i.e. non-slip boundary conditions were used).

The pisoFoam solver (in OpenFOAM) with the PISO (Pressure Implicit with Splitting of Operators) algorithm was used to perform the CFD simulation, since the solver assumes that the flow is transient and incompressible and has a turbulent effect, fitting the mathematical model of this study. Each simulation calculated 20 second time duration with a 0.001-second time-step; at each time-step, the pressure field and the velocity field inside the PAPR breathing zone were determined.

The challenge particles, which were the particles outside of the PAPR breathing zone, were evenly placed at the gap of the loose-fitting area. At every 0.001-second time-step, particles with size 0.1µm and concentration 100,000 /cm^3 were virtually generated. Based on Equation 2.3, 2.4, and 2.5 of the mathematical model, the tool for the Lagrangian particle tracking in OpenFOAM software calculated the particles that leaked into the inlet covering. The interaction between particles and wall boundaries was tracked. We assume that a particle would stick to a wall boundary after the impact happens between them.

2.4 Data Analysis

CFD simulations were conducted to assess factors that affect particle leakage into the loose-fitting PAPR. The factors included breathing workloads and supplied-air flow rates. Cyclic breathing air flows (having both exhalation and inhalation) with minute ventilations of 35, 55, and 85 L/min were applied, simulating light, moderate, and heavy workloads, respectively. The minute ventilations were chosen according to ANDERSON et al. (2006) that determined baseline ventilation data of the general working population. For each of the three breathing workloads, PAPR supplied-air flow rates (85, 115, 145, 175, and 195 L/min) were introduced into the PAPR breathing zone. The supplied-air flow rate 195 L/min was the actual flow rate of the PAPR prototype; other supplied-air flow rates were artificially reduced ones. Note that the minimum flow rate requirement is 170 L/min for loose-fitting PAPRs (NIOSH,

NPPTL, 2005). Total 15 CFD simulations were conducted using the combinations of three workloads and five supplied-air flow rates.

Each CFD simulation determined the flow patterns and pressure distributions inside the PAPR breathing zone at each time step. Each CFD simulation also determined movements of all particles, which were used to calculate the particle concentration of the inhalation air flow at the opening of the mouth during the entire 20 second simulation time. For evaluating PAPR protection against particles, the manikin protection factors (mPFs) is defined as

$$mPFs = \frac{C_o}{C_i} \tag{2.6}$$

where C_o was the challenge particle concentration outside the PAPR and C_i was the particle concentration inside the PAPR breathing zone.

3   Results

Table 3.1 summarizes mPFs values estimated by CFD simulations of different combinations of breathing workloads and supplied-air flow rate. At the light workload, the estimated mPFs were greater than 10,000 for all five supplied-air flow rates. At the moderate workload, the estimated mPF was 31.8 for a supplied-air flow rate of 85 L/min; and for supplied-air flow rates of 115 L/min and above, the estimated mPFs were greater than 10,000. At the heavy workload, the estimated mPFs were 6.6, 10.6, and 43.1 for supplied-air flow rates of 85, 115, and 145 L/min, respectively; and for supplied-air flow rates of 175 L/min and above, the estimated mPFs were greater than 10,000.

Table 3.1 Summary of estimated mPFs of different breathing workloads and supplied-air flow rates.

Breathing Workload	Supplied-Air Flow Rate				
	85 L/min	115 L/min	145 L/min	175 L/min	195 L/min
Light (35 L/min)	> 10,000	> 10,000	> 10,000	> 10,000	> 10,000
Moderate (55 L/min)	31.8	> 10,000	> 10,000	> 10,000	> 10,000
Heavy (85 L/min)	6.6	10.6	43.1	> 10,000	> 10,000

As an example, Figure 3.1 shows a visualization of flow fields at peak inhalation and exhalation in the CFD simulation of light workload and 85 L/min supplied-air flow rate. Simulation results indicate that the velocity distribution, pressure distributions, and streamlines changed almost instantaneously during breathing cycles and that the flow fields at the peak inhalation and the peak exhalation had distinct patterns.
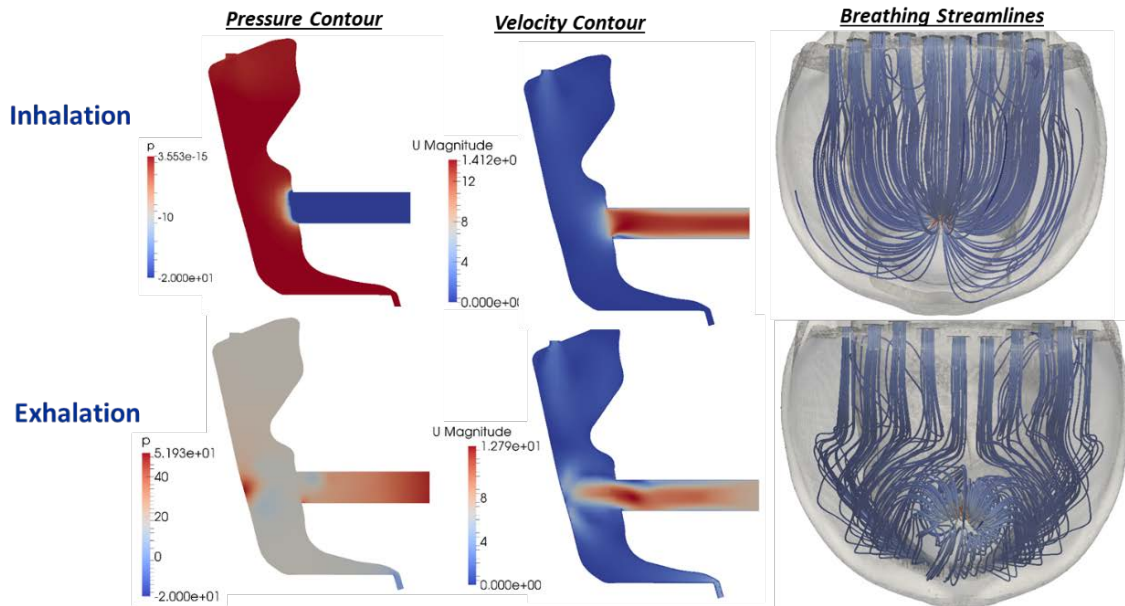
Fig. 3.1 Visualization of flow fields at peak inhalation and exhalation (light workload (35 L/min) and 85 L/min supplied-air flow rate)

As another example, Figure 3.2 shows the particle distribution of the CFD simulation of light workload and 85 L/min supplied-air flow rate at different time instances of a breathing cycle. The particle distributions inside the inlet covering were not homogeneous (i.e., the majority of the leaking particles appeared in the region between the mouth and the loose-fitting area at the neck).
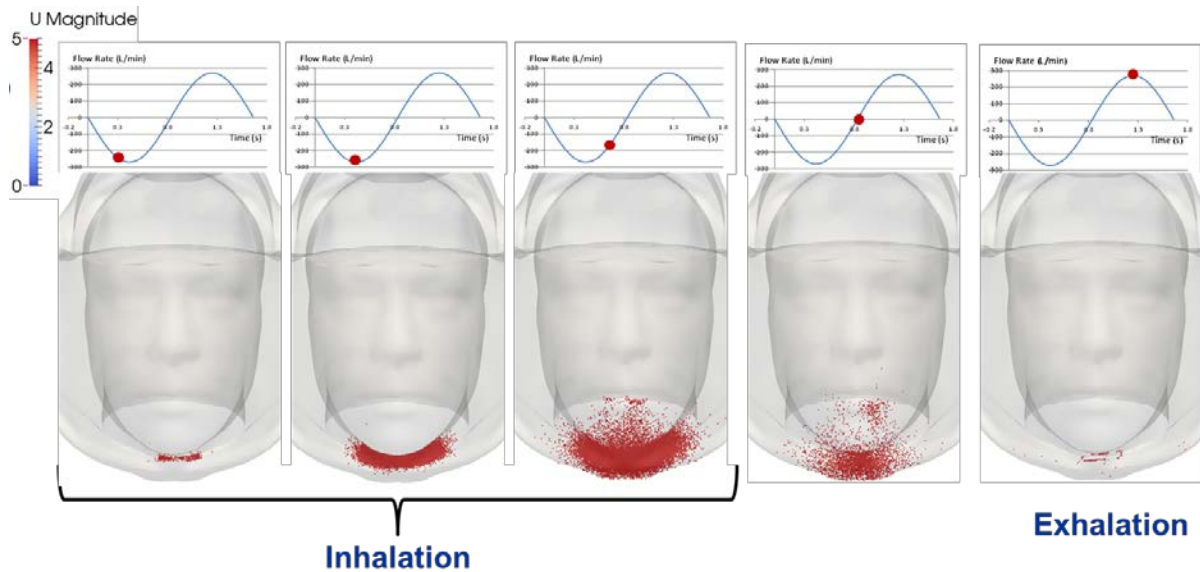
Fig. 3.2 Particle distribution inside the PAPR inlet covering at different time instances of a breathing cycle (low workload and 85 L/min supplied-air flow rate)

4   Discussion

The lower estimated mPFs were found at higher workloads, qualitatively agreeing with the results in (GAO et al. 2016) showing that the particle leakage increased with increasing breathing workload. The particle leakages at the actual supplied-air flow rate (195 L/min) in this study were low at all breathing workloads, different from the results in (GAO et al. 2016), which had relatively high particle leakage. This was because (GAO et al. 2016) used improperly sized and stretched-out loose-fitting PAPR hoods, which artificially introduced high leak gaps. Additionally, this study found that the mPFs decreased with decreasing the supplied-air flow rate. The leakage at the heavy breathing workload and the low supplied-air flow rate was caused by that the supplied-air flow rate failed to provide enough purified air to the breathing flow.

Inside the inlet covering, the velocity distribution, pressure distributions, and flow streamlines, which were visualized by the CFD simulations, could be used to optimize the flow pattern inside loose-fitting PAPR. In experimental studies of loose-fitting PAPR, a pressure sensor and a particle probe are placed inside the inlet covering to measure pressure and particle concentration. The CFD visualization of pressure and flow streamlines may help determine the locations for the pressure sensor and particle probe.

It was assumed that the supplied-air flow had a constant rate in each simulation. However, factors including the battery-operated blower, the inhalation and exhalation (that change pressures inside the PAPR), and the loose-fitting seal (which determines the resistance of air exhaust) affect the supplied-air flow. These factors may make the flow rate inconstant. Future research will consider the effect of inconstant supplied-air flow rate. Additionally, future research is needed to conduct CFD simulations with different loose-fitting PAPR models and different NIOSH headform models. The Brownian motion caused by thermal diffusion is not considered in this study. The Cunningham Correction factor can be used to determine the thermal diffusion. A future study will include the thermal diffusion force in the governing equation for particle motion (Equation 2.3).

This study is the preliminary work of an iFund project award from the U.S. Centers for Disease Control and Prevention (CDC). The iFund project aims to develop advanced methods for evaluating and designing loose-fitting PAPRs. The work described above finished one objective of the iFund project, creating computer simulations of the performance of loose-fitting PAPRs on headforms that simulate breathing. Another objective is to develop a prototype software program which utilizes CFD modeling to simulate particle leakage into PAPR facepieces. The program (using Python programming) will enable users to create computer-aided design models of next generation PAPR systems with an easy-to-use graphical interface. The program will also allow respirator researchers and manufacturers to easily manipulate variables (such as breathing frequency, particle size and concentration, PAPR air flow rate, and shape of facepieces to simulate PAPR performance).

The simulation results in this study have not been validated through experiments. As part of the iFund project, we are conducting experiments using actual physical NIOSH headform models and loose-fitting PAPR prototypes to measure fit factors for

validating the simulation results. Two loose-fitting PAPR prototypes have been collected to test their performance under different breathing workloads.

5 Conclusions

The CFD simulations estimated the protective capacities of PAPRs. These data can potentially assist respirator manufacturers for new product designs. The smaller estimated mPFs were found at heavier workloads and lower supplied-air flow rates. By including additional headform models and PAPR models, future research will extend the usage of digital human modeling in the application of assessing PAPR performance and will create software to help PAPR design.

6 Disclaimer

The findings and conclusions in this report are those of the authors and do not necessarily represent the views of the National Institute for Occupational Safety and Health. Mention of commercial product or trade name does not constitute endorsement by the National Institute for Occupational Safety and Health.

Acknowledgements

List of references

Anderson, N. J.; Casidy, P. E.; Janssen, L. L.; Dengel, D. R.: Peak Inspiratory Flows of Adults Exercising at Light, Moderate and Heavy Work Loads. Journal of the International Society for Respiratory Protection; 23, 2006.

Bergman, M. S.; Zhuang, Z.; Hanson, D.; Heimbuch, B. K.; McDonald, M. J.; Palmiero, A. J.; Shaffer, R. E.; Harnish, D.; Husband, M.; Wander, J. D.: Development of an Advanced Respirator Fit-Test Headform. Journal of occupational and environmental hygiene; 11(2), 117-125, 2014.

Gao, S.; McKay, R. T.; Yermakov, M.; Kim, J.; Reponen, T.; He, X.; Kimura, K.; Grinshpun, S. A.: Performance of an Improperly Sized and Stretched-Out Loose-Fitting Powered Air-Purifying Respirator: Manikin-Based Study. Journal of Occupational and Environmental Hygiene; 13 169-76, 2016.

Lei, Z.; Yang, J.: Computing Carbon Dioxide and Humidity in Filtering Facepiece Respirator Cavity During Breathing Cycles. V01AT02A077, 2014.

Lei, Z.; Yang, J.; Zhuang, Z.; Roberge, R.: Simulation and Evaluation of Respirator Faceseal Leaks Using Computational Fluid Dynamics and Infrared Imaging. The Annals of Occupational Hygiene; 57 493-506, 2012.

Martin, S.; Moyer, E.; Jensen, P.: Integrated Unit Performance Testing of Powered, Air-Purifying Particulate Respirators Using a DOP Challenge Aerosol. Journal of Occupational and Environmental Hygiene; 3 631-41, 2006.

McCoy, M. A.; Domnitz, S. B.; Liverman, C. T. (Eds.): The Use and Effectiveness of Powered Air Purifying Respirators in Health Care: Workshop Summary. National Academies Press, 2015.

National Institute for Occupational Safety and Health (NIOSH), National Personal Protective Technology Laboratory (NPPTL) (2005) Determination of Air Flow for Powered Air Purifying Respirators. NIOSH/NPPTL Standard Testing Procedure #RCT-APR-STP-0012, Revision 1.1.

Roberge, R. J.: Evaluation of the Rationale for Concurrent Use of N95 Filtering Facepiece Respirators with Loose-Fitting Powered Air-Purifying Respirators during Aerosol-Generating Medical Procedures. American Journal of Infection Control; 36 135-41, 2008.

Sinkule, E. J.; Powell, J. B.; Rubinstein, E. N.; McWilliams, L.; Quinn, T.; Pugliese, M.: Physiologic Effects from Using Tight- and Loose-Fitting Powered Air-Purifying Respirators on Inhaled Gases, Peak Pressures, and Inhalation Temperatures During Rest and Exercise. Journal of the International Society for Respiratory Protection; 33(2) 36-52, 2016.

Wizner, K.; Stradtman, L.; Novak, D.; Shaffer, R.: Prevalence of Respiratory Protective Devices in US Health Care Facilities: Implications for Emergency Preparedness. Workplace health & safety; 64 359-68, 2016.

Zhuang, Z.; Benson, S.; Viscusi, D.: Digital 3-D Headforms with Facial Features Representative of the Current US Workforce. Ergonomics; 53 661-71, 2010.

Kouchi & Mochimaru:
Estimation of head shape without hair from a head shape with hair

Kouchi, M., Mochimaru, M.

National Institute of Advanced Industrial Science and Technology (AIST), Japan

Abstract

Data from three-dimensional head scans are commonly used to design equipment worn on the head. It is a normal practice to cover the head while taking a head scan. However, the use of the cover and the presence of hair on the head cause differences in the shape of the head between the scanned image and the actual head without hair, which is a challenge in the design of products worn on the head. In an attempt to obviate this challenge, this study analyzed the differences between the head scans with and without hair in nine subjects to examine the deformation in the head shape due to hair. Each subject was scanned under conditions of with hair and without hair. In the condition of with hair, the hair was covered with a net bandage and hair at the nape and sideburns were covered with thin white athletic tape. A custom-made head scanner developed by NEC Corporation was used. A head support was used to minimize head movement during the scan. The knot in the net bandage was removed from the scan image and the resulting blank areas were filled using Geomagic studio. The scans were analyzed using a head-oriented coordinate system. Each scan was cut by a plane at the neck to separate the head portion. A homologous model was created for each scan by template fitting using 29 landmarks on the head scan and 30 semi-landmarks generated on the cross section at the neck. Polygons of the ears and the neck were removed, and the remaining polygons were divided into "head" region, which is usually covered with hair, and the "face" region. A homologous model with hair was overlapped onto the homologous model without hair of the same subject by minimizing the differences in the "face" region. The "wig" data, that is the differences in the XYZ coordinates of each data point belonging to the "head" region, were then calculated. The "wig" data of each subject was added to the average homologous model without hair and the calculated nine homologous models were analyzed using multidimensional scaling (MDS). The RSQ of the three-dimensional solution was 0.930. MDS dimension 1 (Dim-1) represented the variation in the size of the "wig" while dimensions 2 (Dim-2) and 3 (Dim-3) represented the variation in the shape of the "wig". Examination of the differences between the two scans showed that (1) shape of the nuchal region is considerably influenced by the posture of the head and neck; (2) the net bandage and use of head support may also have affected the variations in the shape change; (3) characteristics of the hair such as thickness affect the size and shape of the "wig". Due to these limitations and the use of small number of subjects from a homogeneous population, it is difficult to generalize the present results for use in head scan surveys. To show a plausible range of variation in "wig" size and shape, average shape with hair and eight virtual shapes were calculated on an ellipse containing 68% of subjects in a distribution map based on scores for Dim-1 and Dim-2, and were compared with the average shape

without hair. The maximum difference between a head with and without hair was approximately 9 mm on average. The results of this study are expected to contribute to the improved designs of industrial products worn on the head.

Key words:

head scan, head shape deformation, homologous modeling, posture

1   Background

Three-dimensional head scan data have been used for designing industrial products that are worn on the head such as personal protective equipment (BRADTMILLER, 1996; NIEZGODA and ZHUANG, 2015). Usually a cap is used to flatten the hair against the head while scanning the head to determine its shape. Covering dark hair is also necessary because head scanners that use light cannot measure dark objects. Because of covering the head, the scanned head is larger than the head without hair and deformed, and the amount of difference between the head with and without hair may depend on the hair and the cap. This makes it difficult to assess the fit and decide the allowance using head scan data when designing equipment worn on the head. Information on the difference between the head shape with and without hair may be important. Therefore, we analyzed the differences between the head scans with and without hair to investigate the deformation pattern of the head shape due to the hair and the cap.

2   Subjects and methods

The subjects used in this study were nine male volunteers. All subjects were Japanese and had dark straight hair. The hairstyle and hair lengths were different in the subjects. The age of the subjects at the time of the first scan ranged from 21 to 37 years.

2.1   Measurement

The scans were conducted in 2002 and 2003. The experimental protocol was reviewed and approved by an institutional review board. Each subject was scanned under two different conditions. In condition 1, the hair was covered with a net bandage (Careful net bandage for head, PIP Co. Ltd.), and hair at the nape and sideburns were covered by thin white athletic tape (Medicare adhesive bandage, Morishita Jintan Co. Ltd.) (Figure 2.1A, Figure 2.1C). The hair was shaved in condition 2. The time gap between the two scans ranged from 0 day to 105 days.

The locations of 70 landmarks were marked with an eyeliner pencil or marker stickers (Figure 2.1C). When both scans were conducted on the same day, the same positions were used for the facial landmarks. The same observer decided the landmark positions in all the scans.

We used a custom-made head scanner based on the phase-shifting method developed by NEC Corporation (MOCHIMARU et al., 2002). Figure 2.2 shows the scanner. The entire head was scanned in 1 s using 10 projector-camera units. We used a head support to minimize the head movement during the scan (Figure 2.1B). The accuracy of the scan was 0.5 mm and resolution was 1.0 mm. The accuracy was not evaluated according to ISO 20685-2 because this standard was not established at the time of conducting this study.
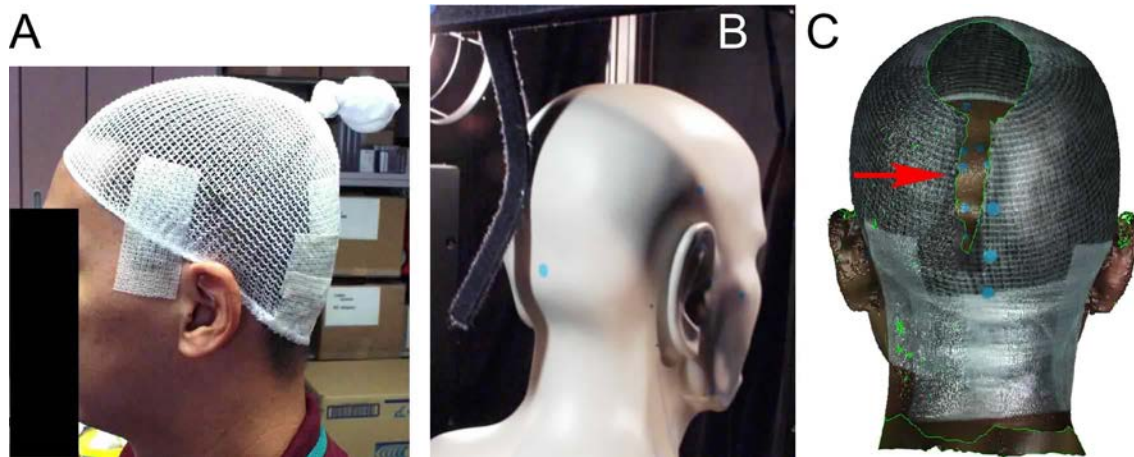
Fig. 2.1 Scanning conditions. A: net bandage, B: head support, C: blank areas previously occupied by the knot or caused by the head support (indicated by the arrow). Light blue circles are marker stickers
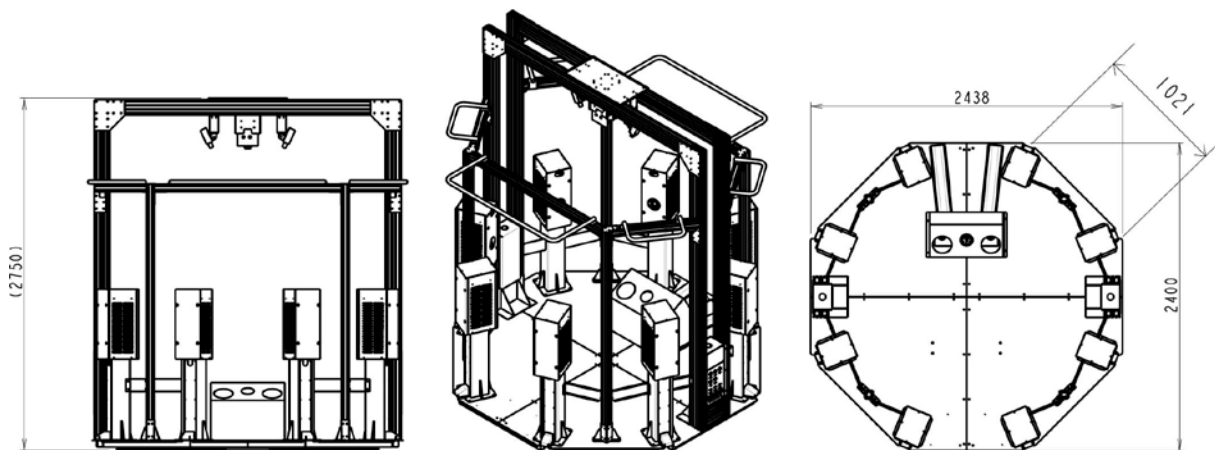

Fig. 2.2 Head scanning system

2.2 Homologous modeling

The knot on the net bandage was removed from the scan data (Figure 2.1C). Large blank areas on the scanned images caused by removing the knot and the head support were filled using Geomagic studio (Raindrop Geomagic Inc.) The locations of 49 landmarks shown in Figure 2.3 were identified manually on each scan. The filling of the holes and identification of landmarks were performed by the same operator. The scan data was analyzed using a head-oriented coordinate system shown in Figure 2.4. The XY plane is defined using the right and left tragions and the left orbitale. The Y-axis is the line connecting the right and left tragions. The origin is the foot of a perpendicular from the sellion to the Y-axis.

The neck of the image was cut at a point below the junction point of the lower surface of the jaw and the front surface of the neck in the median line (arrow in Figure 2.3) by a plane perpendicular to the XZ plane and inclined forward by 20° (Figure 2.5, right). Thirty semi-landmarks were generated on the cross section. The cutting plane was inclined forward by 30° in one image (#118) where the nape area was missing due to a high-necked cape worn by the subject (Figure 2.5A). The homologous model of this

subject is shown with that of another subject (#014) in Figure 2.5. We decided to keep this subject to maximize the number of subjects in the study. The effects of including this subject are considered small because we did not use the homologous models of the subjects themselves as described below.
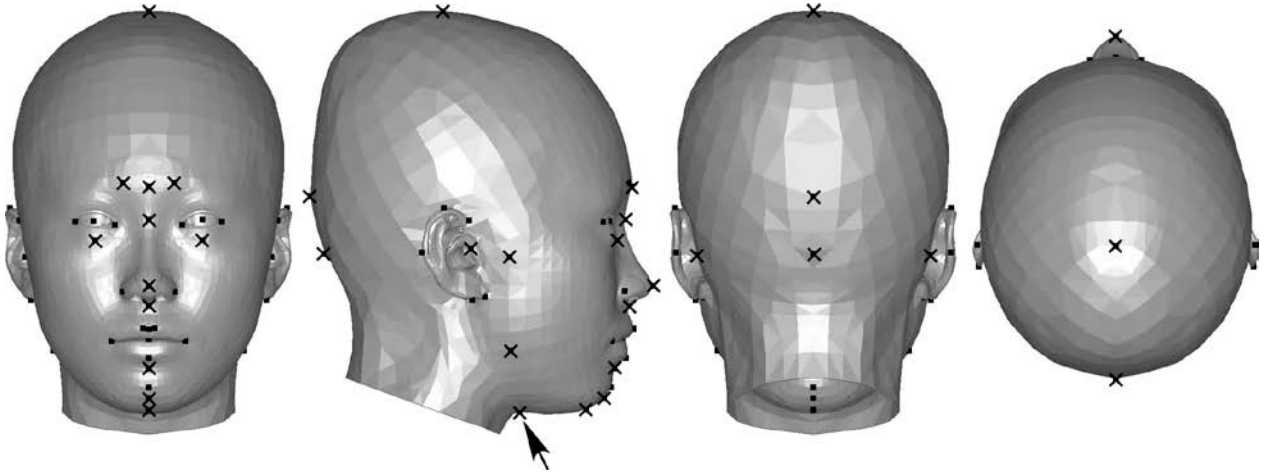

Fig. 2.3 Landmarks. Crosses indicate landmarks marked before scanning, and dots indicate landmarks not pre-marked. The arrow indicates the junction point of the jaw and neck
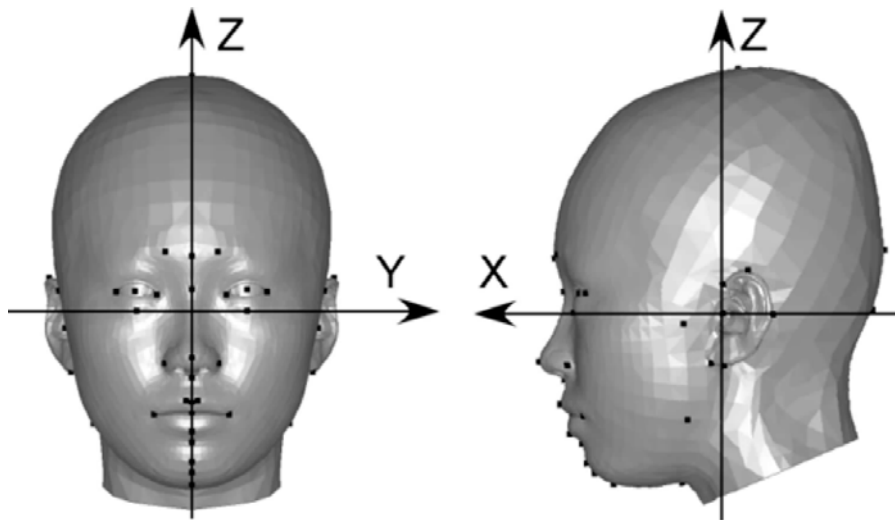

Fig. 2.4 The coordinate system
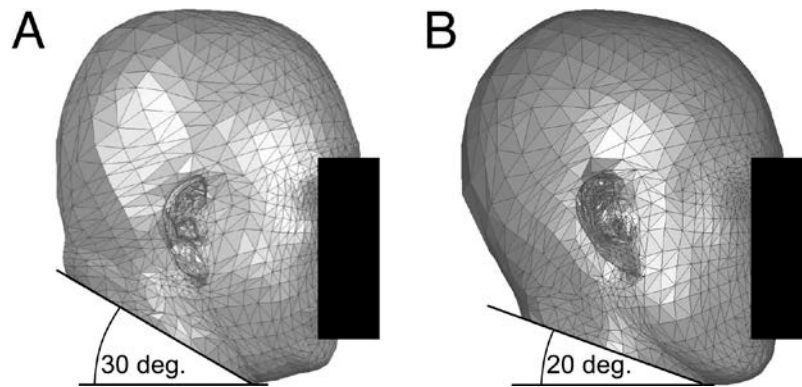
Fig. 2.5   A:The image with the neck cut by a plane inclined forward by 30° (left), B: an image with the neck cut by a plane inclined forward by 20° (right)

A homologous model was created for each scan by template fitting using the 49 landmarks and 30 generated semi-landmarks (HBM, Digital Human Technology Inc.) A modified Dhaiba head (Figure 2.6A) was used as the template. Original Dhaiba head has no data point on the eye-ball region. Blank areas at eyes were filled to place the landmark pupulare (the center of pupil).

2.3 Analysis

The ears and the neck were removed from the models. The remaining polygons of the homologous model were divided into "head" which is usually covered with hair or sideburns (blue area in Figure 2.6B) and "face" (gray area in Figure 2.6B).
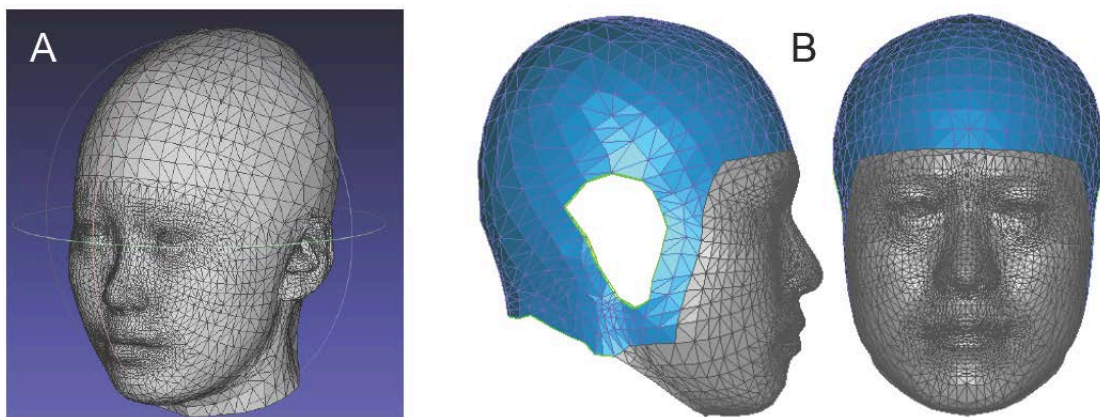
Fig. 2.6   The template (A) and an example homologous model used for analysis(B). The blue area in B indicates the "head" region for which the difference between the two conditions used in the study was calculated. The gray area in B indicates the "face" region

For each subject, the homologous model with hair was overlapped on the homologous model without hair by minimizing the differences between the two "face" regions excluding the region below the lips. The "wig" data, that is the differences in the XYZ coordinates of each data point belonging to the "head" region, were calculated. In order to analyze the variations in the "wig" shape, the "wig" data of each subject was added to the average homologous model without hair. These nine

homologous models (average + "wig" of each subject) were analyzed using principal component analysis (PCA) and multidimensional scaling (MDS) (HBS, Digital human technology Inc.) to identify the head deformation patterns due to the hair. Virtual shapes at −3 standard deviation (−3SD shape) and +3 standard deviation (+3SD shape) on each principal component (PC) axis or each MDS dimension were calculated to interpret the PCs and MDS dimensions.

3   Results

There were four principal components (PCs) with contribution rates larger than 10%. Contribution rates of the first four PCs were 34.8%, 17.9%, 13.5%, and 10.9%, respectively. Their cumulative contribution rate was 77.1 %. The RSQ of the two-dimensional solution of MDS was 0.880 and that of the three-dimensional solution was 0.930. The MDS results explain larger percentage of variations in homologous models with smaller number of new variables than PCA. Therefore we used MDS results for further examination. The correlation coefficient between PC1 and Dim-1 was high (r=−0.991), but the correlation coefficients between PC2 and Dim-2 (r=−0.858) or between PC3 and Dim-3 (R=−0.761) were lower.

Figure 3.1 shows the ±3SD shapes of the first three MDS dimensions, Dim-1, Dim-2, and Dim-3. Theoretically, there were no differences between +3SD shape and −3SD shape in the "face" region, but small differences were observed in the "face" region in the results of the MDS. This is because the free-form deformation transformation grid was used to calculate the ±3SD shapes (MOCHIMARU and KOUCHI, 2000). Figure 3.1 shows that the variation in the "wig" shape is larger in the sagittal direction than in the lateral direction.

Figure 3.2 shows the distribution of subjects based on the scores of MDS—Dim-1 and Dim-2, and Dim-2 and Dim-3—and the scanned images of the subjects. From Figure 3.1 and Figure 3.2, we can interpret that Dim-1 represents the variation in the "wig" volume whereas Dim-2 and Dim-3 represent the variations in the "wig" shape.

The scanned images of subjects #119 and #122 in Figure 3.2 also show that the shape of the nuchal region can change considerably according to the head position.
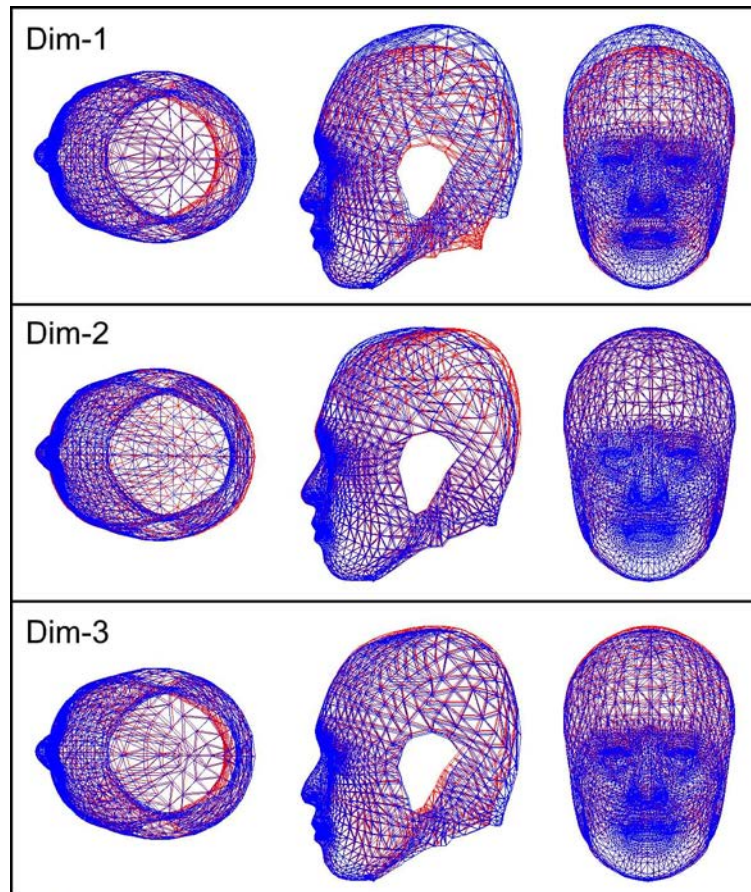
Fig. 3.1   Virtual shapes (VSs) at both ends of the MDS dimensions. Red: +3SD shape, Blue: −3SD shape
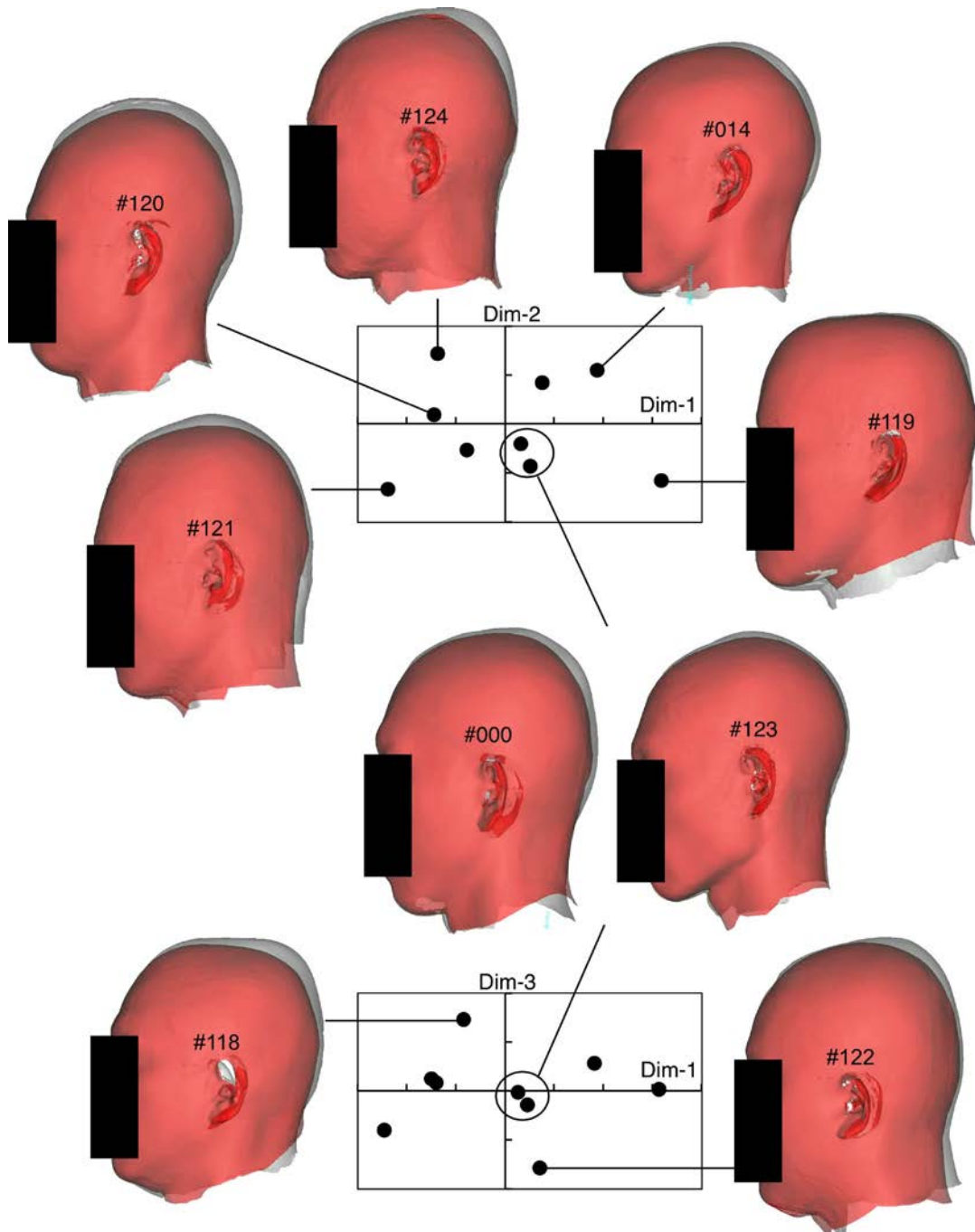
Fig. 3.2 Distribution of subjects based on the scores of MDS dimensions and head scans with hair (gray) and without hair (red)

4   Discussion

Figure 3.2 shows that the shape of the back of the head below the external occipital protuberance is influenced by the neck posture as well as the hair. This suggests that the shape changes of the nuchal area should be taken into consideration when designing equipment worn on the head. Additionally, the position of head and neck must be carefully controlled to minimize the change in shape of the soft tissues when scanning the head when the purpose of the head scanning is estimation of the effects of hair and the cap.

We used net bandage to cover the hair. This may not have been a good choice. There is a blank area at the top of the head when the knot is removed from the scan data (Figure 2.1C). The shape variation around the posterior parietal region (Figure 3.2, subjects #118, #122, #124) could be due to the loose fitting of the cap when a knot is made manually. A cap with a tighter fit may compress the hair more effectively.

The use of a head support might have influenced the head shape deformation pattern. We arranged the position of the subject so that the head support was in contact with the left side of the median line of the head (Figure 2.1 B, C). A slight asymmetry is observed at the back of the head (indicated by the arrow in Figure 4.1, #9) when the average homologous model with hair is compared with the average homologous model without hair.

Head deformation due to hair may depend on the thickness, form (straight, wavy, or kinky), and length of the hair and hairstyle. For example, #123 in Figure 3.2 had longer but finer hair than #120 in the same figure. The volume difference is much larger in #120 than #123.

Another limitation of this study is the small number of subjects from a homogeneous population. All subjects were Japanese and had straight and relatively short hair. None of the subjects had a spiky hairstyle.

Due to the above limitations, the applicability of the present results to other head scan surveys is uncertain. However, the information regarding the extent of shape difference in the data presented by this study may be useful. Figure 4.1 shows the comparisons of the average homologous model without hair and the virtual homologous models on an ellipse containing 68% of the subjects as well as at the center of distribution in the distribution map based on Dim-1 and Dim-2. The maximum "wig" thickness ranged from 8.9 mm in the average model (Figure 4.1, #9) to ≥12.1 mm in #4 and #5 in Figure 4.1.

A larger database consisting of head scans with and without hair and information on the hair and hairstyle is necessary to estimate a possible range of head shapes without hair from head scans with hair.
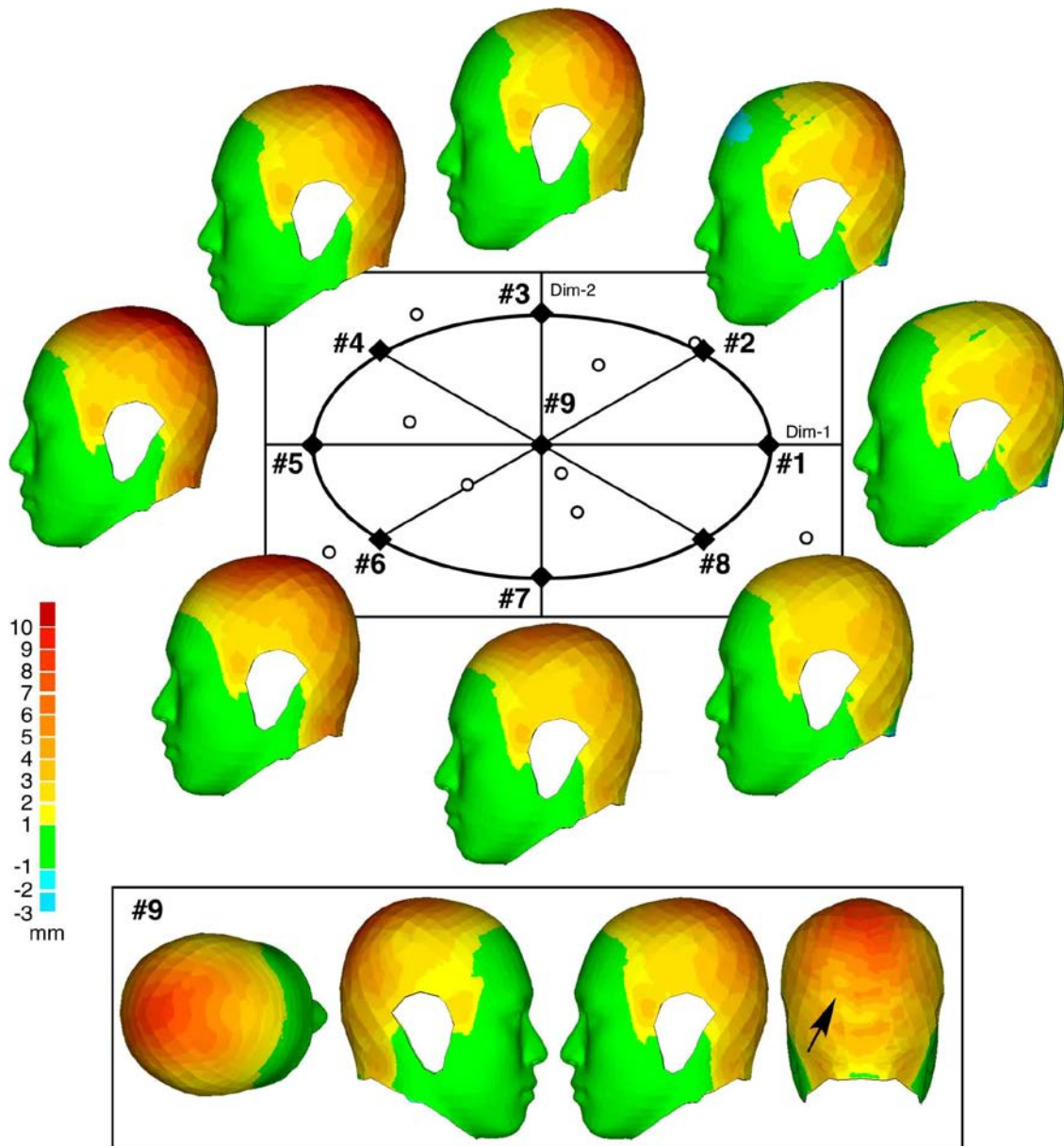
Fig. 4.1 Virtual shapes on an ellipse containing 68% of the subjects (#1 to #8) and the average shape with hair (#9) compared with the average head shape without hair. The yellow to red colors indicate the thickness of the "wig." Slight asymmetry is observed at the back of the head as indicated by the arrow.

List of references

Bradtmiller, B.: Sizing head forms: design and development, 1996, SAE Technical Paper 960445.

Niezgoda, G.; Zing, Z.: Development of headforms for ISO eye and face protection standards, Procedia Manufacturing,2015, 3, pp.5761-5768.

Mochimaru, M.; Kouchi, M.: Statistics for 3D human body forms, 2000, SAE Technical Paper, SAE 2000-01-2149.

Mochimaru, M.; Kouchi, M.; Oya, T.: Rapid and complete body shape scanners, Proceedings of 19th Sensing Forum, 2002, 02 SY 0007, pp.47-52. (in Japanese)

Savonnet et al.:
A parametric model of the thigh-buttock complex for developing FE model to estimate seat pressure

Savonnet, L., Wang, X., Duprey, S.

Université de Lyon, IFSTTAR, France

Abstract

Contact pressure on the seat surface is one of the most important factors to consider when assessing sitting discomfort (DE LOOZE et al., 2003). Several finite element models of the thigh-buttock region have been developed to simulate user-seat interaction. However, the models predominantly match one specific body anthropometric type (often the 50th male percentile in stature), meaning they cannot represent the large range of variation of sitters' population. The objective of this study was to develop a parametric model of the thigh-buttock region including both bones (pelvis and femur) and outer skin of varying ranges of anthropometry.

Thirty-six participants (19 males, 17 females) of varying weight (healthy BMI, obese BMI) and stature (small, average height and tall) were recruited for this study. Using a VICON optoelectronic system, 8 pelvis anatomical landmarks were palpated manually in a seated position. Participants were then scanned using a portable handheld laser scanner (Nikon, ModelMaker MMD x /MMC Handheld Scanner) in a position with a thigh-trunk angle of approximately 110°. The position was maintained by an adjustable kneeling structure so that both the torso and the thighs were not supported, making it more accessible to scan the back, buttocks and thighs.

After having pre-processed the 3D scans, a principal component analysis was first performed on the coordinates of the surface mesh including anatomical landmarks. Then, a statistical linear regression was run on the retained PC scores with stature, BMI and pelvis-femur angle as predictors in order to obtain a statistical shape model (SSM). Regarding bone surfaces, the SSMs of femur and pelvis were obtained using previously collected CT scans of 54 bodies from the University Libre de Bruxelles, Belgium. The bony landmarks predicted by the SSM of external shape were used as the inputs of the SSM of bones surface. Bone surface estimation was assessed with the use of MRI images of one subject.

The parametric model of thigh-buttock complex will be used to generate the meshes of the finite element models to be developed for simulating occupant/seat interaction for a large range of anthropometry.

Key words:

Comfort, Seat, FE model, Statistical Shape Model

1   Introduction

Contact pressure on the seat surface is one of the most important factors to consider for assessing sitting discomfort (DE LOOZE et al., 2003). Many human body models have been developed to help estimate seat surface pressure distribution, either by representing the whole body (CHOI et al., 2007; SIEFERT et al., 2008; XIAOMING et al., 2013) or by representing only the thighs and buttocks (VERVER et al., 2004; MERGL et al., 2004; Al-DIRINI et al., 2016). However, the models typically only represent one specific body size (predominantly, the 50th percentile male in stature) meaning it cannot represent the large anthropometric variation of the sitters' population.

The pressure on the seat pan surface is strongly dependent on the sitter's anthropometry (KYUNG and NUSSBAUM 2008). For example, BMI was found to affect the peak pressure, the contact area and the pressure distribution. The contact area can be multiplied by 1.4 for a person of 97 kg versus a person of 53 kg (SWEARINGEN et al., 1962). HOSTENS et al. (2001) found a linear correlation between the mean contact pressure and BMI. Hip breadth needs to be considered for the design of seat lateral contour as it is highly variable amongst the population. As an example, the 95th female sitting breadth is much larger than the 95th male; they were respectively 432 and 412mm based from the Anthropometric Survey of US Army Personnel in 1988 (GORDON et al., 1988).

This study aims to develop a parametric shape model of the buttock-thigh complex containing both skin and bones (pelvis and femur) for the need of developing finite element models to simulate occupant seat interaction.

2   Material and Methods

2.1   Data collection

3D skin surfaces of the thighs, pelvic and lower torso as well as bony landmarks of the femur and pelvis were collected from 36 participants. Participants were selected to cover a wide range of anthropometry for both males and females. Three stature groups were defined: short (5-15%ile), average height (around 50 % ile) and tall (80-95 %ile, based on an French population) with two BMI caterogies 18.5 - 25 and over 30 kg/m² for each stature group.

In order to estimate the position and the shape of the pelvis and femur, a specific protocol was followed to palpate the bony landmarks. A cluster with 4 reflective markers was attached on the sacrum. This cluster was used as a local reference system attached to the pelvis. Then, using a manual palpator called "A-Palp" (SALVIA et al. 2009), the following bony landmarks were palpated (Figure 2.1): RIAS and LIAS (Right and Left Anterior Superior Iliac Spine), RIPS and LIPS (Right and Left Posterior Superior Iliac Spine), RICT and LICT (Right and Left Ilium Crest Tubercule) and IPJ(Ilium Pubic Joint) (VAN SINT JAN 2007). The positions of the markers for the sacrum and A-palpator were recorded using the VICON optoelectronic system.

Fig. 2.1   Bony landmarks palpation with the A-palp

To obtain the position of the ischial tuberosity, a pressure pad (X3, XSensor, Calgary, AB) was used. The subject was sitting on a flat rigid surface and the locations of the two peaks of pressure on the pressure map were identified as the ischial tuberosity positions.

Then, participants were asked to position themselves on a device (Figure 2.2) that helped them maintain a torso-thigh angle of approximately 110° (representing a relaxed sitting position). Both the torso and the thighs were not supported, making it more accessible to scan the back, buttocks and thighs. The kneeling structure was adjustable to ensure that the same position could be adopted by every participant. The torso-thigh angle was verified using a goniometer.

Reflective markers were attached on the two epicondyles of each femur. Then, the participants were scanned with a hand laser scanner (Nikon ModelMaker MMCx) from the knees to the shoulders.
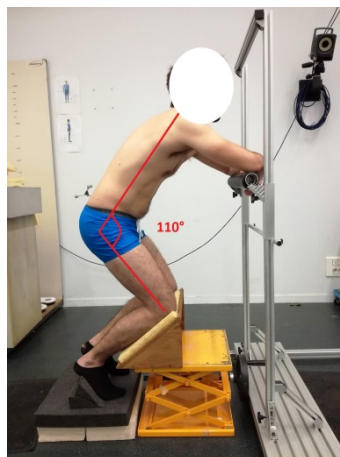

Fig. 2.2   Scanning posture of a participant in the support device

2.2 Data processing

2.2.1 Generation of meshes and landmarks position

The scan data for each participant were first cleaned by filling the holes and deleting the superimposed mesh parts. The surfaces were re-meshed to decrease the number of triangles to 20 000 using the MeshLab Software. The scans were then aligned in the pelvis local reference system with help of the pelvis anatomical landmarks palpated previously according to the ISB recommendations (WU et al. 2002). The scans were then cleaned and segmented to keep only the thigh and the pelvic area (Figure 2.3). The pelvic and thigh surface was delimited by the three plans defined as follows: 1) plan defined by the two markers on the knee and a point located at the poplite, 2) body symmetry (saggital) plan defined by two mid points of two PSIS and two ASIS, and the normal direction by the two ASIS, 3) plan formed by two ASIS and mid point of two PSIS . The previously palpated bony landmarks were merged with the scan thanks to the common cluster reference system which was also scanned.

Cleaned meshes with a same ordered vertices for each subject were obtained by deforming a template on the scan using mHBM software (Markerless Homologous Body Modeling Software, National Institute of Advanced Industrial Science and Technology, Digital Human Research Center). The generic template was created from the data of a subject. In addition to the skin surface, 16 bony landmarks were associated to the shape, including 7 manually palpated bony landmarks; the two ischiums estimated using the pressure map, the two epicondyles at the knee, the two hip joint centers and the lumbosacral (L5/S1) joint center. The joints centers were estimated from the anatomical landmarks using the regression equations provided by PENG et al. (2015).
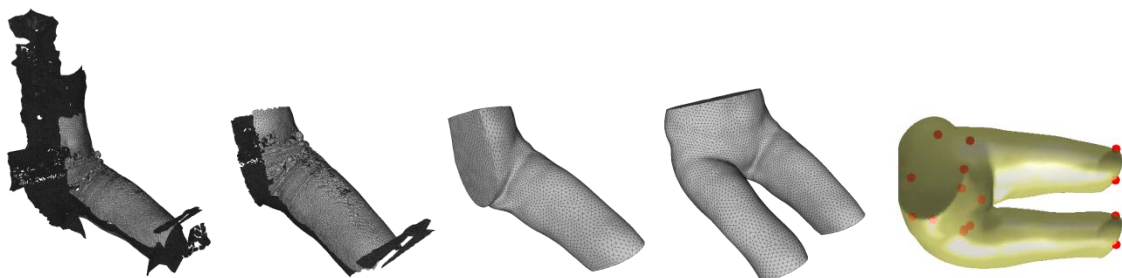
Fig. 2.3 Mesh processing steps. From the left to right show raw scan, raw surface after segmentation, deformed template after having matched with scan, full buttock thigh surface after symmetrisation, landmarks association.

2.2.2 Statistical Shape analysis

A PCA was used (JOLLIFFE, 2002) to reduce the dimensionality in data. The coordinates of the 9 923 mesh vertices from the 36 subjects were gathered in a matrix Ψ_{n*p} with n corresponding to 36 subjects and p to 3*9923 vertex coordinates. The q (= 3*16) coordinates of the 16 bony landmarks were appended to Ψ_{n*p} resulting in a matrix $\Psi_{n*(p+q)}$. A smaller set of ordered variables, called principal

component (PC) score, was obtained with PCA, so that the first PCs retained most of the variation in the original dataset.

From the PCA of data, assume that M main PCs µj (j =1, M) are retained. Then for a subject, the vector Ψ containing coordinates of each p vertex and q landmarks can be expressed:

$$\Psi(1\!:\!p+q) \approx \overline{\Psi}(1\!:\!p+q) + \sum_{j=1}^{M} c_j\, \mu_j(1\!:\!p+q) \qquad\qquad (\textbf{2.1})$$

where $\overline{\Psi}$ is the average from the sample data sets and c_j is the with jth PC score.

A linear regression was performed between the M PC scores $[C]_{N*M}$ and K predictors (ALLEN, CURLESS, and POPOVIĆ 2003)

$$[a]_{(k+1)*M} = \mathrm{inv}\big([P]_{N*(K+1)}\big) * [C]_{N*M} \qquad\qquad (\textbf{2.2})$$

where [P] is the matrix containing the K predictors for the N subjects. Knowing the predictors from a new subject, the PC scores cj can be obtained by

$$c_j \; = a_{0j} + \sum_{i}^{k} a_{ij}\, P_i \qquad\qquad (\textbf{2.3})$$

Then the external shape of the buttock-thigh complex and the bony landmarks of the pelvis and femur can be predicted thanks to (2.1).

2.3   Bones shape prediction

To develop a finite element model of the buttock-thigh complex, bones shapes are needed. From 54 pelvic and femur surfaces from CT scans by the ULB (Université Libre de Bruxelles) (PENG et al., 2015), their PC models were obtained (VALGALIER, 2016) and used to predict the pelvis shape from the 12 pelvis landmarks and the femur shape from the 3 femur landmarks (two epicondyles and joint center). The PC scores were searched for matching the landmarks.
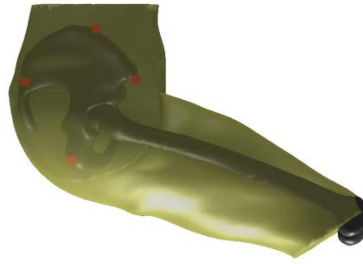
Fig. 2.4   predicted bones and external shape geometry

3   Results

3.1   Principal Component analysis

PCA was performed on the 36 external thigh-buttock shapes placed in the pelvic reference system. 13 first PCs accounted for 99% of the variance in data (Figure 3.4).
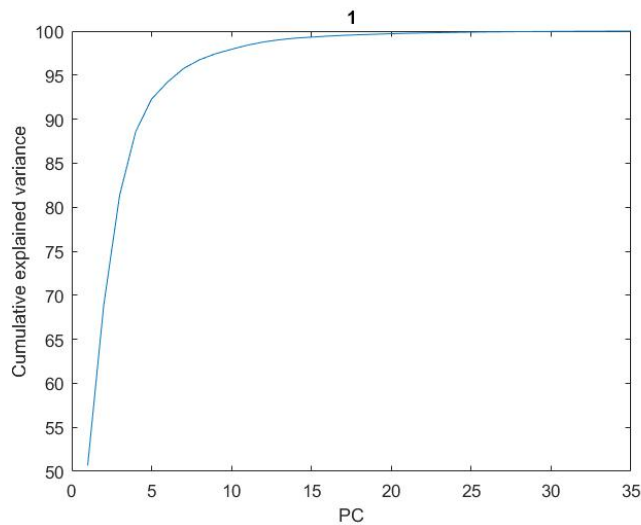
Fig. 3.1   Explained variance of the shape depending on the number of PCs

Figure 3.1 shows the shape variation along the first 4 PCs which account for 88% of total variance. Visually the shape variation along the 1st PC and 2nd PC was mainly explained by trunk-leg angle and leg length (Figure 3.2). The 3rd and 4th components were mainly related to BMI.
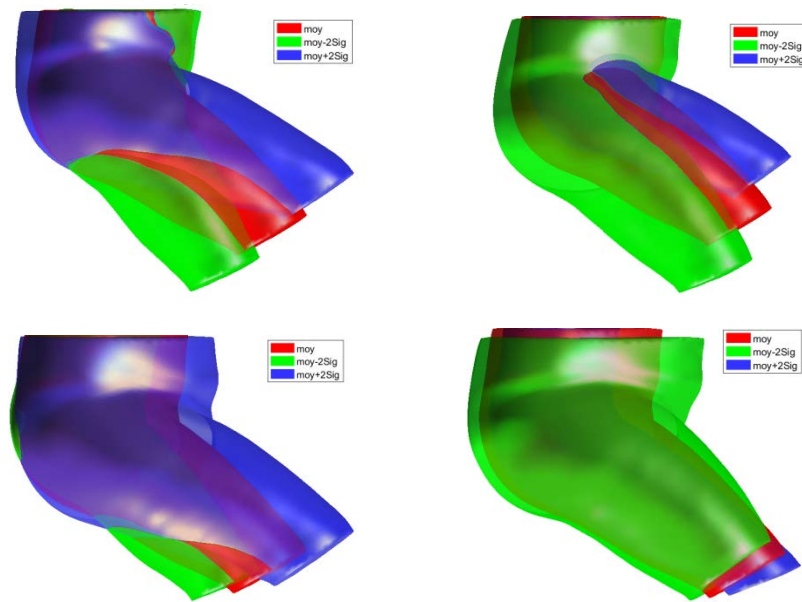
Fig. 3.2 Shape variation along the first 4 PCs (from 1st PC to 4th PC), red = average, blue = average + 2σ, green = average – 2σ

Stature, BMI, gender and torso-thigh angle were selected as predictors. Figure 3.3 shows the effects of BMI, pelvis-femur angle and stature.
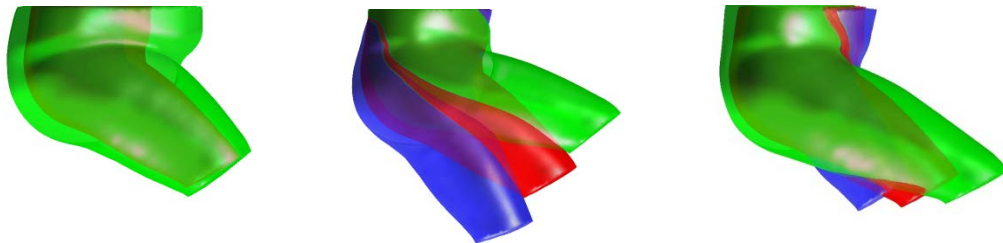
Fig. 3.3 Influence of BMI and Leg angle and stature as predictors. The predictions for the mean (red), mean + 2 standard deviations (blue) and mean – 2 standard deviation (green) are compared for each predictor.

3.2 Leave-one-out validation

A leave-one-out procedure was performed using the data from the 36 subjects to evaluate the prediction of the external shape. The PCA model was first built from n-1 subjects, then the external shape and the bones landmarks of the nth extra subject were predicted using the predictors previously described. This procedure was iteratively repeated until each subject had been considered as an extra subject once. To estimate the accuracy of the predicted geometry, two errors were computed: distance between predicted and palpated landmarks, and distance between the predicted and scanned surfaces. Errors in anatomical landmarks are summized inTable XXX. The smallest errors were obtained for the two illiac landmarks (RIAS,

LIAS) as they were used to align the scans. The two lateral femur epicondyle (LFLE, RFLE) had the largest errors.

Table 3.1 Means and standard deviations of the distances (in mm) between predicted and palpated bones landmarks

	Mean ± Std
RIAS (Right Ilium Anterior Spine)	9.6 ± 8.6
IPJ (Ilium Pubic Joint)	27.7 ± 15.9
RIPS (Right Ilium Posterior Spine)	20.2 ± 14.9
RICT (Right Ilium Crest Tubercle)	25.4 ± 15.5
RHJC (Right Hip Joint Center)	19.1 ± 13.4
LSJC (Lumbo Sacral Joint Center)	15.5 ± 7.7
RIIT (Right Ilium Ischial Tuberosity)	23.7 ± 13.4
RFLE (Right Femur Lateral Epicondyle)	30.2 ± 14.9
RFME (Right Femur Medial Epicondyle)	23.7 ± 12.3
All	21.7 ± 6.2

Table 3.2 Means and standard deviations of the differences (in mm) between predicted and palpated distances from the 36 leave-one-out tests

Lengths	Mean ± Std
Pelvis width between ASIS (L1)	19.2 ± 17.2
Pelvis width between Ischiums (L2)	10.2 ± 8.6
Pelvis height between mid of ASIS and mid of ischiums (L3)	11.6 ± 7.9
Pelvis depth between mid of ASIS and mid of PSIS (L4)	17.9 ± 15.3
Right Hip joint - mid of epicondyles (L5)	16.5 ± 14.6
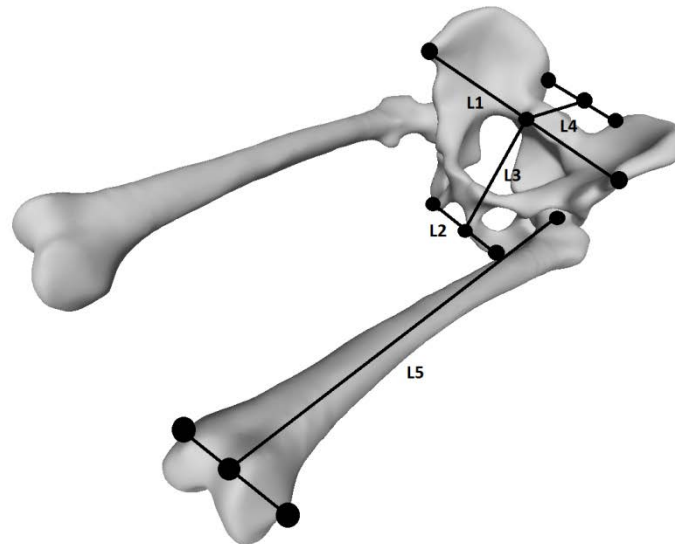
Fig. 3.4   Chosen distances between landmarks

The distances characterizing the pevis (width, height and depth) and femur (length) dimensions are summized in Table 3.2. All dimensions had an error less than 20 mm on average. The smallest error was found for the distance between the two ischial tuberosities, while larger errors were found for pelvis width and depth.

The distance between predicted and corresponding scanned vertices for each subject was also calculated. The average of the mean distances between the predicted and measured external shape was 26.6 ± 9.3 mm (std of the all means) over the 36 subjects. Figure 3.5 shows the mean 3D distances between the predicted and scanned external shape over the 36 subjects on the template. The large error areas are mainly located on the groin, the belly and the knees.
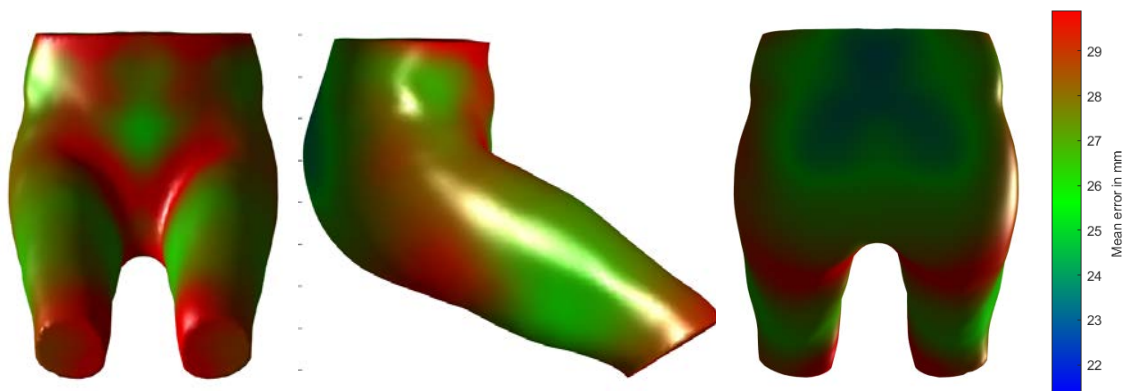
Fig. 3.5   Mean error between predicted and real shape over the 36 subjects.

4   Discussion

In this study, a parametric model of the buttock-thigh complex containing both skin and bones (pelvis and femur) was developed. The model was built from 3D scans of the external shape of 36 participants coupled with 54 CT scans (from cadavers) of the pelvis and femurs .

Stature and BMI were used as anthropometric predictors. Local dimensions such as the thigh length (buttock-popliteal) and waist circumference were also tested. Similar results were obtained suggesting the global predictors such as stature and BMI are good candidates as predictors.

Two limitations were identified for this research study. Fisrtly, bones geometry of the subjects could not be acquired simultaneously. Bones geometry was indirectly estimated from palpated bones landmarks combined using the PC models previously developed with an another dataset. Merging two datasets from two different samples may be an issue. Moreover, manual palpation of bony landmarks and estimation of the ischial tuberosities position may reduce the level of accuracy. Due to lack of data, the estimated bone geometry from palpated points were assessed for only one subject from which both skin and bones were available using MRI. The mean distance between the palpated and digitally palpated anatomical landmarks was 12.9 mm. The mean distance between the predicted skin shape and reconstructed one from MRI was 17.2 mm. Clearly validation should be continued with more subjects. Secondly, only 36 volunteers participated in data collection. Though participants were selected to cover the large range of variation in stature and BMI, the developed parametric model is limited by the small sample size.

The parametric model of thigh-buttock complex developed in the present study will be used to generate the meshes of future finite element models in order to later estimate the contact pressure on a seat for a large range of anthropometry.

Aknowledgement

List of references

Al-Dirini, R. M. A.; Reed, M. P.; Hu, J.; Thewlis, D.: Development and Validation of a High Anatomical Fidelity FE Model for the Buttock and Thigh of a Seated Individual. Annals of Biomedical Engineering 2016 44 (9) pp. 2805–16.

Allen, B.; Curless, B.; Popović, Z.: The Space of Human Body Shapes: Reconstruction and Parameterization from Range Scans. ACM SIGGRAPH 2003 Papers, pp. 587–594.

Choi, H. Y.; Kim, K. M.; Han, J.; Sah, S.; Kim, S.-H.; Hwang, S.-H.; Lee, K. N. et al.: Human Body Modeling for Riding Comfort Simulation. Digital Human Modeling 2007, pp. 813–23.

De Looze, M. P.; Kuijt-Evers, L. F. M.; Van Dieën, J.: Sitting Comfort and Discomfort and the Relationships with Objective Measures. Ergonomics 46 (10) 2003, pp. 985–97.

Hostens, I.; Papaioannou, G.; Spaepen, A.; Ramon, H.: Buttock and Back Pressure Distribution Tests on Seats of Mobile Agricultural Machinery. Applied Ergonomics 32 (4) 2001, pp. 347–55.

Serge van Sint, J.: Color Atlas of Skeletal Landmark Definitions E-Book: Guidelines for Reproducible Manual and Virtual Palpations 2007

Kyung, G.; Nussbaum, M. A.: Driver Sitting Comfort and Discomfort (Part II): Relationships with and Prediction from Interface Pressure. International Journal of Industrial Ergonomics, Seating Dynamics, 38, 2008, pp.5–6

Mergl, C.; Anton, T.; Madrid-Dusik, R.; Hartung, J.; Librandi, A.; Bubb, H.: Development of a 3D Finite Element Model of Thigh and Pelvis. SAE Technical Paper 2004

Peng, J.; Panda, J.; Van Sint Jan, S.; Wang, X.: Methods for Determining Hip and Lumbosacral Joint Centers in a Seated Position from External Anatomical Landmarks. Journal of Biomechanics 48 (2) 2015, pp. 396–400.

Jolliffe, I.: Principal component analysis. John Wiley & Sons, Ltd 2002

Salvia, P.; Van Sint Jan, S.; Crouan, A.; Vanderkerken, L.; Moiseev, F.; Sholukha, V.; Mahieu, C.; Snoeck O.; Rooze, M.: Precision of Shoulder Anatomical Landmark Calibration by Two Approaches: A CAST-like Protocol and a New Anatomical Palpator Method. Gait & Posture 29 (4) 2009, pp. 587–91.

Savonnet, L.; Duprey, S.; Wang, X.: Coupling rigid multi-body and deformable finite element human models for assessing seat discomfort. Digital Human Modeling Symposium 2016

Siefert, A.; Pankoke, S.; Wölfel, H. -P.: Virtual Optimisation of Car Passenger Seats: Simulation of Static and Dynamic Effects on Drivers' Seating Comfort. International Journal of Industrial Ergonomics 38 (5–6) 2008, pp. 410–24.

Swearingen, J. J.; Wheelwright C. D.; Garner, J. D.: An analysis of sitting areas and pressures of man. 1962

Verver, M. M.; van Hoof, J.; Oomens, C. W. J.; Wismans, J. S. H. M.; Baaijens, F. P. T.: A Finite Element Model of the Human Buttocks for Prediction of Seat Pressure Distributions." Computer Methods in Biomechanics and Biomedical Engineering 7 (4) 2004, pp. 193–203.

Wu, G.; Siegler, S.; Allard, P.; Kirtley, C.; Leardini, A.; Rosenbaum, D.; Whittle, M. et al.: ISB Recommendation on Definitions of Joint Coordinate System of Various Joints for the Reporting of Human Joint Motion—part I: Ankle, Hip, and Spine. Journal of Biomechanics 35 (4) 2002, pp. 543–48.

Xiaoming, D; Jindong, R.; Chunlei, S.; Lemeng, L.: Simulation of the Interaction between Driver and Seat. Chinese Journal of Mechanical Engineering 26 (6) 2013, pp. 1234–42.

Upman et al.:
Application of Motion Analyses and Digital Human Modeling for the Ergonomic Evaluation of Handbrakes in Passenger Vehicles

Upmann, A.[1]; Rausch, J. R.[2], Heinrich, K.[3, 4], Fischbein, I.[1], Brüggemann, G. P.[3]

[1] Ford-Werke GmbH, Cologne, Germany
[2] Ford Research & Innovation Center, Aachen, Germany
[3] German Sport University Cologne, Institute of Biomechanics and Orthopaedics, Germany
[4] University of Applied Sciences Koblenz, Department of Mathematics and Technology, Remagen, Germany

Abstract

Comfort is an important factor in product purchase decisions. Consequently, vehicle manufacturers aim for ergonomic vehicles which minimize occupants' discomfort. To achieve this in the past mainly subjective evaluation studies were conducted. Nowadays the use of Digital Human Models (DHMs) has increased. It helps to optimize ergonomics of vehicle control elements early in the product development phase and allows for efficient and objective assessments. Thus the application of DHMs can reduce development costs and raise customer satisfaction. The combination of specialized DHMs allows for consideration of various factors influencing discomfort and thus a holistic ergonomic evaluation. Many studies have shown that physical discomfort is linked to biomechanical parameters and the musculoskeletal system. Hence it is crucial that the ergonomic evaluation with DHMs includes the analysis of the musculoskeletal load which is influenced by kinematics and kinetics. The handbrake is an essential control in vehicles. This work provides the first demonstration that the perceived discomfort of the handbrake application can reliably be predicted based on postural, biomechanical and mathematical modelling.

Methods: In two studies 111 and 40 subjects rated the discomfort for several handbrake variants while their handbrake application motion was recorded using video cameras respectively an optical motion capturing system (infrared cameras). The motion and the external forces were analyzed in the biomechanical software AnyBody Modeling System (AMS). A method to predict key postures of the control task with RAMSIS was developed and applied for selected key percentiles of body height. The postures of the RAMSIS prediction method were compared to the postures derived from subjects during the experiment. Biomechanical parameters such as joint reactions, joint muscle moment measures, muscle activities, joint angles as well as metabolic power and energy were calculated for the key percentiles in AMS. Stepwise regression was applied to develop a prediction model for discomfort based on biomechanical factors.

Results: Handbrake application postures calculated with RAMSIS correspond well to the study postures. The results of motion analyses and posture modeling in RAMSIS

can be used in vehicle development for visualization purposes and clearance checks respectively development of clearance zones. The results can also be utilized as input for biomechanical analyses with AMS and subsequent discomfort prediction. The discomfort calculated with the developed prediction model was proven to be well in line with the ratings derived from the subjective evaluation ($r^2 = 0.96$, $r^2adj = 0.94$). As a result, a user-friendly procedure has been proposed to quantify handbrake discomfort with DHMs which are typically available in automotive development. This method can be applied at early stages of the automotive development to enhance the ergonomics of the vehicle interior. It allows for increasing efficiency and objectivity as well as for saving resources and budget. Handbrake application has been chosen as one ergonomic example to develop a procedure for the reliable prediction of discomfort based on postural, biomechanical and mathematical modeling. Developing similar procedures for other applications – related to vehicle, other products or workplace design – could be a focus of future research.

Key words:

Digital Human Modeling, Ergonomics, Discomfort, Motion Analyses, AnyBody, RAMSIS, Posture Prediction, Handbrake Application

1   Introduction

Comfort is recognized as a major selling argument and an important factor in customers' product buying decisions (HARTUNG, 2006). Therefore, vehicle manufacturers aim to develop ergonomic vehicles outperforming competitors by minimizing discomfort and maximizing comfort. Considerable efforts have been made in recent years to study how to achieve this (DE LOOZE, KUIJT-EVERS & DIEËN, 2003; Hartung, 2006).

Several objective and subjective measurement methods are in use to assess comfort or discomfort (DE LOOZE et. al, 2003). In the past mainly subjective evaluation studies were conducted to assure an ergonomic design of vehicles. Nowadays the use of Digital Human Models (DHMs) has increased, offering several advantages: It decreases the number of resource intensive subjective evaluation studies. It enables objective assessments already at early stages of car development as well as quick evaluations and comparisons of several variants. So, the application of DHMs allows for optimization of vehicle ergonomics, increasing efficiency and decreasing development costs. (GEUß, 1995; NAUMANN & RÖTTING, 2007; BONIN et al., 2014; UPMANN & RAIBER, 2014)

Numerous studies have shown that discomfort is linked to biomechanical parameters and the musculoskeletal system (ZHANG, HELANDER & DRURY, 1996; HELANDER & ZHANG, 1997; KYUNG, 2008). Hence it is crucial that the evaluation with DHMs includes the analysis of the musculoskeletal load which is influenced by kinematics and kinetics. Several studies have been completed on discomfort predictions based on Digital Human Modeling, e.g. WANG, CHEVALOT & TRASBOT (2008). Research is ongoing on combining distinct DHMs for more holistic discomfort assessments (PAUL & LEE, 2011; ULHERR & BENGLER, 2014).

A lot has been published on biomechanical parameters influencing reach posture and reach discomfort as well as their prediction with DHMs (JUNG & CHOE, 1996; ZACHER & BUBB, 2004; WANG, CHEVALOT & TRASBOT, 2008; WANG & TRASBOT, 2011). However, although the handbrake is an essential and security relevant control in vehicles, little has been published about handbrake application (LIETMEYER, 2013).

A handbrake is typically located in the center console and subject to trade-offs between many vehicle components and attributes. Thus it extremely important to understand - and quantify - how changes in the handbrake design influence the customers' discomfort perception.

The aim of the present study was to develop an efficient and reliable procedure to predict the discomfort perception of the handbrake application in passenger vehicles. The intention was to base it on biomechanical criteria derived from the application of Digital Human Models (DHMs) typically used in automotive industry. Consequently RAMSIS (Human Solutions GmbH, Kaiserslautern, Germany) and AMS (AnyBody Technology A/S, Aalborg, Denmark) were chosen due to their modeling capacities. To achieve the overall objective, a multistep study has been accomplished. The entire project consists of five major subprojects:

1. Two empirical studies (customer clinics, chapter 2.1, 2.2) with subjects: preliminary and main study. (HEINRICH et al., 2014; RAUSCH & UPMANN, 2015; UPMANN, 2016)

2. The reconstruction of motion capturing data and development of an AMS (AnyBody Modeling System) handbrake application model, see chapter 2.3. (RAUSCH, POPOVIC & UPMANN, 2014)

3. The development of a RAMSIS procedure for realistic posture prediction for selected key percentiles; summarized in chapter 3.1. (RAIBER, 2015).

4. Calculation of biomechanical parameters in AMS based on RAMSIS postures and analyses of their relation to the subjective ratings from the second empirical study for key perecentiles; see chapter 3.2. (UPMANN, 2016)

5. The development of a mathematical transfer function to predict discomfort ratings for new handbrake variants based on RAMSIS and AMS simulation; see chapter 4. (UPMANN, 2016)

2 Customer clinics

2.1 Study Design

Two studies with subjects were completed, the preliminary study and the main study. First 111 subjects adjusted their seat and steering wheel to their individual position during a test drive in a mass production vehicle. Their respective driving position were transfered to a static mock-up which was used in both studies.

In the preliminary study all subjects were asked to asses the discomfort of handbrake application for seven different handbrake locations (plus one repetition). Their motion was recorded with video cameras. A cluster analysis of the movement patterns revealed three different motion strategies, mainly influenced by body height (RZEPKA, 2015).

40 subjects with good repeatability of the ratings and representative movement patterns were included in the main study. Once again the subjects evaluated the handbrake application discomfort for seven different handbrake locations (plus one repition) in the mock-up. For this purpose, a CP-50 scale (modified from SHEN & PARSONS, 1997) was applied. Aiming for a higher variation in ratings the geometric range of handbrake positions was extended. This time subjects had markers attached and a Vicon Nexus Motion Analyses system was used to capture the motion. The handbrake was equipped with force calibrated stain gauges to accurately record the force and the force direction during the the handbrake application.

In the main study, a cross-sectional experimental design with randomized order of the trials (and repition of the center point) was used. In the factorial design, the three independent variables were handbrake location in x (fore-aft respectively anterior-posterior direction), in y (left-right respectively medial-lateral direction) and in z (height respectively inferior-superior direction). Handbrake locations were the same

for all subjects, independent of seat adjustment. Figure 2.1 compares the location ranges covered by the preliminary (grey) and the main (orange) study.The orange field represents most of the automotive market (UPMANN, 2014) and ensures meaningfull variation of the subjective ratings and movement patterns.
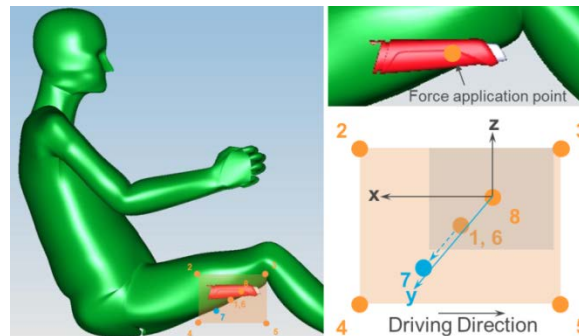
Fig. 2.1 Illustration of the investigated handbrake locations in the main study (modified from UPMANN, 2016, p. 145).

2.2 Analyses of subjective evaluations

For the statistical analysis, the CP-50 ratings e ($1 \leq e \leq 50$) were linearly transformed into the perceived discomfort ratings d ($0 \leq d \leq 100$). The range of 0 - 100 is expected to ease application and interpretation in an engineering environment. A "50" on the CP-50 scale was converted into the value 0 (no discomfort, best rating). A "0" on the scale was converted into a 100 (high discomfort, worst rating) for the further analysis.

To assess the reproducibility, subject's discomfort ratings for the mid location (labeled 1 and 6) were compared. The absolute difference between both ratings was calculated for each subject. As shown in Table 6.2, 40 % of subjects had a shift smaller than 10. These subjects rated obviously more reproducibly than the 30 % of the subjects, which showed a shift larger than 20.

Table 2.1 Difference between the discomfort ratings for the same location (1 resp. 6) (Upmann, 2016, p. 151).

Absolute difference	Percentage of subjects	Cumulative percentage of subjects
0 to 5	20	20
6 to 10	20	40
11 to 15	10	50
16 to 20	20	70
≥ 21	30	100

Table 2.2 (left) shows mean, SD and median for the different handbrake locations. The ratings for some locations were not normally distributed. Pairwise Mann-Whitney tests showed that ratings for several handbrake locations have significantly different medians. Analysis of the data revealed linear relationships between body height and discomfort, see Figure 2.2. This figure also shows that the variation of ratings by people of similar body height is larger than the mean change in discomfort ratings between small and tall individuals (discomfort regression line decline over body height).

So, it is not beneficial to use the discomfort ratings of individual subjects as targets for the discomfort predictions. For the development of mass production vehicles, it is common to focus on average ratings of key customer percentiles. This suggests to consider the same key body height percentiles as typically used in automotive development – 5F and 50 F(5th and 50th percentile female) as well as 50M and 95M (50th and 95th percentile male). This study references bodyheight percentiles (with all other body measures at the corresponding average) according to SizeGERMANY 2013 database. The ratings for the key percentiles ("study ratings") were derived from the regression equations of actual subjects' ratings and the body heights and are shown in Table 2.2 (right). This procedure allows to consider body height dependent characteristics, but exclude characteristics very specific to a single subject. The "x" in Figure 2.2 marks the discomfort for 50 F for handbrake location 4.

Table 2.2 Left: Descriptive statistics of the discomfort ratings the main study (UPMANN, 2016, p. 152). Right: Discomfort target values for the handbrake locations and percentiles The mean discomfort of location 1 and 6 is taken for the analysis. (UPMANN, 2016, p. 177)

| Descriptive statistics				Discomfort of key percentiles			
Handbrake Location	Mean	SD	Median	5F	50F	50M	95M
1	28.85	15.97	24	27.38	27.65	27.95	28.24
2	64.80	17.46	63	72.39	69.01	65.42	61.78
3	46.10	18.23	43	44.43	44.85	45.31	45.77
4	34.25	20.38	29	48.09	38.71	28.74	18.61
5	55.65	23.58	56	41.68	51.78	62.53	73.44
6	32.70	15.46	31	30.90	32.65	34.51	36.40
7	48.40	18.88	50	49.24	49.06	48.88	48.69
8	33.00	15.06	34	32.54	32.07	31.56	31.05
1 and 6	30.78	12.53	28	29.14	30.15	31.23	32.32
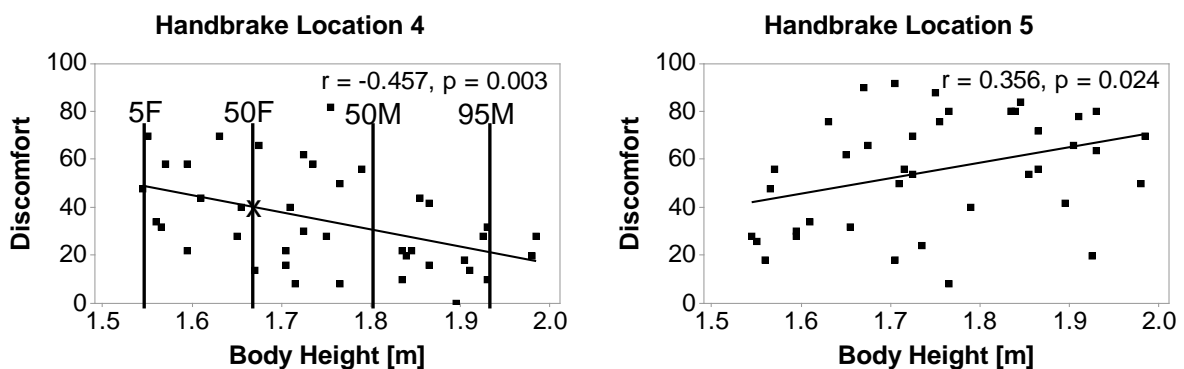
Fig. 2.2 Discomfort ratings versus body height for location 4 (left) and 5 (right) (UPMANN, 2016, p. 153).

2.3 Motion Analysis

In the main study, ten infrared cameras (Vicon MX F40) and Vicon Nexus motion capture software (Version 1.8.2, Vicon, Los Angeles, USA) were used. Recording frequency was 150 Hz. The spring force of the handbrake, the application angle and the 3D tension forces in the handbrake handle were sampled at 1500 Hz. Using this data and the anthropometry of the 40 subjects, the individuals were modeled in RAMSIS and AMS to determine joint angles, reaction forces, joint loads, muscle activity etc.

The subjects were simulated in AMS and their motion was reconstructed using the Vicon motion files. The analysis showed that the motion parameters (such as joint angles and joint coordinates) changed linearly through the handbrake pull operation.

Analysis of the data also revealed linear relationships between body height and joint angles for each of the handbrake locations. Figure 2.3 shows as example the elbow flexion for the right arm for handbrake location 1 at start and end. Here again, it was obvious to focus on the joint angles of key body height percentiles (5F, 50F, 50M and 95M) for further analysis. The "study joint angles" were calculated in the same way as the key percentile ratings for start and end of handbrake application.
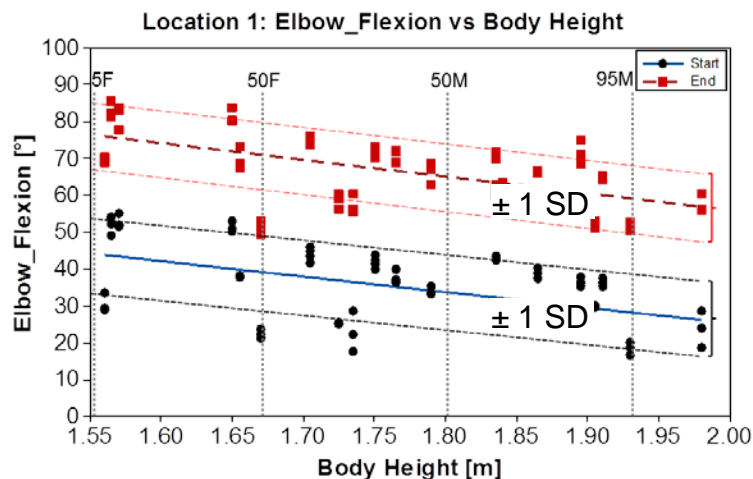
Fig. 2.3 Scatter plot of the elbow flexion for the right arm for handbrake location 1 at start (black dot, solid line) and end (red rectangle, dotted regression line). The dashed lines above and below regression lines as well as the brackets on the right indicate plus/minus one standard deviation. (UPMANN, 2016, p. 156)

3 Human Modeling

3.1 RAMSIS Modeling

The Digital Human Model RAMSIS is widely used for posture prediction. It can model desired percentiles for numerous geographic regions. The aim of the posture modeling in this study was to develop a procedure for reliable posture prediction for the four key percentiles – for both key frames of the handbrake application at all

seven handbrake locations. The development of the procedure comprised three major steps, which are illustrated in Figure 3.1. The bullet points to the right indicate specific challenges and their resolutions.
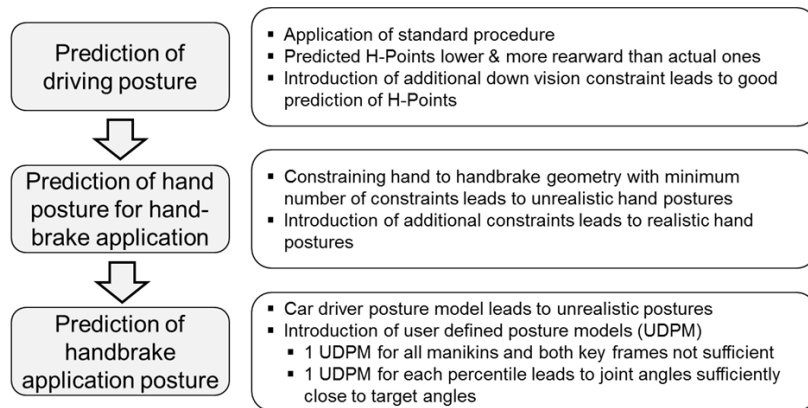
Fig. 3.1   Major steps of developing the procedure for handbrake application posture prediction with RAMSIS (UPMANN, 2016, p. 163).

Firstly the driving posture (step 1) was predicted using the RAMSIS Car Driver Posture Model (CDM). After introducing additional down vision constraints the predicted H-Points and steering wheel positions were well in line with those from the test drive in the preliminary study. Individual participants' H-points were determined via motion capturing analysis in Anybody. Respective regression lines over the body height were used to calculate "mean/typical" values for the key percentiles. For development of the handbrake application posture prediction the H-Point was assumed fixed, the left hand was located on the steering wheel, the right foot was placed on the brake pedal and the left one on the footrest. After choosing the most adequate grasp type and introducing auxiliary geometry with corresponding constraints, the resulting **hand postures** (step 2) provided a good alignment of the hand and the lever handle. It looked sufficiently realistic for all handbrake locations and percentiles. To model the **whole body handbrake application posture** (step 3) the right hand was constrained to the handbrake while the other contraints were kept as specified above.

Fig. 3.2   Left: Typical predicted handbrake posture when using the RAMSIS Car Driver Posture Model (Upmann & Raiber, 2014, p. 13). Right: Predicted RAMSIS postures compared to corresponding subjects in start (left) and end (right) position from side (up) and top (down) view (RAIBER, 2015, p. 85).

The application of the standard CDM for parking brake application resulted in major differences between the predicted postures and observed subjects' postures (e.g. RAMSIS did not flex the elbow while p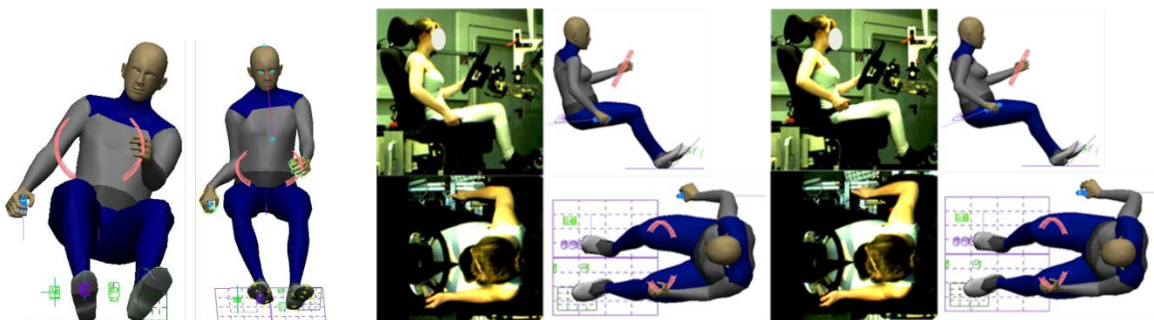ulling the handbrake, see Figure 3.2, left). The original foundation data, the CDM was based upon (GEUß, 1995), seems not sufficiently account for handbrake application.

Thus constraints were kept as before but the CDM target postures were modified by developing User Defined Posture Models (HUMAN SOLUTIONS GMBH, 2014). A single UDPM for all four key percentiles did not facilitate good alignment of model and target (study joint angles). Thus, for each key percentile one dedicated UDPM was developed and used for all handbrake locations. Calculated joint angles were compared to the study joint angles. The acceptable range for the prediction was defined as the target angle plus/minus one standard deviation (compare Figure 2.3). The application of the four resulting UDPMs results in a reliable posture model as exemplary shown in Figure 3.2, right.

3.2   AnyBody Modeling

AMS (AnyBody Modeling Software) is a musculoskeletal modeling system (DAMSGAARD, RASMUSSEN, CHRISTENSEN, SURMA & ZEE, 2006; ANYBODY TECHNOLOGY A/S, 2017) which is also used by several automotive companies. An additional Ford proprietary user interface, the AnyFord Interface (AFI) was applied. It enables the user e.g. to import postures and anthropometric data from RAMSIS to simplify scaling and biomechanical analysis based on RAMSIS simulations (SIEBERTZ & RAUSCH, 2006).

The handbrake application was modeled in AMS (see Figure 3.3) based on the anthropometry and predicted posture of the RAMSIS manikins (four key percentiles, see above), the vehicle and handbrake geometry and handbrake force. AMS can calculate a very large number of biomechanical parameters. A pre-selection of parameters was completed to identify factors with a major impact on the discomfort perception and to quantify their influence. Based on literature research 214 biomechanical parameters calculated by AMS were selected for further analysis. They include the factor groups joint reactions, joint moment measures (created by muscles), muscle activities, joint angles as well as metabolic power and energy. Values were calculated for the four key percentiles, all seven handbrake locations and for three time steps: start of handbrake application without force transfer at handle (suffix S) and with force transfer at the handle (suffix F) and end of handbrake application (suffix E). Also squared values ware calculated because quadratic relations to discomfort were expected (in particular for joint angles). This results in 1252 biomechanical factors.
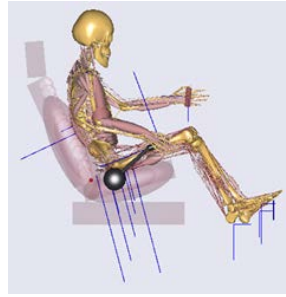
Fig. 3.3 Inverse dynamics results for step 4 of the handbrake application for 50M and handbrake location 8. Blue lines illustrate external forces. (UPMANN, 2016, p. 175)

In each factor group there are several factors with highly significant correlations to discomfort ($p < 0.01$, $r = 0.54 - 0.723$). This confirms strong associations between the biomechanical parameters and the study discomfort ratings. Joint reactions, joint moment measures and muscle activities achieved highest correlation coefficients.

4 Prediction Model

Stepwise regression (BORTZ, 1999; TABACHNICK & FIDELL, 2007) was applied in MINITAB (2015) to establish a discomfort prediction model. Biomechanical values significantly correlating to discomfort were considered for the regression analysis. Factors with very small influence were neglected. So, the regression analysis was conducted with a dataset containing discomfort (compare Table 2.2, right) and 201 biomechanical parameters for all seven handbrake locations and the four key percentiles. Variables with a probability of more than 90% to increase the prediction quality were added to the regression model. Variables with a probability of more than 90 % not to increase the prediction potential were removed. The resulting prediction model contains nine factors (listed in Table 4.1). The values $r^2 = 0.96$, $r^2_{adj} = 0.94$ and the standard error $S = 3.5$ indicate high prediction quality.

Table 4.1 Percentage of variance in the data explained by each factor of the regression equation (UPMANN, 2016, p. 204).

Factor group	Factor	Sequen-tial SS	% total SS	Cum. % total SS
Joint reaction force	RightElbowHumeroUlnar_AxialMoment_E	3029.39	52.30	52.3
Joint reaction force	RightAcromioClavicular_InferoSuperiorForce_E²	1350.78	23.32	75.62
Joint moment measure	RightWrist_AbductionMoment_E	369.1	6.37	81.99
Joint angle	RightGlenoHumeral_ExternalRotation_E²	207	3.57	85.56
Joint angle	RightSternoClavicular_Elevation_E²	203.56	3.51	89.07
Mean muscle activity of shoulder/arm	MeanMuscleActivity_RightPectoralisMajorClavicularPart_F²	159.18	2.75	91.82
Max. muscle activity of shoulder/arm	MaxMuscleActivity_RightTrapeziusScapularPart_F	147.6	2.55	94.37
Met. energy/power	MetabolicPower_RightArm_S	56.19	0.97	95.34
Met. energy/power	MetabolicPower _LLeg_F²	48.16	0.83	96.18

The shares of the variation in discomfort explained by each factor (% of total Sums of Squares [SS]) are listed in Table 4.1. The five predictors explaining the major portion (89 %) of discomfort variation are all related to the end time step. They include two joint reaction forces, one joint moment measure and two joint angles. The four remaining predictors contribute by another 7.1 % to the discomfort variation. They are related to both start time steps (with and without force transfer at handbrake handle). They comprise muscle activities and metabolic power values.

The discomfort index provides a very good prediction of the ratings, see Figure 4.1. There are only minor, non-critical differences: The discomfort index is predicted slightly too high for location 1 for 50F and for location 8 for 95M. The discomfort index is predicted slightly too low for location 3 for 5F and 50F. The small differences are acceptable; especially when considering that the spread of subject's ratings is of the same magnitude for the handbrake location which was assessed twice (labelled 1 and 6, see Table 2.2).

The mean calculated discomfort of 5F, 50F, 50M and 95M was shown to be a good predictor for mean discomfort of all 40 subjects. The same has been proven for the median. (Upmann, 2016)
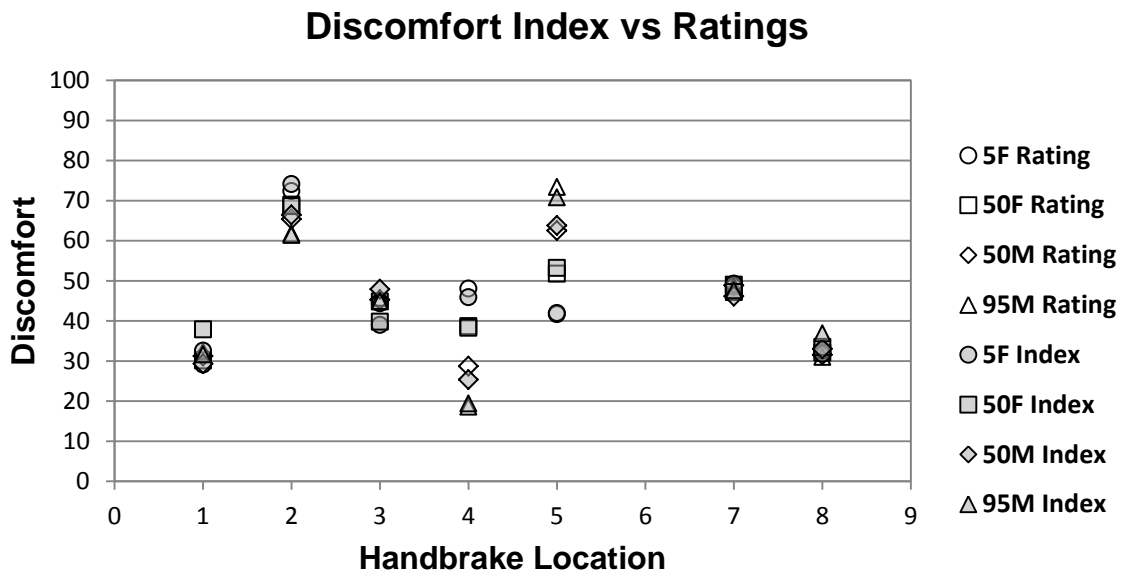

Fig. 4.1   Discomfort index compared to the ratings. (UPMANN, 2016, p. 209)

5   Results & Conclusions

This study indicates that the perceived discomfort of handbrake application ~~can~~ may be predicted reliably (based on postural, biomechanical and mathematical modelling) for key percentiles (5F, 50F, 50M, 95M) and subsequently for the mean rsp. median of a customer group.

A user-friendly procedure has been proposed to quantify handbrake discomfort with DHMs already in use in automotive development. It can be applied early in the development. Thereby it can increase efficiency and objectivity of evaluating handbrake ergonomics and enhance it.

40 subjects of a representative range of age and body height participated in the main study. Handbrake application of a typical handbrake lever was assessed for seven locations covering the spread of typical handbrake locations in passenger vehicles.

Further work is required to validate the developed models. Future research may investigate to what extent the results of this work can be applied to differing driver populations (e.g. with regards to anthropometry, handbrake application habits, age).

Additionally, it will be interesting to understand how far the results can be applied to handbrakes with different designs, handbrake locations beyond the passenger car range (such as in commercial vehicles), handbrakes with restricted accessibility (e.g. by armrest) or other hand operated controls such as the gearshift lever.

In future studies it could be investigated if the discomfort prediction accuracy can by further increased by including pressure distribution at the contact areas of the human and vehicle environment (such as the handbrake handle and the seat) as a factor.

In the present study handbrake application has been chosen as one ergonomic example to develop a procedure for the reliable prediction of discomfort based on postural, biomechanical and mathematical modeling. Similar procedures for other applications – related to vehicle or other (non-automotive) products or workplace design – could be a focus of future research.

Acknowledgement

List of references

AnyBody Technology A/S. (2017). AnyBody Technology Company Website. Retrieved February 25, 2017 from http://www.anybodytech.com/.

Bonin, D.; Wischniewski, S.; Paul, G.; Wirsching, H.-J.; Upmann, A.; Rausch, J.: Exchanging data between Digital Human Modeling systems - A review of data formats. 3rd International Digital Human Modeling Symposium. Tokyo, Japan, 2014.

Bortz, J.: Statistik: Für Sozialwissenschaftler (5. vollständig überarbeitete Auflage). Berlin, Germany: Springer, 1999.

Damsgaard, M.; Rasmussen, J.; Christensen, S. T.; Surma, E.; Zee, M.: Analysis of musculoskeletal systems in the AnyBody Modeling System. Simulation Modelling Practice and Theory, 14(8), 1100–1111.

De Looze, M. P,; Kuijt-Evers, L. F. M.; van Dieën, J.: Sitting comfort and discomfort and the relationships with objective measures. Ergonomics, 46(10), 985–997, 2003.

Geuß, H.: Entwicklung eines anthropometrischen Meßverfahrens für das CAD-Menschmodell RAMSIS. In H. Geuß, R. Krist & A. Seidl (Eds.), Forschungsvereinigung Automobiltechnik E.V. (FAT) (FAT): Vol. 123. RAMSIS - Ein System zur Erhebung und Vermessung dreidimensionaler Körperhaltungen von Menschen zur ergonomischen Auslegung von Bedien- und Sitzplätzen im Auto. Frankfurt, Germany: Forschungsvereinigung Automobiltechnik E.V. (FAT), 1995.

Helander, M. G.; Zhang, L.: Field studies of comfort and discomfort in sitting. Ergonomics, 40(9), 895–915, 1997.

Heinrich, K.; Upmann, A.; Rausch, J.; Lietmeyer, J.; Rzepka, P.; Fischbein, I.; Brüggemann, G.-P.: Projektbericht: Analyse und Beurteilung der Handbremsbetätigung. Cologne, Germany, 2014.

Human Solutions GmbH (2014). RAMSIS NextGen Ergonomics User Guide. Kaiserslautern, Germany: Human Solutions GmbH.

Jung, E. S.; Choe, J.: Human reach posture prediction based on psychophysical discomfort. International Journal of Industrial Ergonomics, 18(2-3), 173–179, 1996.

Kyung, G.: An integrated human factors approach to design and evaluation of the driver workspace and interface: Driver Perceptions, Behaviours, and Objective Metrics (Dissertation). Blacksburg, Virginia, USA: Virginia Polytechnic Institute and State University, 2008.

Lietmeyer, J.: Determinanten von Diskomfort bei Betätigung der Feststellbremse im Pkw (Masterarbeit). Cologne, Germany: Deutsche Sporthochschule Köln, 2013.

Naumann, A.; Rötting, M.: Digital Human Modeling for design and evaluation of human-machine systems. MMI-Interaktiv, 12 (April 2007).

Paul, G.; Lee, W. C.: Interfacing Jack and AnyBody: Towards anthropometric musculoskeletal Digital Human Modeling. 1st International Symposium on Digital Human Modeling. Lyon, France, 2011.

Raiber, P.: Simulation of the handbrake application in RAMSIS NextGen. Body Posture Prediction for Different Handbrake Locations and Customer Groups (Master Thesis). Cologne, Germany: German Sport University Cologne, 2015.

Rausch, J. R.; Popovic, N.; Upmann, A.: AnyBody Handbrake IR Gateway Review. Aachen, Germany: Ford, 2014.

Rausch, J. R.; Upmann, A.: Technical report: Handbrake study. Aachen, Cologne, Germany: Ford, 2015.

Redelmeier, D. A.; Kahneman, D: Patients' memories of painful medical treatments: real-time and retrospective evaluations of two minimally invasive procedures. Pain, 66(1), 3–8, 1996.

Rzepka, P.: Identifizierung und Klassifizierung von Bewegungsstrategien zur Betätigung einer Handbremse (Masterarbeit). Cologne, Germany: Deutsche Sporthochschule Köln, 2015.

Siebertz, K.; Rausch, J. R.: AnyBody Car Driver Model, revision 2: (Technical Report No. SRR-2006-0067). Aachen, Germany: Ford, 2006.

Ulherr, A.; Bengler, K.: Global discomfort assessment for vehicle passengers by simulation (UDASim). 3rd International Digital Human Modeling Symposium. Tokyo, Japan, 2014.

Upmann, A.; Raiber, P.: Simulation of handbrake application. RAMSIS User Conference 2014. Kaiserslautern, Germany, 2014.

Upmann, A.: Application of Digital Human Modeling for the ergonomic evaluation of handbrakes in passenger vehicles (Dissertation). Cologne, Germany: German Sport University Cologne, Institute of Biomechanics and Orthopaedics, 2016.

Wang, X.; Chevalot, N.; Trasbot, J.: Prediction of in-vehicle reach surfaces and discomfort by Digital Human Models. Digital Human Modeling for Design and Engineering Conference and Exhibition, Pittsburgh, Pennsylvania, USA, June, 17-19, 2008. SAE Technical Paper Series No 2008-01-1869. Warrendale, Pennsylvania, USA: Society of Automotive Engineers.

Wang, X.; Trasbot, J.: Effects of target location, stature and hand grip type on in-vehicle reach discomfort. Ergonomics, 54(5), 466–476, 2011.

Zacher, I.; Bubb, H.: Strength based discomfort model of posture and movement. Digital Human Modeling for Design and Engineering Symposium, Rochester, Michigan, USA, June, 15-17, 2004. SAE Technical Paper Series No. 2004-01-2139. Warrendale, Pennsylvania, USA: Society of Automotive Engineers.

Zhang, L.; Helander, M. G; Drury, C. G.: Identifying factors of comfort and discomfort in sitting. Human Factors: The Journal of the Human Factors and Ergonomics Society, 38(3), 377–389, 1996.

Conradi & Alexander:
Comparison of reach envelopes of digital human models and their real counterparts

Conradi, J., Alexander, T.

Fraunhofer FKIE, Germany

Abstract

One of the main features of Anthropometric Digital Human Models (DHM) is the determination of reach envelopes. They help to assess the reachability of a certain spot in 3-dimensional space and therefore are used to design locations of controls in work spaces. However, these reach envelopes rely on the simulated body parts, on arm and hand segments and on integrated simulations of hand, arm and shoulder joints. Different DHMs have different ways of modeling the segments and joints, as well as their interaction. So, distinct DHMs may come to varying reach envelopes for anthropometrically corresponding models. Furthermore, inaccuracies of DHMs compared to their real counterparts may result in differences in their reach envelopes as well. In our survey, we compared the reach envelopes of the right arm of subjects and the modeled reach envelopes of a commercial DHM. The reach envelope of the humans was taken with an infrared tracking system. The subjects moved their hands starting in the forward reach position and then in spirals to the biggest possible extent. The resulting motion path was compared to the calculated reach envelopes of the individual matching counterparts of one commercial DHM. To do so, the reach envelopes were divided in 13 segments. For each segment, individual differences were calculated. We found differences for all segments. The mean subject's reach envelope was mostly moderately bigger than DHMs reach envelope (-0,8 mm to 32.6 mm). Furthermore, we compared the reach envelopes of two commercial DHMs. They differed in all segments, the extent of the difference ranged from 31.5 mm to 141.0 mm.

Key words:

Reach envelopes; Digital Human Model; DHM; comparison; real data; simulation

1   Introduction

Digital Human Models are provided to enhance the design of working places during the CAD-based design process. Therefore, they have visual images of simulated human bodies and provide a variety of additional functionalities to analyze factors concerning human abilities in interaction with the environment (DUFFY, 2009; MÜHLSTEDT, KAUßLER, & SPANNER-ULMER, 2008). One of these functionalities is the reach envelope. It is used to analyze and depict the area, which can be reached by a specified part of the body in a specific scenario. It is based on the moving limbs and body parts functionality of the DHMs.

In human bodies, different kinds of joints facilitate intricate motions and movements. The full digital representation of these joints is highly complicated and the calculation of a model which considers all bones and joints would be very costly. Therefore, in most DHMs software simplified models are used. In some cases, the model may consist of a skeleton reminding of a matchstick man. More intricate joints, e.g. the shoulder joint, are represented by several sticks and point joints. This skeleton can be connected to an outer model, which is based on discs in the form of the horizontal profiles. The outline of these profiles resembles the skin of the model. A motion of the skeleton triggers a motion of the skin (e.g. HUMAN SOLUTIONS, 2015). Other models consist of a number of body segments, which are connected by joints. Based on these simplified bodies and joints, postures and movements in the DHMs are calculated (e.g. SIEMENS, 2015).

Human bodies show a broad range of variation. This is true for total height or weight as well as for proportions. The proportion of torso and legs for example, has a major influence on sitting height and therefore on reach envelopes and eye height. This needs to be considered in ergonomic evaluations. Sophisticated anthropometric models take this into account. They facilitate functionality for different proportion typologies. Furthermore, they provide options to create models with individual dimensions (e.g. HUMAN SOLUTIONS, 2015; SIEMENS, 2015). This often results in high face validity. But as the posture prediction of these models is based on simplified body representations, the validation is questionable (ALEXANDER & CONRADI, 2011; ALEXANDER & PAUL, 2014). Practitioners often report checking the outcome of DHMs by visual inspection and adjusting tested environments according to this. But the validity of the outcome is not ensured. Furthermore, there are only few studies that address this issue (e.g. ALEXANDER & CONRADI, 2003; KAJAKS, STEPHENS, & POTVIN, 2011; PARK, CHAFFIN, RIDER, & MARTIN, 2003). However, for data validation in direct comparison to human data, individual models matching their real counterparts have to be used.

In an earlier study, we compared static anthropometric data of human models with anthropometric data of two DHMs. Therefore, we used specific anthropometric data of human as defined in e.g. ISO 7250 (2008). We found a good representation for some values and sizable differences for others. The circumference of extremities was too small, as well as the torso and hip. Nevertheless, we found differences between the DHMs in forward, upward and sideward reach dimensions. Here, both DHMs show very different results. DHM1 (RAMSIS 3.7) calculated some static anthropometric dimensions correctly (arm span) and underestimated others (forward reach and upward reach); DHM2 (JACK 6.2) overestimated these dimensions. Arm

span and forward reach were overestimated by about 70 mm. These differences in estimations are probably due to the simplified shoulder joints of the DHMs (CONRADI & ALEXANDER, 2016).

In workplace design, the DHM is placed in a given surrounding or workplace. Usually, the intention for using the functionality reach envelope is to analyze the reachability of controls. As the usage of controls varies, this functionality can be adjusted. For example, the end joint as well as the starting joint has to be defined. In many seated positions, e.g. inside a vehicle, the starting joint will be the shoulder; this is true especially for controls which have to be accessible easily. In other scenarios, the inclusion of motions of the back may be acceptable. At the other end of the motion chain, the end joint is of crucial importance. If the usage of the control includes only a slight pressing or a touching gesture, the top of the index or middle finger may be used as end joint. However, if grasping or even a powerful movement of the fist is needed, the whole hand has to be considered.

DHMs provide functionalities regarding different end as well as starting joints. In Figure 1.1, left hand side, the calculated reach envelope for the tip of the right middle finger is depicted. In some cases, flexing on an included joint, e.g. the elbow. In Figure 1.1, three different reach envelopes for different conditions are given, i.e. comfort zone (second from left), the reach envelope (second from right) and the different joint (right hand side).

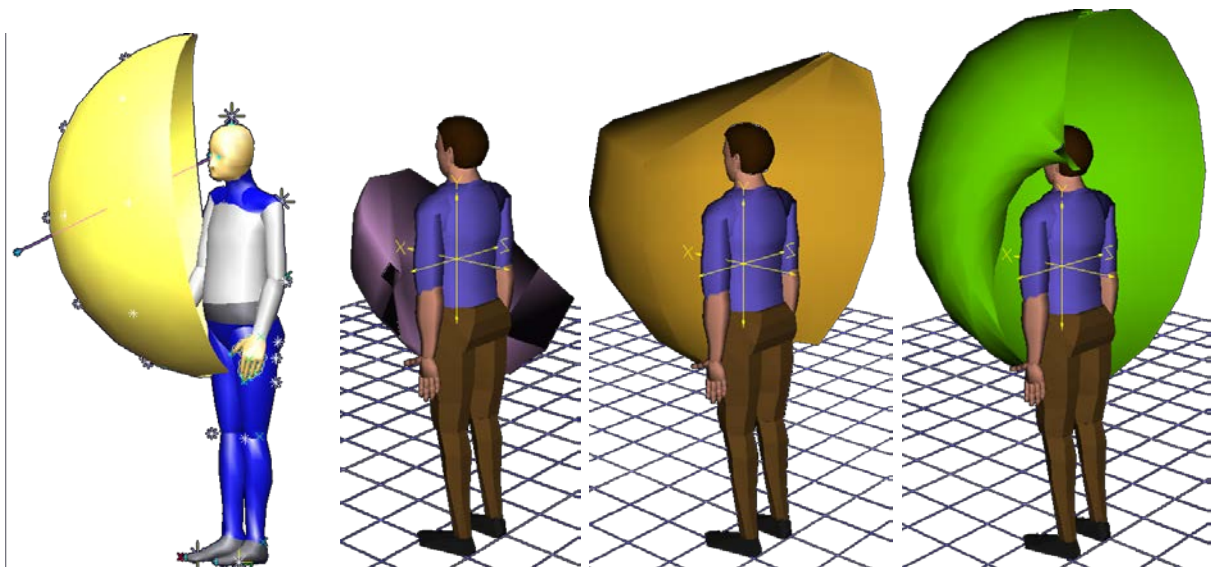**Fig. 1.1**   Calculated and depicted reach envelopes of DHM1 (left) and DHM2 (right)

For these reasons, the outcome of DHMs must be validated. Therefore, we performed a validation study for reach envelopes of DHMs. We used data from a motion study with humans and compared the data with reach envelopes calculated by DHM1. Additionally, we compared the calculated reach envelope of DHM1 and DHM2.

2 Method

In our study, n=27 healthy participants volunteered. They were aged 21.6 ± 2.0 years (mean ± standard deviation, SD). Based on their anthropometric data, individual human models for each of them were created by the anthropometric editors of DHMs.

Available anthropometric digital human models had to be selected. To be able to meet the purpose of the study, they had to provide editors for body dimensions. Therefore, we used the DHMs RAMSIS 3.7 (DHM1) and Jack 6.1 (DHM2). Both of them facilitate the design of mannequins with individual anthropometric dimensions. Using this, models were created which matched their real counterparts as close as possible. In case of DHM1 we used all 18 editable anthropometric dimensions to design the models; this included the three control dimensions body height, sitting height and waist circumference as well as 15 free dimensions including length dimensions of the arms and legs as well as breadth and depths dimensions of the trunk. In DHM2, seven different dimensions were edited: height, weight, sitting height, arm length, hip breadth, buttock to knee length and bideltoidal breadth. Editing of further dimensions triggered automated changes in the previously adjusted dimensions; therefore editing was stopped at this point.

To determine the reach envelope of the humans, they had to fulfill a specially designed motion task. During this task, they were equipped with passively reflecting infrared markers which covered all relevant body parts. Marker positons relevant for measuring the reach envelopes were shoulder (acromion) and fingertip of the middle finger (dactylion III). The positions of the markers were recorded by means of an A.R.T. infrared tracking system (frequency: 50Hz). The participant's task was to stretch the right arm to the front. From this position, they moved the stretched arm and hand in an enlarging spiral toward their motion limit. During the procedure, the participants were told to keep the rest of the body as still as possible. In Figure 2.1, a single motion path of a participant's right fingertip is depicted (red).
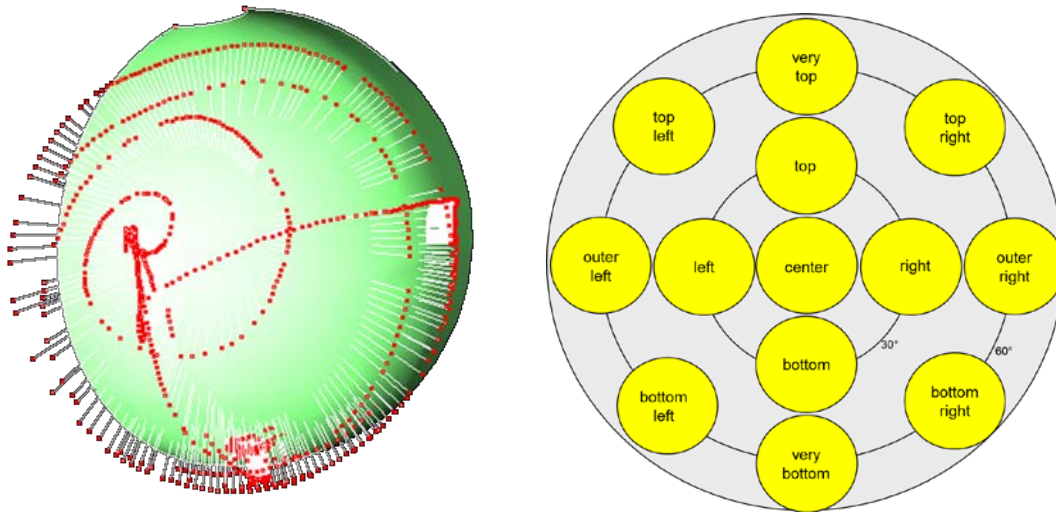
Fig. 2.1 Left hand side: Motion path of the right middle finger tip (red), calculated reach envelope of DHM1 (green) and distance between human data and DHM sphere (grey); right hand side: Zones and their location on the reach envelope

The motion path and the position of the acromion were matched according to the position of the acromion (see Figure 2.1). This was done for each participant's individual motion path and their corresponding digital model, the minimum difference between the reach envelope and each point on the motion path was calculated.

The difference showed a big variance even for individuals. The deviation changed for different locations of the reach envelope. To cover this, the data was allocated to 13 different circular zones on the hemisphere. The center zones was set at the center of the reach envelope, which resulted in 1 zone; the next set of zones was set at 30° from the center, which resulted in 4 zones and the third set at 60° from the center, resulting in 8 zones. An illustration of the zones and their location on the hemisphere can be found in Figure 2.1, right hand side. The zones are shown in the perspective of the participant (right hand).

For DHM2 comparison between the motion paths and reach envelope was not possible. To facilitate an evaluation of DHM2's reach envelopes, it was imported into DHM1. The difference between the envelopes of DHM1 and DHM2 was assessed by calculating the minimum distance in the abovementioned zones. This was done for one individual model. This model represented a person close to the mean dimensions (i.e. height: 64. percentile; sitting height: 51. percentile, waist circumference: 63. percentile)

3   Results

Concerning the deviation of the motions paths and the reach envelope of DHM1, the results are given in Table 3.1. Besides the mean and SD of the difference in mm, the minimum and the maximum of the difference is given. This is done to show the overall range of the data. Positive differences indicate higher values in the real counterparts and consequently an underestimation of real reaching capabilities by the DHM; negative numbers are found in zones, in which the person's reaching motion is overestimated by the DHM.

Table 3.1 Deviation of participant's motion paths and reach envelope of DHM1 in mm; positive numbers indicate an underestimation of human values.

Zone	Mean	SD	Min	Max	n
very top	8.5	37.0	-42.5	173.5	23
top left	-0.8	33.6	-67.1	36.6	12
Top	10.2	22.2	-57.0	36.1	24
top right	0.4	1.4	-0.8	6.9	24
outer left	-2.9	57.7	-79.3	61.2	7
left	13.3	51.4	-77.8	64.8	24
Center	21.4	35.0	-60.4	50.4	25
Right	16.0	15.1	-25.7	37.7	25
outer right	2.7	6.6	-14.1	16.9	23
bottom left	10.7	82.3	-95.3	91.9	7
Bottom	32.6	56.8	-66.7	157.3	24
bottom right	14.5	32.9	-59.1	54.9	23
very bottom	19.7	60.1	-83.8	78.0	19

In the right column, the number of participants that created evaluable data in each zone is given. Originally, n=27 subjects participated in the survey. However, some of the data had to be excluded due to technical reasons, so only a maximum of n=25 created data for the zones center and right. These zones are in the middle of the reach envelope and represent the initial phase of the arm moving task. Therefore, most participants created a high number of data in this zone. In other zones, namely outer left and bottom left (7 participants each) and top left (12 participants) were reached only by a low number of participants. These zones are on the very left of the reach envelope, the low n probably results from the fact, that many of the participants were not able to reach this zone with stretched arm and therefore created no data.

The highest mean difference was found in the bottom zone (32.6 mm), followed by the center (21.4mm) and very bottom (19,7mm). These zones are in the lower part of the very front of the participant. In this part, the reach envelope underestimates the arm reach. In the zones top (10.3 mm), left (13.3 mm), right (16 mm), bottom left (10.7 mm) and bottom right (14.5mm) the distance is still underestimated 10-20 mm. These zones are grouped around the zones with a higher difference. In the other zones, the mean difference is less than 10mm. However, we found a high variability in almost all zones, according to the standard deviation as well as by the high range of the minimum and maximum.

To assess the reach envelope of DHM2, it was integrated in the graphic editor of DHM1. In Figure 3.1, a depiction of the two envelopes is given. The reach envelope of DHM1 (yellow) is smaller than the reach envelope of DHM2 (green). Additionally, the reach envelope of DHM2 integrated a simulation of the partly bowed elbow in the top left part of the envelope, while DHM considers a bigger portion of sideways and slightly backward reaching on the right side of the envelope.
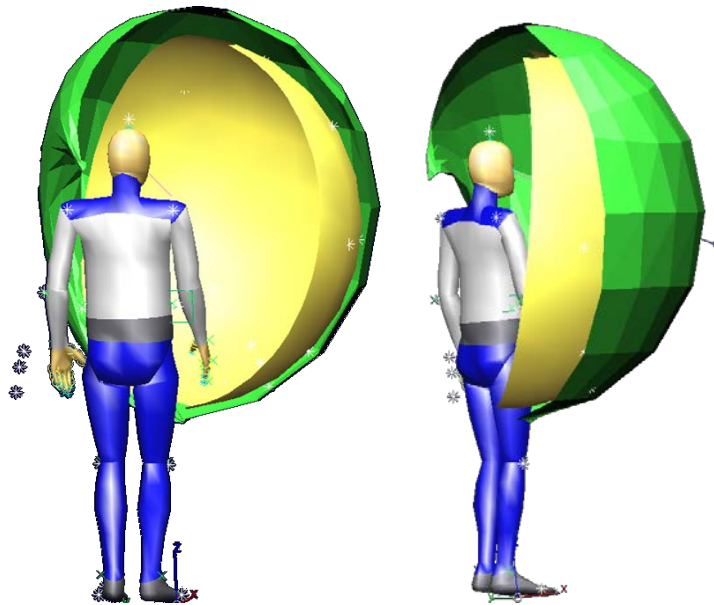
Fig. 3.1 Visual representation of the reach envelopes of both DHMs in two different perspectives (DHM1: yellow, DHM2: green)

For a middle-sized model, the difference of the simulated reach envelopes was calculated by means of the abovementioned zones (see Table 3.2).

We found difference of up to 140 mm, whereas in all zones DHM2 simulated a bigger reach envelope than DHM1. Highest differences were found in the very top (140.9 mm), top left (117.3 mm) and top right (129 mm). In the lower zones on the right hand side, lower differences were found (e.g. bottom right: 31.5 mm).

Table 3.2 Differences between the reach envelopes of the DHMs, positive numbers indicate a bigger reach envelope in DHM2.

Zone	Difference [mm]	Zone	Difference [mm]
very top	140.9	right	50.4
top left	117.3	outer right	-
Top	96.2	bottom left	75.1
top right	129.0	bottom	48.6
outer left	99.7	bottom right	31.5
left	93.5	very bottom	60.0
Center	63.1		

4   Conclusion

In this study, we compared reach data of participants with simulated reach envelopes of DHMs. In DHM1 we found moderate mean differences. In the front and downward direction they proved to be about 20 mm, adjourning zones showed mean differences of 10-20 mm. In the top, we found differences of less than 10 mm. This confirms earlier findings, where the anthropometric dimensions arm span and forward reach were calculated smaller in DHM1 than found in participants (CONRADI & ALEXANDER, 2016). However, while we found a difference of 21.4 mm in the forward zone, the anthropometric data showed a mean difference of 102 mm. This gap might be caused by the different tasks. While in our study stretching the arm to the front was only part of a bigger task, in anthropometric measuring the main focus is set on stretching forward and the participant perceives the measuring. In contrast, measuring motion paths by infrared is not perceived directly and therefore may cause a little more relaxed pose. The inaccuracies we found result in underestimating reaching abilities. This leads to a conservative workplace design and ensures that a high number of humans will be able to reach the predicted reach zones. However, variability of differences was very high, with standard deviations of up to 82 mm. This was confirmed by the value of minimal and maximal difference, which showed a range of -95 up to 173mm. Thus, there has to be expected a number of users whose needs cannot be satisfied by means of the DHM. All in all DHM1 showed a good representation of the mean reaching abilities of humans. However, human motion behavior shows a much bigger variability and individuality than DHM1 gives reason to expect.

The comparison of the reach envelopes of two DHMs showed differences of up to 140 mm. especially in the top regions; DHM2 simulated a distinctively bigger reach envelope for the right middle finger than DHM1. Regarding the fact that DHM1 showed a quite accurate simulation especially in this area, DHM2's simulation overestimates human abilities. Manual controls, which are placed in this part of the envelope, can be expected to cause reaching problems. In the front and in the middle areas, differences were lower, about 45-80 mm. Here DHM2 still overestimates human reaching abilities, but the differences are much lower than in the top regions. These results are in accordance to an earlier survey, where we found that DHM2 calculated forward reach 70 mm longer in DHM2 (CONRADI & ALEXANDER, 2016). In the lower zones on the right, the difference decreases to 31 mm and overestimated mean human reach only by about 10-20 mm. However, variability of human reaching abilities varies very much, and it is to be expected, that some users are still able to reach the whole predicted reach envelope, while others users will fail to reach most of the predicted regions.

List of references

Alexander, T.; Paul, G.: Ergonomic DHM Systems - Limitations and Trends – A Review Focused on the 'Future of Ergonomics'. In: Proceedings of the 3rd Digital Human Modeling Symposium in Tokyo, JP, 2014.

Alexander, T.; Conradi, J.: On the Applicability of Digital Human Models for Personal Equipment Design. In: HCI International 2011, Vol. 174 Communications in Computer and Information Science. Berlin, Heidelberg: Springer, 2011, p. 315-319.

Alexander, T.; Conradi, J.: Analysis of Anthropometry and Range Validity of the Digital Human Model RAMSIS.Transactions-Journal of Passenger Cars-Mechanical Systems. Warrendale, US: Society of Automotive Engineers, 2003.

Conradi, J.; Alexander, T.: Analysis of Reach Accuracy for Digital Human Models and their Real Human Counterparts. Proceedings of the Digital Human Modeling Conference, Montreal, Canada, 2016.

Duffy, V. G.: Human factors and ergonomics. Handbook of digital human modeling: Research for applied ergonomics and human factors engineering. Boca Raton: CRC Press, 2009.

Human Solutions: RAMSIS NextGen 1.1, Ergonomics User Guide. Kaiserslautern, 2015.

ISO 7250: Basic human body measurements for technological design – Part 1: Body measurement definitions and landmarks, 2008.

Kajaks, T.; Stephens, A.; Potvin, J. R.: The effect of manikin anthropometrics and posturing guidelines on proactive ergonomic assessments using digital human models. International Journal of Human Factors Modelling and Simulation, 2011, 2(3).

Mühlstedt, J.; Kaußler, H., Spanner-Ulmer, B.: Programme in Menschengestalt: Digitale Menschmodelle für CAx- und PLM-Systeme. Zeitschrift für Arbeitswissenschaft, 62(2), 2008, pp79–86.

Park, W.; Chaffin, D. B., Rider, K., Martin, B. J.: Simulating Complex Manual Handling Motions via Motion Modification: Performance Evaluation of Motion Modification Algorithm. In Proceedings of SAE Digital Human Modeling for Design and Engineering Conference . Montreal, June 16-19, 2003.

Siemens: Classic Jack. Retrieved from http://www.plm.automation.siemens.com/de de/products/tecnomatix/assembly_planning/jack/classic_jack.shtml, 2015

Reed & Park:
Comparison of Boundary Manikin Generation Methods

Reed, M. P., Park, B.-K. D.

University of Michigan Transportation Research Institute, USA

Abstract

Ergonomic assessments using human figure models are frequently conducted using a small family of manikins chosen to span a large percentage of target user population with respect to anthropometric variables. Boundary manikins have most frequently been generated through a process that uses a principal component analysis of selected standard anthropometric variables to establish target dimensions that are subsequently used to scale a figure model. The availability of three-dimensional body shape data and associated statistical methods provides some alternatives. In particular, the principal component analysis can be conducted on the vertices that define the body size and shape and boundary manikins can be selected in that space. This paper compares two methods of generating manikin and provides some guidance on both manikin generation and application.

Key words:

body scanning, body shape modeling, boundary manikins

1   Introduction

For many ergonomic analyses, the distribution of body size among the target user population is an important consideration. Scaling of figures in digital human modeling software systems to represent people with a range of sizes is considered a baseline capability and considerable effort has been focused on developing and evaluating this functionality.

Ideally, virtual ergonomic assessments would be conducted with thousands of avatars representing the target user population, each possessed of not only appropriate body dimensions but also strength, range of motion, skills, and preferences. However, with current software systems and procedures, only body size and shape is typically varied, although range of motion and strength capability are also parameterized. Importantly, efficiently evaluating a candidate design with thousands of virtual users is currently beyond the capability of most systems. The question then arises as to which small number of manikins should be used for the analysis.

Many design decisions are made "in the tails" of the anthropometric distributions, i.e., a particular design feature might disaccommodate people who are either large and small on some dimension. Hence, manikins are commonly chosen on the "boundary" of some anthropometric space so that the family of manikins to be used includes individuals who are large and small on various dimensions.

A variety of methods have been proposed for selecting boundary manikins. Often manikins are chosen based on univariate percentiles on one or two dimensions, such as 5th-percentile stature and body weight. It is immediately apparent that such manikins do not provide meaningful accommodation estimates, because stature and body weight are rarely limiting dimensions.

Recognizing that most ergonomic analyses involve multiple dimensions, researchers and practitioners have employed a range of multivariate methods. A set of standard anthropometric variables are chosen that are related to particular analysis or, more commonly, a variety of possible analyses. Values for these variables are obtained from a population assumed to be representative of the target user population. A multivariate statistical analysis is then conducted to determine "cases", i.e., vectors of anthropometric variables, that lie relatively far from the center of the distribution. The most common statistical method is principal component analysis (PCA), which identifies the eigenvectors and eigenvalues of either the covariance or correlation matrix of the anthropometric variables for the selected population. This is usually performed separately for men and women.

PCA performs a rotation of the data into a new space (coordinate system) such that each axis (eigenvector or principal component - PC) is orthogonal to every other and the values of the observations on these axes are uncorrelated. By convention, the first PC is oriented in the direction that the data have the highest variance, the second PC is the orthogonal direction with the next highest variance, and so on. Thus, the first few PCs may capture most of the variance in a dataset, depending on how correlated the variables are.

For large numbers of observations, the distribution of the data in the PC space becomes approximately multivariate normal. As a consequence, parametric methods for establishing a volume within which a desired percentage of the population lies (under the multivariate normal assumption) are attractive. Most commonly, an ellipsoid assumed to contain 95% of the single-sex population is constructed and boundary manikins are defined on the surface of the ellipse. Although the method can be applied at any dimension up to the number of variables in the anthropometric dataset, conventionally manikins have been generated in the space defined by the first 3 PCs. Selecting manikins where the axis intercept the ellipse generates 6 manikins. An infinite variety of other manikins can be generated on the ellipse surface. Choosing midpoints between axes gives an additional 8 manikins for a total of 14 each sex.

Given that the space of the male and female manikins intersects, those female manikins lying within the male space are sometimes deleted along with male manikins lying within the female space (GUAN et al. 2012). At the conclusion of this step, these "manikins" are vectors of standard anthropometric variables. For human figure model analysis, they must be turned into 3D software manikins. Each software provider has a different methodology for scaling their figure given standard anthropometric inputs. Some problems are immediately apparent. First, the list of variables used in the PCA may not match the list of variables required for scaling the figure. Second, the method for scaling the figure may not result in realistic manikins because other variables not specified may not be set appropriately.

An alternative approach to generating body shapes as a function of standard anthropometric variables has been available for some time (ALLEN et al. 2004) The locations of mesh vertices defining the body surface are predicted using statistical regression using data from body scan studies. Typically, a PCA is first conducted to obtain a reduced- dimension representation of the body shape space prior to regression. However, these methods are not yet widely used in commercial human modeling software.

The process described above begins with a fairly small number of standard anthropometric dimensions (lengths, breadths, circumferences) and ends with a 3D manikin. The availability of high-fidelity whole-body scan data provides an opportunity to generate boundary manikins directly. Using PCA, the process proceeds in the same manner as with the standard approach, except that the PCA is conducted on the vertices of a polygonal mesh defining the body surface. In this manner, the analysis considers a large number of body features simultaneously, rather than only a few selected dimensions.

This paper compares manikins generated using these alternatives and discusses the implications for ergonomics evaluation. The contexts in which one approach would be preferred are also discussed.

2 Materials and Methods

2.1 Data Source

The current analysis was conducted using data from 236 U.S. Army Soldiers gathered as part of the Seated Soldier Study (REED and EBERT 2013). Standard anthropometric measures were also obtained and each participant was scanned minimally clad using a VITUS XXL laser scanner in a standing posture. The scan data were fit using a homologous template mesh and procedures published previously (PARK and REED 2015). The template produces a watertight mesh with 14427 vertices and 14454 polygons. Following fitting, the meshes were made symmetrical by averaging left and right vertices. Pose correction to achieve consistent upper-extremity angles was conducted using a morphing method based on radial basis functions.
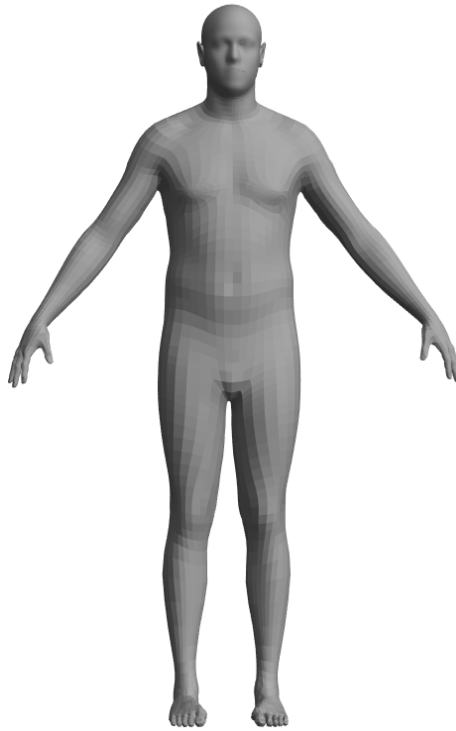
Fig. 2.1 Mean figure

2.2 Anthropometry PCA Boundary Manikins (A-PCA-BM)

The anthropometry PC was conducted using the variables listed in Table 2.1. These variables were selected in previous work (REED et al. 2014) as a minimal set able to represent the primary aspects of anthropometric variation. The PCA was conducted using the covariance matrix. The first 3 PCs accounted for 95.5% of the variance. Boundary manikins were computed on the surface of an ellipsoid on the first 3 PCs enclosing 95% of the distribution under the multivariate normal assumption. In addition to the 6 manikins defined by the intersection between the axes and the ellipsoid surface, 8 additional manikins were defined at {±1, ±1, ±1} in the normalized space.

To obtain 3D manikins, the anthropometry vectors were input to a regression model predicting PC scores as a function of anthropometric variables. The resulting scores were used to generate manikins, using all PCs.

Table 2.1 Body Dimensions Used for PCA On Standard Anthropometry (A-PCA)

Stature	BMI†
Biacromial Breadth	Knee Height, Sitting
Chest Circumference	Waist Circumference
SH/S'*	Hip Circumference
Head Circumference	

† Body mass index, kg/m2

* Ratio of erect sitting height to stature

2.3   Body Shape PCA Boundary Manikins (BS-PCA-BM)

The PCA on the body shape data was conducted using a geometry vector that included standard anthropometric variables, the coordinates of 96 body landmarks, and the coordinates of the vertices of the template mesh. Manikins generated in the space defined by the first 3 principal components, which accounted for 85% of the variance. Because the standard anthropometric variables were included in the geometry vector used for PCA, the associated body dimensions could be obtained.

3   Results

3.1   A-PCA-BM

Table 3.1 lists summary statistics for the anthropometry vectors (all BMs are listed in the appendix). For each variable, the minimum and maximum are presented, since the typical boundary manikin analysis assesses all manikins against a design. The percentiles of the associated minimum and maximum values relative to the original dataset are also presented.

Several trends that reveal functional aspects of the A-PCA-BM procedure are apparent in the percentile values. As expected, the percentiles for individual variables are extreme, with the minimum BM values for 6 variables smaller than any individual in the dataset. The upper tail values are between the 90_{th} and 99_{th} percentiles. The range of percentiles is smallest for SH/S due to the relatively small range of this variable.This illustrates that the scale of a variable, and the number of other selected variables with which it is correlated, strongly influence the outcome of the PCA. BMI and chest, waist, and hip circumference are well correlated and represent four of the nine variables, and hence have similar (and extreme) percentile values. In contrast, the percentile range for SH/S and biacromial breadth are smaller. Table 2 reinforces the fact that BMs generated using the A-PCA method will have unpredictably extreme values, depending on the particular variables included in the analysis.

Table 3.1 Summary Statistics for A-PCA-BM

Manikin	Min	Max	Min%	Max%
Stature	1576	1932	0,0 %	98,7 %
BMI	16.8	37.0	0,0 %	98,3 %
SH/S	0.505	0.541	11,4 %	89,8 %
Biacromial Breadth	378	436	5.5 %	94,5 %
Knee Height, Sitting	485	626	0,0 %	97,9 %
Head Circ	553	589	9,3 %	90,3 %
Chest Circ	811	1272	0,0 %	98,3 %
Waist Circ	619	1206	0,0 %	98,3 %
Hip Circ	841	1249	0,0 %	98,7 %

3.2 BS-PCA-BM

For comparison, Table 3.2 shows statistics for the standard anthropometric variables obtained using the BS method. As expected, the values differ from those obtained using the A-PCA method. The range of stature values is similarly extreme, and the range for SH/S is very similar. For the other variables, the range of body dimensions is generally less extreme. This is expected, because in general variables not closely related to the first 3 PCs will not vary widely in the resulting BMs. BMI, in particular, spanned only the central 50% of the population in this analysis.

Table 3.2 Summary Statistics for BS-PCA-BM*

Manikin	Min	Max	Min%	Max%
Stature	1570	1938	0,0 %	98,7 %
BMI	24.0	29.8	25,4 %	78,8 %
SH/S	0.506	0.541	11,9 %	89,8 %
Biacromial Breadth	387	427	11,4 %	86,4 %
Knee Height, Sitting	482	629	0,0 %	98,3 %
Head Circ	556	586	14,4 %	84,7 %
Chest Circ	966	1116	17,8 %	81,8 %
Waist Circ	826	1000	23,3 %	80,5 %
Hip Circ	964	1126	12,7 %	86,9 %

* Based on reconstructions from the PC score vector generated from the BM-generation procedure.

Figures 5.1 and 5.2 show the manikins generated using the two techniques, sorted by stature. As suggested by Tables 3.1 and 3.2, the manikins span a similar range of stature, but the range of circumferences and BMI is larger in the set of manikins generated by standard anthropometry.

4   Discussion

With current human modeling software, the ideal of conducting ergonomics analysis with thousands of manikins representing the user population is generally not feasible, so analyses must be conducted with smaller numbers of carefully chosen manikins. The outcomes from the widely-used A-PCA-BM approach are strongly dependent on the choice of input variables. For example, choosing multiple variables correlated with body weight will result in less extreme values for length dimensions in the resulting manikin families. This may be seen as a strength of the method, in that dimensions can be chosen that are closely related to the application. In practice, though, not all of the selected anthropometric variables will be equally important and most assessments will be single-tailed, i.e., only affected by large or small body dimensions and not both.

In the current study, BMs generated using a set of standard anthropometric data and rendered in 3D using a statistical body shape model showed a wider range of BMI and segment circumferences than BMs generated in the first 3 PCs of the body shape space. In both cases, manikins with a wide range of stature and a comparable range of SH/S were generated.

An advantage of the BS-PCA-BM method is that no decisions are needed with respect to the variables to be included. However, the choice of the number of manikins to select and where they are to be located in the body shape space is arbitrary. For consistency with typical practice, both the A-PCA and BS-PCA manikins were selected in the space of the first 3 PCs, but other approaches are possible. For example, BMs could be selected on the surface of a hyperellipsoid in 5-dimensional space, then culled based on whether they represented boundary cases on any variables of interest.

Most importantly, neither method is "correct". In addition to being dependent on the underlying database, accommodating the manikin families generated by these techniques does not guarantee any particular level of accommodation. Because PCABMs tend to be extreme, designing to accommodate all of a family of BMs may be unnecessarily limiting.

5   Conclusion

PCA-BMs can be generated in a body shape space rather than using standard anthropometry. This eliminates the need to select a set of body dimensions of interest a priori, but may produce a set of BMs that are less extreme. Care must be taken in interpreting the results of a BM analysis because the selection of manikins is essentially arbitrary, because no principled reason exists to prefer one method of generation over another, and analyses with BMs do not produce any particular level of accommodation in designs.
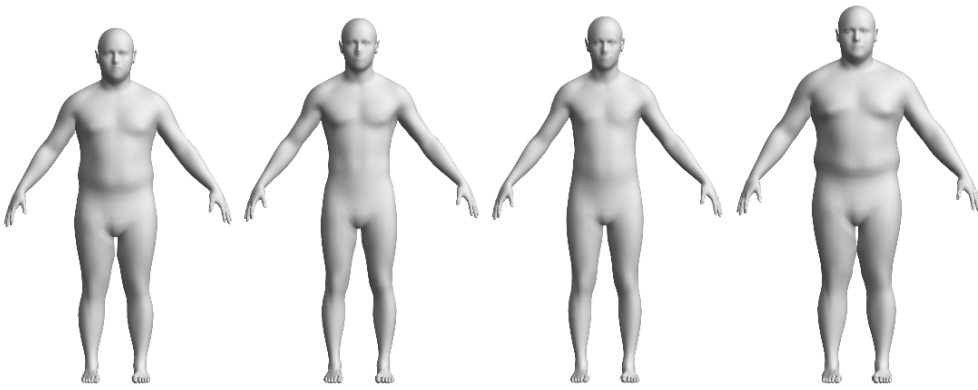
5   11   12   7
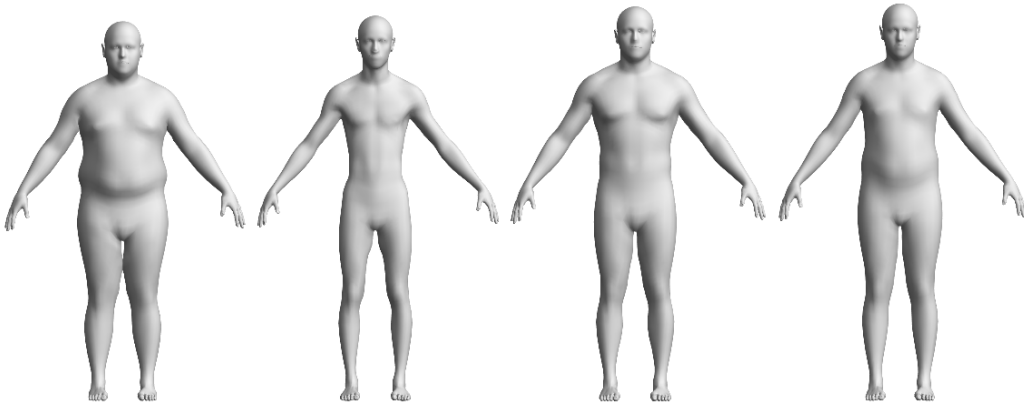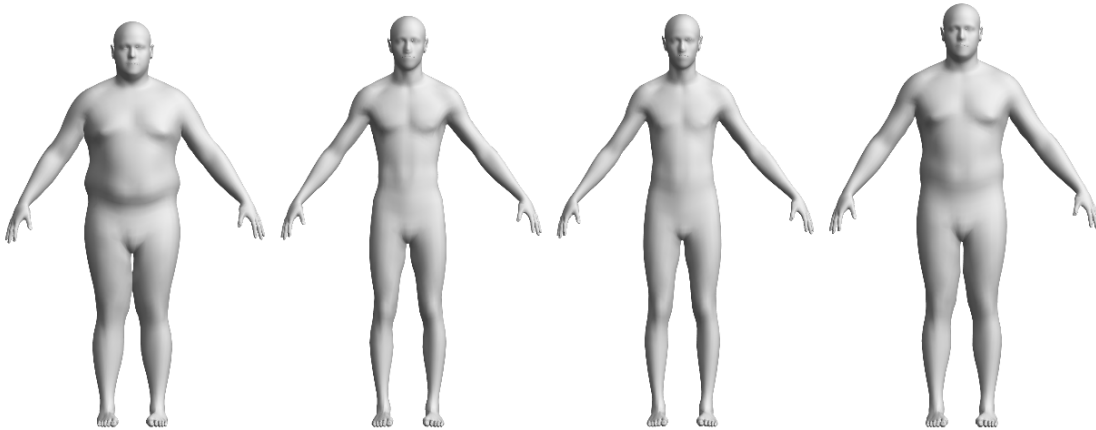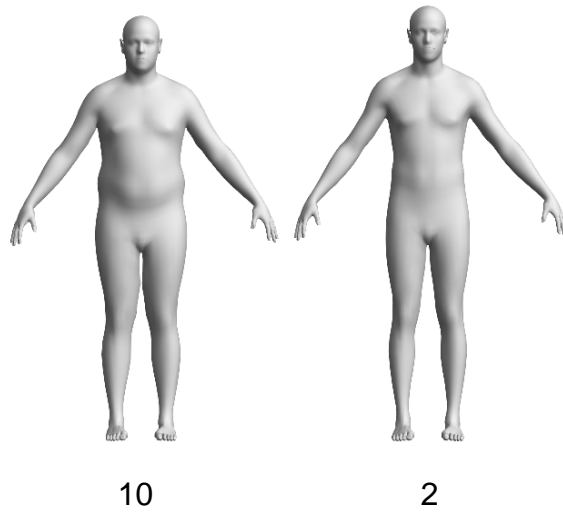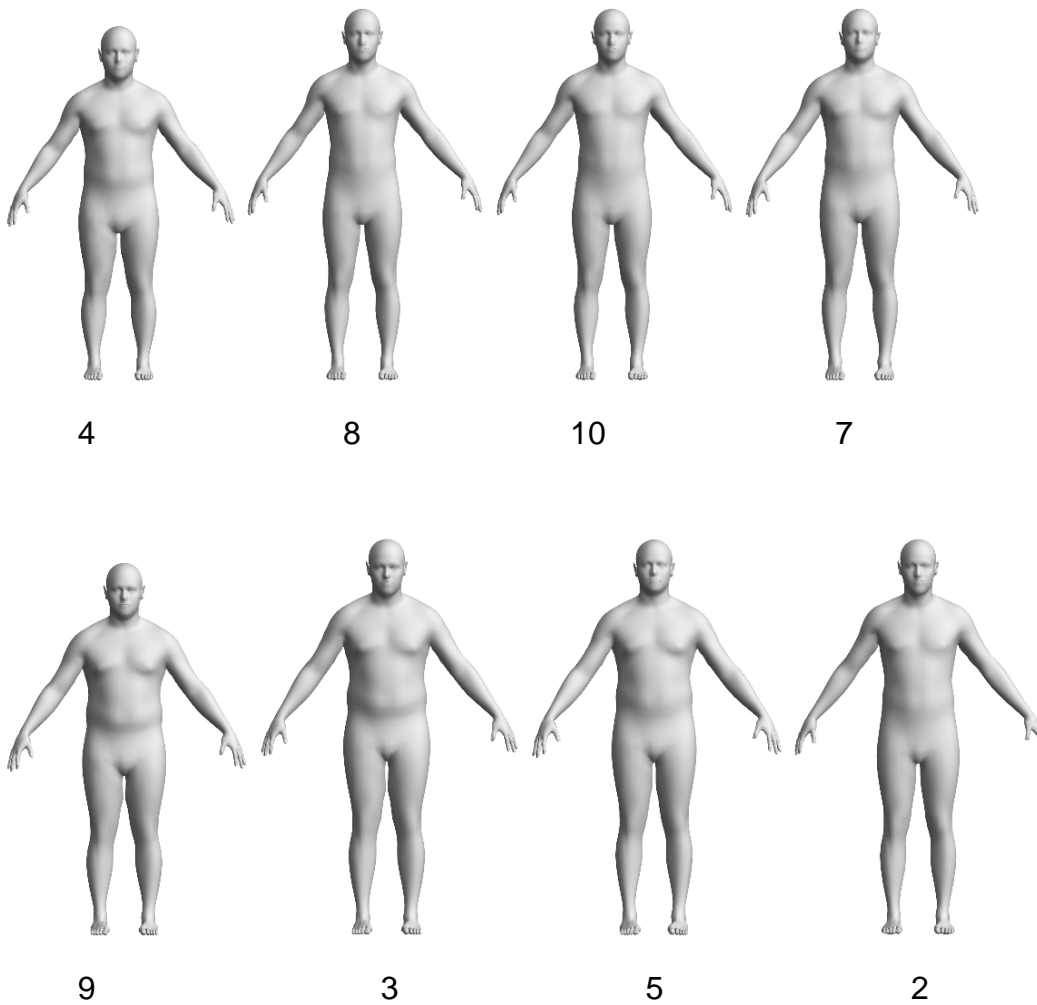
8   1   6   3

4   13   14   9

Fig. 5.1 Boundary manikins generated from standard anthropometry. Numbers refer to Table A1.
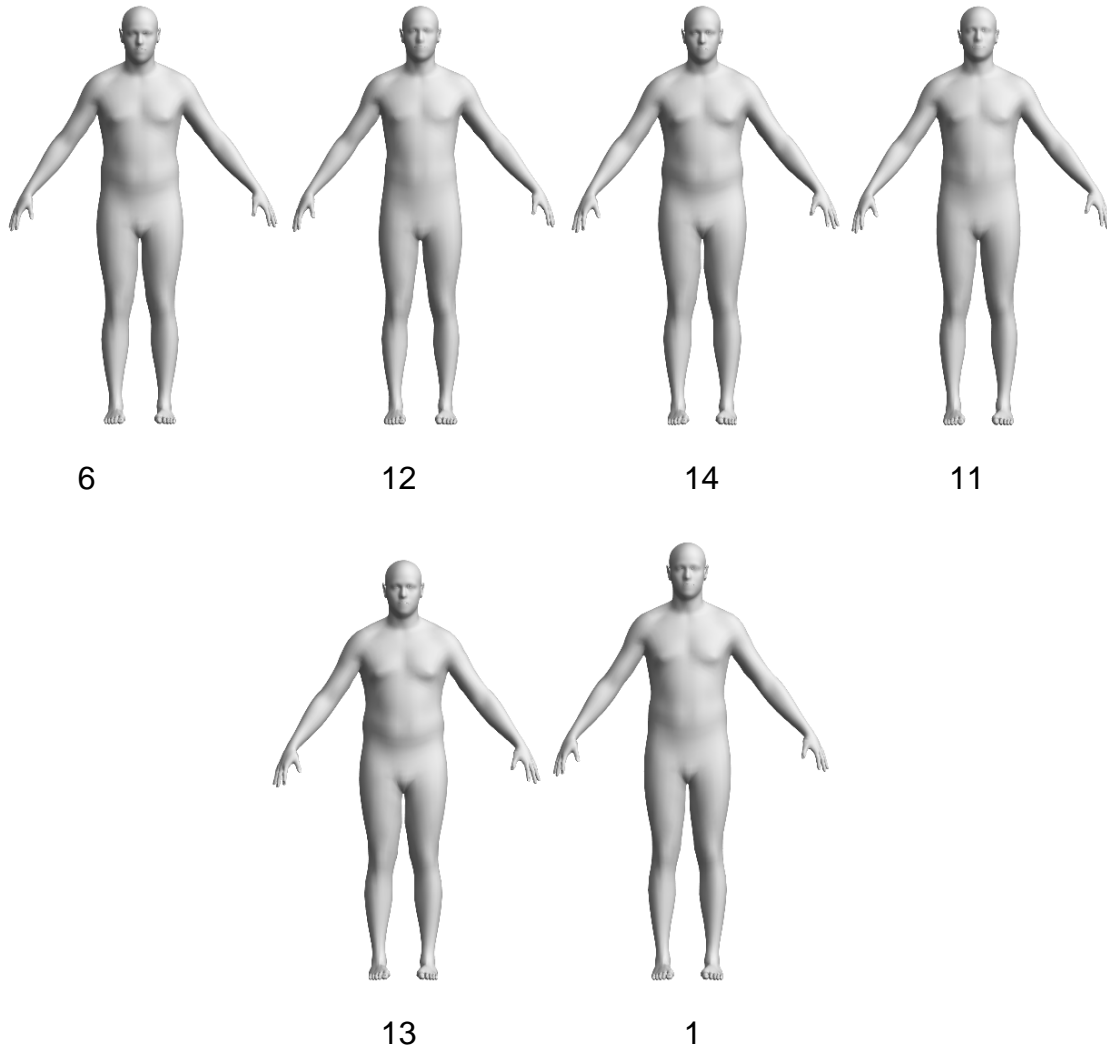
Fig. 5.2 Boundary manikins generated from 3D body shape data. Numbers refer to Table A2.

List of references

Allen, B.; Curless, B.; Popovic, Z.: Exploring the space of human body shapes: Data-driven synthesis under anthropometric control. In Proceedings of Conference on Digital Human Modeling for Design and Engineering. SAE International,2004.

Guan, J.; Hsiao, H.; Bradtmiller, B.; Kau, T.; Reed, M. P.; Jahns, S. K.; Loczi, J.; Hardee, H. L.; Piamonte, D. P. T.: U. S. truck driver anthropometric study and multivariate anthropometric models for cab designs. Human Factors, 54 (5), pp.849-871, 2012.

Reed, M. P.; Park, B-K.; Kim, K. H.; Raschke, U.: Creating custom avatars for ergonomic analysis using depth cameras. Proceedings of the 2014 Human Factors and Ergonomics Society Annual Meeting. HFES, Santa Monica, CA, 2014.

Park, B.-K. and Reed, M. P.: Parametric body shape model of standing children ages 3 to 11 years. Ergonomics, 58(10):17141725.10.1080/00140139.2015.1033480, 2015.

Reed, M. P.; Parkinson, M. B.: Modeling variability in torso shape for chair and seat design. DETC2008-49483. Proceedings of the ASME Design Engineering Technical Conferences. ASME, New York, 2008.

Reed, M. P.; Ebert, S. M.: The Seated Soldier Study: Posture and Body Shape in Vehicle Seats. Technical Report UMTRI-2013-13. University of Michigan Transportation Research Institute, Ann Arbor, MI, 2013.

Technical Session 6 – Industrial Applications of DHM

Ruiz Castro et al.:
IPS IMMA for designing human-robot collaboration workstations

Ruiz Castro, P.[1], Mahdavian, N.[1], Brolin, E.[1], Högberg, D.[1], Hanson, L.[1,2]

[1] School of Engineering Science,University of Skövde, Skövde, Sweden
[2] Industrial Development, Scania, Södertälje, Sweden

Abstract

The global competition has forced manufacturing companies to further increase their productivity. This, together with technology development and changes in regulations, have led to the introduction of new types of workstations in production lines, where human operators collaborate with industrial robots to perform work tasks. As any type of product, these workstations need to be designed in the most optimal way to deliver the expected value. In the design process of these collaborative workstations, separate virtual simulations of industrial robots and human operators can be made with multiple commercial software. Separate simulations reduce the efficiency of the design process and makes it harder to identify successful design solutions. Hence, there is a need for software tools that are capable of simultaneous simulation of the human-robot collaboration in a workstation. Providing engineers with such tools will assist their tasks to optimize the human and robot workflow, while proactively ensuring proper ergonomic conditions for operators.

This paper describes and illustrates how the digital human modelling (DHM) tool IPS IMMA can aid in the design of human-robot collaboration workstations. A use case where the human operator collaborates with a robot to produce a section of a pedal car in a virtual scenario is described. The use case illustrates the current capabilities and limitations of the software to simulate human-robot collaborations in workstations. Hence, the use case aims to provide input for further development of DHM tools aimed to assist the design of human-robot collaboration workstations.

Key words:

Digital Human Modelling, Human-Robot Collaboration, Simulation, Workstation Design.

1 Introduction

1.1 Human-robot collaboration

Production systems in manufacturing companies are evolving due to the constant change in the market and in the competition. The technology required for these new production systems is also changing, becoming more advanced and digitalized, but also more user-centered, taking ergonomics and safety requirements into consideration (MAURICE et al., 2017). This has led to the development of workstations in production settings where robots are starting to have a closer interaction with human operators, by sharing workspaces and handling complex or physically demanding assembly tasks (KRÜGER et al., 2009; MICHALOS et al., 2015). The term **human-robot collaboration** can be defined to represent the condition when there is a common goal that can be achieved jointly between the human and robot, as mentioned by BAUER et al. (2008). Since human and robots have different skills and capabilities, a design objective is to find optimal solutions for how to collaborate most efficiently in such hybrid workstations (CHERUBINI et al., 2016). The objective of the human-robot collaboration is to take advantage of the strength, precision and repetition capabilities of robots, as well as the sensorimotor skills and problem solving capacities of humans (FABER et al., 2015).

Even though the concern of how to successfully distribute work tasks between human and machine has a long history of investigation (FITTS, 1951), the advanced capabilities of contemporary robots and the openings in regulations have led to a revival of the area of how humans and machines successfully can work together. This has led to the definition of different levels of interaction between a human and a robot in a production environment, where safety standards define this interaction in relation to the movements and stop functions of the robot. According to ISO 10218-1:2011, there are four different types of collaborative operations, based on safety:

1. Safety rated monitored stop: no robot motion can happen when operator is in the collaborative workspace.
2. Hand-guiding: there is collaborative robot motion only through direct input from operator.
3. Speed and separation monitoring: collaborative robot motion only when there is a safety distance separation between robot and human.
4. Power and force limiting inherent design or control: collaborative robot motion that allow collision. But the forces from the robot in a collision in this mode are limited to reduce and avoid injuries on the human.

1.2 Virtual simulations

Currently, due to time and cost reasons there is a tendency to avoid or delay physical evaluations during the design process of workstations. This has led to increased use of evaluations done in digital environments, e.g. using virtual scenarios to evaluate human work (CHAFFIN, 2007). This has presented several advantages, like detailed biomechanical measurements and the possibility to test the workspace with a variety of human morphologies simultaneously. Correspondingly, computerized models are

used to define the robotic tools for a specific environment, by evaluating the required workspace and safety, prior to acquiring the industrial robot (ORE et al., 2015).

Virtual simulations of industrial robots and human operators can be made separately with multiple commercial software, but only few existing software is capable of simultaneous simulations of the human-robot collaboration in a workstation (MAURICE et al., 2017). Therefore, there is need for virtual simulation tools that can aid in the design of collaborative systems by enabling the investigation of design alternatives and foreseeing human-robot interactions (ORE, 2015). Providing engineers with such tools will assist their tasks to optimize the human and robot workflow, while proactively ensuring proper ergonomics conditions for operators. An associated aspect of such a tool is that it should aid the consideration of variety among the human operators, e.g. related to anthropometry and strength.

1.3   Aim of the study

The aim of this study is to test, describe and illustrate how the digital human modelling (DHM) tool IPS IMMA can aid in the design of human-robot collaborative workstations.

2   Method

A virtual simulation was required to evaluate a use case scenario with a collaboration between a human and a robot in an open, without fences, workstation. The selected use case scenario involves collaboration between a human operator and a robotic welding arm. This was simulated in a DHM tool, where the tool had to be able to aid in the evaluation of a human-robot interaction, facilitating the decision making during the design of the collaborative workstation.

2.1   Digital human modelling tool

The DHM tool selected to simulate the virtual environment and the human-robot interaction was the IPS software (IPS, 2017) with two of its modules: IMMA manikin (HÖGBERG et al., 2016) and robotics module (BOHLIN et al., 2014). This version of the software is under development and works by merging the two modules, enabling the simulation of a collaborative workstation.

The manikin in IPS IMMA is steered by entering definitions of tasks that the manikin should perform. Based on the task definitions, the DHM tool automatically compute manikin motions by the use of mathematics and optimization algorithms, where the manikin avoids collisions, move according to ergonomics guidelines and stay in balance. The same task definitions can then be used to steer manikins of different anthropometry, where unique motions are computed for each manikin (BOHLIN et al., 2012). The software has ergonomics assessment functionality and a timeline that allows to evaluate the efficiency level of the workstation. The software version used in this study uses parts of the EAWS ergonomics evaluation method for the assessment (SCHAUB et al., 2012). The evaluations are given by a colour coded assessment, in which **green** is considered risk-free, **yellow** ought to be investigated further, and **red** needs immediate attention and should be analysed in detail.

Following input was required to simulate the collaborative workstation:

— **Type of industrial robot**: the software currently supports 6-axis arm industrial robot geometries. The robot in the simulation was a 6-axis welding robot from ABB (IRB 1660-4 155). To steer the robot, the software requires the appropriate geometry and the definition of the 6 axes.
— **Type of humans**: A family of 5 manikins was defined based on Swedish population data (HANSON et al., 2009), using stature and body weight as key measurements in IPS IMMA's anthropometry module (BROLIN, 2014).
— **Task definitions**: To steer the manikins, the software requires the user to define grasps and viewpoints and manually attach them to rigid bodies in the simulation.
— **Type of interaction/collaboration**: the definition of the collaboration provides security constrains that should be considered when designing the workstation. The selected use case was a collaboration of the **Safety rated monitored stop** type (see Section 1.1), in which the human and robot interact in an open environment, without fences.
— **Diagram and CAD of the workstation**: External obstacles or equipment were considered as well. The software allows import of CAD files to create the workstation accurately and with the path planning features it can avoid collisions in the simulation.
— **Input and output of the workstation**: since the workstation was part of a production line, it was important to consider how the input materials were presented as well as the type of output that was delivered. The appropriate CAD files of the parts were added in the simulation.

2.2   Use case

The selected use case scenario was part of a welding station in the production line of a pedal car.
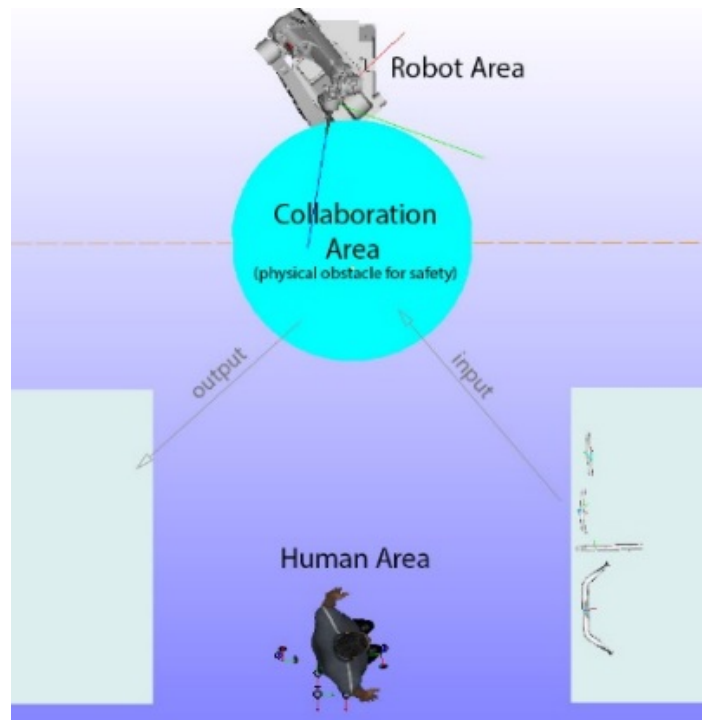
Fig. 2.1 Layout of the use case

Due to the task carried out in the workstation, the safety standard suiting the use case was considered **Safety rated monitored stop** (see Section 1.1). In this case, there was a rotating table which acted as a physical barrier and limited the access to the human operator, preventing him/her from having close contact with the robot or the parts being welded (Figure 2.1). The input of the station were the parts of the pedal car front. These were moved by the human operator into the rotating table. Once all parts were in place, the table rotated and the robot started the welding process. After welding, the table rotated again and the human operator then took the welded assembly into the next working table, finishing the cycle of the workstation.

3 Results

3.1 Virtual simulation results

The use case scenario was created in IPS IMMA, using CAD geometry to simulate the workstation for the pedal car assembly (Figure 3.1).
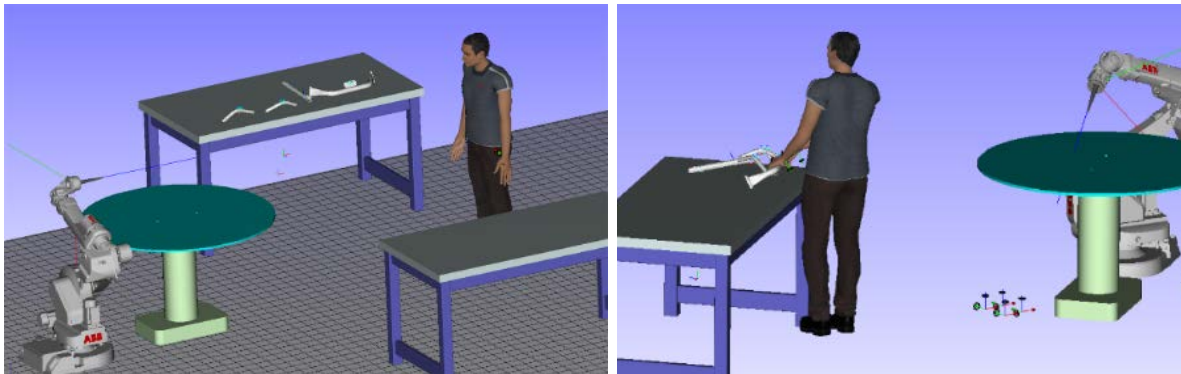
Fig. 3.1 (Left) Collaborative space in virtual simulation (Right) Output of workstation: welded front of pedal car

The simulation of the interaction between the manikin and the objects was built up by pre-planned paths of moving objects (as rigid bodies) as well as user-defined **grasps** and **viewpoints**. Equivalently, the robot interaction with the objects was calculated using certain reference points placed by the user. The robot movements were also defined by specific axis rotations to ensure correct robot functionality (Figure 3.2).

Fig. 3.2 Virtual area of collaboration, with rotating table as a safety obstacle

The output results provided by the software are graphically presented through a timeline that includes the sequence of actions. The workstation can be analysed from an efficiency perspective by evaluating the time spent on work, walking and waiting, both for the rob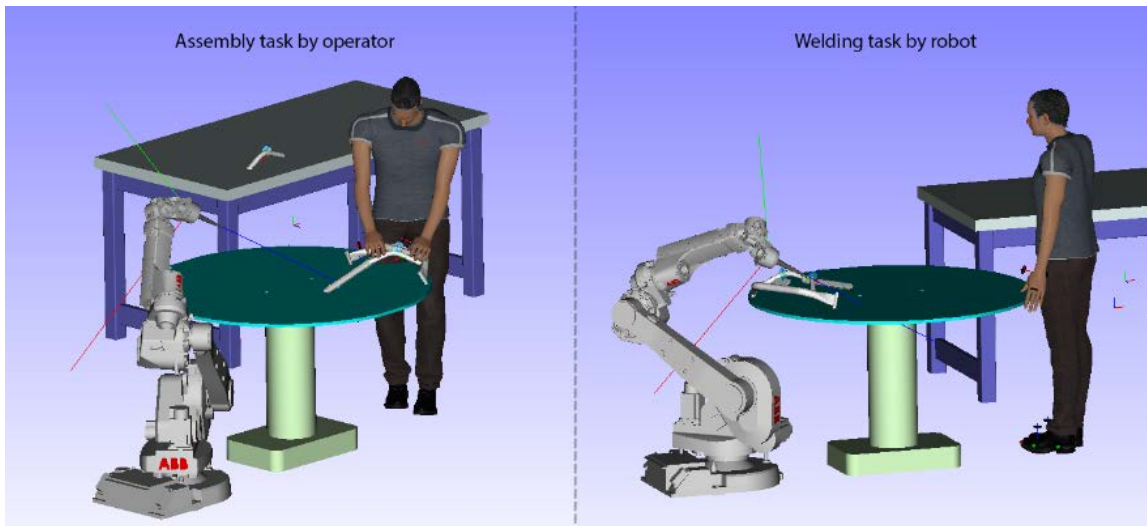ot and the operator (Figure 3.3). From the obtained results, the workstation needs improvements, e.g. since the efficiency of work is not spread equivalently between the robot and the operator, leaving a long period of wait for the robot while the operator arranges all the parts.

Part of the evaluation of a workstation is to verify it through an ergonomics assessment. To have a general overview of how the station might function for different operators, the software allows to simultaneously simulate the tasks for a family of manikins and show the results for the entire family. As seen in Figure 3.4 (left), the software provide a general overview of the ergonomics evaluation for each manikin, where the small squares represent the average evaluation of a specific ergonomic criteria during the simulated task, and the big squares on the right give a general ergonomics evaluation for a specific manikin during the full simulation. In this case, the results obtained for all 5 manikins are green as a general ergonomics overview because the detailed results are also green for every criteria. This means that there is low risk for strain-related disorders and therefore the workstation can be considered acceptable from an ergonomics point of view.
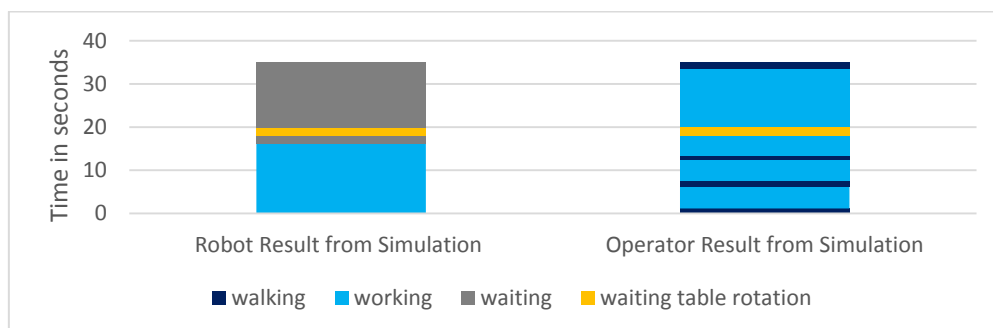

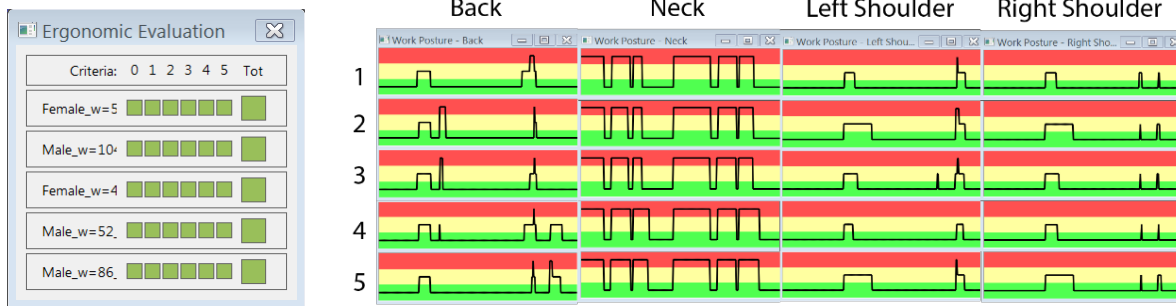**Fig. 3.3** Workstation efficiency evaluation

Fig. 3.4 Overview of ergonomics assessment for a family of manikins

A more detailed graphical result of the ergonomics evaluation is also provided (Figure 3.4, right). The data shown here is a sample of graphs provided by the software for the first half of the simulation. The graph provides information for each manikin in separate rows and the specific criteria in separate columns. These graphs use the same colour coded system as explained for the general overview. The colours are shown in the background of the graphs to show the change of risks during the simulation. The black line represents the results of the ergonomics evaluation made through time for different criteria. This provides a general view of how/when the flow of the workstation tasks will affect the postures of the operators, highlighting the moments where the operators could be at potential risk. Since different manikins use different motions, the ergonomics evaluation results varies between manikins.

3.2 Sequence editors

Manikins and robots are defined separately in the tool, and the sequence of actions through the simulation are defined in separate editors. The IRB (ABB Industrial Robot) editor handles the actions of the robot and simulates the robot movements, according to the robot specifications, through collision free segments which can be saved as actions and used with other editors of the software.

The Operation Sequence editor in IPS IMMA can simultaneously handle the different elements of the simulation, by defining the actions of the manikin and importing the actions previously created for the robot. The editor can also handle the motion segments of each rigid body. Each of these elements are independently defined in the operation sequence, but are placed in a parallel arrangement that allows synchronized interactions between the elements.

In this second editor, postures and movements of the manikin can be defined as independent sections of the sequence. Editing the manikin motions through the operation sequence editor can be done when the actions are not related to the movement of objects.

3.3 Compatibility

In order to design collaborative workstations, the simulation software has to handle different types of CAD files and allows for manipulation of them. For this use case it was required to import geometries of a workstation, of a specific robotic arm and of the parts of the assembly. This was possible to do with IPS IMMA software, but there was a limitation when importing mechanisms from other CAD software, which resulted in a longer process to simulate the adequate paths of all the elements.

The software allowed to import commercial robot files for the specific simulation, which allowed to correctly manipulate the movements of the robotic arm through the IRB editor. The specifications suggested by the robot manufacturer limited the speed and rotation of each axis which gave a realistic result of the robot movements in the simulation.

4   Discussion

To illustrate how DHM software, like IPS IMMA, can aid in the design of collaborative workstations, the use case was selected to represent a typical industrial case. Since collaborative workstations need to take many safety factors into account, a use case with a **safety rated monitor stop** was selected, which could demonstrate the use of the software starting from a basic collaboration. Other more complex types of collaborations would also be possible to simulate with the software. For example, collaborations with a closer interaction, where the manikin and the robot hold and move an object simultaneously, is possible to simulate in the software. This could aid in the design of future workstations by simulating different arrangements within a station and testing them at an early stage in the design process.

From the evaluation of the use case with the software it was possible to simulate both the human manikin and the robot through the available IRB and Operation Sequence editors. This enabled the specification of each element independently and gave a more accurate simulation, which still was easy to modify.

The ergonomics and efficiency results provided by the software were clear and gave a general view of how the station would work and what possible complications might occur. Getting such feedback supports engineers to draw conclusions and to make decisions of appropriate design modifications. Still, the results obtained might be limited for detailed evaluations of the workstation, since the time and efficiency assessments might not be as accurate as in reality. The obtained robot result for the efficiency evaluation shown in the graph (Figure 3.3) was also compared with estimated times of a welding robot (ROBOTWELDING, 2017). A variation in the time estimations for the robot task was observed since the simulated robot lacked welding time calculations and only calculated the robot motions. Similarly, the ergonomics assessment provided by the software gives a general overview of the operators in the workstation. Even though the manikin movements can be defined through the Operation Sequence editor, when the manikin grasps an object then its movements are constrained by the pre-planned path of that object, which is fixed and defined separately to avoid collisions of the object and its environment (i.e. not regarding the manikin). This means that the pre-planned object path may not allow for the software to find ergonomic manikin motions in an optimal way. Hence the predicted manikin motions may have a reduced correspondence with how the task would be carried out in reality. In turn this affects the results of the ergonomics assessment. However, development work is carried out to reduce this effect by allowing the optimal manikin motions to influence object paths.

The ergonomics evaluation method utilised in this use case is based on a so called observational assessment method, designed to be used by ergonomists assessing ergonomics mainly by visual observation. Observational assessment methods have been reported to have reliability limitations (FORSMAN, 2016). Still, this type of simulated ergonomics assessments can provide fast and important evaluations at early stages in the workstation design process.

For future research, multiple use cases with different types of collaborations between humans and robots are planned to be performed to evaluate the software capabilities further and to support the development of the software. Also simulations of multiple robots and operators are planned.

Acknowledgment

List of references

Bauer, A.; Wollherr, D.; Buss, M.: Human–robot collaboration: a survey: International Journal of Humanoid Robotics 5 (2008) 47-66.

Bohlin, R.; Delfs, N.; Mårdberg, P.; Carlson, J. S.: A Framework for Combining Digital Human Simulation with Robots and Other Objects: Tokyo, Japan (2014).

Bohlin, R.; Delfs, N.; Hanson, L.; Högberg, D.; Carlson, J. S.: Automatic creation of virtual manikin motions maximizing comfort in manual assembly processes: 4th CIRP Conference on Assembly Technologies and Systems:USA Conference on Assembly Technologies & Systems (2012) 209-212.

Brolin, E.; Högberg, D.; Hanson, L.: Design of a Digital Human Modelling Module for Consideration of Anthropometric Diversity. Advances in Applied Digital Human Modeling. Duffy, V.G. (Ed.). AHFE Conference (2014) 114-120.

Chaffin, D. B.: Human motion simulation for vehicle and workplace design: Human Factors and Ergonomics in Manufacturing & Service Industries 17 (2007) 475-484.

Cherubini, A.; Passama, R.; Crosnier, A.; Lasnier, A.; Fraisse, P.: Collaborative manufacturing with physical human–robot interaction: Robotics and Computer-Integrated Manufacturing 40 (2016) 1-13.

Faber, M.; Bützler, J.; Schlick, C. M.: Human-robot Cooperation in Future Production Systems: Analysis of Requirements for Designing an Ergonomic Work System: Procedia Manufacturing 3 (2015) 510-517.

Fitts, P. M.: Human engineering for an effective air-navigation and traffic-control system: (1951).

Forsman, M.: Ergonomic risk assessments – a need for reliable and attractive methods: Reports and Studies in Health Sciences, 48th Annual Conference of Nordic Ergonomics and Human Factors Society (2016) 28-32.

Hanson, L.; Sperling, L.; Gard, G.; Ipsen, S.; Vergara, C. O.: Swedish anthropometrics for product and workplace design: Applied ergonomics 40 (2009) 797-806.

Högberg, D.; Hanson, L.; Bohlin, R.; Carlson, J. S.: Creating and shaping the DHM tool IMMA for ergonomic product and production design: International Journal of the Digital Human 1 (2016) 132-152.

IPS: (2017). http://industrialpathsolutions.se/

ISO 10218-1:2011: Robots and Robotic Devices-Safety Requirements for Industrial Robots-Part 1: Robots: International Organization for Standardization, Geneva, Switzerland (2011).

Krüger, J.; Lien, T. K.; Verl, A.: Cooperation of human and machines in assembly lines: CIRP Annals - Manufacturing Technology 58 (2009) 628-646.

Maurice, P.; Padois, V.; Measson, Y.; Bidaud, P.: Human-oriented design of collaborative robots: International Journal of Industrial Ergonomics 57 (2017) 88-102.

Michalos, G.; Makris, S.; Tsarouchi, P.; Guasch, T.; Kontovrakis, D.; Chryssolouris, G.: Design Considerations for Safe Human-robot Collaborative Workplaces: Procedia CIRP 37 (2015) 248-253.

Ore, F.: Human− industrial robot collaboration: Simulation, visualisation and optimisation of future assembly workstations: Mälardalen University (2015).

Ore, F.; Hanson, L.; Delfs, N.; Wiktorsson, M.: Human-Industrial Robot Collaboration - Development and application of simulation software: International Journal of Human Factors Modelling (2015).

Robotwelding: (2017). http://www.robotwelding.co.uk/robot-cycle-times.html

Schaub, K. G.; Mühlstedt, J.; Illmann, B.; Bauer, S.; Fritzsche, L.; Wagner, T.; Bullinger-Hoffmann, A. C.; Bruder, R.: Ergonomic assessment of automotive assembly tasks with digital human modelling and EAWS: International Journal of Human Factors Modelling and Simulation 3 (2012) 398-426.

Ulherr et al.:
Implementation of an artificial neural network for global seat discomfort prediction by simulation

Ulherr, A., Yang, Y., Bengler, K.

Chair of Ergonomics, Technical University of Munich, Garching, Germany

Abstract

Assessments of car seat (dis)comfort using physical prototypes and test subjects are state of the art nowadays to meet the customer's comfort requirements. To reduce time and cost, an evaluation tool for the virtual design phase of the product development process using digital human models was implemented within the project UDASim, funded by the German federal ministry of education and research. Seating discomfort depends on a va-riety of parameters, which correlations are unknown. The digital human models can simu-late only single factors involved in the subjective discomfort sensation. Therefore, an arti-ficial neural network was implemented to predict the global discomfort using computational results of three established digital human models (AnyBody, CASIMIR/Automotive, RAMSIS). For the training and evaluation 360 data sets were recorded during a large-scale seat discomfort study. All test subjects and configurations had to be simulated by the three digital human models, since an artificial neural network needs to be trained with the same kind of data as will be used for the intended application. Due to time constrains and limitations of the simulations, only 56 datasets could be used to train the artificial neural network. The chosen concept of the implemented artificial neural network (ANN) contained a feed-forward architecture, nine hidden nodes and a hyperbolic tangent activation func-tion. The ANN is implemented in python and based on 288 input factors. The output factor is the global discomfort for a specific car seat. The ANN was trained using error back propagation (BP) and tested in two different ways. The first test scenario used the identical datasets for training and testing (RSME (n=56) = 0.27; Discomfort scale [0, 50]). For the second scenario, 40 datasets for training and 16 datasets for testing were randomly se-lected (RMSE (n=16) = 9.76; Discomfort scale [0, 50]).

Based on the RMSE (root mean square error), the implemented ANN proved to be a prom-ising approach to predict discomfort of car seats considering several parameters involved. Regarding the huge amount of input factors and the small amount of test and training datasets, further investigations and interpretations are necessary.

Key words:

Digital Human Model; Discomfort; Seating; Artificial Neural Network

1 Introduction

Reducing discomfort and fulfilling comfort requirements are mandatory development goals (KOLICH, 2008). Currently, discomfort assessments still require prototypes for subjective and objective measurements during largescale subject studies. Therefore, those studies are usually conducted in a later phase of the development process. Besides the required large amount of time for subject studies, consequential changes of the design are more expensive compared to an earlier phase (RÖMER et al., 2001). The assessment of seating discomfort within the virtual design phase could reduce time and costs. Digital human models simulating human interaction with products are already well-established evaluation tools in virtual environments (CHAFFIN, 2001). Ad-ditionally, simulations by digital human models can provide objective and reproducible statements independent of human subjects' variances.

HERTZBERG (1958) and SHACKEL et al. (1969) regard comfort and discomfort as opposites on one continuum. Yet, the current state of research contradicts this state-ment. The subjective sensations 'comfort' and 'discomfort' are independent entities and can occur simultaneously (ZHANG et al., 1996). Both, comfort and discomfort, depend on physical and biomechanical features, but only comfort is influenced by sub-jective preferences for, among others, aesthetic factors (HELANDER et al., 1997). Fur-ther comfort/discomfort models support this proposition and conclude that discomfort, compared to comfort, must correlate better with objective measurements because of its independence of design features (LOOZE et al., 2003; MOES, 2005; VINK et al., 2012).

The subjective seating discomfort depends on a variety of parameters such as, among others, seat pressure distribution (GYI et al., 1999; ZENK et al., 2006; KYUNG et al., 2008) and posture (GRONDIN et al., 2013; VERGARA et al., 2002). To date, digital human models are able to predict only single parameters of seat discomfort. MARX et al. (2005) predicted the seat pressure distribution using digital human models and com-bined the findings with comfort assessments. KYUNG et al. (2009) used digital human models to define comfortable driving postures.

Since humans process a variety of sensory inputs via different modalities simultane-ously (MATHER, 2009), the subjectively perceived discomfort depends on a combina-tion of the different sensations involved. Hence, various parameters must be ac-counted for a discomfort prediction method. However, studies investigating combined influences of multiple parameters on discomfort are not published, yet.

An artificial neural network (ANN) is loosely based on the idea of the highly elaborate functionality of the human brain, with the ability to combine stimulus combinations with complex patterns from experience and by training. Therefore, interconnected neurons (units) process inputs and forward the results with weights to the next. Such a network of neurons is able to find correlations between given information. This allows the ANN to develop complex mathematical models based on given inputs and the correspond-ing outputs, to adopt the model with every new set of input and output data, and to use the model to predict an output based on new given input. The ability to generalize, to predict, and even to deal with uncertainties is the reason why

artificial neural networks are a promising approach to forecast human behavior (ZHANG et al., 2006).

Artificial neural networks are already used for ergonomic purposes. Successful applications of ANN can be found in the research fields of posture prediction (BATAINEH et al., 2013; CARENZI et al., 2005; Jung, E. S. et al., 1994; Mora, M. C. et al., 2012; Perez, M. A. et al., 2008; REZZOUG et al., 2008; ZHANG et al., 2010), and comfort/dis-comfort forecasts (ALBERS et al., 2002; FISCHER-VON RÖNN et al., 2014; KOLICH, 2004; STAMMEN et al., 2007; Wong, A. S. W. et al., 2003; SEÇKINER, 2009).

According to KOLICH et al. (2004) artificial neural networks are even more fitting for predicting seat comfort than linear regression. Comparing these two approaches, the ANN produces a lower RMSE (root mean square error) and a higher coefficient of determination ($r2$) (KOLICH et al., 2004). BURKE et al. (1996, S. 451) and SEÇKINER (2009, S. 801) even state that regression models are "inadequate to explain comfort". Especially since the relationship of all parameters involved in car seat comfort are ap-parently nonlinear and the high number of input factors limit the application of regres-sion methods (BURKE et al., 1996).

2   Objective

Combining digital human models and using multiple discomfort parameters to predict the global discomfort of car seats, was the aim of the project UDASim ('Umfassende Diskomfortbewertung für Autoinsassen durch Simulation' [Eng. meaning 'Global discomfort assessment for vehicle passengers by simulation']), funded by the German federal ministry of education and research (BMBF). The project chose an artificial neu-ral network approach, for the potential of ANN to solve complex prediction tasks, and since the correlations between the various discomfort parameters are unknown (ULHERR et al., 2014). The inputs for the artificial neural network are computational results of three established digital human models (the multi-body system AnyBody, the FE-model CASIMIR and the 3D-CAD human model RAMSIS). The output of the ANN is the estimated global discomfort. Figure 2.1 shows the flowchart for the artificial neural network developed in the project UDASim.
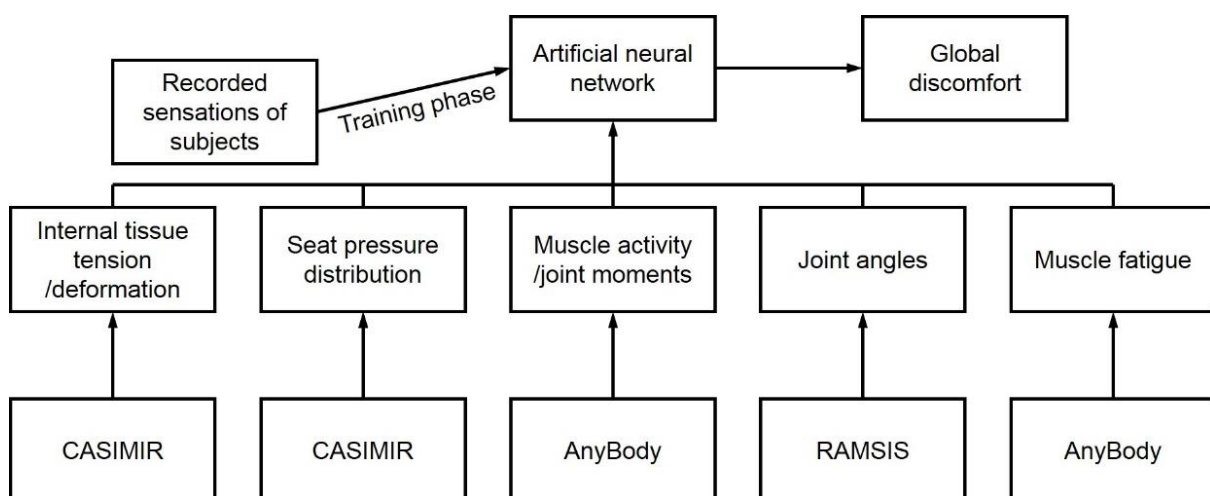

Fig. 2.1   Flowchart for the prediction of the global discomfort using an artificial neural network (ULHERR et al., 2017).

3   Method

3.1   Experimental Data for Model Development

The 360 sets of raw data to train and evaluate the artificial neural network were gathered by a largescale seat discomfort study (ULHERR et al., 2017).

Since the ANN should be used with data provided by the three digital human models, the training had to be with data in the very same format. So all test subjects and experiment conditions had to be simulated by all three digital human models. Before the data were usable for the simulations, it was necessary to conduct an extensive data post-processing. Posture and anthropometry of the test subjects were measured with an electronic measurement system called PCMAN (SEITZ et al., 1999) and afterwards imported in the CAD-model of the experiment setup, which has also been adapted to the respective configuration.

3.1.1   Input Factors

Six files containing a total of 288 input factors resulted from the simulation data and the demographic data. AnyBody provided three files for joint moments, joint reaction forces and muscle activations with 153 input factors, CASIMIR one file for the parameters of the seat pressure distribution (load fraction, maximum pressure, and maximum gradient) containing 51 input factors, RAMSIS one file for the anthropometry (segment lengths) and the posture (joint angles) with 80 values, and four input factors were in the file with the demographic data (age, gender, body height and body weight).

3.1.2   Data Pre-Processing

A python script (readfile.py) transferred the input data from the six files per data set into one file and created a matrix with 288 columns, in which every row contained the data of one data set. For the training of the neural network, the respective, experimen-tally determined global discomfort value (output) for each data set was added to the matrix as the 289th column. The global discomfort value was given by the subjects during the largescale discomfort study (ULHERR et al., 2017)

The raw input data have very different units, scales and distributions, which would lead to wrongfully high influences of the input parameters with a wider range or bigger val-ues. To deal with this issue, all data were normalized to make them adequate to use with the ANN. The input data were normalized so that the square sum of each element of one dimension (column) was one. And the output data was divided by 50, the highest possible discomfort value.

The standardization also allows the training process to converge faster, and avoids possible saturations of the activation function, which would cause a slow or unsuccess-ful learning phase.

3.1.3 Network architecture

An artificial neural network with a feed-forward architecture was programmed in python. It consists of 288 input units, one hidden layer with nine hidden units, and one output unit for the global discomfort as the result. The number of the hidden units resulted from two reasons: firstly, the accuracy of the calculation increases from two hidden units to nine, and secondly, no successful calculation was possible for 10 or more units. The activation functions of the implemented ANN are the hyperbolic tangent, which is necessary for presumably non-linear correlations.

The chosen training method for the artificial neural network is the established back-propagation that uses 2000 adaptation iterations to reduce the occurring mean-squared error. For the training, the learning rate was 0.5 and the momentum factor was 0.1. The learning rate defines the size of adjustment steps during each iteration loop, and the momentum factor helps to overcome local minimum or saddle points by taking the previously made change into account.

4   Results

Due to the limited project runtime, only 162 of the 360 recorded data sets could be post-processed and forwarded to the digital human models for the required simulations. The digital human models successfully simulated 56 data sets and returned the computational results. 56 data sets to train and to validate the artificial neural network are much less than was expected at the beginning of the project, therefore the strategy for the training and the validation had to be changed.

Two test scenarios were created for validating the implemented artificial neural network to predict the global discomfort. In both cases the root mean square error (RMSE) was calculated to measure the precision of the trained artificial neural network. The RMSE is a commonly used measurement to assess the prediction performance of a devel-oped model (SHEINER et al., 1981).

$$RMSE = \sqrt{\Sigma (\hat{y}_t - y_t)^2 n_{t=1}^{n}} \qquad (4.1)$$

$\hat{y}_t = predicted\ discomfort\ value\ (ANN); y_t = true\ discomfort\ value\ (experiment)$

4.1   First Test Scenario

To verify whether the ANN was correctly implemented and able to identify correlations between input and output data, the training and the testing was executed with the all 56 data sets. The more successful the training phase has been, the more similar the calculated and the measured global discomfort should be, and the lower the RMSE. In this case, using identical training and test data, the RMSE (n=56) was 0.27 (CP50 scale [0; 50]), which corresponds with a well-trained network. This shows that the im-plemented ANN was adequate to its given task.

4.2   Second Test Scenario

The second test scenario used 16 randomly selected data sets for the testing and the remaining 40 data sets for the training of the artificial neural network. The RMSE (n=16) for this case was 9.76 (CP50 scale [0; 50]), which is a tolerance that is acceptable for subjective data use. As expected, this RMSE value is considerably higher than in the first test scenario.

5   Conclusion

Considering the high amount of input factors combined with the low number of usable data sets for the training and the validation, the results of the both test scenarios show great promise for the artificial neural network to be an adequate tool to predict global discomfort of car passenger seats using three digital human models. Nevertheless, the main limitation of the presented work is the small amount of usable data to train and to validate the implemented artificial neural network.

The limited project time did not allow further investigations and the finalization of the artificial neural network using all available data sets. However, the carried-out work so far and therefore the aim of the project UDASim proved to be a reasonable and prom-ising approach. If the remaining data sets will still get post-processed and simulated by the digital human models, the implemented artificial neural network can be trained and validated in a way to become a useful and interesting tool for the car seat devel-opment process.

On top of that, the collected data hold for sure even more interesting findings about sitting discomfort. Up until now, such a largescale sitting discomfort study is not pub-lished. The methodically variations of influencing factors combined with the high num-ber of measurements (ULHERR et al. 2017) offer the promising opportunity to investi-gate the correlations between input factors, and effects of the experimental design in-tensively. These results then will increase the knowledge about sitting discomfort and improve the quality of conducted discomfort studies.

6   Acknowledgement

List of references

Albers, A.; Albrecht, M. C.: Prediction of subjective comfort ratings by means of artificial neural networks [Vorhersage subjektiver Komforturteile mittels künstlicher neuronaler Netze], VDI Berichte 2002 (1701), pp. 401–420

Bataineh, M.; Marler, T.; Abdel-Malek, K.: Artificial neural network-based prediction of human posture, Bd. 8026. In: Duffy, V. G. (eds.): Digital Human Modeling and Applications in Health, Safety, Ergonomics, and Risk Management. Human Body Modeling and Ergonomics. DHM 2013. DHM 2013. Berlin, Heidelberg: Springer, 2013 (Lecture Notes in Computer Science, vol. 8026), pp. 305–313 7

Burke, L. I.; Storer, R. H.; Lansing, L. L.; Flanders, S. W.: A neural-network approach to prediction of vehicle driving comfort, IIE Transactions (Institute of Industrial Engineers) 1996, 28 (6), pp. 439–452

Carenzi, F.; Gorce, P.; Burnod, Y.; Maier, M. A.: Using generic neural networks in the control and prediction of grasp postures. In: ESAAN'2005 Proceedings, 2005

Chaffin, D. B.: Digital human modeling for vehicle and workplace design: Society of Auto-motive Engineers Warrendale, PA, 2001

Fischer-Von Rönn, N.; Meywerk, M.: Predicting the ride comfort of passenger cars for single-obstacle crossings through an innovative feature extraction method consisting of non-linear geometric approximations of wavelet-transformed acceleration data and airborne sound, Proceedings of the Institution of Mechanical Engineers, Part D: Journal of Automobile Engineering 2014, 228 (4), pp. 357–369

Grondin, D. E.; Triano, J. J.; Tran, S.; Soave, D.: The effect of a lumbar sup-port pillow on lumbar posture and comfort during a prolonged seated task, Chiropractic & Manual Therapies 2013, 21 (1)

Gyi, D. E.; Porter, J. M.: Interface pressure and the prediction of car seat discomfort, Applied Ergonomics 1999, 30 (2), pp. 99–107

Helander, M. G.; Zhang, L.: Field studies of comfort and discomfort in sitting, Ergonomics 1997, 40 (9), pp. 895–915

Hertzberg, H. T. E.: Seat comfort, "Annotated bibliography of applied physical anthropol-ogy in human engineering," WADC Technical Report 1958, pp. 30–56

Jung, E. S.; Park, S.: Prediction of human reach posture using a neural network for ergonomic man models, Computers and Industrial Engineering 1994, 27 (1-4), pp. 369–372

Kolich, M.: Predicting automobile seat comfort using a neural network, International Jour-nal of Industrial Ergonomics 2004, 33 (4), pp. 285–293

Kolich, M.: A conceptual framework proposed to formalize the scientific investigation of au-tomobile seat comfort, Applied Ergonomics 2008, 39 (1), pp. 15–27

Kolich, M.; Seal, N.; Taboun, S. M.: Automobile seat comfort prediction: statistical model vs. artificial neural network, Applied Ergonomics 2004, 35 (3), pp. 275–284

Kyung, G.; Nussbaum, M. A.: Driver sitting comfort and discomfort (part II): Relationships with and prediction from interface pressure, International Journal of Industrial Er-gonomics 2008, 38 (5-6), pp. 526–538

Kyung, G.; Nussbaum, M. A.: Specifying comfortable driving postures for ergo-nomic design and evaluation of the driver workspace using digital human models, Ergonom-ics 2009, 52 (8), pp. 939–953

De Looze, M. P.; Kuijt-Evers, L. F. M.; van Dieën, J.: Sitting comfort and discom-fort and the relationships with objective measures, Ergonomics 2003, 46 (10), pp. 985–997

Marx, B.; Amann, C.; Verver, M.: Virtual Assessment of Seating Comfort with Human Models. Warrendale, PA, United States: SAE International, 2005 (SAE Tech-nical Paper Series).

Mather, G.: Foundations of sensation and perception. 2nd ed. Hove, East Sussex [Eng-land], New York: Psychology Press, 2009

Moes, N. C.: Analysis of sitting discomfort, a review. In: Bust, Philip D.; McCabe, P. T. (Ed.): Contemporary ergonomics 2005. London: Taylor & Francis, 2005, pp. 200–204

Mora, M. C.; Sancho-Bru, J. L.; Pérez-González, A.: Hand posture prediction using neural networks within a biomechanical model, International Journal of Advanced Ro-botic Systems 2012, 9 (4)

Perez, M. A.; Nussbaum, M. A.: A neural network model for predicting postures dur-ing non-repetitive manual materials handling tasks, Ergonomics 2008, 51 (10), pp. 1549–1564

Rezzoug, N.; Gorce, P.: Prediction of fingers posture using artificial neural net-works, Journal of Biomechanics 2008, 41 (12), pp. 2743–2749

Römer, A.; Pache, M.; Weißhahn, G.; Lindemann, U.; Hacker, W.: Effort-saving product representations in design—results of a questionnaire survey, Design Studies 2001, 22 (6), pp. 473–491

Seçkiner, S. U.: A neural network-based system for prediction of computer user comfort, Applied Artificial Intelligence 2009, 23 (8), pp. 781–803

Seitz, T.; Bubb, H.: Measuring of Human Anthropometry, Posture and Motion. In: Digital Human Modeling For Design And Engineering Conference And Exposition. Warren-dale, PA, United States: SAE International, 1999 (SAE Technical Paper Series).

Shackel, B.; Chidsey, K. D.; Shipley, P.: The Assessment of Chair Comfort, Ergonomics 1969, 12 (2), pp. 269–306

Sheiner, L. B.; Beal, S. L.: Some suggestions for measuring predictive performance, Journal of Pharmacokinetics and Biopharmaceutics 1981, 9 (4), pp. 503–512

Stammen, K.; Meywerk, M.: Using artificial neural networks as a tool to estimate vehicle ride comfort [Künstliche Neuronale Netze als Hilfsmittel zur Abschätzung des Komfortemp-findens], VDI Berichte 2007 (2014), pp. 323–339

Ulherr, A.; Bengler, K.: Global Discomfort Assessment for Vehicle Passengers by Simulation (UDASim). In: Proceedings of 3rd International Digital Human Modeling Sympo-sium DHM 2014, 2014

Ulherr, A.; Zeller, F.; Bengler, K.: Simulating Seat Discomfort: An Experimental Design for Using Digital Human Models. In: 8th International Conference on Applied Human Factors and Ergonomics, 2017

Vergara, M.; Page, Á.: Relationship between comfort and back posture and mo-bility in sitting-posture, Applied Ergonomics 2002, 33 (1), pp. 1–8

Vink, P.; Hallbeck, S.: Editorial: Comfort and discomfort studies demonstrate the need for a new model. In: Vink, Peter; Hallbeck, Susan (eds.): Applied Ergonomics: Special Section on Product Comfort, 2012 (43), pp. 271–276

Wong, A. S. W.; Li, Y.; Yeung, P. K. W.; Lee, P. W. H.: Neural network predictions of human psychological perceptions of clothing sensory comfort, Textile Research Journal 2003, 73 (1), pp. 31–37

Zenk, R.; Mergl, C.; Hartung, J.; Sabbah, O.; Bubb, H.: Objectifying the Comfort of Car Seats. In: SAE 2006 World Congress & Exhibition. Warrendale, PA, United States: SAE International, 2006 (SAE Technical Paper Series).

Zhang, B.; Horváth, I.; Molenbroek, J. F. M.; Snijders, C. J.: Using artificial neu-ral networks for human body posture prediction, International Journal of Industrial Ergonom-ics 2010, 40 (4), pp. 414–424

Zhang, L.; Helander, M. G.; Drury, C. G.: Identifying Factors of Comfort and Dis-comfort in Sitting, Human Factors: The Journal of the Human Factors and Ergonomics Soci-ety 1996, 38 (3), pp. 377–389

Zhang, Z.; Vanderhaegen, F.; Millot, P.: Prediction of human behaviour us-ing artificial neural networks. In: Yeung, D. S.; Liu, ZQ.; Wang, XZ.; Yan, H. (eds.): Advances in Machine Learning and Cybernetics. Berlin, Heidelberg: Springer, 2006 (Lecture Notes in Computer Science, vol. 3930).

Mahdavian et al.:
Digital human modelling in a virtual environment of CAD parts and a point cloud

Mahdavian, N.[1], Ruiz Castro, P.[1], Brolin, E.[1], Högberg, D.[1], Hanson, L.[1,2]

[1] School of Engineering Science, University of Skövde, Skövde, Sweden
[2] Industrial Development, Scania, Södertälje, Sweden

Abstract

Manual assembly is a time and cost consuming phase of production. It is crucial to design the assembly process so that overall system efficiency, quality output and human well-being meet desired levels. Since manual assembly involve humans, one support in the production design process is to use digital human modelling (DHM) tools to model and assess different design scenarios prior to the actual production process. In the traditional way, various CAD tools are used by engineers to model the production layout and the workstations. Then, these models typically are imported into a DHM tool to simulate human work, and to apply ergonomic evaluation methods on the simulated work tasks. This work, supported by CAD and DHM, can be a time consuming and iterative process as precise information and measurements of the actual assembly environment are needed, e.g. related to actual geometries of factory premises or of facilities surrounding the workstations. However, introducing point cloud scanning technology can provide the user with a more correct and realistic virtual representation of the environment, which allows for a faster and more precise design process.
The aim of this paper is to present the developments and capabilities of the DHM tool IPS IMMA (Intelligently Moving Manikins) in an assembly process and in a virtual environment provided by point cloud scanning.

Key words:

digital human modelling (DHM), point cloud, assembly, IPS IMMA

1 Introduction

There is a tight competition between automotive companies to continuously improve the value of their products while reducing costs. One approach for companies to reduce costs is to improve their production processes so that they are efficient and flexible. The objective to improve production processes can be supported by the concept of digital factories, i.e. by doing virtual simulations of the production systems before realizing the systems in the real world (GLÄSER et al., 2016). This as a way to support communication between different team members and to facilitate testing of different design alternatives to identify successful solutions, while saving time and money by not having to build physical prototypes or having to do large modifications afterwards (GLÄSER et al., 2016; LINDSKOG et al., 2016; YU et al., 2016)

Different methods and tools have been developed and used to help in designing assembled products, assembly tools and assembly processes (BOËR et al., 2001). In the digital modelling world, CAD modelling has been used for many decades to create 2D and 3D virtual models of products, production lines and factory layouts. However, to simulate assembly tasks, besides having the rough geometry of parts and working areas, exact plans of the workstation and tool installations are needed (LINDSKOG et al., 2016; YU et al., 2016). However, geometries in CAD models do sometimes not conform completely with the reality that the CAD models aim to represent, especially in the area of production facilities. This may cause design errors and force costly redesign actions (LINDSKOG et al., 2016). 3D point cloud scanning technology is an efficient way to gather exact and current environmental data, and can hence provide more detailed and realistic layout planning and geometry analyses than CAD models (LINDSKOG et al., 2012; MARUYAMA et al., 2016; REX AND STOLI, 2014). Improvements in texture, colour and positioning in virtual simulation modelling improve the rendering quality and user experience for designers (LINDSKOG et al., 2012). 3D scanning provides, in contrast to *as-planned* environments in CAD models, *as-is* environments, which provides a more precise basis for doing studies of human work, movements and accessibility (MARUYAMA et al., 2016). Hence, 3D scanning can be used for representing the shop floor, but also to facilitate redesign of production systems (LINDSKOG et al., 2016). The combination of CAD and point cloud geometries (hybrid models), improves interaction, planning, understanding of the virtual environment, finding errors in advance and evaluating different design alternatives (LINDSKOG et al., 2016; REX AND STOLI, 2014; YU et al., 2016).

Humans typically play a main role in assembly processes. Humans have certain capabilities that are either very hard or costly to make machines to carry out. Hence there is a need to simulate humans within the digital factory concept. Digital human modelling (DHM) tools have been developed to support such virtual production design processes. DHM tools assist analyses of system behaviour of digital factories, and can facilitate planning and simulation of manual tasks easier compared to experiments or physical mock-ups used in traditional ways (BOËR et al., 2001; GLÄSER et al., 2016). In most DHM based simulations, the virtual environments (such as workstations and equipment) are either modelled in the DHM tool itself, or created by importing CAD data. It is rarer that virtual environments in DHM based simulations are built up from point clouds. The aim of this paper is to present the

developments and capabilities of the DHM tool IPS IMMA (Industrial Path Solutions - Intelligently Moving Manikins) in a production process and in a virtual environment provided by point cloud scanning.

2   Method

The IPS software platform was used for simulation (IPS, 2017). The three components used in IPS were: IMMA, a digital manikin (HÖGBERG et al., 2016), a rigid body path planner (HANSON et al., 2014) and point cloud tools (INGELSTEN et al., 2016). To illustrate the functionality, a pedal car assembly scenario was established. Four sources were input in the simulation: 1) a pedal car, 2) assembly sequence of the pedal car, 3) anthropometric descriptions of workers, and 4) a point cloud scanned environment.

The pedal car was modelled in the CAD software CATIA, encompassing 23 main components that were assembled at four main stations. Every station was divided by its main tasks, and tasks were divided by detailed steps of making that part from scratch. The pedal car frame was positioned on the first station's assembly stand. To prevent a crowded environment and large file size, all parts and stations were removed except the selected first station's parts.

A family of digital manikins was imported into the scene and placed in front of the first task of the first station. The manikin family was based on Swedish population data. The key anthropometric measurements were defined and a manikin family covering the majority of the population considering those criteria was automatically generated (BROLIN, 2016). All the family members were instructed simultaneously using view and grip points, which are components that cause the manikins to move, look and act. Controlling the motions in a way so that the manikins act naturally is based on motion controller parameters and algorithms (BOHLIN et al., 2012)

Different technologies available for capturing spatial data can traditionally be classified into tactile methods and non-contact methods (BERGLUND et al., 2016). For this study, the non-contact method, a Faro terrestrial laser scanner, was used to scan the factory area and the data, gathered from different camera sources, was modified and combined to one coherent dataset containing millions of points through registration in FARO Scene software. A 3D laser scanner provides comprehensive data in short time. One scan indoors takes something between 5 and 10 minutes and typically collects 30-50 million data points (BÖHLER, 2005). Structure light and photogrammetry are the low cost alternatives for 3D laser scanning if the workstation area is small and the quality is not an important issue (BERGLUND et al., 2016).

The size of the point cloud is manageable by using central hosting of the files, selective streaming of data or neutral standard file format .e57 (BERGLUND et al., 2016). The point size, the quality of render and the region of the work to be visible, were modified afterwards. To make the desired parts visible, the ceiling of the point cloud was cut out. Then, extra points showing sections other than the target area got cut and saved as a new region to reduce the visible area and make it focused on the selected work station for pedal car assembly (see Figure 2.1).

The company premises was visited in order to recognise the factory sections, specifically the assembly stations in the point cloud file.
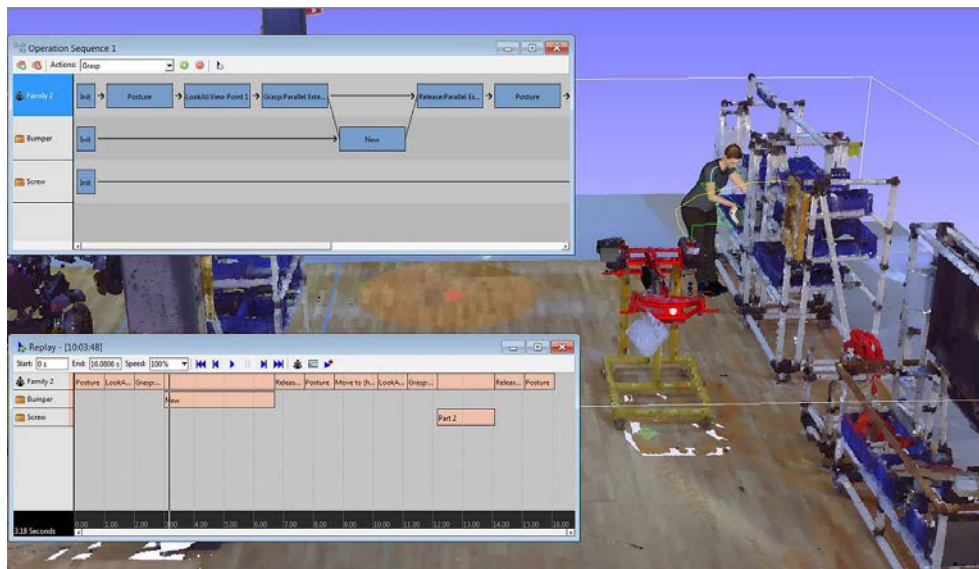

Fig. 2.1   Manikin assembling a pedal car in a point cloud environment

2.1 Simulation procedure

The general steps of the procedure of assembling each part of the pedal car were quite the same, only some modifications in options of the steps were required. As an example, the procedure of how to instruct the manikins to assemble one of the mudguards is explained below.

First, the manikin took the part, i.e. the mudguard, from the shelves. The mudguard was converted to a rigid body to work with the path planner tool. To define the task, a parallel extension grip was selected in the hand grip library available in IMMA (HANSON et al., 2014). Left and right hand grips were inserted into the scene, assigned to the manikin, moved and rotated to get the right place and direction on the object. Then, a view point was created and assigned to the mudguard to define the place for the manikin to look at.

Second, the manikin carried the object to the station where other parts of the frame were already assembled. To control these actions, an automatic path through the rigid body planning window was created by: setting up the points on the path, assigning the mudguard as the rigid body and selecting obstacles in the manikin's way from taking the part to assembling it; here shelves, the pedal car and its stand were obstacles.

Third, the manikin went back to take the nuts from another basket on the shelves and finally assembled the mudguard.

Fourth, the operation sequences that specifies actions for the manikin on the path were specified. In the operation sequence window, the manikin family, the mudguard

and nuts were added as actors. Grasp/release, look at/stop look at, move to and posture were the available actions for the manikin. To move the mudguard and the nuts, related paths were created by the rigid body path planner and then assigned to the items. The operation sequence was continued by doing the same actions for all the assembly parts. It was only needed to instruct one manikin family member of how to perform all assembly tasks. The other family members followed the same instructions, but automatically used other postures and motions due to different anthropometry.

The next action was to execute the simulation. As a last step, ergonomics assessment was done within the DHM tool, looking at the ergonomic load exposure of the following body sections: Left Wrist, Right Wrist, Left Forearm, Right Forearm, Back and Neck for each member of the manikin family. The method for ergonomics assessment was a subset of the EAWS method (SCHAUB et al., 2012). As a complementary input for work assessment, the DHM tool calculated the walking distance used when performing the assembly tasks.

3   Result

The results showed that IPS is capable to work with the IMMA manikins, CAD models and point cloud simultaneously (see Figure 2.1). All the components were editable in the software after importing. Then, the pedal car got assembled based on the assembly scenario steps.

A manikin family was proposed by the software based on the constraints applied. The manikins' postures and walking collision free paths were set precisely using predefined postures and grips; individual settings for each part's assembly were applied. The ergonomics assessment results were represented in colours (see Figure 3.1), where different colours express the degree of health risks: green means risk-free action, yellow requests more evaluation and red calls for immediate consideration (SCHAUB et al., 2012).

Fig. 3.1   Part of the ergonomics assessments of the simulated task

Various paths were tried, by modifying the way points, to find the shortest and most ergonomic paths, using ergonomics and walking evaluation results as indicators of successful solutions. For instance, for the mudguard simulation, a path was defined that gave green indication for all body parts and all manikins, except for the back of one manikin. Two reasons that may have caused this outcome are: 1) the manikin

was relatively tall compared to the lower storage shelf, 2) the manikin was staying a long time in a risky position.

4   Discussion

The research stemmed from problems caused by lack of correctness between real and virtual geometries of premises and workstation layouts. These differences normally occur due to the time consuming process of CAD modelling. Lack of correctness leads to reduced confidence and precision in production design processes, which can cause costly design errors (LINDSKOG et al., 2016). IPS IMMA provides a good virtual interaction and integrity between different related software via its different modules and import possibilities, e.g. the point cloud module. This combination makes the virtual environment in IPS IMMA more similar to the reality, both related to geometrical agreement between the real and the virtual environment, but also related to the completeness of the virtual representation since all physical items in the real world are being scanned into the virtual model. Another valuable feature is that the scanned representation resembles the real world to a high degree as the scan captures colours of the environment, creating a photo-like 3D representation. These characteristics are considered to support the designer to better visualise, understand, design and evaluate human-system interaction issues (HÖGBERG et al., 2016).

The sequence of importing components into the simulation does not make difference in the simulation. However, for this simulation, based on the component size and volume and work needed for a specific modification, importing point cloud, CAD geometry and manikins respectively eases the workflow. Additionally, to avoid a crowded environment, using hide/show options for every part of every component is advised to ease the simulation work.

It is possible to import the complete point cloud of an entire factory building into IPS IMMA. However, to have a better visualisation and to use the point cloud more precisely in the simulation, it is better to cut it to the intended area. The scanned area helps in understanding the spatial relationships between objects and assembly constrains, which makes the assembly simulation process more precise (YU et al., 2016).

There were some points in the point cloud file that were not accurate or some extra and irrelevant points. This normally happens due to disturbances such as reflections, blockings or moving objects (REX AND STOLI, 2014). The point cloud properties were modified to make the simulation smoother; when the render quality or point size was reduced it was easier to orient around the factory model and work on the simulation. Otherwise it sometimes took time to execute certain commands, e.g. move or zoom. In addition, it would be a great development if it was possible to convert point cloud information to mesh or NURBS. Clash detection features available in CAD software can be used also in point cloud to detect collisions (REX AND STOLI, 2014). However, if the file size is big, this function is currently not applicable directly in IPS.

Besides working with point clouds, IPS IMMA is considered as competitive to other similar DHM tools in terms of providing realistic postures and motions, having collision detection, instructing manikins by a high-level language, ability to work with manikin families to consider human diversity and assessing full work sequences (BJÖRKENSTAM et al., 2016; GLÄSER et al., 2016; HÖGBERG et al., 2016; MÅRDBERG et al., 2014). The purpose of having manikin families is to be able to apply the same tasks to different people in a range. This reduces the time for giving manikin instructions, and enables the consideration of human diversity among the assembly staff (HANSON et al., 2014).

The predefined postures and hand grips ease the manikin movement settings. However, manikins' postures can be set manually if needed, which takes more time but can be more exact. The manikin can also move in different ways, e.g. *walking,* which makes the movement more natural. However, to apply walking, distance of some steps is currently needed between the start and the end position.

Having digital manikins to simulate a work does not mean that real humans would act exactly as the manikins. Rather, the ambition of the DHM tool is to support engineers to make better and quicker decisions in production design processes, so that design solutions that offer expected levels of human well-being and overall system performance can be found (HÖGBERG et al., 2016).

Acknowledgment

List of references

Berglund, J.; Lindskog, E.; Johansson, B.: On the trade-off between data density and data capture duration in 3D laser scanning for production system engineering: Procedia CIRP 41 (2016) 697-701.

Björkenstam, S.; Delfs, N.; Carlson, J. S.; Bohlin, R.; Lennartson, B.: Enhancing Digital Human Motion Planning of Assembly Tasks Through Dynamics and Optimal Control, in: R. Soderberg (Ed.), 6th CIRP Conference on Assembly Technologies and Systems, CATS 2016, Elsevier B.V., 2016, pp. 20-25.

Boër, C. R.; Pedrazzoli, P.; Sacco, M.; Rinaldi, R.; De Pascale, G.; Avai, A.: Integrated computer aided design for assembly systems: CIRP Ann Manuf Technol 50 (2001) 17-20.

Bohlin, R.; Delfs, N.; Hanson, L.; Högberg, D.; Carlson, J. S.: Automatic creation of virtual manikin motions maximizing comfort in manual assembly processes, In

Technologies and Systems for Assembly Quality, Productivity and Customization : Proceedings of the 4th CIRP Conference on Assembly Technologies and Systems, 2012, pp. 209–212.

Brolin, E.: Anthropometric diversity and consideration of human capabilities: Methods for virtual product and production development.(Doctoral dissertation,Chalmers University of Technology), 2016.

Böhler, W.: Comparison of 3D laser scanning and other 3D measurement techniques: Recording, Modelling and Visualisation of Cultural Heritage (2005) 89-99.

Gläser, D.; Fritzsche, L.; Bauer, S.; Sylaja, V. J.: Ergonomic Assessment for DHM Simulations Facilitated by Sensor Data, in: R. Teti (Ed.), 48th CIRP International Conference on Manufacturing Systems, CIRP CMS 2015, Elsevier, 2016, pp. 702-705.

Hanson, L.; Högberg, D.; Carlson, J. S.; Bohlin, R.; Brolin, E.; Delfs, N.; Mårdberg, P.; Gustafsson, S.; Keyvani, A.; Rhen, I.-M.: IMMA–Intelligently moving manikins in automotive applications: Proceeding of ISHS (2014).

Högberg, D.; Hanson, L.; Bohlin, R.; Carlson, J. S.: Creating and shaping the DHM tool IMMA for ergonomic product and production design: International Journal of the Digital Human 1 (2016) 132-152.

Ingelsten, S.; Mark, A.; Edelvik, F.; Logg, A.; Österbring, M.: Urban CFD Simulation Using Point Cloud Data, 29th Nordic Seminar on Computational Mechanics, Gothenburg, Sweden, 2016.

IPS:Industrial Path Solutions (2017) http://industrialpathsolutions.se/

Lindskog, E.; Berglund, J.; Vallhagen, J.; Johansson, B.: Layout Planning and Geometry Analysis Using 3D Laser Scanning in Production System Redesign, in: R. Soderberg (Ed.), 6th CIRP Conference on Assembly Technologies and Systems, CATS 2016, Elsevier B.V., 2016, pp. 126-131.

Lindskog, E.; Berglund, J.; Vallhagen, J.; Berlin, R.; Johansson, B.: Combining point cloud technologies with discrete event simulation, 2012 Winter Simulation Conference, WSC 2012, Berlin, 2012.

Maruyama, T.; Kanai, S.; Date, H.; Tada, M.: Motion-capture-based walking simulation of digital human adapted to laser-scanned 3D as-is environments for accessibility evaluation: Journal of Computational Design and Engineering 3 (2016) 250-265.

Mårdberg, P.; Carlson, J. S.; Bohlin, R.; Delfs, N.; Gustafsson, S.; Högberg, D.; Hanson, L.: Using a formal high-level language and an automated manikin to automatically generate assembly instructions: International Journal of Human Factors Modelling and Simulation 2 4 (2014) 233-249.

Rex, D.; Stoli, S.: Applications of 3D Laser Scanning in a Production Environment: Chalmers University of Technology (2014).

Schaub, K. G.; Mühlstedt, J.; Illmann, B.; Bauer, S.; Fritzsche, L.; Wagner, T.; Bullinger-Hoffmann, A. C.; Bruder, R.: Ergonomic assessment of automotive assembly tasks with digital human modelling and the 'ergonomics assessment worksheet'(EAWS): International Journal of Human Factors Modelling and Simulation 3 (2012) 398-426.

Yu, A.; Liu, Z.; Duan, G.; Tan, J.; Che, L.; Chen, X.: Geometric Design Model and Object Scanning Mode Based Virtual Assembly and Repair Analysis, in: R. Soderberg (Ed.), 6th CIRP Conference on Assembly Technologies and Systems, CATS 2016, Elsevier B.V., 2016, pp. 144-150.